Università degli Studi di Ferrara

DOCTORAL COURSE IN
ENGINEERING SCIENCES

CYCLE XXXI

DIRECTOR Prof. Trillo Stefano

MULTISPECTRAL PROXIMAL REMOTE SENSING BY UNMANNED AERIAL VEHICLES (UAVS): LOW-COST SENSORS APPLICATION IN PRECISION AGRICULTURE AND COASTAL MONITORING

Scientific/Disciplinary Sector (SDS) ICAR/06

Candidate
Dott. Taddia Yuri

_____
(signature)

Supervisor
Prof. Russo Paolo

_____
(signature)

Co-Tutor
Prof. Pellegrinelli Alberto

_____
(signature)

Years 2015/2018

Abstract

In the last few years the use of Unmanned Aerial Vehicles (UAVs), or simply *drones*, has involved many fields.

Their extreme versatility has made them effective devices also in the field of remote sensing, thanks to the increasing availability of instrumentation that can be installed onboard, from LiDAR (Light Detection And Ranging) systems to digital cameras of different types.

Among these, the number of low-cost multispectral cameras able to detect spectral information in the near infrared region has increased significantly. Thanks to the high geometric resolution (at a centimetre level) made possible by the use of UAVs, the applications of these cameras may now space from the precision farming (or precision agriculture) to the detection and characterization of the different ground cover types.

However, the effective reliability of the data sensed depend on both the knowledge of the spectral sensitivity of the used sensors and the actual environmental light conditions at the time of each image acquisition.

Therefore, this PhD thesis analyses the results retrievable by the use of some low-cost multispectral cameras with particular regard to the precision farming and the coastal monitoring of the submerged seaweed in the lagoon of Goro, both in terms of final accuracy and effectiveness in using radiometric calibration procedures.

The results highlight how multispectral low-cost cameras can be successfully used to assess the health status of crops as well as detecting the seaweed. However, it is only applying rigorous radiometric calibration procedures that becomes possible to perform a monitoring over time, computing accurate and reliable reflectance values. In lack of devices such as downwelling light sensors or known reflectance panels it is only possible to compute spectral indices with a temporal validity limited to the single survey.

Riassunto

Negli ultimi anni l'uso di Aeromobili a Pilotaggio Remoto (APR), o semplicemente *droni,* ha interessato molti campi.

La loro estrema versatilità li ha resi efficaci strumenti anche nel campo del telerilevamento, grazie alla crescente disponibilità di sensoristica installabile a bordo, da sistemi LiDAR (Light Detection And Ranging) a camere digitali di vario tipo.

Tra queste ultime, è aumentato il numero di camere multispettrali a basso costo capaci di acquisire informazioni spettrali nel campo del vicino infrarosso. Grazie all'elevata risoluzione geometrica (centimetrica) che è possibile raggiungere mediante l'uso di APR, le applicazioni di queste camere multispettrali possono oggi spaziare dall'agricoltura di precisione alla determinazione delle varie coperture al suolo attraverso procedure di classificazione.

L'effettiva attendibilità dei dati acquisiti dipende tuttavia sia dalla conoscenza della sensibilità spettrale dei sensori impiegati, sia dalle reali condizioni di illuminazione ambientale al momento dell'acquisizione di ogni singola immagine.

In questa tesi di dottorato vengono pertanto analizzati i risultati ottenibili attraverso l'impiego di alcune camere multispettrali a basso costo con particolare riguardo all'agricoltura di precisione e al monitoraggio costiero delle alghe nella Sacca di Goro, sia in termini di accuratezza finale conseguita che di necessità ed efficacia nell'impiego di procedure di calibrazione radiometrica.

Dai risultati ottenuti si evince come sia possibile utilizzare con successo camere multispettrali a basso costo sia nell'ambito della caratterizzazione dello stato di salute di una coltivazione che nel monitoraggio algale. Tuttavia è solamente grazie a procedure rigorose di calibrazione radiometrica che diventa possibile effettuare un monitoraggio nel tempo, grazie alla possibilità di calcolare valori di riflettanza accurati ed attendibili. In mancanza di dispositivi quali sensori di irradianza ambientale o pannelli a riflettanza nota risulta solamente possibile effettuare computi di indici spettrali con una validità temporale limitata al singolo rilievo.

Table of Contents

Introduction

In the last decade and especially in the last few years, Unmanned Aerial Vehicles (UAVs) have become crucial devices able to perform a multitude of tasks.

The number of their applications is becoming really huge and involves almost every field, from surveillance to ecology. UAVs also represent a revolutionary device for geoscience purposes, including environmental monitoring, ecohydrology, forest studies and land mapping.

A UAV can be considered as a sort of a little robot with the capability to fly autonomously and being remotely piloted by a ground operator. Depending on the instruments mounted onboard, these robots (usually called “drones” due to the noise they produce whenever their propellers are quickly rotating) can practically perform any kind of task or even measurement.

The traditional remote sensing by satellite, including the acquisition of multispectral data, and the proximal remote sensing, carried out by the means of airplanes equipped by aerial cameras, has experienced an important development thanks to the introduction of the UAVs.

The miniaturization process of the sensors, in fact, allowed to produce smaller and lightweight devices to be mounted on drones in the past years.

The use of simple RGB cameras on a UAV enables the acquisition of information in the visible region of the spectrum. This data can be used for a more classical photogrammetric approach in order to reconstruct three-dimensional models, orthophotos and digital elevation models.

Nowadays, advanced computer vision techniques are also available for the automatic detection of tie points and the reconstruction of dense point clouds, with a density level comparable to terrestrial laser scanners for high resolution image captures.

The development of multispectral and even thermal sensors for drones allows to acquire additional information in other regions of the spectrum, involving further wavelengths.

The cost of these cameras, sometimes consisting in a real detection and processing system, is becoming to decrease.

Low-cost systems comprise a wide range of solutions, from simply modified cameras with the application of a bandpass filter, but that are still related to the classical manufacturing layout of photographic digital cameras (such as the presence of Bayer's patterns), to multi-optics sensors interfaced with devices devoted to the measure of the environmental irradiance.

Most of the more performant systems are already able to apply radiometric corrections to the raw data sensed by the use of a Downwelling Light Sensor (DLS) that measures the solar irradiance at the top of the drone.

Alternatively, a known reflectance panel, whose response at different wavelengths is accurately measured in order to assume the panel as a reference standard, can be used. In this way the relationship between the radiance retrievable by the means the images and the actual reflectance may be computed by using a simple scale factor. The DLS is crucial for accounting for change in environmental irradiance whenever a panel is used.

Multispectral cameras can be used for precision agriculture and crop management, allowing to assess the health status of the vegetation and planning the most effective strategy of intervention for both eliminating weeds or managing the fertiliser and avoiding an excessive introduction of nutrients within the groundwater.

Other applications regard the detection of ground cover types, similarly to the classification of satellite imageries. In this case, the detection may also be addressed in order to assess the evolution of a certain cover type for monitoring over time purposes.

However, for any application of multispectral imageries at least two factors are crucial.

The first is represented by the accuracy of the data sensed by the sensors, both geometrically and radiometrically. The former aspect is overcome thanks to the use of onboard GPS or by the deployment of Ground Control Points allowing a post processing georeferencing. The latter has been improved within the last few years with onboard DLSs.

The second factor is the cost of the system. In fact, hyperspectral cameras are also becoming available, but their still high cost (up to some tens of thousands of

euros) represents a limit. Furthermore, the weight is still much higher of any multispectral sensor.

For these reasons, this PhD dissertation presents a study concerning the applications of low-cost multispectral sensors, from the use of simply modified cameras in precision agriculture to the more challenging seaweed detection and quantification over time in the lagoon of Goro.

The effects of different radiometric calibration procedures are therefore analysed for a better understanding of whether a calibration is always needed or not. Also, the differences in using a DLS or a known reflectance panel, or even both them, are discussed.

A general introduction on remote sensing physical principles is presented in Chapter 1, from electromagnetic radiation to bidirectional reflectance, spectral indices and image classification.

Chapter 2 presents an introduction to the use of unmanned aircraft with particular regard to remote sensing applications as well as how digital sensors work. In addition, both geometric and radiometric calibration procedure are discussed, together with a brief introduction of the Structure from Motion (SfM) approach used to stitch multispectral imageries.

The experimental part of this PhD thesis is reported in the following chapters. Chapter 3 presents the studies conducted within the precision farming, from the first campaigns using MAPIR cameras and the Sentera Single sensor, to the comparison between the latter and a Parrot Sequoia multispectral camera equipped with a DLS.

Chapter 4 reports a prelude to the following one and it is focussed on the coastal monitoring of embryo dunes.

Finally, Chapter 5 presents all the results obtained using the MicaSense RedEdge-M multispectral camera for the submerged seaweed monitoring in the context of the lagoon of Goro. The study was not focussed on the detection and quantification of the seaweed only, but regarded also the comparison between two of the most common SfM processing software (Agisoft PhotoScan Professional and Pix4D Mapper Pro) and the effectiveness of the radiometric corrections.

CHAPTER 1

REMOTE SENSING: THEORY AND DEFINITIONS

1.1 Introduction

Life on Earth strongly depends on the light coming from the Sun. Thanks to this incoming radiation, the plants are able to convert the carbon dioxide in the atmosphere into molecular oxygen through the photosynthesis process. This impacts in many ways:

- an improper high concentration of atmospheric CO_2 is responsible for the greenhouse effect and thus influences the overall balance of terrestrial energy;
- the availability of atmospheric O_2 allows all the animals, including human beings, to breathe.

Plants are also at the basis of any food chain and the health of the vegetation is therefore crucial for any ecosystem all around our planet. The assessment of such a vegetation health status can be conducted through biochemical studies on tissue extracts, but this kind of analysis is generally limited in its spatial extent and certainly destructive.

Remote sensing techniques represent an alternative and non-destructive way to assess the vegetation status: they exploit the radiations coming from the Sun to analyse the response of the so-called “canopy”. This term refers to the aboveground portion of a plant community and is thus the same portion visible looking down on a forest. Like any other material, the leaves and more generally any vegetative surface are characterized by particular absorption and reflection rates in the different wavelengths of the electromagnetic spectrum. This principle is at the basis of any remote sensing detection.

In this chapter a physical background on electromagnetic radiations and their properties, like the interaction with the matter, is therefore provided, focusing on remote sensing implications.

The classical approach in remote sensing techniques is to use satellite platforms observing the Earth from the space.

The first reference to the term "remote sensing" meaning a detection and measurement technique of an object without touching it (contactless) was made in the 1960. Through the decades, the term was mainly used in relation with the Earth observation's disciplines.

In the 1966 the planning of the Earth Resources Observation Satellite (EROS), the first earth observing system, started, while the first observations by satellite occurred many years later. The first Landsat satellite (initially called ERTS-1 and subsequently renamed) was launched in 1972.

Nowadays, many satellite imageries are public thanks to the US National Aeronautics and Space Administration (NASA) initiative of making its data free in 2008 and the recent Copernicus project of the European Spatial Agency (ESA) with Sentinel satellites.

1.2 The electromagnetic radiation

The electromagnetic radiation is characterized by both an electric and magnetic field that are time-varying. This means that the magnitude and/or the direction changes with time. In particular, the magnitude of the electric and magnetic vectors changes regularly since the electromagnetic radiation is composed of a magnetic field and an electric field that are oscillating in phase at right angles to each other. The magnitude of both vectors changes sinusoidally, so the term "wave" is commonly used when referring to an electromagnetic radiation (Figure 1.1).

Electromagnetic waves can travel not only in a medium, but also in the vacuum, unlike other kind of waves (e.g. acoustic waves) that cannot do that.

The spatial distance between two consecutive peaks (maximum values) in an electromagnetic wave is called "wavelength" (denotated with the Greek letter lambda λ), whereas the number of cycles in the time unit is called "frequency" (denotated with the letter f).

Since the speed of any electromagnetic wave is a constant value in the vacuum given by

$$c \approx 2.99792458 \times 10^8 \ \left(\mathrm{m\ s^{-1}}\right) , \qquad \text{(Eq 1.1)}$$

the following relationship between the frequency and the wavelength exists for any electromagnetic wave:

$$\lambda = \frac{c}{f} . \qquad \text{(Eq 1.2)}$$

This means that waves with a higher frequency have a shorter wavelength and vice versa.

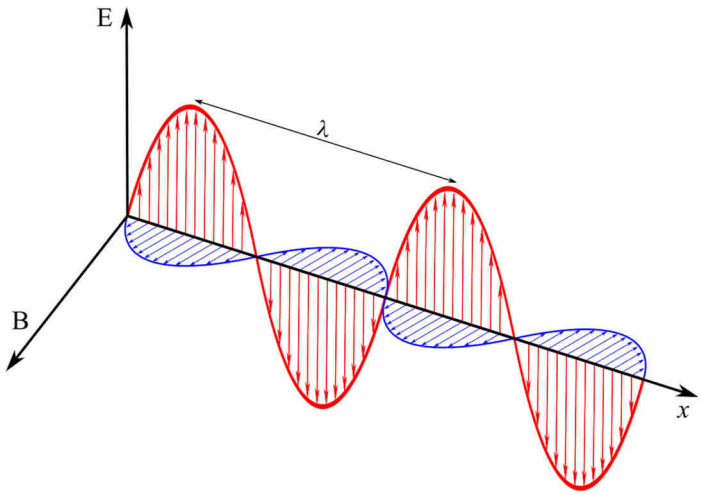

Figure 1.1 An electromagnetic wave: the electric (*E*) field is represented in red, while the blue is the magnetic field (*B*). Both fields' vectors change with time along the propagation direction (*x*) of the wave.

1.2.1 Electromagnetic spectrum

The electromagnetic radiation is conventionally divided in regions:

- γ ray, with wavelengths smaller than 0.03 nm;
- X ray, with wavelengths between 0.03 nm and 3 nm;
- UV rays, with wavelengths between 3 nm and 400 nm;
- Visible rays, with wavelengths between 400 nm and 700 nm:
    - Blue is in the range 400 nm ÷ 500 nm;
    - Green is in the range 500 nm ÷ 600 nm;
    - Red is in the range 600 nm ÷ 700 nm;

- Infrared rays, with wavelengths between 700 nm and 1 mm. This region is very wide and it's therefore subdivided in:
    - Near Infrared (NIR), ranging from 700 nm and 1300 nm;
    - Short Wave Infrared (SWIR), ranging from 1.3 μm and 3 μm;
    - Medium Wave Infrared (MWIR), ranging from 3 μm and 7 μm;
    - Thermal Infrared (TIR), ranging from 7 μm and 20 μm;
    - Far Infrared (FIR), ranging from 20 μm and 1 mm.
- Radio waves with wavelengths larger than 1 mm (including microwaves, having wavelengths between 1 mm and 1 m).

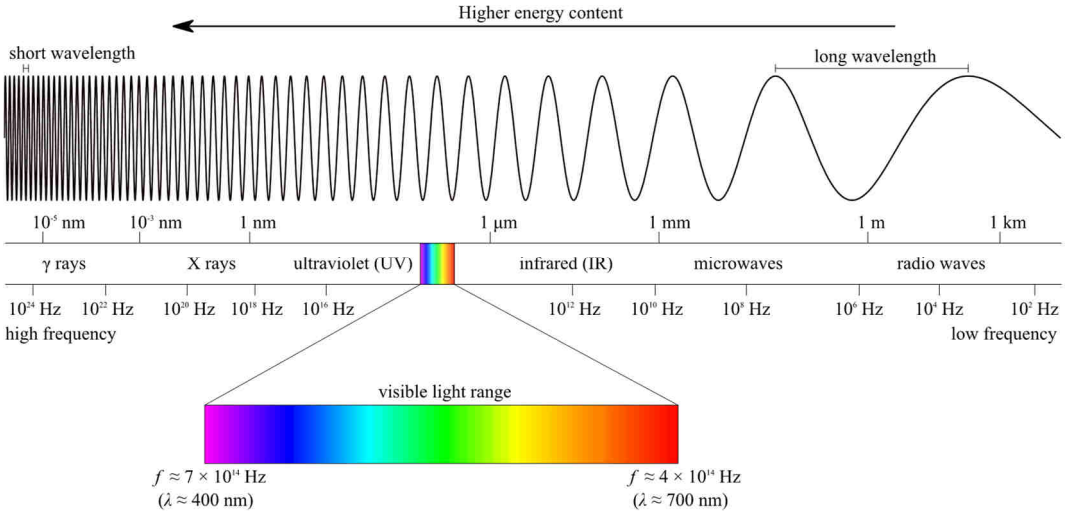

Figure 1.2 Electromagnetic spectrum: energy content is higher for short wavelengths. The visible light range is very narrow if compared to the whole spectrum extent (colours are qualitative).

1.2.2 Electromagnetic energy

Electromagnetic waves carry an amount of energy, since they combine an electric field and a magnetic field. In particular, the energy content of an electromagnetic wave increases with its frequency. The energy is therefore also a function of the wavelength given by

$$E(\lambda) = h \cdot f = \frac{h \cdot c}{\lambda} \qquad \text{(Eq 1.3)}$$

where $h = 6.626 \times 10^{-34}\,(\mathrm{J\ s})$ is the *Planck's constant*. Since the quantity at the numerator is a constant, given by the product of two fundamental physical

constants, the energy depends only on the wavelength. More precisely, the energy content of an electromagnetic wave is inversely proportional to its own wavelength.

Substituting a wavelength value in (Eq 1.3), the corresponding energy amount refers to a sort of energy unitary quantity that is called *quantum*.

The quanta have a particular behaviour: according to the branch of *quantum mechanics*, a quantum behave a bit like a particle, since its effect is localized and not much distributed like should be if distributed along a wave.

The name of this kind of particle, related to electromagnetic waves, is called *photon*. A simple substitution in (Eq 1.3) demonstrates that the energy carried by a γ-ray photon is much higher than the energy carried by a radio wave photon, due to the different wavelengths of the waves their selves.

1.2.3 Radiation sources

The electromagnetic energy can be generated through many different physical processes. The decay of radioactive materials and the changes in energy levels of electrons (transitions) inside atoms are examples of these radiation generating processes.

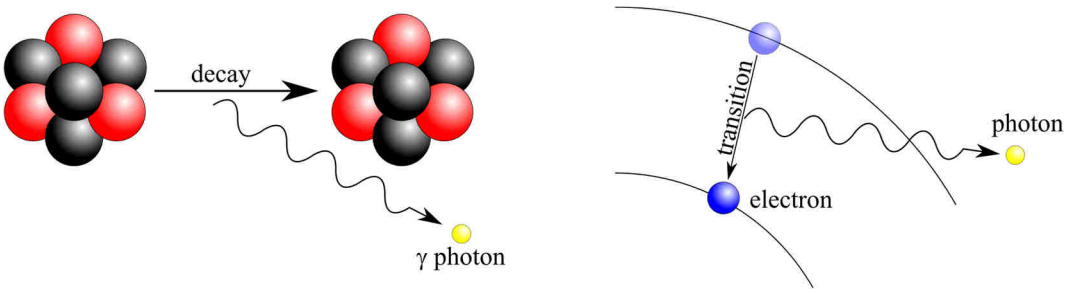

Figure 1.3 Examples of radiation sources: an electron transition (on the left) and a radioactive isotope decay (on the right). Both the processes generate a photon.

Furthermore, any body with a temperature above the absolute zero (0 K equivalent to ≈ -273.15 °C) represents a source of electromagnetic radiations due to the internal motion of the particles that form the matter. Higher it is the motion of the particles in unit time and higher it is the temperature of the material consisting in those particles. Usually, an ideal source is defined when referring to this kind of electromagnetic energy source: the *black body*. A black body have a behaviour that consists in being a total absorber and emitter of radiations; in other words, all of the total incident radiation received by the black body's surface is

absorbed and then it emits the maximum possible amount of radiation. This latter quantity is strictly related with the black body's temperature.

The Stefan-Boltzmann law describes this relationship between the total amount of energy (E) emitted by a black body with a specific absolute temperature (T), in unit time and per unit area of the body:

$$E = \sigma \cdot T^4 \qquad \text{(Eq 1.4)}$$

where $\sigma = 5.67 \times 10^{-8} \left(\mathrm{W\ m^{-2}\ K^{-4}} \right)$ represents the Stefan-Boltzmann constant. In the expression (Eq 1.4), *E* is an energy flux in $\mathrm{W\ m^{-2}}$ and it is called *radiant exitance*.

The generalization of the Stefan-Boltzmann law for real bodies, known as Kirchhoff's law, requires to introduce the concept of *emissivity* of a body, denotated with the Greek letter ε:

$$E = \varepsilon \cdot \sigma \cdot T^4 \qquad \text{(Eq 1.5)}$$

The emissivity can be considered like a sort of efficiency of a real body in emitting radiations in comparison with the amount of energy that is emitted by a black body having the same temperature. Thus, the emissivity can assume any value from 0 (white bodies that do not adsorb nor emit any energy) to 1 (black bodies). However, the emissivity ε generally depends on the wavelength, so it is more correct to speak about *spectral emissivity* $\varepsilon_\lambda = \varepsilon(\lambda)$. Bodies with a non-wavelength dependent emissivity ε in the range $0 < \varepsilon < 1$ are called *grey bodies*.

Considering again a black body, the energy distribution is given by the Planck's distribution law. In particular, the following expression gives the spectral radiant exitance, that is a power emitted per unit area of the black body from the range of wavelength between λ and $\lambda + \mathrm{d}\lambda$:

$$E_\lambda = \varepsilon_\lambda \cdot \mathrm{d}\lambda = \frac{2hc^2}{\lambda^5 \left(e^{\frac{hc}{\lambda k T}} - 1 \right)} \cdot \mathrm{d}\lambda \qquad \text{(Eq 1.6)}$$

where h is the Planck's constant, c is the speed of light in the vacuum and $k = 1.381 \times 10^{-23} \left(\mathrm{J\ K^{-1}} \right)$ is the Boltzmann's constant.

The wavelength value that maximize E_λ in (Eq 1.6) is given by Wien's displacement law and equals to

$$\lambda_{\max} = \frac{b}{T} \qquad \text{(Eq 1.7)}$$

where $b = 2.89777 \times 10^{-3} \left(\mathrm{m\ K}\right)$ is the Wien's displacement constant.

For example, considering a black body having the same effective temperature of the Sun, that is ca. $5800\ \mathrm{K}$, the spectral distribution of the radiation emitted is shown in Figure 1.4 and the peak value is found for the wavelength $\lambda_{\max} = \frac{b}{T} = \frac{2.89777 \times 10^{-3} \left(\mathrm{m\ K}\right)}{5800\ (\mathrm{K})} \approx 500\ \left(\mathrm{nm}\right)$.

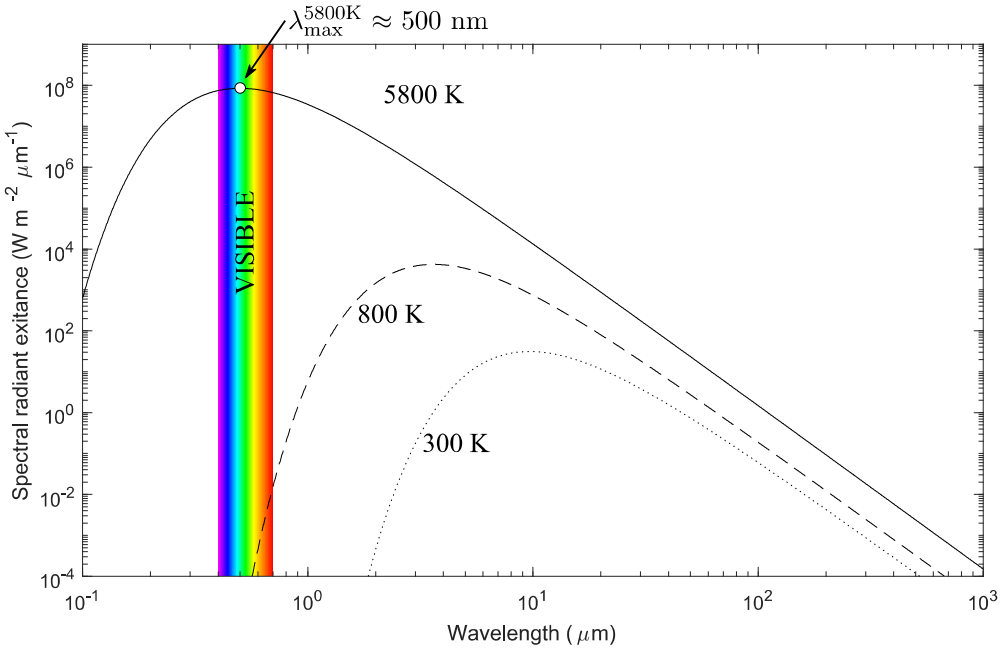

Figure 1.4 The spectral radiant exitance of black bodies at different temperature according to Planck's law (into a hemisphere). Notice that the peak wavelength for a 5800 K black body's temperature (that is approximately the effective temperature of the Sun) is ca. 500 nm.

Starting from the expression (Eq 1.6) it is possible to deduce the Stefan-Boltzmann law by performing an integration over all the wavelengths. Since the unit area of the black body that has been considered as the radiation source lies on a plane, the radiation will spread into a hemisphere. Furthermore, since a black body has a perfect diffusive behaviour, according to Lambert's cosine law:

$$I = I_{\max} \cdot \cos\theta \qquad \text{(Eq 1.8)}$$

where θ is the zenith angle, the total radiation emitted by a black body's unit area over the hemisphere is given by:

$$\int_0^{2\pi}\int_0^{\pi/2} I_{\max} \cdot \cos\theta \cdot \sin\theta \; \mathrm{d}\varphi \; \mathrm{d}\theta = \pi \cdot I_{\max} \qquad \text{(Eq 1.9)}$$

The quantity $\sin\theta$ is the determinant of the Jacobian for the spherical coordinates transformation and φ is the azimuth angle; since we are referring to steradians, the radius r does not appear due to the r^2 normalization.

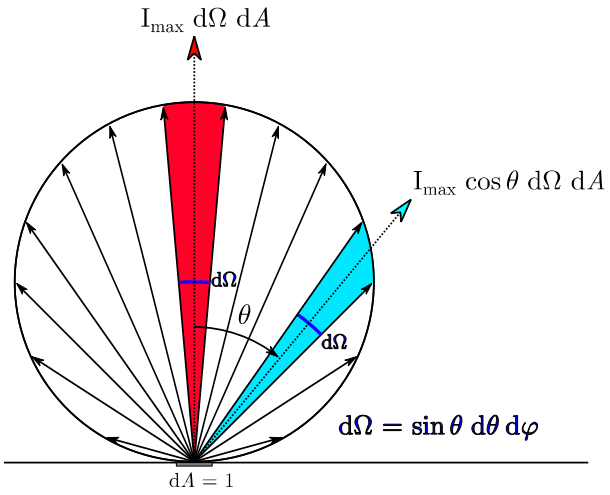

Figure 1.5 Schematization of the irradiance of a black body obeying to Lambert's cosine law: the irradiance is maximium along the normal to the surface. The quantity Ω represents the solid angle in steradians.

Thus, the integral of E_λ from $\lambda = 0$ to $\lambda = +\infty$ over the hemisphere is

$$E = \int_0^{\infty} \frac{2\pi hc^2}{\lambda^5 \left(e^{\frac{hc}{\lambda k T}} - 1 \right)} \cdot \mathrm{d}\lambda = \sigma \cdot T^4 \qquad \text{(Eq 1.10)}$$

where the Stefan-Boltzmann constant σ is defined as

$$\sigma = \frac{2\pi^5 k^4}{15 c^2 h^3} \qquad \text{(Eq 1.11)}$$

1.2.4 Radiometric definitions

When speaking about radiations that are adsorbed or emitted by the matter, many are the quantities we can refer to. In the previous paragraph we discussed about energy, radiant exitance and so on. A quite comprehensive list of terms that

are commonly used in remote sensing is thus given here with the purpose of focusing on the many different definitions.

As a remark, the substantive "spectral" is generally used when we want to highlight that a quantity is dependent on the wavelength. In this case, it is also common to use the subscript λ .

- **Radiant Energy** $(\mathbf{E})$: it is the total energy that is radiated in all the directions. Since it is an energy, the unit is the Joule (J).
- **Radiant Flux** $(\mathbf{\Phi})$: it is defined as the radiant energy per unit time. Its unit is joules per second, thus Watt (W).
- **Radiant Flux Density** $(\mathbf{R})$: it is the radiant flux through a surface, expressed per unit area. The unit is therefore watts per square metre $\left(\mathrm{W\,m^{-2}}\right)$.
- **Irradiance** $(\mathbf{I})$: it is the radiant flux incident on unit area; the unit is watts per square metre again $\left(\mathrm{W\,m^{-2}}\right)$.
- **Radiance** $(\mathbf{L})$: the radiance is the radiant flux per unit area per unit solid angle. The unit is watts per square metre per steradian $\left(\mathrm{W\,m^{-2}\ sr^{-1}}\right)$.
- **Radiant Exitance** $(\mathbf{M})$: this term refers to the total energy that is radiated in all the directions in unit time per unit area $\left(\mathrm{W\,m^{-2}}\right)$.
- **Spectral Irradiance** $(\mathbf{I}_\lambda)$: it is the irradiance per unit wavelength. In the International System the unit should be $\mathrm{W\ m^{-3}}$, but it is more common to use watts per square metre per micrometre $(\mathrm{W\,m^{-2}\ \mu m^{-1}})$, since this is particularly useful for visible and infrared wavelengths.

For example, using these definitions, we can write that the radiant exitance for a black body with a perfect diffusive (Lambertian) behaviour emitting radiations into a hemisphere is given by:

$$\mathbf{M} = \pi \cdot \mathbf{L} \qquad \text{(Eq 1.12)}$$

1.2.5 The solar constant

The real Sun spectrum is slightly different in comparison to the spectral distribution given by the Planck's law for a black body at the same effective temperature. Furthermore, the total amount of solar radiation that is received at the top of the atmosphere $\left(\mathbf{I}_{\text{toa}}\right)$ is a parameter that strongly affects both the weather and the climate on the Earth. This quantity seasonally fluctuates, mainly due to the fact that the Sun-Earth distance varies through the year with a minimum (perihelion) on January and a maximum (aphelion) on July [1]. In 2018, the perihelion occurred on January, 3rd at 05:35 UTC while the aphelion occurred on July, 6th at 16:47 UTC [2].

The above-mentioned total amount of solar radiation at the top of the atmosphere is called *solar constant*. It has been measured since the 1837, by Pouillet, obtaining a value of $1230\ \mathrm{W\ m^{-2}}$ [3]. A recent value for the solar constant, defined by the American Society for Testing and Materials International in 2000, is $1366.1\ \mathrm{W\ m^{-2}}$ [4]. This value was further confirmed in 2004 by Gueymard [5].

The solar constant S_C thus represents the integral of the solar irradiance over all the wavelengths:

$$S_C = \int_0^\infty E_\lambda \mathrm{d}\lambda \qquad \text{(Eq 1.13)}$$

However, a re-evaluation of the solar constant published in April 2018 by Gueymard [3] and based on a 42-year of total solar irradiance time series, that takes also into account the progress in space radiometry since the determination of the previous solar constant value in the early 2000s, shows that the revised solar constant is $1361.1\ \mathrm{W\ m^{-2}}$, thus approximately $5\ \mathrm{W\ m^{-2}}$ less than the previous one. The estimated standard uncertainty of the new value is $0.5\ \mathrm{W\ m^{-2}}$, so the difference is significant and it is not due to error propagation.

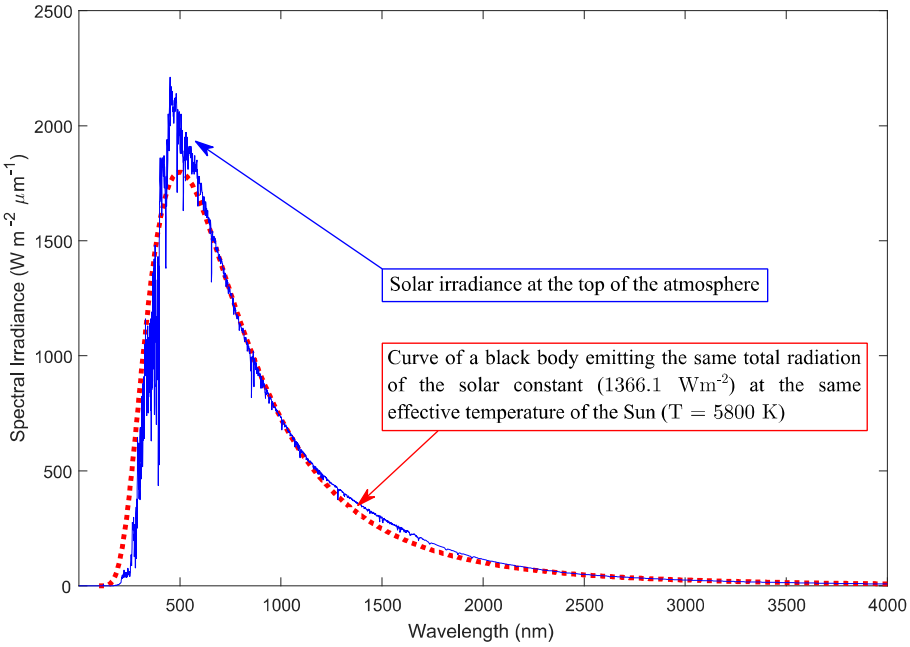

Figure 1.6 A comparison between the solar irradiance at the top of the atmosphere and the corresponding theorical irradiance of a black body having the same effective temperature of the Sun (ca. 5800 K) and emitting a total of 1366.1 W m^{-2}, which is the solar constant. The extraterrestrial spectrum in [5] has been used as the solar irradiance at the top of the atmosphere for this figure.

1.3 The interaction with the matter

Whenever an electromagnetic radiation hits a material, an interaction between the photons and the matter particles takes place. Previously, we spoke about electron transitions inside atoms like a source of electromagnetic waves: a similar, but reverse, phenomenon can be the result of a photon that interacts with an atom. In other words, if the energy carried by the photon, according to (Eq 1.3), is the same energy the electron needs for its transition, then the electron will change level. In this case the photon is absorbed. If the same atom is excited by some process (like by electricity currents or by heating), photons with an equal content of energy can be emitted, so the same wavelength is involved in both absorption and emission of the electromagnetic radiation. This behaviour is common for wavelengths that belong to the visible region of the spectrum.

At lower energy contents, when wavelengths are longer, such as in the thermal infrared region (TIR), the interaction consists more often in molecular vibrations. This kind of interaction is not strictly related to a specific needed amount of energy by the particles, like in the case of electron transitions, so a wider range of these wavelengths can interact with a substance.

For visible and infrared (up to TIR) wavelengths, it is the electric field of the electromagnetic radiation that mainly interacts with the matter. Instead, for radio waves, thus including microwaves, it is the magnetic field the responsible for the interactions with substances. The water is characterized by a very strongly absorption in the microwaves region, since it is a highly polar liquid. In remote sensing this implies that the water content of the upper layer of the soil strongly limits the penetration of microwaves into the ground.

The absorption and the emission are not the only way through which the energy is conserved during an interaction with the matter. More generally, when an electromagnetic incident radiation hits the matter, part of it is reflected by the surface of the material, part is absorbed as previously stated, and part can be transmitted by the material (Figure 1.7):

$$E_{I(\lambda)} = E_{R(\lambda)} + E_{A(\lambda)} + E_{T(\lambda)} \qquad \text{(Eq 1.14)}$$

Since the energy is conserved, each component on the right side of the above expression can be written as a fraction of the incident radiation:

$$E_{I(\lambda)} = \rho \cdot E_{I(\lambda)} + \alpha \cdot E_{I(\lambda)} + \tau \cdot E_{I(\lambda)} \qquad \text{(Eq 1.15)}$$

Thus, dividing by $E_{I(\lambda)}$, the following relationship between the parameters ρ, α, τ exists:

$$\rho + \alpha + \tau = 1 \qquad \text{(Eq 1.16)}$$

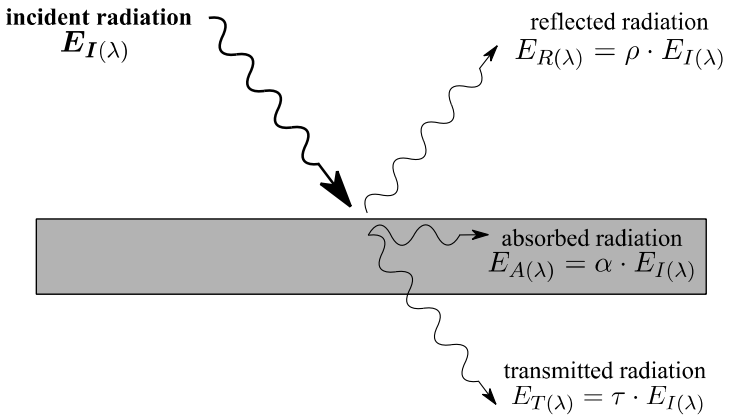

Figure 1.7 Interaction between an incident radiation and a material: three components are respectively reflected, absorbed and transmitted. However, the total amount of energy is conserved.

These parameters are respectively the *reflectance* (ρ), the *absorptance* (α) and the *transmittance* (τ) of the material. They depend on the surface type and conditions of the material itself. Furthermore, since each of these parameters are wavelength dependent, as it was the emissivity, we should strictly speak about *spectral reflectance* (ρ_λ), *spectral absorptance* (α_λ) and *spectral transmittance* (τ_λ).

In optical remote sensing, when visible wavelengths are used, the component that is detected is the reflected one. However, in the case of thermal remote sensing an emitted radiation adds to the reflected radiation: since the temperature of the Earth's surface is about $300\ \mathrm{K}$, and the peak in spectral radiant exitance of a black body with this temperature is $9.66\ \mu\mathrm{m}$, thus in the TIR region.

1.3.1 Interaction with the atmosphere

In satellite remote sensing, both the incident radiation that comes from the Sun and the reflected or emitted radiation that comes from the Earth's surface interact with the terrestrial atmosphere.

The atmosphere is a mixture of gases where molecular nitrogen N_2 (ca. 78%) and molecular oxygen O_2 (ca. 21%) are the main constituents. The remaining 1% contains water vapour, carbon dioxide, ozone, methane and aerosols. Even though nitrogen and oxygen are approximately uniformly distributed around the world, the distribution of the other constituents is highly spatially variable, since they can be generated and/or destroyed in specific location on the Earth. Higher concentrations of carbon dioxide are typically found in human activity areas, while water vapour is common above the oceans. Also concerning the vertical distribution, we can notice that the carbon dioxide tends to be well distributed from the ground to the upper atmosphere. Water vapour, on the contrary, is confined to the troposphere and is present up to no more than 15 km altitudes.

The atmosphere is responsible for two different effects, at least:

- the attenuation, in both Sun-Earth and Earth-satellite directions, of the radiations which traverse the atmosphere. Referring to the Sun-Earth path only, for simplicity, this phenomenon implies that, for each

wavelength, only the fraction that is transmitted by the atmosphere can reach the ground A fraction of the remaining part is reflected and is thus scattered, the other is absorbed whilst passing through the atmosphere.

- the addition of the fraction of the incident (sunlight) radiation that is scattered by the atmospheric constituents back to the satellite sensor and that has neither reached the Earth's surface, nor has ever pass through the whole atmosphere.

The first of these effects can be modelled considering the behaviour of a monochromatic radiation that traverse a gas. When the incoming radiation passes through a layer with a thickness equal to $\mathrm{d}x$, then the signal is attenuated by the measure of $\mathrm{d}\mathbf{I}_\lambda$. Introducing the *extinction coefficient* k_λ, this attenuation is thus given by

$$\left|\mathrm{d}\mathbf{I}_\lambda\right| = \mathbf{I}_\lambda \cdot k_\lambda \cdot \mathrm{d}x \qquad \text{(Eq 1.17)}$$

The integration of the (Eq 1.17) on a finite path length leads to the expression of the *Beer-Lambert law*. The transmitted radiation $\mathbf{I}_{t,\lambda}$ exhibits an exponential decay:

$$\mathbf{I}_{t,\lambda} = \mathbf{I}_{i,\lambda} \cdot e^{-k_\lambda \cdot x} \qquad \text{(Eq 1.18)}$$

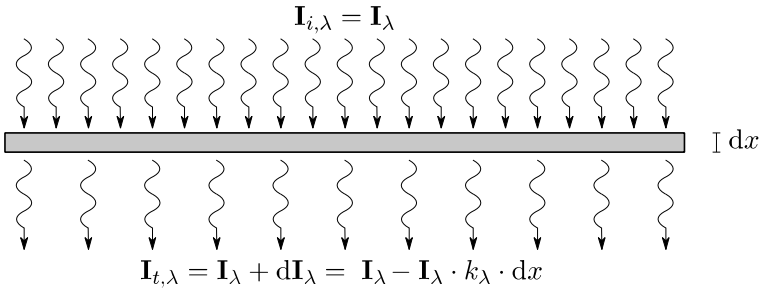

Figure 1.8 Absorption effect of a layer with thickness dx on an incident radiation. The integration on a finite path length gives the Beer-Lambert law.

When the transmission takes place along a vertical path, with a null zenith angle, then the term $k_\lambda \cdot x$ is defined as *optical depth*, denotated (once again as it was for the transmittance) with the Greek letter τ. In order to avoid confusion, this symbol will henceforth be replaced with $\tilde{\tau}_\lambda$ when discussing about the optical depth, where the subscript highlights the wavelength dependency.

Since in the expression (Eq 1.18) the quantity $\mathbf{I}_{i,\lambda}$ is the incident irradiance and $\mathbf{I}_{t,\lambda}$ is the transmitted irradiance, the transmittance can be calculated as

$$\tau_\lambda = \frac{\mathbf{I}_{t,\lambda}}{\mathbf{I}_{i,\lambda}} = e^{-k_\lambda \cdot x} = e^{-\tilde{\tau}_\lambda} \qquad \text{(Eq 1.19)}$$

For estimating the attenuation of radiations with a non-null zenith angle of incidence, the *optical air mass* $\left(m\right)$ concept is introduced. The air mass is defined as the ratio between the atmosphere's mass per unit cross-sectional area that a solar beam is actually passing through and the corresponding mass per unit cross-sectional area referred to a sea level site with the solar beam coming from the zenith. With this definition, the expression (Eq 1.18) becomes

$$\mathbf{I}_{t,\lambda} = \mathbf{I}_{i,\lambda} \cdot e^{-\tilde{\tau}_\lambda \cdot m} \qquad \text{(Eq 1.20)}$$

where the value of m increases with the solar zenith angle, but decreases with the elevation above the sea level, proportionally to the ratio between the atmospheric pressure at a *z* altitude $\left(P_z\right)$ and the atmospheric pressure at sea level $\left(P_0\right)$. According to the Lambert's cosine law, the increasing amount of the air mass with the solar zenith angle can be quantified as $1 / \cos\theta$, thus:

$$m = \frac{P_z}{P_0} \cdot \frac{1}{\cos\theta} \qquad \text{(Eq 1.21)}$$

An estimation of $P_z \ / \ P_0$ is given by introducing the further concept of *scale height* $\left(H\right)$, with an approximate value of $8 \times 10^3 \ \left(\mathrm{m}\right)$ at $T = 273 \ \mathrm{K}$:

$$\frac{P_z}{P_0} = e^{-\frac{z}{H}} \qquad \text{(Eq 1.22)}$$

In the expression (Eq 1.20), the air mass thus applies a correction that accounts for the actual path of a sunlight beam, whilst the transmittance considers the real concentration of the particles (atoms and molecules, but also the dust) in the atmosphere that are responsible for both the scattering and the absorptance effects.

However, even if the attenuation applies to all the frequencies, only few wavelengths are strongly affected by this phenomenon.

It is well known how the ozone absorbs most of the UV wavelengths, so very few UV radiation can reach the ground, but also carbon dioxide and water vapour absorb specific wavelengths. The effects of the water vapour absorption are stronger in the region of the spectrum between the near infrared (NIR) and the short-wave infrared (SWIR), as shown in Figure 1.10.

Models of the atmosphere have been developed by the US National Renewable Energy Laboratory (NREL) for computing spectral irradiance spectra, such as SPCTRAL2 [6] and SMARTS2 [7,8] (*Simple Model of the Atmospheric Radiative Transfer of Sunshine*) predicting clear-sky spectral irradiances.

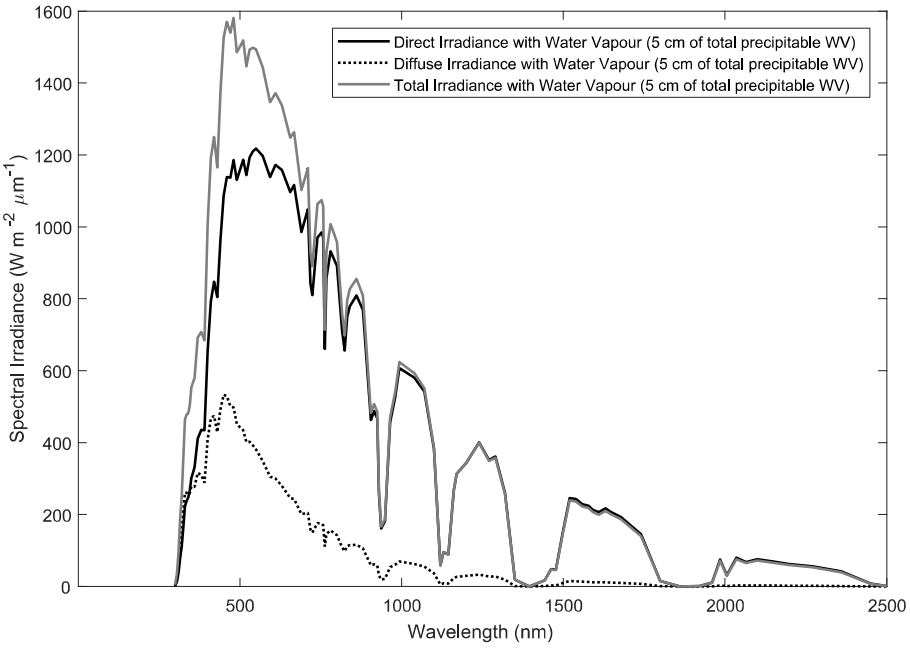

Figure 1.9 Direct, diffuse and total irradiances on a horizontal surface for a clear sky at Ferrara (44.8333°N, 11.5982°E) on July, 1st. The total precipitable water vapour content of the atmosphere, that is the total thickness of all water in a column of atmosphere if it were condensed at the surface, is 5 cm. SPCTRAL2 [6] has been used for calculating the curves.

Since the resulting detected signal contains information not only about the Earth's surface, but also related to the atmosphere, corrections need to be applied to the satellite remote sensed data for removing extra and unhelpful information.

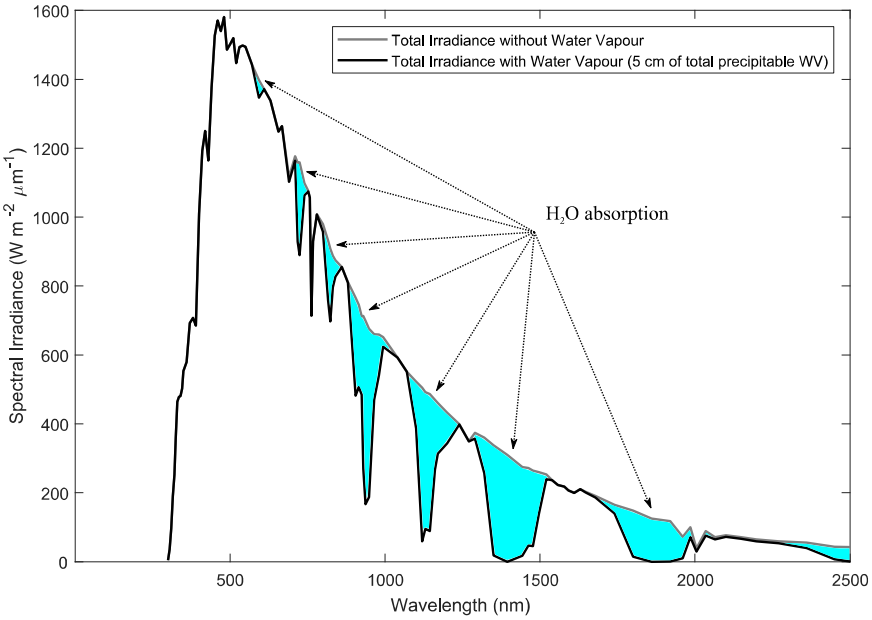

Figure 1.10 Solar irradiance on a surface with different water vapour content of the atmosphere: the absorption due to H_2O is stronger in near infrared (NIR) and short-wave infrared (SWIR) wavelengths. SPCTRAL2 [6] has been used for calculating both the curves.

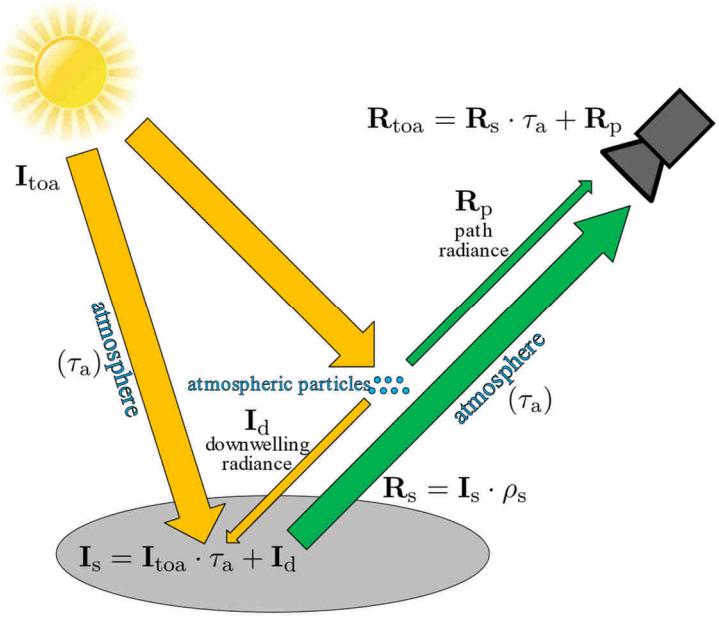

Figure 1.11 Spectral radiant flux density $\mathbf{R}_{toa}$ measured by a satellite sensor: the total amount considers both a scattering component due to atmospheric particles and the reflected spectral radiant flux density from a "ground" surface.

The application of an accurate and appropriate atmospheric correction is essential especially when not performing just a standalone detection or classification, since in multispectral and multitemporal data acquisitions the need

for referring to "absolute", and then *comparable*, values is crucial for reliable analysis.

Different approaches for applying these corrections have been developed through the years and they can be divided into *direct* and *indirect*:

- *direct techniques*: a procedure for collecting or calculating atmospheric information is used, then the acquired data are corrected for removing the noise;
- *indirect techniques*: atmospheric effects are not quantified, but they are minimized or avoided using spectral indices that have been specially developed for this purpose.

However, the direct methods are both the most used and the most effective ones. The use of atmospheric models and the performing of ground calibration measurements are examples of these methods.

1.3.2 Interaction with a surface

As previously discussed, whenever a radiation hits a surface, different fractions are respectively reflected, absorbed and transmitted by the material.

The reflection exhibits two different and opposite kinds of behaviour:

- the first, mainly related to metallic surfaces, is the *specular reflection* where the reflected beam has a zenith angle that is equal to the one of the incident beam;
- the second is a *diffuse reflection*. The ideal behaviour of a diffuse reflecting surface is described by the *Lambert's cosine law* (as it was for the process of emitting radiations by a black body). It states that the luminance viewing from any direction of the hemisphere is equal.

The reason why materials exhibit diffuse reflection is that the surface is not the only parameter involved. The roughness of the surface affects the amount of specular reflection. However, part of the incident radiation may be transmitted just below the external reflecting surface and here it is further reflected inside the first layers beneath the surface, until the radiation will finally emerge. Since the final

emerging radiation zenith angle will be different from the incident radiation one, the reflection is diffuse in the whole hemisphere.

Since in remote sensing it is crucial to understand as well as possible how the solar irradiance, once attenuated by the atmosphere, is reflected by the Earth's surface, the concept of *reflectance* as defined in (Eq 1.15) should be further investigated. Any surface is obviously bidimensional and then also the reflectance has to be considered to depend on both the horizontal (azimuth) angle and the zenith angle. For an ideal and perfectly diffusive surface with a Lambertian behaviour, the reflectance does not depend on the incident and/or reflected directions. However, real surfaces generally do not exhibit such an ideal behaviour and the *spectral reflectance* depends on many parameters: the zenith θ_i and the azimuth angle φ_i of the incident light beam as well as the zenith θ_r and the azimuth angle φ_r of the reflected beam influence it.

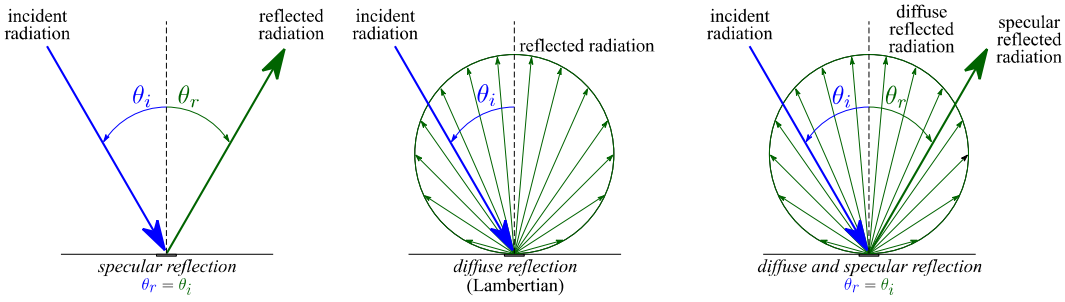

Figure 1.12 Specular reflection (typical for metals and mirrors), perfect diffuse reflection (for ideal Lambertian surfaces) and mixed reflection where a fraction is specular and the other is diffuse (for generic real surfaces).

Introducing the *Bidirectional Reflectance Distribution Function* (*BRDF*) [9], the following expression represents the relationship between the reflected spectral radiance $\mathbf{L}_r$ and the incident spectral irradiance $\mathbf{I}_i$ in all directions:

$$BRDF(\theta_i,\varphi_i,\theta_r,\varphi_r) = \frac{\mathrm{d}\mathbf{L}_r\left(\theta_r,\varphi_r\right)}{\mathrm{d}\mathbf{I}_i\left(\theta_i,\varphi_i\right)} \ (\mathrm{sr}^{-1}) \ . \qquad \text{(Eq 1.23)}$$

For a Lambertian surface, the *BRDF* equals to $1/\pi$.

Since both incident angles and reflected angles can be considered widely as a hemisphere or "concentrated" along a specific direction, many definitions of bidirectional reflectance can be given:

- *Bidirectional reflectance* (or *directional – directional reflectance*), whenever both the incident radiation zenith and azimuth angles (θ_i, φ_i) and the reflected ones (θ_r, φ_r) are infinitesimally small angles;
- *Directional – hemispherical reflectance*, whenever the incident radiation comes from infinitesimally small zenith and azimuth angles (θ_i, φ_i), but the reflected beams spread into the whole hemisphere and the sensor's field of view is able to detect all of this scattered radiation. In remote sensing, this is called *black-sky albedo* and used to refer to the scattering of direct solar radiation [10];
- *Hemispherical – directional reflectance*, whenever the whole sky contributes to the incident radiation amount, but the sensor has an infinitesimally small view angle;
- *Hemispherical – hemispherical reflectance* (or *bihemispherical reflectance*), whenever each direction contributes to the incident radiation and the measurement is performed through an integration over all the hemisphere. In remote sensing, this is called *white-sky albedo* and used to refer to the scattering of direct solar radiation [10].

Generally, radiations are detected through the mean of sensors having a finite field of view and also the light source is "concentrated" in small, but finite, solid angles. Since these angles are not really infinitesimal, it is more correct to speak about *conical* reflectance instead of *directional* reflectance [11]. However, the term directional in more commonly used when referring to a non-hemispherical reflectance of this kind.

It is useful to define the *Bidirectional Reflectance Factor* (*BRF*) [11], representing the ratio between the reflected radiance flux (from a surface $\mathrm{d}A$) and the corresponding radiance flux that would be reflected in the same view direction if the surface were Lambertian, with an identical single direction illumination.

Since an ideal Lambertian surface reflects the same radiance in all the directions, thus the behaviours of such a surface does not depend on (θ_r, φ_r):

$$BRF(\theta_i,\varphi_i,\theta_r,\varphi_r) = \frac{\mathrm{d}\boldsymbol{\Phi}_r^{\text{real surface}}\left(\theta_i,\varphi_i,\theta_r,\varphi_r\right)}{\mathrm{d}\boldsymbol{\Phi}_r^{\text{Lambertian}}\left(\theta_i,\varphi_i\right)} = \frac{\mathrm{d}\mathbf{L}_r^{\text{real surface}}\left(\theta_i,\varphi_i,\theta_r,\varphi_r\right)}{\mathrm{d}\mathbf{I}_i\left(\theta_i,\varphi_i\right)} \cdot \frac{\mathrm{d}\mathbf{I}_i\left(\theta_i,\varphi_i\right)}{\mathrm{d}\mathbf{L}_r^{\text{Lambertian}}\left(\theta_i,\varphi_i\right)} = \pi \cdot BRDF(\theta_i,\varphi_i,\theta_r,\varphi_r)$$

(Eq 1.24)

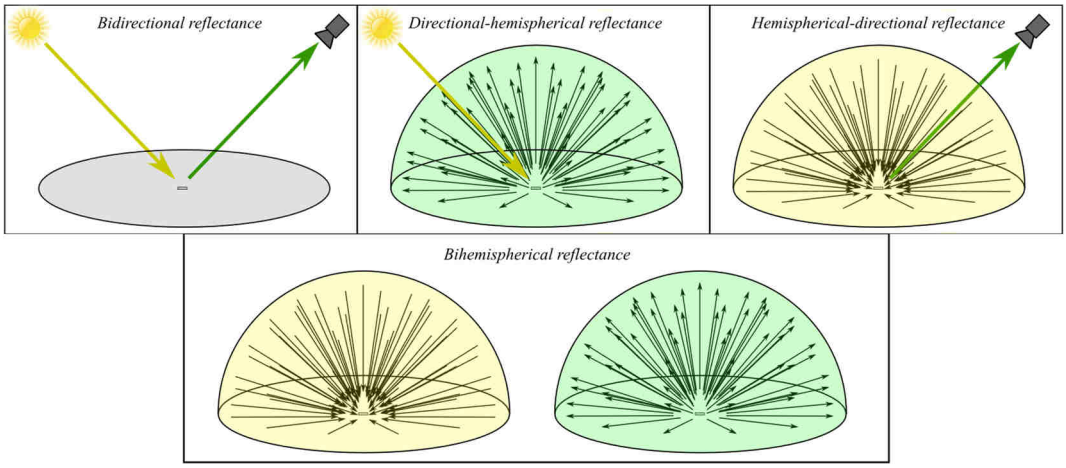

Figure 1.13 Graphical schematization of the different bidimensional kinds of reflectance (the conical reflectance has been approximated by the directional formulation).

However, whenever a field measurement is conducted, a *hemispherical – directional reflectance factor* is measured. In fact, the irradiance comes not only from a specific direction, but instead it is diffuse and then comes from the entire hemisphere. The consequence is therefore that this quantity depends also on both the actual atmospheric conditions and the reflectance of the objects that surrounds the considered reflecting surface:

$$HDRF(\theta_i,\varphi_i,2\pi,\theta_r,\varphi_r) = \frac{\mathrm{d}\boldsymbol{\Phi}_r^{\text{real surface}}\left(\theta_i,\varphi_i,2\pi,\theta_r,\varphi_r\right)}{\mathrm{d}\boldsymbol{\Phi}_r^{\text{Lambertian}}\left(\theta_i,\varphi_i,2\pi\right)} \quad \text{(Eq 1.25)}$$

The expansion of expression involves the ratio of two double integrals [11]; separating a direct (θ_0,φ_0) and a diffuse (2π) contributions to the total spectral irradiance $\mathbf{L}_i$, finally we obtain:

$$HDRF(\theta_i,\varphi_i,2\pi,\theta_r,\varphi_r) = R(\theta_0,\varphi_0,\theta_r,\varphi_r)\cdot d + R(2\pi,\theta_r,\varphi_r)\cdot(1-d)$$

(Eq 1.26)

where $d \in [0,1]$ corresponds to the fractional amount of the direct radiant flux $\mathbf{\Phi}_{i,\mathrm{dir}}$.

In remote sensing applications, the vegetation often represents the reflecting surface. The behaviour of canopies is different with respect to the simple combination of a specular and a diffuse reflection as shown in Figure 1.12. In fact, the area where the reflectance, thus the *BRF*, is higher is located along the same direction of the sunlight incident radiation. This area, located around the same view direction of the solar angle (θ_i, φ_i) is called *hotspot*. Its spatial extent as well as its magnitude depends on the canopy characteristics, such as the leaf size, the height of the canopy, the mean leaf orientation, and so on. This anisotropic behaviour can be also justified thinking to the very high roughness of the "ground" reflecting surface whenever plants, including trees, are present. In the case the behaviour

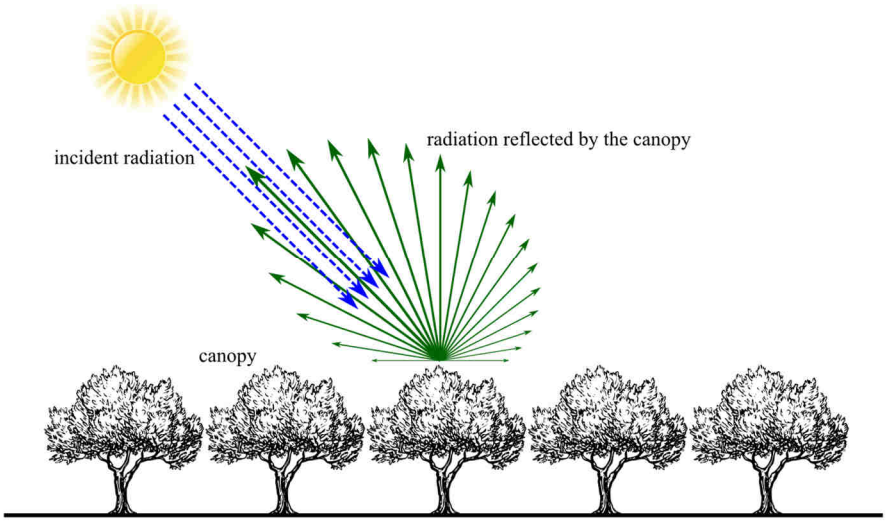

Figure 1.14 Canopy reflectance: the hotspot is located in the same view direction of the solar angle. The BRF is thus slightly higher around this portion of the hemisphere.

The BRF is wavelength dependent and the reflectance along the same direction is not equal for all the radiation frequencies: this affects also the ratio between the detected radiance on different wavelengths and the vegetation indices that can be calculated. Even if this effect is generally small, there is a remarkable difference between red and near infrared reflectance with the view angle. Most of this effect is related to a change in the visible soil fraction, that has a maximum around the null zenith angle direction. However, the soil fraction is not the only

parameter that influences the resulting reflectance, since it is possible to notice an effective change in the light quality [10].

1.4 Radiative properties and spectral signatures

The reflectance of canopies depends on their own radiative properties. The leaves, as well as the stems and the soil, strongly affect them.

Since the reflectance ρ_λ depends on these specific material properties and each substance exhibits a different reflectance value for a certain wavelength λ, the accurate measure of the reflectance varying the frequency of the incident radiation allows to reconstruct the function $\rho(\lambda)$ for a material's sample. This is called *spectral signature* and allows to recognize different materials.

The reconstruction of the spectral signature requires the use of instruments able to detect the reflectance at the many different wavelengths, with narrow bands and within an operative range of the spectrum. Such a device is called *spectrometer*, or, if it is both spectrally and radiometrically calibrated, *spectroradiometer* [12].

For the leaves, the magnitudes of the absorptance, reflectance and transmittance certainly depend on the wavelength. However, this is not the only parameter. The leaf age and thickness as well as the specific chemical composition of the leaf itself, its structure and its water content are further parameters that influences the behaviour of the leaf's surface when a radiation hits it.

The presence of pigments, such as the chlorophyll that is responsible for the photosynthetic process, represents one of the most important factors that influence the spectral properties of leaves, especially in the visible region. Also, carotenoids and flavonoids contribute to the response in this region and are responsible for the autumn leaf colours. The water content instead, affects the spectral response in the infrared region. The absorption due to the water is strong in some characteristics bands [10] in the mid-infrared at $\approx 1450\ \mathrm{nm}$, $\approx 1950\ \mathrm{nm}$ and $\approx 2500\ \mathrm{nm}$ wavelengths. The different response in these bands allows to detect the status of the vegetation and can be combined to the response in the thermal region of the spectrum. However, for thermal radiation also the emitted radiation should be properly considered.

Figure 1.15 shows the reflectance of grass for different drought levels. The spectral signatures data used are available from the *USGS Spectral Library Version 7* [13]. We can notice that:

- the water absorption is higher in the above mentioned mid-infrared bands when the water content is higher;
- the response in the near infrared decreases for a drier vegetation;
- the reflectance in the red wavelengths increases for a drier vegetation.

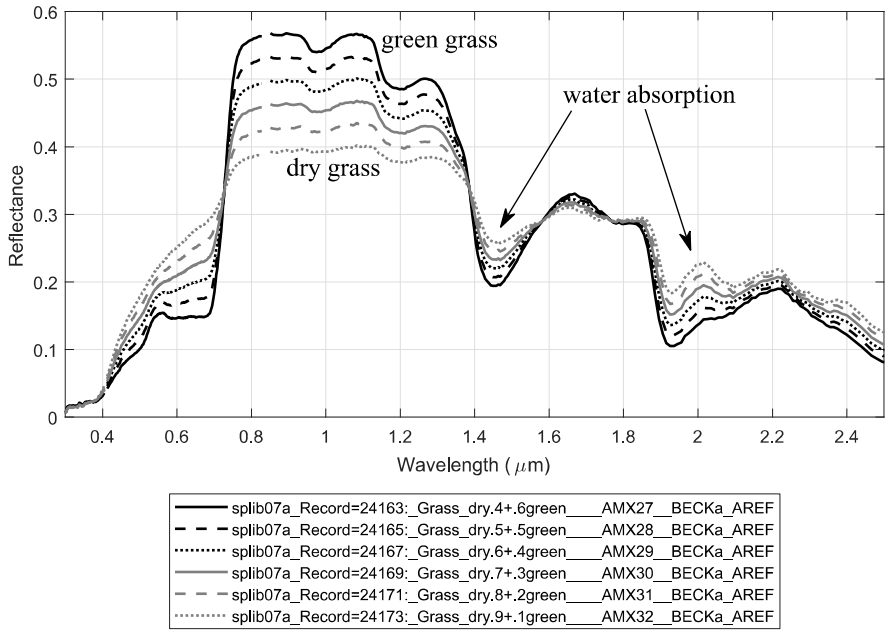

Figure 1.15 Reflectance of grass for different drought levels (source of spectral signatures: *USGS Spectral Library Version 7* [13]).

For broadleaves plants species the spectral signature characterization by the means of spectroradiometers is quite simple, while for coniferous needles it has been considered much more difficult for decades. Due to their small size, in fact, the needles do not cover the whole sample ports of integrating spheres [14].

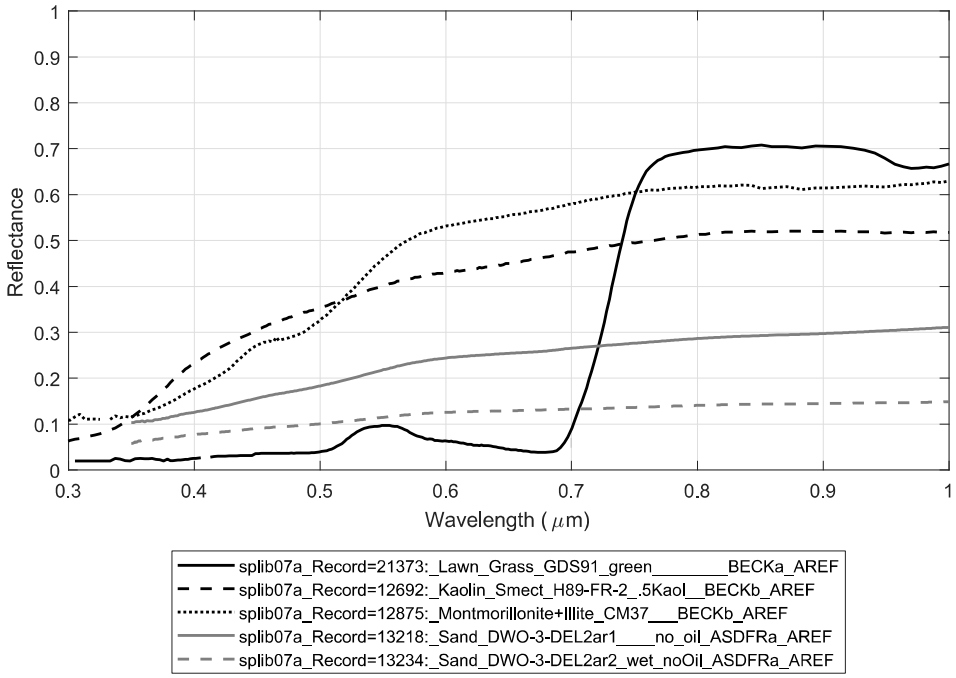

Figure 1.16 Spectral reflectance for different surfaces. Both sand and clay minerals, that typical examples of soil components, exhibit gradually variations in the spectral reflectance. The vegetation instead, has a strong reflectance in the *red edge* position.

1.5 Spectral Indices

Remote sensed information can be used to generate new variables as a combination of two bands, or even more. The purpose is to establish a stronger correlation between the new parameters and some particular properties of the analysed material. However, the combination of bands that have significantly different wavelengths, can lead to the artificial introduction of differences in the detected reflectance that are related to the structural features of a canopy. Therefore, it is a common practice to compute combination using wavelengths that are fairly close each other [10]. These new variables are called *spectral indices* [15,16].

1.5.1 Basic indices

For vegetation and crop assessment, a great variety of indices and descriptors has been defined through the decades. The most used bands for computing basic spectral indices are the *red* and the *near infrared*. The reason why using them, is that they satisfy the requirement to be fairly close in order to compare reflectance values detected with a similar structural behaviour of the canopy and they exhibit properties that are opposite each other. For example, when the water content of the

grass decreases, the red reflectance increases whilst the near infrared response becomes lower. In this way, the change in the canopy properties is enhanced.

The simplest approach for computing a combination (index) based on both the red and near infrared information, is to make a difference. This index is thus called *difference vegetation index*:

$$DVI = \rho_{NIR} - \rho_R \qquad \text{(Eq 1.27)}$$

The higher it is the vegetated fraction of a surface, the higher the DVI value will be, since the difference will be larger. Notice that the DVI, even if still dimensionless because the reflectance is it, represents a reflectance value (that is a difference, of course). This contributes to make this index sensitive to illumination conditions and the use of reflectances rather than the raw radiance or the raw digital numbers do not help to overcome this issue.

Another way is thus to combine the same two bands, calculating the ratio instead of making a difference. In this way, we obtain the *ratio vegetation index*:

$$RVI = \frac{\rho_{NIR}}{\rho_R} \qquad \text{(Eq 1.28)}$$

that is able to consider the illumination conditions and correcting for them, at least partially. However, there is another approach to perform a normalization that is the basis for most of further vegetation indexes computation. The expression of this normalization process represents the *normalized difference vegetation index*:

$$NDVI = \frac{\rho_{NIR} - \rho_R}{\rho_{NIR} + \rho_R} \qquad \text{(Eq 1.29)}$$

Theoretically, the range of the NDVI is $-1 \leq NDVI \leq 1$. Practically, since vegetation is characterized by higher reflectance in near infrared rather than in red wavelengths, the common NDVI range is thus limited to $0 \leq NDVI \leq 1$.

A strength of this index is that it is applicable both to reflectances and radiance values. Even though the use of the radiance detected at the sensor as input for the NDVI computation is widely common in practice, it is certainly preferable to use reflectances, since their use improves the corrections for differences in the incident radiation and for absorption and scattering in the atmosphere [10].

Usually, vegetation indices tend not to assume the extreme values within their theoretical range. For example, the NDVI do not tend to assume 0 and 1 values respectively for bare soil and for a total vegetation covering. In order to compensate for this effect, the index can be scaled to match its minimum value with 0 and its maximum value with 1. For a generic vegetation index VI, the approach is the following:

$$\widetilde{VI} = \frac{VI - VI_{\min}}{VI_{\max} - VI_{\min}} \qquad \text{(Eq 1.30)}$$

The $VI_{\min}$ and $VI_{\max}$ values can be assumed as the minimum and maximum values from the raw digital numbers or imposed by a threshold. This technique can help to increase the contrast and to enhance the difference in the vegetation index values throughout a scene. However, since the minimum and maximum recorded digital numbers will be different with changing illumination conditions as well as for the repetition of the data acquisition over time, particular care should be adopted whenever this kind of technique is used in a monitoring of the same object.

The normalized difference vegetation index still represents the most common vegetation index. However, in order to enhance particular properties, further indices have been defined through the years.

The *green normalized difference vegetation index* (*GNDVI*) replaces the red reflectance with the green reflectance to improve the index sensitivity for dense vegetation with higher leaf-area index. It has the following expression:

$$GNDVI = \frac{\rho_{NIR} - \rho_G}{\rho_{NIR} + \rho_G} \qquad \text{(Eq 1.31)}$$

Another issue that can be minimized is the influence of the underlying soil, especially for low density vegetation, where the visible soil fraction is higher. In this case, the vegetation can act like a sort of filter, absorbing red wavelengths and allowing NIR to reach the soil and be consequently reflected. This implies that the reflectance of the soil in the near infrared region is higher only due to the fact that few red radiations really reach the soil itself. In order to overcome this issue, a *soil-adjusted vegetation index* (*SAVI*) [17] has been developed:

$$SAVI = \frac{\rho_{NIR} - \rho_R}{\rho_{NIR} + \rho_R + L} \cdot (1 - L) \qquad \text{(Eq 1.32)}$$

The parameter *L* is a soil adjustment factor that considers the soil's influence on the canopy spectra. It varies from 0 for high leaf-area index canopy to 1 for low LAI. Negative values for this coefficient have been found to give satisfactory results in reducing soil noise for arid grasslands [18].

Many indices related to the chlorophyll content have been also developed. A list of some of these indices is reported in the literature [19]:

- the *chlorophyll vegetation index*: $CVI = \frac{\rho_{NIR} \cdot \rho_R}{\rho_G^2}$;
- the *chlorophyll index – green*: $CI\text{-}G = \frac{\rho_{NIR}}{\rho_G} - 1$;

In all of the above indices, the near infrared refers to the range between $760\ \mathrm{nm}$ and $900\ \mathrm{nm}$, while the visible wavelengths are comprised respectively in:

$$VIS \begin{cases} 630\ \mathrm{nm} \leq \rho_R \leq 690\ \mathrm{nm} \\ 520\ \mathrm{nm} \leq \rho_G \leq 600\ \mathrm{nm} \\ 450\ \mathrm{nm} \leq \rho_B \leq 520\ \mathrm{nm} \end{cases}.$$

1.5.2 Red edge indices

The rapid increasing in the reflectance at about $700 - 730\ \mathrm{nm}$, from lower values in the red to higher values in the near infrared region, has always been considered important since it can provide information related to the biochemical composition [20]. This region, that exhibits an ascending slope in the spectral signature of the vegetation, is referred to as the *red edge*.

The red edge reflectance has thus been used also to estimate the leaf chlorophyll content (LCC). The red edge position (REP) , defined as "the position with wavelengths of maximum derivative spectra in the red edge region" [20], is a parameter related with the LCC, since it shifts toward the near infrared region

(longer wavelengths) when the LCC increases. Studies have also confirmed that the correlation between the red edge and leaf-area index is high [21].

The red edge information can be used for computing a normalized index where the red reflectance it is replaced with the red edge one. This index is called *normalized difference red edge index* (*NDREI*, or simply *NDRE*):

$$NDRE = \frac{\rho_{NIR} - \rho_{RE}}{\rho_{NIR} + \rho_{RE}} \qquad \text{(Eq 1.33)}$$

Similarly, a *chlorophyll index – red edge* that considers the red edge instead of the green reflectance can be calculated:

$$CI\text{-}RE = \frac{\rho_{NIR}}{\rho_{RE}} - 1 \qquad \text{(Eq 1.34)}$$

1.5.3 Atmospherically resistant indices

A particular mention, among the many different variants of the NDVI, should be given for two indices that have been developed in order to taking account of differences in the transmission of different wavelengths as a result of mutation in atmospheric conditions.

The *atmospherically resistant vegetation index* considers the blue reflectance in addition to the NDVI formulation and is defined as:

$$ARVI = \frac{\rho_{NIR} - \left[\rho_R - \beta(\rho_B - \rho_R)\right]}{\rho_{NIR} + \rho_R - \beta(\rho_B - \rho_R)} \qquad \text{(Eq 1.35)}$$

The combination of ARVI and SAVI represents the *soil and atmospherically resistant vegetation index* (*SARVI*):

$$SARVI = \frac{\rho_{NIR} - \left[\rho_R - \beta(\rho_B - \rho_R)\right]}{\rho_{NIR} + \rho_R - \beta(\rho_B - \rho_R) + L} \cdot (1 + L) \qquad \text{(Eq 1.36)}$$

1.6 Image Classification

One possible aim to exploit the multispectral information in the field of remote sensing consists in the detection of the different ground covers assessing their actual spectral response.

The image classification therefore represents a fundamental tool to perform this task. In this way it is also possible to produce a thematic map showing the spatial distribution of the detected objects.

Even though the starting data is always represented by the spectral information sensed in each wavelength, different classification approaches exist. For example, a single pixel can be classified with regard to the solely information that itself contains or considering a wider region in order to detect a pattern around it. Similarly, the distribution of the data (in terms of statistics) may be assumed *a priori* for hypothesis or even addressed as an unknown.

One of the most important distinction that applies to the different classification procedures regards the specification of a training dataset prior to the classification process. In this way, the classifier can extract signatures from these [10] and use them to derive a thematic class for each type of cover. Conversely, if no training dataset is provided, the classifier needs to operate on the basis of the solely spectral information contained within the image itself. In this case, the operator will perform an additional work in order to both label the detected classes and merging those which will be similar. This latter approach is called *unsupervised classification*, while procedures based on training dataset constitute a *supervised classification*.

Specialised software exists for performing accurate classifications. The ENVI package is one of the most popular and it is able to perform both supervised and unsupervised classifications. It is worth noting that the number of classes that can be detected into an image, and then separated, strongly depends on both the number of the spectral bands available and the uncorrelation between them. Therefore, more are the uncorrelated spectral information for each channel and more will be the number of classes that may be distinguished.

Generally, the use of hyperspectral imageries thus provides better classification than multispectral ones, beyond allowing a comparison of each class with a database of known spectral signatures.

A general strategy for spectral-based image classification can be summarised as follows [22]:

- *feature extraction*, that involves the transformation of the data to detect salient information to further support the separation into distinct classes;
- *spectral classification*, that represents the actual process with the task of assigning a different material to each detected spectrum;
- *class labelling*, that finally consists in assigning a name representing a physical identification to the classes recognized in the previous step.

Again, all of the above stages may be performed in an autonomous way or with an operator's supervision.

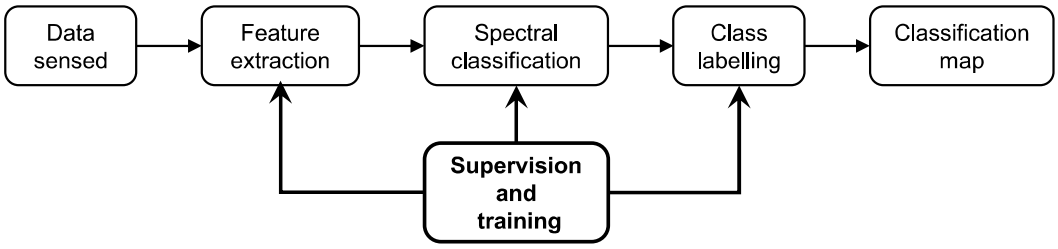

Figure 1.17 A general strategy schematization for spectral-based image classifications [22].

1.6.1 Unsupervised classification

Whenever no input data is provided for the training, the classifier groups similar pixels within a same class. This similarity is computed on the basis of the spectral statistics only and the number of groups is generally predetermined by the user. Another common term for referring to a group is *cluster*, therefore the unsupervised classification itself is often called *clustering*.

Clusters may be represented in a multidimensional space, thus the separation between two pixels *a, b* can be defined in terms of a Euclidean distance computed as

$$D_{ab} = \sqrt{\sum_{i=1}^{n} \left(a_i - b_i \right)^2} \qquad \text{(Eq 1.37)}$$

in which *n* are the channels, each of those it is the *i*-th. The data points are consequently assigned to the nearest class.

The principle at the basis of any unsupervised procedure is substantially similar to the computation of such a multidimensional distance. Means of each class

are generally computed at every iteration and then pixels are reclassified on the basis of the new statistics. At the same time, the classes may be split or merged at any stage and finally some pixel might remain unclassified. These latter aspects depend on the threshold values set for the decision rules.

Examples of methods based on an unclassified procedure are the *k-means* and the *ISODATA*.

The former consists in a linear classification algorithm that minimises a mean-squared error (MSE) computed using the class mean vectors $\boldsymbol{m}_q$ for a number of Q classes:

$$MSE = \frac{1}{N}\sum_{q=1}^{Q}\sum_{\mathbf{x}_i \in \omega_q}\left(\mathbf{x}_i - \boldsymbol{m}_q\right)^t\left(\mathbf{x}_i - \boldsymbol{m}_q\right) \qquad \text{(Eq 1.38)}$$

The *k-means* algorithm estimates the class mean vectors at every iteration and then makes new class assignments through a nearest mean classification rule.

The iterations continue until a convergence is reached, thus the change in the classification is small enough.

It is worth noting that the number of classes is assumed arbitrarily at the initial stage within this unsupervised approach. To overcome *k-means* issues, different variations have been developed, like the *iterative self-organizing data analysis technique* (ISODATA). This represents a common classification procedure in the field of remote sensing. The user is required to set several parameters prior to perform the classification, such as:

- the maximum number of iterations,
- the desired number of classes,
- the maximum number of class pairs to be merged within an iteration
- the minimum number of elements (pixels) forming a class,
- a threshold value for the standard deviation of a class.

1.6.2 Supervised classification

Conversely to the unsupervised algorithms, the supervised classification methods start from the identification of particular regions on the image to be

classified. These areas define a certain number of classes. Since the spectral information of any pixel belonging to a region is also known, the statistics for each class can be computed. It is important noting that the regions defining each class should be as homogeneous as possible, in order to achieve low standard deviations. In addition, it is also crucial to specify classes that are really separated.

The supervised classifier attempts to assign all of the pixels that were not prior manually classified to some of the input classes. A simple way to do this consists in computing the centroid of each class in the multidimensional spectral space and assigning the pixel to the nearest class. If a threshold is set by the operator for this latter distance, the pixel may also remain unclassified if no class meets the minimum distance criterion.

More robust classification methods are based on probability instead of a simple distance. The *maximum likelihood* classification uses the training dataset to estimate both the mean and the variance for each class. Hence it is possible to compute the probability that a pixel may belong to a class.

The classification with this method is performed [23] assuming that a pixel $\boldsymbol{x}$ belongs to the class ω_i if the corresponding probability is higher than the probability associated to all of the other classes, thus:

$$\boldsymbol{x} \in \omega_i \text{ if } p(\omega_i \mid \boldsymbol{x}) > p(\omega_j \mid \boldsymbol{x}) \quad \forall j \neq i \qquad \text{(Eq 1.39)}$$

The problem in doing what the (Eq 1.39) states lies in the fact that the probability $p(\omega_i \mid \boldsymbol{x})$ are actually unknown. By using a suitable and sufficient training data for each class, thus for each type of ground cover, it is possible to estimate the probability distribution $p(\boldsymbol{x} \mid \omega_i)$.

The desired and available probabilities estimated from the training data, respectively $p(\omega_i \mid \boldsymbol{x})$ and $p(\boldsymbol{x} \mid \omega_i)$, are related as follows:

$$p(\omega_i \mid \boldsymbol{x}) = p(\boldsymbol{x} \mid \omega_i)p(\omega_i) \,/\, p(\boldsymbol{x}) \qquad \text{(Eq 1.40)}$$

in which $p(\omega_i)$ represents the probability that the class ω_i occurs in the image and $p(\boldsymbol{x})$ is the probability, at the location $\boldsymbol{x}$, of finding a pixel from any class.

The expression (Eq 1.39) thus becomes:

$$\boldsymbol{x} \in \omega_i \text{ if } p(\boldsymbol{x} \mid \omega_i)p(\omega_i) > p(\boldsymbol{x} \mid \omega_j)p(\omega_j) \quad \forall j \neq i \qquad \text{(Eq 1.41)}$$

and now the probabilities $p(\boldsymbol{x} \mid \omega_i)$ are known by the use of the training data. Introducing the *discriminant functions* $g_i(\boldsymbol{x})$ as the natural logarithm of $p(\boldsymbol{x} \mid \omega_i)p(\omega_i)$, it is possible to write that

$$g_i(\boldsymbol{x}) = \ln\left[p(\boldsymbol{x} \mid \omega_i)p(\omega_i)\right] = \ln p(\boldsymbol{x} \mid \omega_i) + \ln p(\omega_i),$$

thus obtaining that the (Eq 1.41) translates into:

$$\boldsymbol{x} \in \omega_i \text{ if } g_i(\boldsymbol{x}) > g_j(\boldsymbol{x}) \quad \forall j \neq i \qquad \text{(Eq 1.42)}$$

An assumption generally made at this point for a maximum likelihood classification is that the probability distributions for all the classes are in the form of a multivariate normal model and this leads to some simplification. The discriminant functions become:

$$g_i(\boldsymbol{x}) = \ln p(\omega_i) - \frac{1}{2}\ln\left|\Sigma_i\right| - \frac{1}{2}(\boldsymbol{x} - \boldsymbol{m}_i)^t \Sigma_i^{-1}(\boldsymbol{x} - \boldsymbol{m}_i) \qquad \text{(Eq 1.43)}$$

in which $\boldsymbol{m}_i$ and Σ_i are respectively the mean vector and the covariance matrix for the data belonging to the spectral class ω_i. The symbol $\left|\Sigma_i\right|$ denotates the determinant of the covariance matrix and Σ_i^{-1} is the inverse of the covariance matrix.

In order to make decisions, thresholds are applied to the discriminant functions. If the significant threshold value T_i is adopted for a class ω_i, the final decision rule is as follows:

$$\boldsymbol{x} \in \omega_i \quad \Leftrightarrow \quad g_i(\boldsymbol{x}) > g_j(\boldsymbol{x}) \quad \forall j \neq i \quad \wedge \quad g_i(\boldsymbol{x}) > T_i \qquad \text{(Eq 1.44)}$$

The maximum likelihood classifier is one of the most commonly used algorithm to perform a supervised classification in the field of the remote sensing.

1.6.3 Assessment of classification accuracy

A crucial task that any operator needs to perform after obtaining the results of a classification algorithm, whether it was supervised or unsupervised, consists in evaluating the accuracy achieved.

A ground reference dataset should therefore be provided and the results of the classification should be compared for each pixel in it. The error analysis conducted in this way makes use of the so-called *confusion matrix* where the columns refer to the ground truth regions and the rows consequently represent the classification results.

Correctly classified pixels of each class contribute to the value of their respective element on the diagonal of the confusion matrix, while out-of-diagonal elements are the count of classification mistakes. A simple approach to evaluate the final level of accuracy it is therefore to compute the ratio between the sum of all the elements belonging to the diagonal and the sum of all the elements composing the confusion matrix. This value is called *overall accuracy*:

$$OA = \frac{\sum_{i=1}^{Q} x_{i,i}}{N} \qquad \text{(Eq 1.45)}$$

in which Q is the size of the confusion matrix, hence the number of classes, $x_{i,i}$ is the generic element on the diagonal and N is the sum of all the elements of the confusion matrix.

A different parameter introduced by Cohen [24], called *Kappa coefficient*, may be also used to assess the accuracy of the classification. According to [25], the *Kappa coefficient* serves to measure the relationship of beyond chance agreement to expected disagreement. In fact, it considers not only the element lying on the diagonal of the confusion matrix, but all the its values.

The expression of this parameter is [23]:

$$\kappa = \frac{N\sum_{k} x_{kk} - \sum_{k} x_{k+}x_{+k}}{N^2 - \sum_{k} x_{k+}x_{+k}} \qquad \text{(Eq 1.46)}$$

where $x_{i+} = \sum_{j} x_{ij}$ represents the sum of all the columns for the row *i* and $x_{+j} = \sum_{i} x_{ij}$ represents the sum of all the rows for the column *j*.

With regard to the considerations made for the comparison of supervised classifications performed with and without the application of radiometric corrections, the *overall accuracy* already represented a reliable parameter to assess the level of accuracy.

CHAPTER 2

UAV SPECTRAL REMOTE SENSING

This chapter presents an introduction to the sensors and the techniques for handling both the geometrical and multispectral information retrievable by the mean of UAVs. A particular attention is reserved to the radiometric calibration of the raw data sensed. This represents a crucial task, especially for the monitoring over time.

2.1 The use of UAVs in remote sensing applications

Unmanned aerial vehicles represent a unique and very powerful solution for the remote sensing applications.

First of all, the geometric resolution that can be normally achieved by the means of drones is very high, with a ground sample distance (GSD) of few centimetres for multispectral cameras at one hundred meters flight altitudes. This fact implies the capability of any remotely piloted aircraft to potentially acquire detailed information about land covers.

The revisiting time, also known as temporal resolution, represents a parameter that is completely customizable in the case of drones and does not affect their capability to sense data even in an almost continuative way.

The cloud coverage does not impact on the detection by UAVs, since they fly under the clouds, while it represents a serious issue for the satellite imageries.

Conversely, the extent of the sensed area is generally much smaller than satellite imageries, even if some types of drones are able to perform detection flying at high speed.

With regard to other aircrafts, unmanned ones are usually a safer option if compared to the piloted aerial vehicles, since they can be flown at lower altitudes without risks for the pilot, as well as they do not necessarily need a runway, thus

representing a very flexible solution. The cost of UAVs is also much lower than any kind of manned aircraft.

All the above reasons explain why the unmanned aerial vehicles started to be used for all the proximal remote sensing applications. Their use has increased exponentially in the last years and a huge variety of sensors are available nowadays to be mounted on any kind of drone.

2.1.1 Basics of UAV's operations

On a technical basis, the UAVs can be mainly divided in two classes: multicopters and fixed wing (Figure 2.1). Intuitively, the formers are more similar to helicopters while the latter ones work like airplanes.

Multicopters, also called multirotors, are equipped with propellers producing a vertical thrust that enables the drone to take off and hovering above the ground. The motion is the result of a tilt of the drone: in such a way, the thrust generated by the propellers' air flow has a component along the flight direction that enables it to move. The number of the propellers should be always is even and their rotation is alternatively clockwise and counter clockwise, in order to have a null total angular momentum. Multicopters are thus able to take off vertically into the air, so they require a very limited space to reach their planned flight altitude.

On the contrary, fixed wing drones require more space for the flight operations, Generally, it consists in a runway without any obstacles. This is a requirement for both taking off and landing operations. However, these drones can reach higher flying speeds, up to 80 km/h, instead of an average value of about 50 km/h for multicopters. The wings are made of a very lightweight material, such as polystyrene, with winglets. Despite the name, the wings are not really fixed. Since some of these drones may have a wingspan up to more than one and a half meters, the wings may be detachable for a transportation convenience. Fixed wing drones have a natural gliding capability whenever they are flying, thanks to the lift generated by the wings' air flow.

With regard to the capability in acquiring images, the camera may be set up in a fixed arrangement for fixed wing drones, while multicopters have usually a camera gimbal. The gimbal is a device that maintains the camera in a certain view

direction in term of yaw, pitch and roll. This latter Generally, the absence of a gimbal may not represent a serious issue for land mapping if images are acquired using a nadiral arrangement.

In addition, fixed wing drones are usually able to cover wider extensions thanks to their higher speed. However, they consequently need to be flown at higher altitudes and the ground sample distance (GSD) may become much higher than using a multicopter.

Figure 2.1 Examples of a multicopter (source: https://www.dji.com/phantom-3-pro) and a fixed wing drone (source: https://www.parrot.com/global/drones/parrot-disco#parrot-disco) of two of the major manufacturers.

Another classification that applies to all the drones is based on their overall weight, which is the weight of the aircraft at the take off. Drones lighter than 0.3 kg are considered to be harmless by the Italian regulations [26] if the propellers (rotating parts) safeguards against impacts and the maximum flight speed does not exceed 60 km/h. For heavier UAVs, further regulations apply with a differentiation between unmanned aircrafts up to 25 kg and beyond 25 kg. A license is needed to operate with any aircraft exceeding the 0.3 kg threshold and different authorization applies for both critical and non-critical scenarios.

Flight rules significantly differ from nation to nation, even though a harmonisation process is currently on the way [27] in the European Union's countries, thanks to the effort of the European Aviation Safety Agency (EASA).

Nevertheless, some universal principles are recognizable in every UAV regulation, such as the general requirement to conduct an aircraft with a visual line of sight (VLOS), not to fly over people and not to exceed a certain altitude above the ground, in such a way to fly in an uncontrolled air space.

2.1.2 Applications for land mapping

Proportionally to the operative mass of an aircraft, the maximum payload on a multicopter varies according to its specific characteristics. Lighter drones are designed and manufactured in order to carry a compact camera that is usually integrated within the entire UAV system. Heavier aircrafts, characterized by higher payloads (up to 2 kg), allows the complete customization of the instrumentation that can be mounted and used for aerial surveys.

In land mapping applications the most common devices are RGB cameras, multispectral or even hyperspectral sensors as well as LiDAR (Light Detecting and Ranging) systems.

The use of simple RGB cameras on a UAV to reconstruct the three-dimensional morphology of any kind of object, from the cultural heritage to the production of detailed cartography, has been widely experimented in the last years. Thanks to algorithms derived from the computer vision branch, an innovative approach was applied to the digital photogrammetry [28]. The so-called “Structure from Motion” (SfM) has therefore used to reconstruct models consisting in dense clouds made of up to tens of million points. In the meanwhile, the miniaturization process involved also the laser scanner sector and lightweight LiDAR sensors started to be produced. However, the cost of these latter devices is still much higher than a simple camera and the combined use of visible cameras with SfM software is able to produce reliable products both in terms of precision and accuracy. Similarly, the multispectral sensors for UAV applications have experienced a high development rate in the last few years, starting from the basic approach of modifying existing compact cameras by the applications of a filter, to the more complex realization of an actual multi-band sensor with different optics and interfaced with environmental light measuring devices. Concurrently, the cost of the multispectral sensors decreased significantly.

The common link between RGB cameras and multispectral sensors consists in the same typology of raw data that is acquired. In both cases, in fact, images are captured. However, all the imageries need to undergo a rigorous process of calibration in order to produce reliable and accurate results.

The process for applying the geometric and radiometric corrections to the raw data acquired, especially focussing on the sensors used in the experimental part of this dissertation, is presented in the following paragraphs. Also, the SfM workflow is introduced for a general understanding of the process leading to merge the multispectral imageries into a comprehensive multiband orthomosaic

2.2 Digital sensors

2.2.1 CCD and CMOS

In the modern digital photogrammetry, the images are no longer acquired by means of a photographic emulsion like in the past. Conversely, sensors made up of a large number of light-sensitive detector elements, arranged in lines or arrays on a semi-conductor module, are used.

Each detector, called *picture element* or simply *pixel*, generates an electric charge whenever a radiation hits its surface (Figure 2.2) [29]. The higher it is the amount of radiation, in terms of photons, the higher will be the difference of potential generated. However, not all of the photons really contribute to electrically charge the particles of the sensor element and this amount is related to the actual quantum efficiency of the sensor. More precisely, this latter efficiency depends on both the sensor's material and the specific considered wavelength and it is expressed as:

$$\eta = \frac{n_E}{n_P} \qquad \text{(Eq 1.47)}$$

where n_E it is the number of charged particles and n_P it is the number of incident photons on a detector element. However, there is a maximum amount of possible charged particles. If this amount is reached in a detector, then no more photons will be able to charge further particles in spite of the real amount of the incident radiation. Whenever this happens, a saturation (or overflow) charge is

achieved and the corresponding information collected by those detectors is far-fetched. For spectral sensing it is crucial to avoid the occurrence of such a situation at the time of the image acquisition. In fact, no further techniques can be applied in post-processing for compensating this issue, since the correlation between the "measure" and the "measured physical quantity" has been definitely lost due to the saturation.

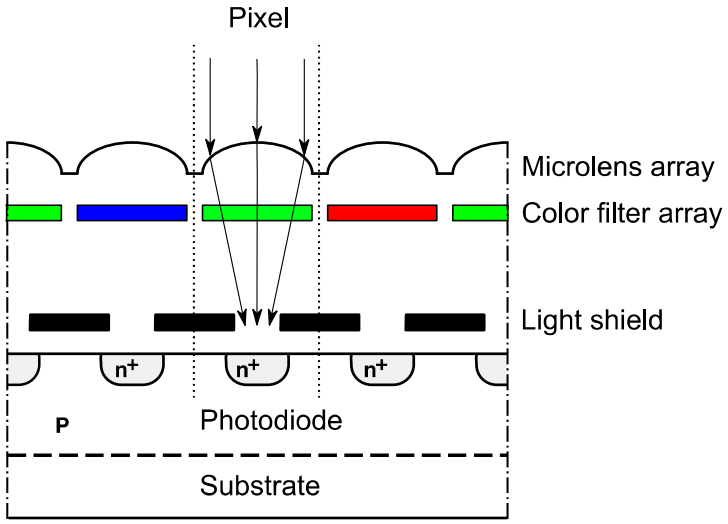

Figure 2.2 Schematic structure of a picture element (pixel) of the sensor [29].

The sensor elements can be arranged along a line. For such arrangement, the problem consists in the transportation of the charge, that is stored on each sensor element, to an output. The principle for solving this issue is that each single charge is shifted in the direction of the output and this process is continued until every charge will reach the read-out register at the end of the line. Here, the charge is read-out and converted into an actual electrical voltage signal. This process is usually referred to as the Charge Coupled Device (CCD) process.

However, most of the current digital sensors used in photogrammetry is structured in an array of detectors instead of a line. This implies to create a more complicated system for the transfer and the read-out of the charges. Different layouts exist:

- The frame transfer, that consists of two physically separated areas on the sensor. The light-sensitive one is dedicated to the photons' detection whereas the opaque one is used for the storage. After the

exposition, the charges move from the first zone to the second, where they are rapidly shifted line by line into the read-out register.

- The full-frame transfer, that consist in having only an imaging zone from where the charges are directly transferred to the read-out register and they do not transfer to a separate storage area. During the read-out operation the sensor may not be exposed for preventing a data alteration.
- The interline transfer, where a linear light-sensitive CCD array alternates with a linear opaque CCD array and so on. In this way, after the exposure the charges are shifted sideways into the opaque arrays and then further transferred for the read-out.

Since the main disadvantage of the interline transfer layout is that only about the 25% of the total area of the sensor is actually light-sensitive, current sensors employ a microlens in order to address the light captured over a whole element to a smaller area that is the sensitive one. In this way, the fill factor of every pixel increases.

Besides the CCD technology, another technique has become widely used for the design imaging sensors. The Complementary Metal Oxide Semi-conductor (CMOS), originally used for the design of memory chips and computer processors, has significantly advantages like a smaller power consumption (up to 1/10 of CCD sensors), higher frame rates and lower manufacturing costs (Figure 2.3).

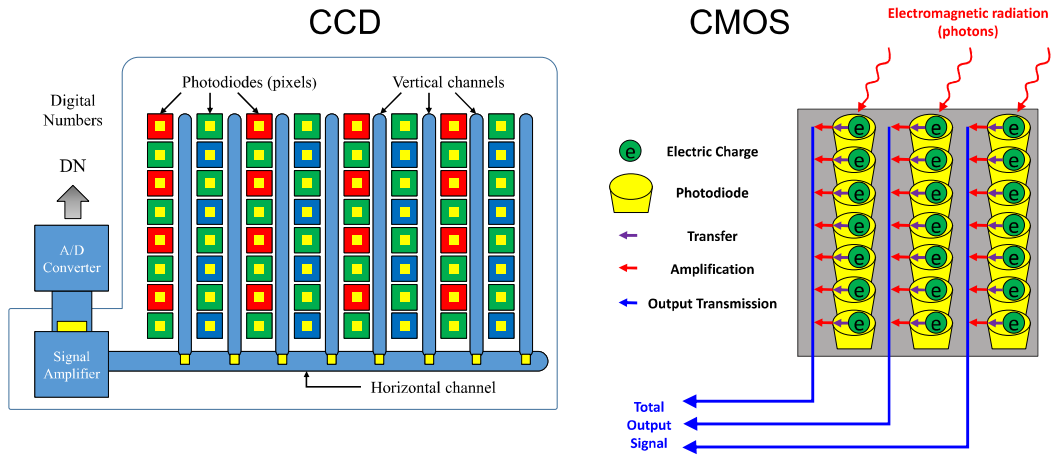

Figure 2.3 On the left: simplified scheme of a Charge Coupled Device (CCD) sensor. On the right: simplified scheme of a Complementary Metal Oxide Semi-conductor (CMOS) sensor.

In addition, CMOS detectors are based on photodiodes or transistor elements where the charge is directly processed through an integrated amplifier and then digitised by a processing unit that is attached to the pixel element itself. This implies that no charge transfer is needed, even though the fill factor of CMOS sensors is slightly smaller than full-frame transfer CCD ones. For this latter reason CMOS sensors are generally equipped with microlens.

The CMOS technology is widely use on reflex cameras as well as on smartphone devices. Advanced multispectral sensors make use of CMOS sensors too, for all of the above reasons.

2.2.2 Colour detection

As mentioned, in each pixel a charge formation process takes place, whereby the incident light is converted in an electric charge regardless of the wavelengths of each single radiation. This translates into the inability of the sensors to distinguish between colours. In facts, no information of this kind is ever collected by any pixel. In order to overcome this issue, different approaches exist. For the UAV cameras, the most relevant one is the application of a filter mask in front of the pixel array. Additive colours, thus red, green and blue, are then detected. The most common filter is represented by the Bayer pattern where the amount of green filter elements is the double with respect to the single red and blue amounts (Figure 2.4). The arrangement of the pattern is made in such a way to allow the computation of the non-recorded colours by an interpolation process based on the information acquired by the adjacent pixels.

However, it is worth noting that the presence of the Bayer pattern may represent an issue for the very low-cost multispectral sensors realised by the simple modification of existing compact cameras since the missing information is computed by interpolation, thus reducing the actual geometric resolution of the camera.

Once the light has traversed the microlens and the filter (Figure 2.2), finally it will hit the sensor's surface. As well as it happens when it interacts with any other material, the radiation can be reflected, absorbed within the semi-conducting layer or even transmitted in the case of high-energy photons. The absorption takes place

whenever the wavelength is shorter than a threshold value λ_g. This latter amount depends on the radiated material and is defined as:

$$\lambda_g = \frac{h \cdot c}{E_g} \qquad \text{(Eq 1.48)}$$

In which c it is the *speed of light in the vacuum* and h it is the *Planck's constant*.

The quantity E_g represents the energy between conduction and valence band and assumes a value of about $1.12\ \mathrm{eV}$ for the silicon used in manufacturing CCD sensors. The corresponding threshold wavelength it is $\lambda_g \approx 1097\ \mathrm{nm}$. This value belongs to the near infrared radiation; hence CCD and CMOS sensors are able to detect and record the radiation up to this region of the spectrum and not only in the visible region.

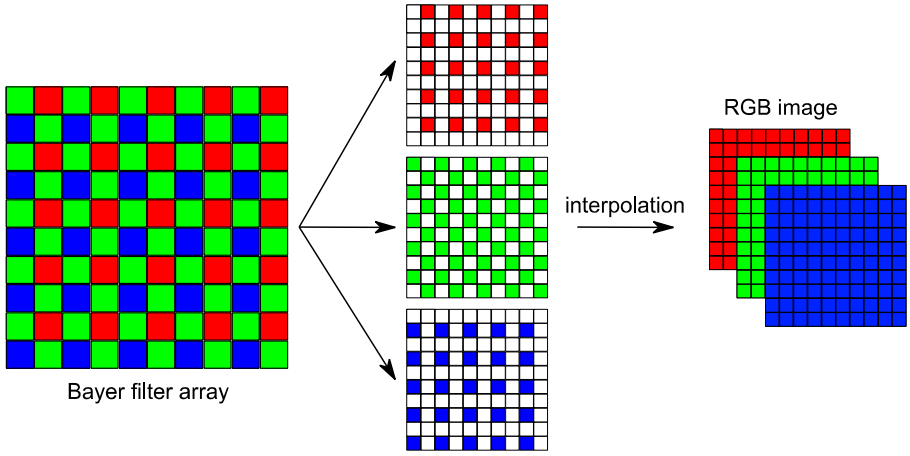

Figure 2.4 Bayer filter array for the detection of colours: the final image contains full matrices where non-recorded information has been computed by interpolation using adjacent pixel locations.

However, cameras used in photography are generally provided with an infrared filter in order to eliminate the contribution of NIR photons in generating the electric charge and to restrict the detected radiation to the only visible wavelengths.

This fact has to be considered whenever modifying compact cameras to make them sensible in the NIR region and is completely overcome in the most recent multi-optics multispectral sensors.

2.2.3 Dark current

The incident radiation is not the only responsible for the final generation of the electric charge within each pixel even though it is certainly the major contributor.

In fact, the thermal effects within the semi-conducting layers are responsible for the generation of small, but not negligible, charges. These represent a background noise, known as *dark current* [28], in the signal detected by the sensor and it depends on both the temperature and the integration time.

Some multispectral cameras, such as the MicaSense RedEdge-M, have optically-covered pixels on the imager in order to measure the dark current.

2.2.4 Signal-to-Noise Ratio

The dark current therefore represents a source of noise with respect to the actual incident radiation measurement.

It is possible to assess the level of influence that the noise has with respect to the signal by defining the Signal-to-Noise Ratio (SNR) as:

$$SNR = \frac{S}{\sigma_S} = 20 \log \frac{S}{\sigma_S} \ [\mathrm{dB}] \qquad \text{(Eq 1.49)}$$

where S it is the maximum signal amplitude and σ_S it is an indicator of the overall system noise. Every sensor is characterized by its own SNR value. For instance, CCD sensors have a *SNR* that is generally comprised within the range from 1000:1 to 5000:1, thus from ≈ 60 dB to ≈ 74 dB.

2.2.5 A/D conversion

Once converted into an actual electrical voltage signal, the charges need to be "measured" and then stored. An analog-to-digital (A/D) converter digitises the signals performing this task.

The conversion essentially consists in attributing an integer number, known as *digital number* (*DN*), to each detected voltage level. The accuracy of the process strongly depends on the total amount of possible values that the digitiser can assign to the input voltage levels. Generally, since the data is stored in terms of bytes, the

range of values is given in the binary form of 2^n. Usually the value of the exponent *n* is thus used to express the *radiometric resolution*, which is the capability of the imager to distinguish different levels of detected intensity after the A/D conversion. Ordinary compact digital cameras have a 8-bit resolution, whereas the most recent multispectral sensors can digitise voltage signals up to a 16 bit resolution.

This means that the digital number can assume $2^8 = 256$ possible values, within the range $[0, 255]$, for ordinary images and $2^{16} = 65536$ for some high radiometric resolution imageries.

Each DN value is finally stored in a matrix array that corresponds to the arrangement of the pixels.

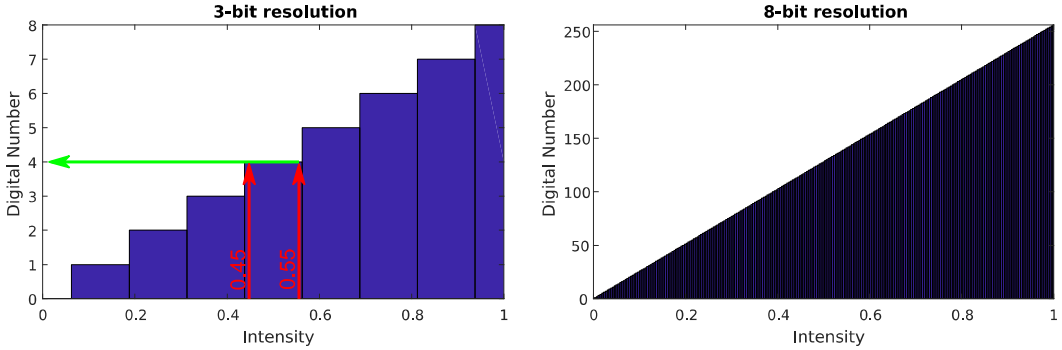

Figure 2.5 Example of different radiometric resolutions. Notice how it is not possible to distinguish between the input intensity values of 0.45 and 0.55 with a low-resolution approach, since the digital number 4 is assigned to both them by the digitiser.

2.3 Lens and distortions

Even though the radiation is actually detected and recorded by the sensor, the electromagnetic waves have to pass through a complex optical system made of lenses prior to reach the imager.

The most basilar physical law in geometric optics is expressed by the well-known *thin lens equations*. These equations provide the relationship linking the real object, its corresponding image and some characteristics of the lens. The expressions [28] are:

$$\frac{1}{a'} + \frac{1}{a} = \frac{1}{f'} \qquad \text{(Eq 1.50)}$$

$$z \cdot z' = -f'^2 \qquad \text{(Eq 1.51)}$$

where a represents the object distance and a' the image distance, f and f' are respectively the external and internal focal lengths, z and z' are the object and image distances relative to the principle foci (Figure 2.6).

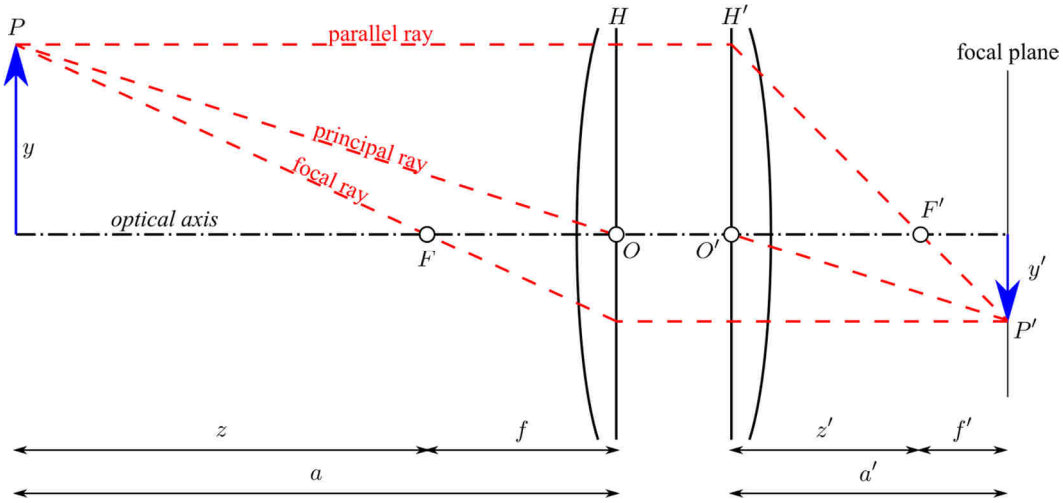

Figure 2.6 Typical scheme for a thin lens system.

The principle points O and O' are the centres of the principal planes H and H' and the line joining these points represents the optical axis. A further definition introduces the concept of nodal points as those points on the optical axis where a ray crossing the makes the same angle on both object and image spaces. If the refractive index is the same on both sides, then nodal points correspond to principal points. The optical axis intersects the focal plane on a point that it is defines as *autocollimation point*. This latter one represents the centre for the symmetry of lens distortions with centred lenses and with principle planes orthogonal to the optical axis.

The presence of the lenses in front of the sensor array is the responsible for the introduction of aberrations. The most important for the multispectral proximal remote sensing regards both the geometric aspects, in term of distortions, and the chromatic (thus spectral) aberrations.

Geometrically, the lenses cause a deviation of the ray emerging in the image space. For multispectral cameras, where no fish-eye or spherical lenses are ever used, the total distortion mainly consists in its symmetric radial component. A quartic distortion model is already able to accurately accounting for this deformation. According to the radial distortion model, the image observed

coordinates are displaced away from the image centre (barrel distortion) or toward it (pincushion distortion) by an amount that is proportional to the image radius. The image radius is referred as the quantity:

$$r = \sqrt{x_c^2 + y_c^2} \qquad \text{(Eq 1.52)}$$

where (x_c, y_c) are the image coordinates after a perspective division. This means that if (X, Y, Z) are the coordinates within the local camera coordinate system, thus follows that $x_c = X / Z$ and $y_c = Y / Z$.

The model's equations with a low-order polynomial formulation are:

$$\begin{aligned} x_c' &= x_c(1 + k_1 r_c^2 + k_2 r_c^4) \\ y_c' &= y_c(1 + k_1 r_c^2 + k_2 r_c^4) \end{aligned} \qquad \text{(Eq 1.53)}$$

in which k_1, k_2 are radial distortion parameters. The final pixel coordinates can hence be computed by:

$$\begin{aligned} x_s &= f x_c' + c_x \\ y_s &= f y_c' + c_y \end{aligned} \qquad \text{(Eq 1.54)}$$

Further effects can be considered in a more advanced modelling of the geometric optic distortion, like the tangential and decentring components, the affinity and the skew. The formers are related to a decentring and a misalignment of the individual lenses' elements, the latters describe a deviation in terms of orthogonality and scale of the coordinate axes.

However, all these effects are significantly smaller than the radial distortion and they should be therefore considered only when the accuracy demand is very high. For instance, in the case of the multispectral camera MicaSense RedEdge-M, that is one of the most currently performant low-cost sensors available for UAVs and it was used in the experimentation shown in this dissertation, the results of a calibration procedure used to estimate the various distortion components proved that the radial distortion was clearly the main component. In fact, the radial distortion in Figure 2.7 exhibits a magnitude order higher than the decentring distortion in Figure 2.8. Therefore, an accurate modelling of the radial distortion (Figure 2.9) could be satisfactory in order to adequately remove the lens distortion.

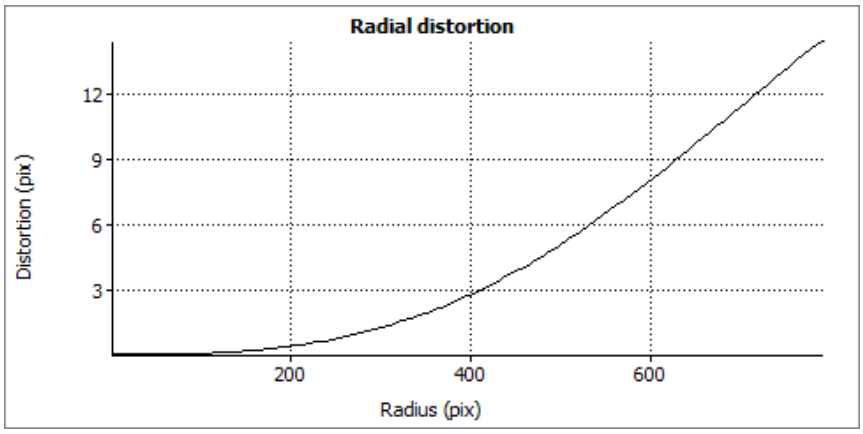

Figure 2.7 Symmetric radial distortion for the multispectral camera MicaSense RedEdge-M. The graph refers to the near infrared optic, but since the others differ only for the bandpass filters' transmittance, no significant deviations are present.

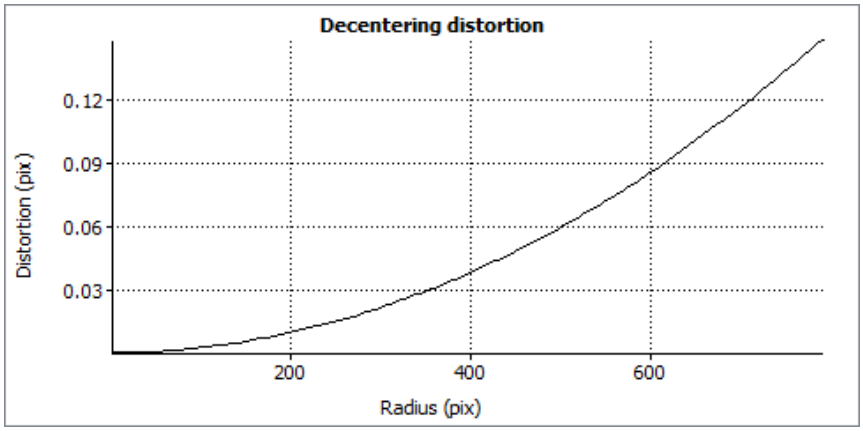

Figure 2.8 Decentring distortion for the multispectral camera MicaSense RedEdge-M. The same considerations of Figure 2.7 does apply.

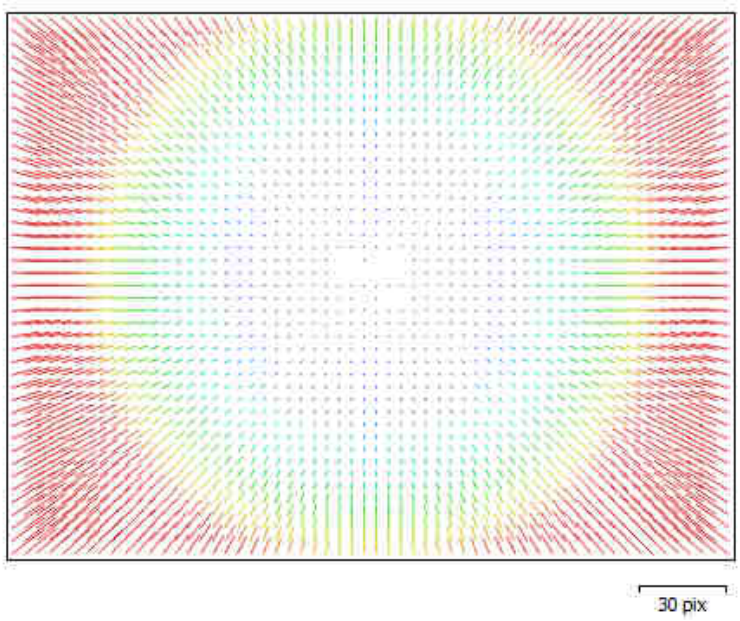

Figure 2.9 Distortion of the lenses for the MicaSense RedEdge-M (NIR band): the main distortion is along a radial direction.

2.4 Digital number to radiance

Since the radiometric calibration represents a fundamental task in order to produce reliable sensed data from the raw acquisitions, all the aberrations involving an alteration in the recorded radiance are crucial.

The chromatic aberration consists in a different as well as wavelength-dependant dispersion by the lens. A longitudinal (or axial) chromatic aberration implies that every wavelength has its own focus (Figure 2.10). Consequently, white objects are not focussed in a same point, but instead within a small range. This fact limits the sharpness of an image and could be limited by imposing the focus in the mid-wavelength like the green for visible cameras. Similarly, a lateral (or transverse) chromatic aberration is responsible for a small difference in the image scales depending on the radial position. In the case of the multispectral sensors, these aberrations are not significant whenever a bandpass filter is mounted in front of the sensor array, since a small range of wavelengths is transmitted. Conversely, for low-cost sensors with high-pass filters, these effects could affect the recorded data.

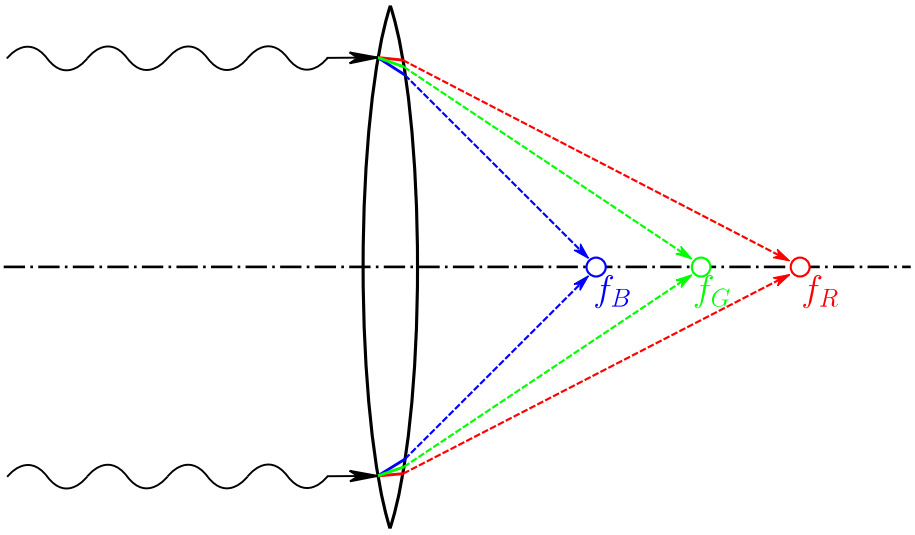

Figure 2.10 Longitudinal (axial) chromatic aberration [28].

Moreover, the lens system causes a constant luminous intensity I to be reduced proportionally to the field angle τ . The image becomes therefore darker towards its periphery and this effect is stronger for wide-angle lenses. The intensity that is effectively detected on the imaging plane of the sensor is given by:

$$I' = I \cdot cos^4\tau \qquad \text{(Eq 1.55)}$$

This reduction, that is hence proportional to a $\cos^4$ factor, can be amplified if the *vignetting* is also taken into account. The vignetting is due to physical obstructions caused by the mounting parts of the lens [28].

With particular regard to multispectral cameras, the vignetting is modelled through a polynomial radial function by analogy with the symmetric radial geometric distortion. In fact, the effect owns an axial symmetry [30] (Figure 2.11). The centre of this symmetry is the vignetting centre (v_x, v_y). Denotating the radius r as the distance between an image point and the vignetting centre, the polynomial has the form:

$$v = 1 + \sum_{i=1}^{N} c_i r^i \qquad \text{(Eq 1.56)}$$

The order of the polynomial depends on the adopted value of N, while the parameters c_i are the vignetting coefficients. These parameters can be estimated through a calibration procedure, e.g. using a known intensity light source covering all the imaging plane with no saturation.

Figure 2.11 Vignetting for the multispectral camera MicaSense RedEdge-M. The graph refers to the near infrared optic, but other bands are similar. The vignetting causes peripherical pixels to be significantly darker than those nearer to the image centre.

Most of the software used for the processing of multispectral imageries collected by drones implement this radial polynomial model, such as Pix4D Mapper Pro [31].

For performant multispectral cameras, such as the MicaSense RedEdge-M sensor, these parameters are provided to the user through the metadata attach to each image file and they have been obtained through a laboratory calibration.

In this latter case, the order of the polynomial is six and coefficient up to the magnitude of 10^{-17} are provided within the image metadata of each capture:

$$v = 1 + c_1 r + c_2 r^2 + + c_3 r^3 + c_4 r^4 + c_5 r^5 + c_6 r^6 \qquad \text{(Eq 1.57)}$$

The resulting vignette map is computed for each pixel location and consists in a $V(x, y)$ function.

Moreover, multispectral sensors are usually equipped with a global shutter instead of a rolling shutter. This means that all the pixel locations start the integration at the same time and the image is not acquired “line-by-line”.

However, the integration of the dark current on the storage node is responsible for a gradient in the dark level of the CCD sensors. This further effect can be taken into account, also for CMOS sensor according to the implementation proposed by the manufacturer of the MicaSense RedEdge-M [32], and it is modelled through a row gradient correction that depends on the *y* coordinate only:

$$R = \frac{1}{1 + a_2 \cdot \dfrac{y}{t_{\text{exp}}} - a_3 \cdot y} \qquad \text{(Eq 1.58)}$$

where t_{exp} it is the exposure time and a_2, a_3 are radiometric coefficients that are determined through a calibration procedure and finally provided to the user within the metadata of the captured images.

The intensity $\tilde{L}$ is thus computed applying corrections to the raw digital numbers for both the vignetting and the row gradient as well as shifting in order to consider the dark current, for each pixel location:

$$\tilde{L} = V \cdot R \cdot (DN_{\text{raw}} - \text{dark current}) \qquad \text{(Eq 1.59)}$$

The DN_{raw} in the expression (Eq 1.59) represents the digital number recorded in a pixel after the exposure and therefore already converted from the voltage signal by the digitiser. Here, the $dark\ current$ it is the digital number recorded by optically-covered pixels on the imager. These pixels are exposed for the same duration of non-covered pixels and since no light is able to reach their photodiodes, they actually measure the dark current intensity. This information is hence used to apply an offset to the raw recorded data in order to compensate for part of the sensor's noise. Similarly, V and R are matrices that apply corrections for the vignetting and the row gradient element-wise respectively.

The final computation of the actual radiance can be performed by additionally taking into account the ISO sensitivity at the time of the image capture. This setting, that is usually managed by the camera on its behalf, allows the amplification of the voltage signal so it will be digitised exploiting the full resolution of the digitiser. The amplification effect can be expressed by a *gain* as the ratio between the digital number of the pixel with the current ISO and the corresponding value that the same intensity would have been produced with a standard ISO 100. Moreover, the effective exposure time has to be considered as well for converting a recorded intensity level to a radiance, since higher it is the time of the exposure and higher will be the electric signal generated within a pixel.

Thus, denotating with res the radiometric resolution of the digitiser (2^n for a *n*-bit resolution), the actual spectral radiance can be computed as

$$L_\lambda = \frac{\tilde{L}}{gain \cdot t_{\mathrm{exp}}} \cdot \frac{a_1}{\mathrm{res}} \quad (\mathrm{W\ m^{-2}\ nm^{-1}\ sr^{-1}}) \qquad \text{(Eq 1.60)}$$

where the parameter a_1 is a radiometric coefficient that is provided to the user together with the a_2 and a_3 coefficients previously used to perform the row gradient correction.

Actually, the calibration procedure reported above, from (Eq 1.58) to (Eq 1.60) represents the model proposed by MicaSense [32] for its RedEdge-M multispectral camera. Slightly different calibration models exist, such as the one that Parrot proposes for its Sequoia sensor [33]. In this latter, the f-stop is also considered. However, since most of the multispectral camera, including the

MicaSense RedEdge-M and the others used in the following experimentations in this dissertation have a fixed f-stop, this implies a simple scale factor difference with respect to the model formerly presented.

2.5 Radiance to reflectance

Once that the raw digital numbers have been transformed into radiance values, it is therefore necessary to consider a radiometric calibration source in order to further perform the conversion from radiance to reflectance.

It is important to distinguish between a *relative* radiometric calibration and an *absolute* radiometric calibration [22]. The former refers to the main need to reduce the spatial noise effects on the imagery, while the latter approach enables to generate an image product that maintains an absolute radiometric information.

In the case of multispectral UAV cameras, the absolute radiometric calibration approach allows to finally compute reflectance values from the raw data sensed, hence to compute reliable spectral indices. Moreover, thanks to an absolute approach, the data may be compared over time, e.g. for survey repetitions or monitoring purposes.

However, the absolute calibration requires a source that is traceable to a reference standard, thus the source should have a known spectral irradiance. In addition, it is not possible to directly use the radiation coming from such a source for the calibration, since its spatial distribution is strongly directional. Thus, a diffuse illumination from the source should be obtained using a Lambertian scatterer. Sintered PTFE panels, such as the Spectralon® from Labsphere, exhibit an almost Lambertian behaviour. They may reach a reflectance around 99% over the solar spectrum [10], even if they still show significant deviations from the ideal diffusive behaviour at low angles.

These panels can be used during field surveys in order to establish the relationship between the detected radiance and the reflectance of the canopy or, more generally, of a sensed surface.

Prior to this, each panel must be radiometrically calibrated by reconstructing its spectral signature. This task, that may be performed in laboratory by detecting its corresponding spectral response in very narrow wavelength ranges, enables to

use the panel as a reference standard over the region of the spectrum where its spectral characteristics have been measured.

Assuming that no significant change in the environmental light conditions occurs between the time of capturing a panel picture and performing the aerial survey, the relationship between radiance and reflectance could thus be estimated exploiting the panel's photograph. In particular, a consistent part of the photographed panel can be used to compute the mean value of the radiance once that the raw digital numbers have been previously corrected for accounting for dark current vignetting, row gradient, actual exposure time and ISO setting. In other words once that a radiance has been computed. Similarly, thanks to the known transmittance of the bandpass filter mounted in front of each optic, the mean reflectance value of the panel in the spectral sensed region can be computed by its calibration data, that represents the spectral signature of the panel itself.

The scale factor κ to convert radiance to reflectance within the panel's region is therefore given by the ratio:

$$\kappa = \frac{\text{mean reflectance}}{\text{mean radiance}} \qquad \text{(Eq 1.61)}$$

Since the assumption of no significant irradiance change was previously made, the same conversion factor may be applied to the radiance of aerial survey's images in order to compute the corresponding reflectance as follows:

$$\text{image reflectance} = \kappa \cdot \text{ image radiance} \qquad \text{(Eq 1.62)}$$

The process for converting radiance values into reflectance values seems to be relatively simple, since it mainly consists in the estimation of a scale factor. However, there are some remarks:

- the satisfaction of the negligible change in the environmental light conditions hypothesis may be hard in case of an overcast sky. In this case an additional device on the UAV is needed for a continuous tracking of the actual irradiance;
- the panel's image has to be acquired without overexposed pixels. In fact, whenever the pixel saturation occurs, the relationship between the incident radiation and the electric charges generated by the sensor's detectors is lost. Thus, while the reflectance of the panel is

still known, the radiance on the photographed panel becomes unknown. This means that the brightness should be adequately assessed and the panel's photograph should be acquired standing in front of the panel (placed on a flat ground) with the sun at the back to reduce specular reflection effects.

- shaded pixels will be identified by low reflectance values on the final image product even though the reflectance does not vary from sunlit surfaces to shaded ones. This effect is due to a change in the actual amount of radiation that hits a shaded area, that is much smaller than a sunlit area. The result is that for these regions the scale factor is not able to convert the detected radiance into a real reflectance, since the panel was sunlit at the time of its image acquisition.

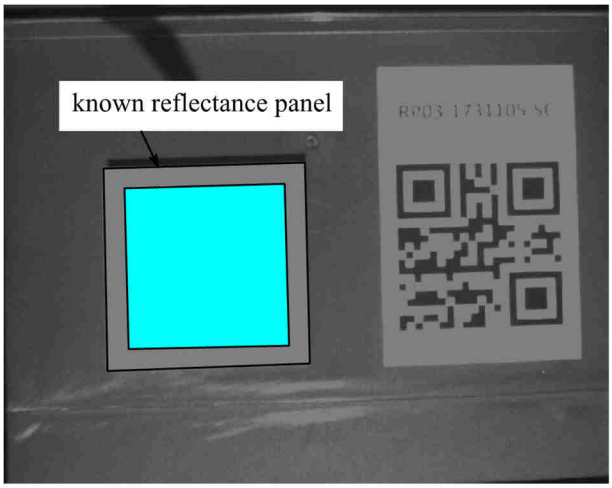

Figure 2.12 Image of the known reflectance panel: the Agisoft PhotoScan Professional software is able to self-detect the region (highlighted in cyan) where calculating the mean radiance thanks to the QR code included in the image itself.

2.5.1 Accounting for irradiance variations

The conversion from radiance values to reflectance ones by using a calibrated reflectance panel that exhibits an almost perfect Lambertian behaviour represents a reliable approach to compute actual reflectances. However, in many situations, the environmental light conditions may change, for instance due to the presence of clouds. The occurrence of such a variation in the real irradiance is highly probable if the UAV flights have a duration of 15 minutes or more.

Whenever this happens, the relationship between radiance and reflectance estimated on the basis of the panel's image captures is lost. In particular, the correlation gets weaker as the irradiance change becomes higher.

In order to operate in such situations without losing accuracy in the computation of the final reflectance values, a new onboard device is needed to continuously measure the irradiance.

Downwelling Light Sensors (DLS) are devoted to this task. Most of the more recent and performant UAV multispectral cameras are provided with a DLS and they are interfaced with it. Essentially, the DLS consists in a further sensor that measures the energy coming from the whole sky's hemisphere, thus the irradiance (Figure 2.13). This sensor is made of the same number of CMOS sensors of the multispectral cameras and each one is equipped with a narrowband filter with the same transmittance of the corresponding one on the multispectral camera. A diffuser is mounted on the top of the sensor to gather light. Generally, it is made with polycarbonate or polytetrafluoroethylene (PTFE).

At least two different factors should be considered in the measurements performed through the DLS:

- both a direct and a diffuse irradiance components contribute to the formation of the total irradiance. In addition, the irradiance detected by the DLS decreases with the angle from the surface normal. The reduction is proportional to a $\cos^4 \varphi$ factor.
- the Fresnel effect has to be considered for the DLS, since the diffuser causes part of the incident radiation to be reflected and part to be transmitted, thus refracted.

The intensity of this latter component is given by the Fresnel equations. The transmitted fraction $T = \frac{I_t}{I_i}$ can be expressed as a function of incident radiation angle φ_i and the refracted radiation angle φ_t [34]:

$$T = 1 - 0.5\left[\frac{\sin^2\left(\varphi_t - \varphi_i\right)}{\sin^2\left(\varphi_t + \varphi_i\right)} + \frac{\tan^2\left(\varphi_t - \varphi_i\right)}{\tan^2\left(\varphi_t + \varphi_i\right)}\right] \qquad \text{(Eq 1.63)}$$

Also in this case the effect's magnitude depends on the angle that the beam forms with the surface normal, besides the actual refractive indices of the media.

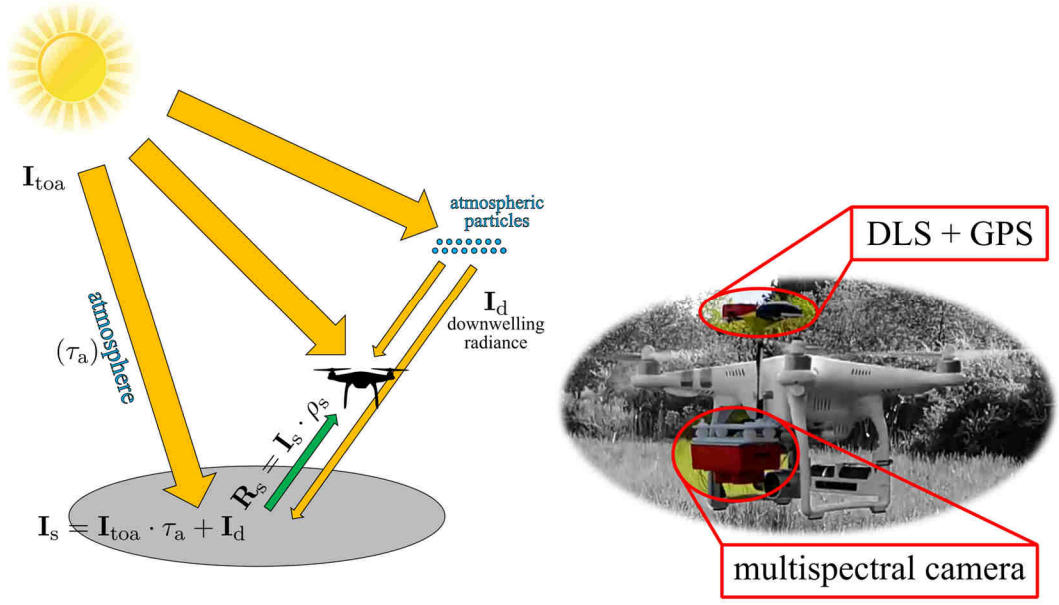

Figure 2.13 On the left: scheme of Figure 1.11 for a UAV-mounted multispectral camera with a DLS installed on the top of the aircraft. On the right: detail on a DJI Phantom 3 equipped with the multispectral system in the same configuration of the scheme (the MicaSense RedEdge-M).

If no reflectance panel is available, the DLS on its own already allows to convert the image radiance into a reflectance value. This approach considers the fact that the DLS measures the radiation energy coming from the sky in $\left(\mathrm{Wm^{-2}}\right)$ and the multispectral camera measures the corresponding fraction that is reflected by the ground or the canopy in $\left(\mathrm{Wm^{-2}sr^{-1}}\right)$. More precisely, since the detection are performed by using narrowband filters, we should strictly speak about spectral quantities, thus the first it is a *spectral irradiance* $\left(\mathrm{Wm^{-2}nm^{-1}}\right)$ and the second it is a *spectral radiance* $\left(\mathrm{Wm^{-2}nm^{-1}sr^{-1}}\right)$.

However, since the spectral irradiance is measured on the overall sky, thus from the entire hemisphere, while the spectral radiance is detected from a small solid angle by the camera, the two quantities are not directly comparable. Similarly to the computation of (Eq 1.9), a π factor allows to match the two measurements.

In this way, the *spectral reflectance* could be computed by the simple ratio:

$$\rho_\lambda = \pi \cdot \frac{\mathbf{L}_\lambda}{\mathbf{I}_\lambda} \quad \text{(Eq 1.64)}$$

Even though this process effectively enables the computation of a reflectance value, many factors can affect the results. For example, deviations of the real characteristics of the diffuser from the modelled ones may affect the irradiance measurement as well as the actual solar angle at the time of the image capture.

For such reasons the best approach consists in using a known reflectance panel and exploiting the extra information consisting in the DLS measured irradiance to assess the variation of the environmental light conditions and compensate for them.

In order to do that, an initial image of the panel need therefore to be acquired ensuring that the DLS is correctly exposed and oriented to the sunlight. This means that the DLS should be kept horizontal and the operator should cover the smallest sky portion. In this way the DLS is used for a computation of an radiometric correction that may avoid drifts due to a change in the actual irradiance but exploiting the high accuracy in using the panel for the calibration.

Further approaches for the computation of the reflectance are reported in the literature. Tu et al. [35] proposed methods for both normalising all the raw images using the image having the lowest DLS-recorded irradiance in order to avoid saturation issues as well as computing the reflectance ρ with the expression:

$$\rho = Kf^2 \frac{(DN - B) \cdot G\Gamma}{(At_{\text{exp}}\gamma) \cdot \text{Count}} \quad \text{(Eq 1.65)}$$

where K represents n unknown arbitrary number that can be estimated using at least one known reflectance target for solving such an arbitrariness, f is the f-number of the camera, t_{exp} is the exposure time, DN is the digital number, γ is the ISO value, Count, G, Γ are parameters of the irradiance sensor that represents arbitrary irradiance level, gain and exposure time and A, B, C are calibration coefficients recorded in the metadata (since the authors used a Parrot Sequoia in their study). However, this approach does not differ significantly from the correction model presented above.

2.5.2 BRDF considerations

The bidirectional reflectance of the canopy, already discussed in Section 1.3.2, represents a further aspect that should be considered in order to compute the most accurate reflectance values, including the case of multispectral cameras on unmanned aircrafts.

Applying corrections for the BRDF may increase the brightness homogeneity of the merged images [36,37]. The implementation of such corrections can be performed using correction models proposed in the literature.

The Walthall model [38], for instance, has been implemented by Tu et al. [35] in the form:

$$\rho = a\theta_v^2 + b\theta_v \cos(\varphi_v - \varphi_s) + c \qquad \text{(Eq 1.66)}$$

in which ρ is the reflectance, θ_v, φ_v are the viewing zenith and azimuth angles, φ_s is the sun azimuth angle and a, b, c are parameters of a (multivariate) linear regression. A similar approach was also followed by Honkavaara and Khoramshahi [39] to implement the same Walthall model using radiometric control points (RCP) made of reflectance panels.

Especially for hyperspectral imageries, the accurate computation of BRDF correction provides more faithful reflectance values and makes it possible to determine more reliable spectral indices.

2.6 Structure from Motion

Once that the imagery dataset has been radiometrically calibrated and the reflectance values have been computed, the following crucial task for any aerial survey conducted by the means of UAVs consists in merging the images in order to generate a comprehensive orthomosaic.

For narrowband multispectral sensed data, most of the times a single image is provided for any of the sensor's optics. Since the captures are generally synchronised, the entire images subset contains all of the spectral information in the different bands. The main difference with a real multiband capture consists in the

fact that images does not totally overlap since there is a small, but significant, offset between the various optics.

The estimation of the orientation of the camera centres in the space at the time of each capture can be performed by classical photogrammetry principles and consists in the so-called *exterior orientation*.

At the same time, a camera model should be determined by performing a calibration procedure that estimates the position of the *autocollimation point* (or *principal point*), the *principal distance* and the coefficients of the assumed distortion model. This set of parameters represent the *interior orientation*.

As long as the digital photogrammetry began its development thanks to the availability of digital sensors and images, the new branch of the *computer vision* started to provide robust algorithms for the estimation of the three-dimensional geometry from a set of bidimensional images and to reconstruct dense point of clouds [40].

The *structure from motion* lies precisely in the estimation of a real geometry (the so-called *structure*) from a set of images taken all around an object (the so-called *motion*). Images are aligned thanks to the detection of common features that are matched and treated as tie points.

The feature detection is based on the recognition of image patches. During this stage, no information about which other image locations the feature will be matched to is ever available. Therefore, each feature is tested for small displacements of itself to evaluate its metric stability in form of the *auto-correlation function* [41]:

$$E_{\mathrm{AC}}(\Delta \boldsymbol{u}) = \sum_i w(\boldsymbol{x}_i)[I_0(\boldsymbol{x}_i + \Delta \boldsymbol{u}) - I_0(\boldsymbol{x}_i)]^2 \qquad \text{(Eq 1.67)}$$

Whenever this function exhibits a strong minimum, the corresponding feature could be well localized. After the detection of the features, denotated also as *keypoints*, have been performed, a descriptor is used to characterize the feature for accounting for possible changes in its scale and orientation through the various images and even also for an affine deformation due to perspective distortions. Many descriptors exist, e.g. the *scale invariant feature transform* (*SIFT*) [41].

Once that each feature has been extracted from two or more images and it has been characterized through a descriptor, it can be matched. Some preliminary matches could be established through a *matching strategy* that determines which correspondences may be further processed. In addition, efficient algorithms should be devised to perform the matching task in the shortest possible time.

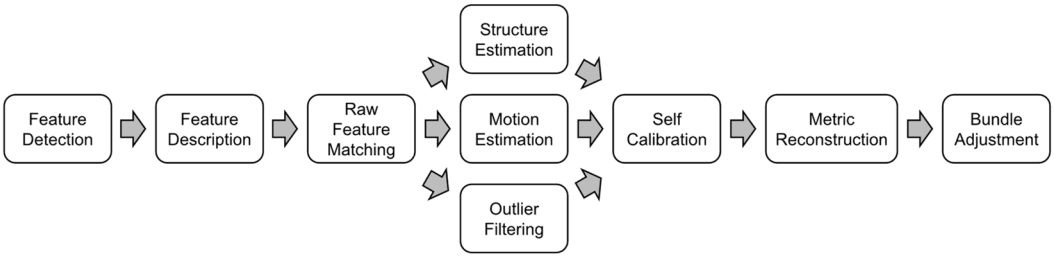

Figure 2.14 ***Structure from Motion*** **(*SfM*) workflow from the feature detection on each image (keypoints) to the final bundle adjustment.**

The multi-image processing is then performed through a *bundle adjustment*. It is a method for a numerical fit of a large (even almost unlimited) number of images forming a bundle of rays. The fit is conducted simultaneously for all of them. The procedure makes use of measured image points, survey observations and an absolute reference system in which the object is framed. Using the tie points that are detected through the matching above, single images are merged into a unique and global model. Thus, the object surface can be reconstructed in its three-dimensionality.

The model of the object may be reconstructed in an arbitrary reference system with an arbitrary scale factor. The availability of a set of *ground control points* (*GCPs*) allows to convert the object's coordinate from this latter arbitrary reference system to an absolute one through a seven-parameter transformation.

Even though the GCPs are the only points allowing to frame the model in an absolute reference system, they are not the only one that contributes to the estimation of the external orientation of the cameras. In fact, an important geometric constraint is that all image rays that pertain to the same tie point should intersect in the corresponding object point (theoretically unique) with a minimum uncertainty.

Since a large number of features are generally detected and matched, this latter constraint gives robustness at the bundle adjustment procedure providing a

strong ray bundles geometry and makes it the most accurate and powerful method for the image orientation in photogrammetry.

In particular, the strengths of the bundle adjustment consist in:

- solving for very large systems of normal equations;
- generating approximate values for the initial unknows;
- detecting (and thus filtering) gross errors.

Mathematically, the bundle adjustment is based on the well-known collinearity equations [28] and each iteration determines the three-dimensional object coordinates for any new detected point, the exterior orientation of each image and the interior orientation of the camera (in particular of each camera if more than one were used). Therefore, the interior orientation of the camera can be estimated within the bundle adjustment: this calibration procedure is called *self-calibration*.

The Structure from Motion approach allows then to obtain a sparse point cloud essentially made of tie points. However, another strength of the SfM consists in looking for additional correspondences on the images once that the entire dataset has been aligned. This task is facilitated by the computation of projective depth maps [41] for each image and finally leads to a significant densification of the initial sparse cloud. Once that a dense point cloud has been reconstructed, the surface of the object can be thus modelled through a mesh surface on which it is possible to apply a texture. The final projection on a reference view is performed through a further coordinate transformation with the aim of creating a comprehensive orthomosaic that represents all the remote sensed extents.

With particular regard to the multispectral UAV cameras, it is important to highlight that a Structure from Motion approach enables to:

- frame the survey in an absolute reference system;
- model the lens distortion;
- estimate the orientation of each image whilst performing an overall least-square adjustment;
- generate a dense point cloud and even a digital elevation model if needed;

- stitch all the images into a comprehensive georeferenced orthomosaic.

In addition, the most common commercial software based on a SfM approach (e.g. Agisoft PhotoScan Professional and Pix4D Mapper Pro) can handle the images captured by some multispectral cameras (e.g. Parrot Sequoia and MicaSense RedEdge-M). This implies that the final orthomosaic obtained by the software contains the spectral information in as many bands as the multispectral camera's optics. However, some slight difference pertains to the procedure used for balancing colours when merging the images. In fact, the Pix4D Mapper Pro software [42] allows to both create an orthomosaic presenting a colour balancing and reflectance map without any balancing. The former is a more visually pleasing result, while the latter is a more faithful product.

The SfM approach therefore represented the method used for merging all the multispectral imageries acquired during the flight mission of any experimentation campaign.

2.7 Current multispectral sensors

Thanks to the development in the sensor technology and in the miniaturization process during the last decade, especially joined to the lower prices of the last few years, many multispectral sensors are currently available for unmanned aerial vehicles.

The challenge for any multispectral sensor consists in acquire reliable spectral data at a limited overall cost of the system. In addition, the use of 2D imagers allows to reconstruct a reflectance map of a land portion with a structure from motion approach.

2.7.1 Spectrometers

Spectrometers are devices able to detect the spectral signature of an object with a high level of detail. However, their measurement is punctual and it is conducted on a small area (footprint) related to both the field of view of the sensor and the distance from the detected object. Spectrometers mounted on a UAV have been widely tested in the last years.

In 2014 an Ocean Optics STS microspectrometer was successfully used for field spectroscopy [43] performing hyperspectral measurements within the range from 350nm to 800nm, thus from the visible to the near infrared, with a full width at half maximum (FWHM) value of no more than 3nm for each band. The weight of the system was only 216g and the flight altitude was limited to 10 meters. The aerial measurements proved to have a standard deviation much smaller than the hand-held ones.

A more recent implementation of a spectrometer system on a UAV platform for land cover classification has been conducted by Natesan et al. [44] using a FLAME-NIR near-infrared spectrometer that was used to perform hyperspectral detections. The weight of the instrument is 265g and it has a spectral resolution of 10nm (FWHM). In addition, RGB images were captured simultaneously to the spectrometer data. Spectrometer's classification was compared with the results obtained through an object classification using a maximum likelihood classifier. The latter ones were assumed as reference. The accuracy of the classification proved to be higher (78%) for homogeneous land covers and smaller (50% on average) for mixed land covers.

Besides point spectrometers, pushbroom spectrometers are able to record a line of spectral information instead of a simple sampling point. State-of-the-art sensors of this latter typology have a typical weight of about 1 kg [12]. This value is much higher than the spectrometer's systems, even though it will probably decrease in the future.

Both point spectrometers and pushbroom spectrometers need additional on-board devices to accurately georeference the performed measurements.

2.7.2 Spectral 2D imagers

The use of 2D imagers represents another technique that has been widely developed in the last years. Thanks to their bidimensional array of detectors, these imagers can acquire a multispectral, or even hyperspectral, picture for each exposure. This fact therefore introduced new approaches for the imaging spectroscopy. One of the first multispectral sensors was the Tetracam MCA made of four to six cameras equipped with a narrowband filter in front of each one.

The *rolling shutter*, consisting in an exposure row by row instead of a global one, which is performed to maximise frame rates, represented a significant issue for this camera since not all of the image content was recorded at the same time and thus the drone movement caused a sort of image distortion.

For this reason, most of the latest multispectral sensors use a global shutter technology. Very compact and lightweight systems are currently available, such as the Parrot Sequoia, the MicaSense Red Edge-M as well as new Tetracam devices and the MAIA camera. This latter is a nine sensors system with eight monochromatic sensors and an RGB one. Each of the first ones is equipped with a bandpass filter in order to detect the same wavelength intervals of the Digital Globe's WorldView-2 satellite within the range from 395nm to 950nm. However, the weight of the MAIA camera is 420g and its cost is of about 13500 € as of November, 2018 [45]. The Parrot Sequoia and the MicaSense Red Edge-M have a smaller number of sensors (respectively 4 narrowband + RGB for the first one and 5 narrowband for the second one). These instruments are lighter (both are less than 200g) and cheaper (between 4000€ and 5000€) than the MAIA camera, even though less performant. More details on the MicaSense RedEdge-M will be given in the Chapter 3.

Figure 2.15 The MAIA system, one of the multispectral cameras with the highest number of sensors (8 mono + 1 RGB) (source: https://www.spectralcam.com/).

In addition to the above multi-camera imagers, sequential and snapshot imagers have been developed. The first ones represent a sensing system that records a set of spectral bands sequentially in time [12]. This implies that the acquisitions are not synchronised, thus affected by a time lag. Once again, this may represent an issue whenever the sensor is mounted on an unmanned aircraft since the bands need to be co-registered in post processing. Snapshot imagers, instead, are able to detect all of the bands at the same time.

The Senop Rikola hyperspectral camera and the Vito COSI camera are examples of hyperspectral imagers.

The former is an up to 380 spectral bands capable imager, with a default spectral range of 500-900 nm and a spectral resolution of 10 nm (FWHM). Its weight is of about 720 grams not including additional GPS and DLS [46].

The latter was developed by VITO and it covers the range from 600 to 900 nanometres in 72 spectral bands. Each one covers an 8 pixels height on the sensor, thus 8 lines, on a 2048×1088 pixels sensor size. Each pixel size is 5.5 μm [47,48].

Even though hyperspectral sensors still have costs much higher of any multispectral camera, up to 40,000 euros as of November, 2018, they represent the most probable direction for future UAV spectral imagers thanks to the continuous miniaturization process.

CHAPTER 3

LOW-COST SENSORS IN PRECISION AGRICULTURE

3.1 Introduction

The recent availability of lightweight sensor for UAV applications, both multispectral and newer hyperspectral, has involved also the field of the agriculture. The so-called *precision agriculture* represents the implementation of advanced techniques of *crop management* [10], from the assessment of the health status of the plants to the scheduling of the interventions and their punctual execution with GPS-interfaced machines.

Unmanned aircrafts may be used in almost all the stages of this chain. With a remote sensing approach, however, UAVs are particularly useful in the first detection of the actual vegetation status by the means of spectral cameras.

One of the first studies in this direction was conducted in 2015 by Candiago et al. [49] and highlighted the great potential of high-resolution UAV data applied to the agricultural context for collecting multispectral imageries and computing spectral indices.

Concurrently, Matese et al. [50] started working on a comparison between satellites, airplanes and UAV platforms in the field of precision viticulture, remarking the very high difference in terms of geometrical resolution of these approaches.

Moreover, Matese continued the research in the field of the viticulture estimating the water stress in grapevines [51], confirming the strategical interest of a precision approach in the field of wine production.

Due to the increasing interest in the field of the UAV spectral sensing in the field of the precision agriculture, an experimental campaign with low-cost multispectral sensors started in the early 2016 with the prior acquisition of a DJI Phantom 3 Professional aircraft on December, 2015. This aircraft was equipped with the addition of a Sentera Single sensor. Concurrently, a 3DR Solo drone equipped with MAPIR cameras was bought.

This research project was part of an experimentation funded by the *Chamber of Commerce, Industry, Craftsmanship and Agriculture* of the province of Ferrara. The main focus of the entire project was to investigate the potential of the use of drones equipped with near infrared capable sensors characterized by the lowest possible cost, in order to enable local farmers to exploit the benefits of cutting-edge precision agriculture techniques.

The experimentation in the multispectral sector was thus prosecuted acquiring a more recent sensor in December 2017: the MicaSense RedEdge M. This latter can be still classified as a low-cost one if compared to hyperspectral sensors, but it is certainly more performant thanks to both the presence of a downwelling light sensor able to measure the diffuse irradiance and including a calibrated reflectance panel for the adjustment of raw digital numbers and the subsequent computation of reflectance values. The research conducted by using the MicaSese RedEdge-M camera, however, was focussed on a costal environment and regarded the seaweed monitoring over time. This study is presented in detail in Chapter 1.

For each precision agriculture experimentation, all of the acquired data processing was performed by both commercial specialized software, such as Agisoft PhotoScan Professional, and MATLAB scripts for a more accurate analysis.

The workflow that has been followed for testing the performance of low-cost sensors was focused on the best possible compromise between the reliability of the information detected by the sensor and the need to perform the additional data processing. However, it is worth noting that an excessive data processing may compromise and defeats the advantage of using a low-cost sensor. Therefore, throughout all of the experimentation we always beard in mind that the amount of this step should be proportionate to the overall cost of the acquiring system.

3.2 The low-cost sensors

All of the multispectral sensors used in the experimental campaign were CMOS sensors. The application of different kind of filters, bandpass or high-pass, allowed only to certain frequencies, thus wavelengths, to pass through the filter itself and finally reach the sensor array.

A variety of different sensors and cameras was tested in the experimentation. The first sensors, acquired in December 2015, were the MAPIR cameras and the Sentera Single sensor.

Other sensors were used later: a Parrot Sequoia (now commercialized as "MicaSense Parrot Sequoia") was used to investigate the differences in using such a more recent sensor and a previous model like the Sentera Single. This test was performed in spring 2017 and it is shown in detail in Section 3.4.4.

In December 2017, based on the outcome of this latter comparison, a MicaSense RedEdge M sensor was thus bought for replacing the Sentera Single sensor on the DJI Phantom 3 Professional aircraft.

3.2.1 MAPIR cameras

The very first low-cost sensors we started using in this research project were the MAPIR cameras. Since nowadays (in 2018) they are currently commercialized in their third version, it is important to highlight that the MAPIR Survey 1 cameras were tested here, representing the first edition of these kind of sensors (Table 3.1).

The complete set of sensors was formed by six cameras:

- BLUE: the blue one was equipped with a bandpass filter at about $450\ \mathrm{nm}$;
- GREEN: the green one was equipped with a bandpass filter at about $548\ \mathrm{nm}$;
- RED: the red one was equipped with a bandpass filter at about $650\ \mathrm{nm}$;
- INFRARED: the infrared (more exactly near infrared) one was equipped with a bandpass filter at about $808\ \mathrm{nm}$;
- NDVI (BLUE + NIR): the NDVI version one was equipped with a bandpass filter at both wavelengths of about $446\ \mathrm{nm}$ and about $800\ \mathrm{nm}$;
- RGB: the RGB (visible) one was a typical GoPro like camera, with an infrared cut filter (Figure 3.2).

It is worth noting that the non-RGB versions are likely the RGB where no infrared cut filter is applied and with the further application of a bandpass filter (Figure 3.3). Therefore, each camera presented a stable mounted Bayer filter array. Moreover, the NDVI version (Figure 3.1), in spite of its name, does not record any red information. On the contrary, it records the blue data. Due to the spectral characteristics of the filter mounted on this camera, there is no cross talk between the two bands. This issue was overcome in the Survey 2 version, in which the infrared data were collected at about $850\ \mathrm{nm}$ and the red data at about $660\ \mathrm{nm}$.

Figure 3.1 MAPIR camera "NDVI". The dimensions are comparable to a GoPro camera. (source: https://www.mapir.camera/ accessed on August 20th, 2018).

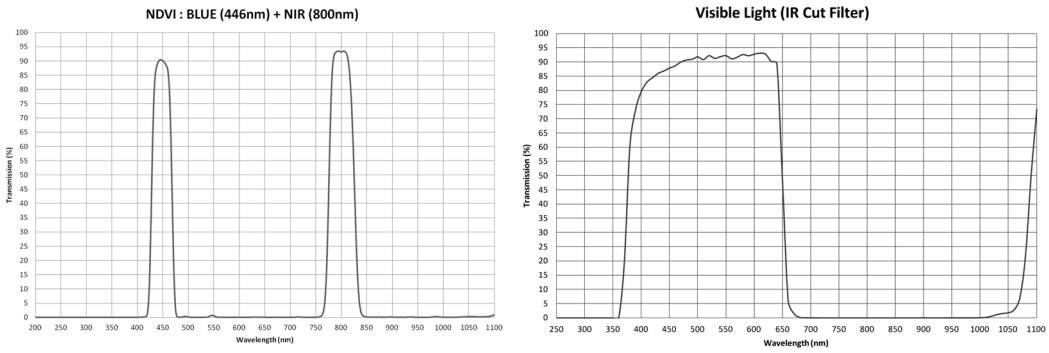

Figure 3.2 On the left: spectral transmittance of the filter applied to the NDVI MAPIR camera version. On the right: spectral transmittance of the infrared cut filter of the MAPIR RGB camera. (source: https://www.mapir.camera/ accessed on August 20th, 2018).

An important specification for MAPIR cameras is that they were able to capture an image every 3 seconds. This setting cannot be modified by the user in any way, so the flight speed should be calculated considering both the planned flight altitude and the desired longitudinal overlap.

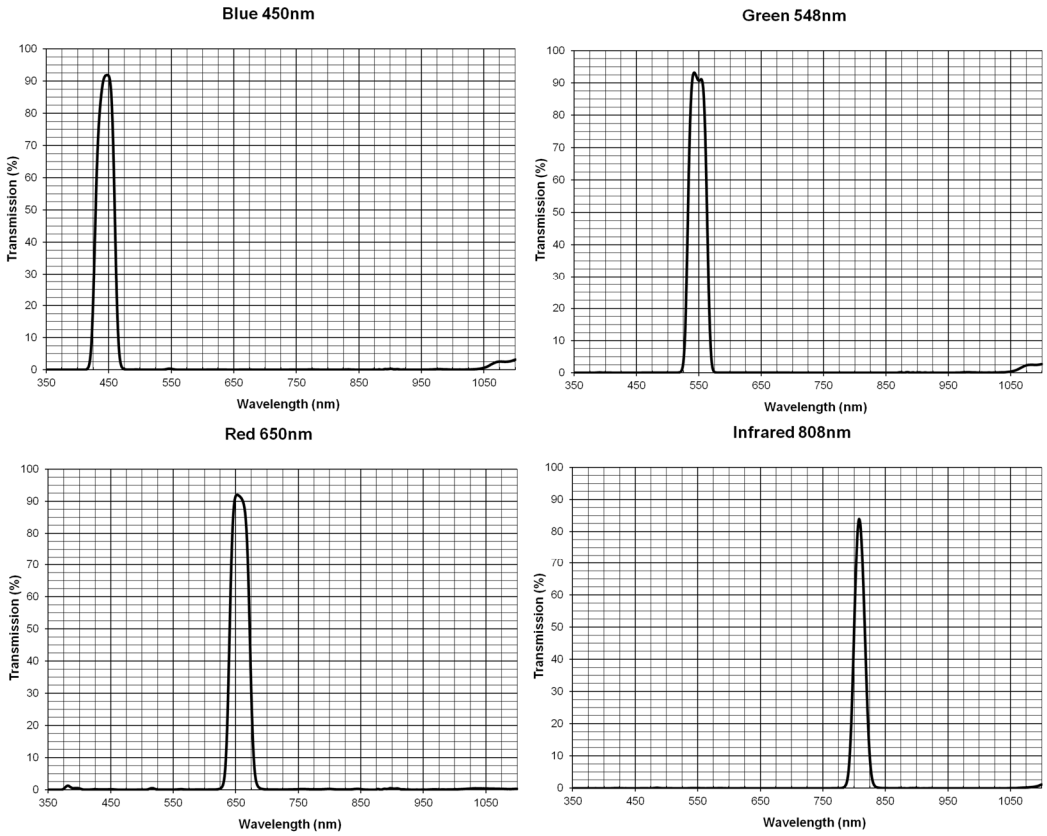

Figure 3.3 Spectral transmittance of the bandpass filters applied to the blue, green, red and near infrared MAPIR cameras. (source: https://www.mapir.camera/ accessed on August 20th, 2018).

Table 3.1 MAPIR cameras specifications.

Sensor	CMOS, 12 Megapixel, Rolling Shutter
Size	59.2 mm × 41.0 mm × 29.8 mm
Weight	47 grams (64 grams with battery)
Capture Speed	1 image every 3 seconds
Image Format	JPEG
Field of View	60° HFOV
GSD	5.7 cm at 100 m altitude
Cost	$ 250 (RGB camera) $ 300 (the other cameras) (VAT excluded)

3.2.2 *Sentera Single sensor*

The Sentera Single sensor was the second used in the initial phase of the multispectral tests. This sensor is characterized by a lower resolution of 1.2 megapixels if compared to the MAPIR cameras, but with the advantage to be a global shutter. This means that the scene is entirely acquired simultaneously and not scanned row by row. Considering that the sensors are mounted on aerial vehicles flying at a certain non-null speed, this fact contributes to ensure a sharp image definition. This sensor is particularly light-weight: the additional payload due to the camera is limited to only 25 grams (Figure 3.4, Table 3.2). The flight time of a drone equipped with this camera thus remains the same of the original and unmodified aircraft.

Figure 3.4 On the left: DJI Phantom 3 Professional equipped with the Sentera Single sensor. On the right: detail on both the RGB native camera of the DJI Phantom 3 and the added Sentera Single sensor, mounted in a fixed nadiral arrangement.

The Sentera Single sensor contains a high-pass filter that cuts wavelengths shorter than $575\ \mathrm{nm}$, in addition to the traditional RGB micro-filters that are still transmissive in the near infrared region. The resulting acquired images thus contain the near infrared information in the blue channel, whereas the green and red ones remain the same. In this way, an $R - G - NIR$ image is obtained and the $NDVI$ can be computed directly. However, due to both the real sensitivity of the CMOS and the filters, the equation (Eq 1.29) cannot be simply used. Instead, a quantification of the real radiances that are detected in the red and near infrared channels is necessary.

These two amounts differ significantly each other, since the quantum efficiency in the near infrared region of a CMOS is much lower than in the visible

region. In addition, the red channel is "affected" by the near infrared information, thus a true red radiance should be computed.

The radiance detected at the red channel for a certain amount of reflected radiant flux density, is given by the integral:

$$\boldsymbol{R}_{\text{red}} = \int_{575\ \text{nm}}^{1100\ \text{nm}} QE_{\text{red}}(\lambda)\ \mathrm{d}\lambda \qquad \text{(Eq 2.1)}$$

in which the lower limit of the integral represents the cut-off wavelength and the higher limit the longest wavelength where CMOS is still sensitive. The blue channel, instead, detects the near infrared radiation. Thus, similarly:

$$\boldsymbol{R}_{\text{NIR}} = \int_{575\ \text{nm}}^{1100\ \text{nm}} QE_{\text{NIR}}(\lambda)\ \mathrm{d}\lambda \qquad \text{(Eq 2.2)}$$

The true red is finally obtained by subtracting the quantity computed in (Eq 2.2) form the previous in (Eq 2.1):

$$\boldsymbol{R}_{\text{true red}} = \boldsymbol{R}_{\text{red}} - \boldsymbol{R}_{\text{NIR}} \qquad \text{(Eq 2.3)}$$

The NDVI can be computed using $\boldsymbol{R}_{\text{true red}}$ and $\boldsymbol{R}_{\text{NIR}}$:

$$NDVI = \frac{\mathrm{R}_{\text{NIR}} - \mathrm{R}_{\text{true red}}}{\mathrm{R}_{\text{NIR}} + \mathrm{R}_{\text{true red}}} \qquad \text{(Eq 2.4)}$$

The spectral sensitivity and thus the quantum efficiency for a CMOS sensor is shown in Figure 3.5, where the computed integrals values (areas) are highlighted.

The real quantum efficiency of the Sentera Single sensor, as well as the exact formula for computing the NDVI value from the recorded blue channel (corresponding to near infrared) and red channel data, are not explicitly written in the following, since they both represent proprietary information of the manufacturer. However, the exact formula has been applied for all the further analysis, provided as courtesy of the Sentera LLC.

The Sentera Single sensor is more advanced in comparison to the MAPIR cameras. It has an especially developed firmware that enables the user to select between different modes to capture images:

- GPS distance trigger, that allow to acquire an image whenever the aircraft has moved from its previous position by a specified distance;

- GPS time trigger, that acquires an image every *n* seconds, in which *n* is user-defined;
- GPS overlap trigger, that automatically calculates when taking a picture depending on both the altitude and the specified longitudinal overlap. The user can also specify a fixed altitude.

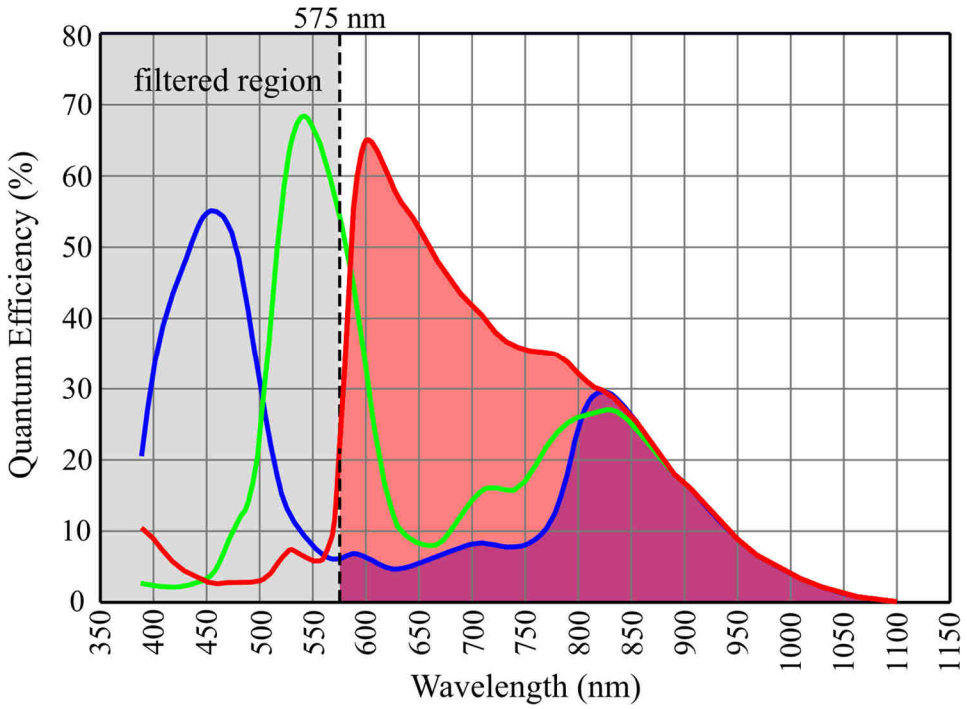

Figure 3.5 Quantum efficiency of a CMOS sensor: the application of a cut-off filter at 575 nm in the Sentera Single sensor allows to record near infrared information in the blue channel. However, there is a significant difference between the efficiency in the red and near infrared regions that requires to be considered before computing indices.

Table 3.2 Sentera Single camera specifications.

Sensor	CMOS, 1.2 Megapixel, Global Shutter
Size	25 mm × 33 mm × 38 mm
Weight	25 grams
Power Consumption	2 Watts
Image Format	JPEG, TIFF
Field of View	44° HFOV
GSD	6 cm at 100 m altitude
Cost	$ 1789 (VAT excluded)

In this experimentation the triggering method was usually set up to the "GPS overlap" mode, specifying a longitudinal overlap of 80% and allowing the camera to self-compute whenever activating the shutter.

3.2.3 Parrot Sequoia

The Parrot Sequoia, commercialized also as MicaSense Parrot Sequoia, is a five optics sensor developed to be mounted on unmanned aerial vehicles. It has a 16 Megapixel RGB rolling shutter camera and, in addition, four CMOS sensors (1.2 megapixel, global shutter) with a bandpass filter for detecting green, red, red edge and near infrared spectral data (Table 3.3). The radiometric resolution of the images of these latter ones is up to 10 bits. The camera is configurable through a web browser interface accessible by connecting to the camera itself by Wi-Fi.

The Parrot Sequoia camera includes an external "sunshine sensor" (Figure 3.6). This is a downwelling light sensor able to measure the diffuse radiance. In addition, it has a GPS, an IMU and a magnetometer in order to be completely independent from the aircraft on which the camera is mounted, maintaining the advantage of taking georeferenced pictures (Figure 3.7).

Figure 3.6 On the left: the body of the Parrot Sequoia camera. The green, red, red edge and near infrared dedicated sensors are well visible. The other optic is the 16Mpix RGB sensor. On the right: view of the top part of the downwelling light sensor (the so-called "sunshine sensor). Beneath the "white" plastic cover there are sensors with the same characteristics of the body camera ones and equipped with the same bandpass filters, in order to measure the diffuse irradiance.

Figure 3.7 DJI Phantom 3 Professional equipped with the Parrot Sequoia: the camera (body) is mounted in a fixed nadiral arrangement, while the downwelling light sensor, containing also the GPS antenna, is on the top.

Table 3.3 Parrot Sequoia camera specifications.

Sensors	RGB: CMOS, 16 Megapixel, Rolling Shutter G, R, RE, NIR: CMOS, 1.2 Megapixel, Global Shutter
Size	Camera body: 59 mm × 41 mm × 30 mm Sunshine sensor: 47 mm × 40 mm × 19 mm
Weight	72 grams (body) + 35 grams (sunshine sensor)
Power Consumption	5 Watts (body) + 1 Watt (sunshine sensor)
Image Format	JPEG (RGB), TIFF (G, R, RE, NIR)
Field of View	66° (RGB), 62° (G, R, RE, NIR)
GSD	2.7 cm (RGB), 9.4 cm (G, R, RE, NIR) both at 100 m altitude
Central Wavelength	550 nm (G), 660 nm (R), 735 nm (RE), 790 nm (NIR)
FWHM	40 nm (G), 40 nm (R), 15 nm (RE), 40 nm (NIR)
Cost	$ 3500 (VAT excluded)

3.2.4 MicaSense RedEdge M

The MicaSense RedEdge M (Figure 2.13, on the right) was the ultimate sensor bought for the multispectral experimentations.

Even though it was not used for the precision agriculture test, it is preferable to already include it among the sensors for a better understanding of all the sensors used within this dissertation.

The MicaSense RedEdge-M camera has five dedicated optics to acquire the blue, green, red, red edge and near infrared bands (Figure 3.8). No RGB image is directly captured by this sensor. However, exploiting the image registration process for single snapshots or a more complex structure from motion aligning procedure for an extensive imagery dataset, an overall orthomosaic with true colours can be reconstruct.

All of the CMOS sensor are global shutter and synchronized. The entire scene is then captured once and simultaneously for each sensor. Many triggering options are available:

- Timer mode: the user can set the time interval between two captured pictures. The minimum is 1 second;
- External trigger mode: in this case the camera will capture an image whenever an external triggering signal is detected;
- Overlap mode: the user can set specify both an altitude above the ground level and a longitudinal overlap setting. Then, the camera will start to capture images once it reaches an altitude that is 50 meters less than the specified altitude and any time that a distance *d* has been travelled, where $d = \text{specified altititude} \cdot (1 - \text{overlap})$.

The most suitable option for the experimental campaign was the overlap one. The side overlap was thus ensured by an accurate flight planning.

The MicaSense RedEdge M has a Downwelling Light Sensor (DLS) able to measure the diffuse irradiance of the sky. It is a 5-band sensor that connects directly to the camera: in this way, the corresponding measurements are stored in the metadata information of each captured image.

In addition, it has an external GPS antenna to store also a georeferencing tag, as well as for computing whenever triggering in the overlap mode.

The DLS must be mounted on the top of the aircraft in such a way that no further elements can shade part of it.

Figure 3.8 On the left: the body of the MicaSense RedEdge M camera. The blue, green, red, red edge and near infrared dedicated sensors are recognizable. On the right: view of DLS connected both to the camera and to the GPS antenna. (source: RedEdge M user manual by MicaSense)

The MicaSense RedEdge M kit also includes a known reflectance panel (Figure 2.12, Figure 5.9) to be photographed just before and just after performing any flight. In this way, it is possible to compute reflectances processing the images and exploiting the fact that the DLS can detect change in the illumination conditions. It is worth noting that this sensor is sold in a standard kit that already includes this calibrated reflectance panel, while the other sensors generally require that it has to be bought separately.

Even though the DLS alone it is able to provide an information that significantly improves the quality of the sensed data, the panel generally allows to calculate accurate reflectances and thus to obtain the most reliable results.

The bands of this camera are narrower (Table 3.4) in comparison to the respective bands of the Parrot Sequoia (Table 3.3). In this way the collected data are less dispersed along a range of wavelengths and more correlated to the central wavelength. However, in spite of having the same name, the bands of each camera actually differ in their central wavelength's value, so they would not be not directly comparable.

Table 3.4 MicaSense RedEdge M specifications.

Sensors	CMOS, 1.2 Megapixel, Global Shutter
Size	Camera body: 94 mm × 63 mm × 46 mm Sunshine sensor: 52 mm × 33 mm × 15 mm
Weight	170 grams (DLS included)
Power Consumption	4 Watts
Image Format	12-bit TIFF
Field of View	47.2° HFOV
GSD	6.7 cm at 100 m altitude
Central Wavelength	475 nm (B), 560 nm (G), 668 nm (R), 717 nm (RE), 840 nm (NIR)
FWHM	20 nm (B), 20 nm (G), 10 nm (R), 10 nm (RE), 40 nm (NIR)
Cost	$ 4900 (VAT excluded)

3.3 Unmanned Aerial Vehicles

All of the sensors were mounted on unmanned aircrafts. Two different kinds were used:

- a 3DR SOLO, able to carry up to four MAPIR cameras simultaneously. Generally, the set up was made in order to have the RGB camera, the so-called NDVI (NIR+Blue) camera and both the near infrared and red cameras to acquire all the multispectral data combinations and to have also visible images.
- A DJI Phantom 3 Professional equipped with its own RGB camera and, in addition, the Sentera Single sensor fixed in a nadiral arrangement (Figure 3.4).

A second DJI Phantom 3 Professional were used when using the Parrot Sequoia camera, since both the aircraft and the sensor were property of *AdriaRilievi* that participated in the collaboration for testing the sensor.

It is also worth noting that the Sentera Single was definitely removed in January 2018 in order to install the MicaSense RedEdge M on the same aircraft.

Figure 3.9 MAPIR camera mounted on a 3DR Solo with a quad static mount (source: https://www.mapir.camera/).

3.4 Tests on a wheat field

The sensors previously described above were used to perform different flight test for the spectral sensing of a wheat cultivated field.

Various configurations were therefore tested.

3.4.1 MAPIR Red+NIR cameras

The combination of the MAPIR cameras with respectively a red-wavelengths bandpass filter and a near infrared-wavelengths bandpass filter was the first approach tested for using low-cost multispectral cameras.

The first survey was conducted on a wheat cultivated field in spring 2016. The flight plan (whose strips are visible in Figure 3.10) was made in order to ensure an overlap of 80% longitudinally and 60% transversally. The flight altitude was

assumed as 40 meters, ensuring a centimetre-level ground sample distance. A total of about 190 images were captured with each camera.

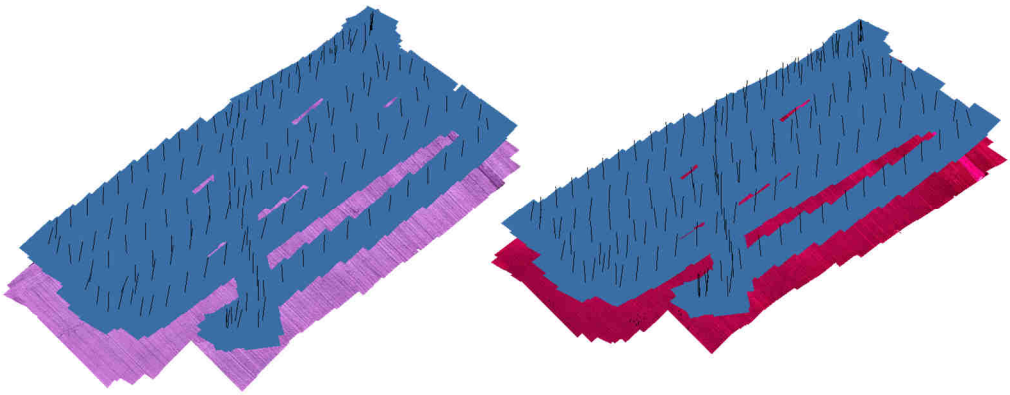

Figure 3.10 Geometry reconstruction with the near infrared (left) and red (right) cameras: the flight plan was the same since the images were captured simultaneously.

Two different approaches were adopted for processing the acquired images. Since the cameras were manually synchronized by activating both the trigger buttons at once and then exploiting the fixed time-lapse of 3 seconds, the first one was to register the red camera images to the corresponding near infrared camera ones. The resulting registered bands could be used to generate new images to be further aligned through the Structure from Motion process, in order to reconstruct the orthomosaic. However, the image registration result was affected by significative errors (an example is highlighted in showing the error on a target used as Ground Control Point) and sometimes the process was unable to register the images at all, thus this approach revealed to be weak instead of exploiting the Structure from Motion potential in performing an overall alignment.

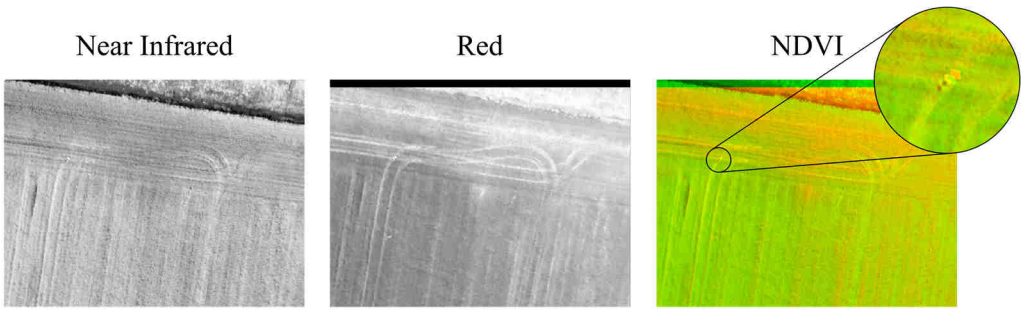

Figure 3.11 Image registration approach for MAPIR NIR and Red cameras. On the left: the near infrared and red bands extracted from each camera after the coregistration process. On the right: the same two bands combined in an image; the detail on a target used as ground control points shows a noticeable registration error.

The second approach was therefore to reconstruct an orthomosaic for each dataset of the two different cameras and then to combine the channels containing the red and near infrared data to calculate the NDVI. For both the orthomosaic, the channel to be considered for performing this computation it is the first one.

It is possible to follow this alternative workflow because each orthomosaic is georeferenced thanks to the use of the Ground Control Points. In this way, the images can be precisely aligned by estimating the camera estrinsics with a final bundle adjustment. In addition, the camera intrisics are also estimated and the lens distortion can be modelled, increasing the overall accuracy of the orthomosaic itself.

After the creation of both the near infrared and red orthomosaics, it is possible to calculate any index that uses those spectral bands. We focused our attention on one of the most used spectral indexes, the NDVI. Figure 3.12 shows the index values obtained by performing the computation using the raw digital numbers:

$$NDVI = \frac{DN_{\mathrm{NIR}} - DN_{\mathrm{red}}}{DN_{\mathrm{NIR}} + DN_{\mathrm{red}}} \qquad \text{(Eq 2.5)}$$

The result highlights values that are far from the truth. Negative values (shown in black) are present in bare soil areas and no vegetation reaches a value of 0.4 at least. Furthermore, differences in the health status are unrecognizable.

Using the quantum efficiency of the sensor, we tried a basic equalization process to make the near infrared and red values comparable each other. Due to the unavailability of the actual quantum efficiency of the MAPIR cameras' sensor, a generic CMOS sensor has been considered for this purpose, characterized as shown in Figure 3.5. In addition, the application of the bandpass filters has been taken into account. Since the central wavelengths are respectively $650\ \mathrm{nm}$ and $808\ \mathrm{nm}$ for the red and the near infrared, the quantum efficiency can be estimated as $QE_{\mathrm{red}} = 0.54$ and $QE_{\mathrm{NIR}} = 0.27$.

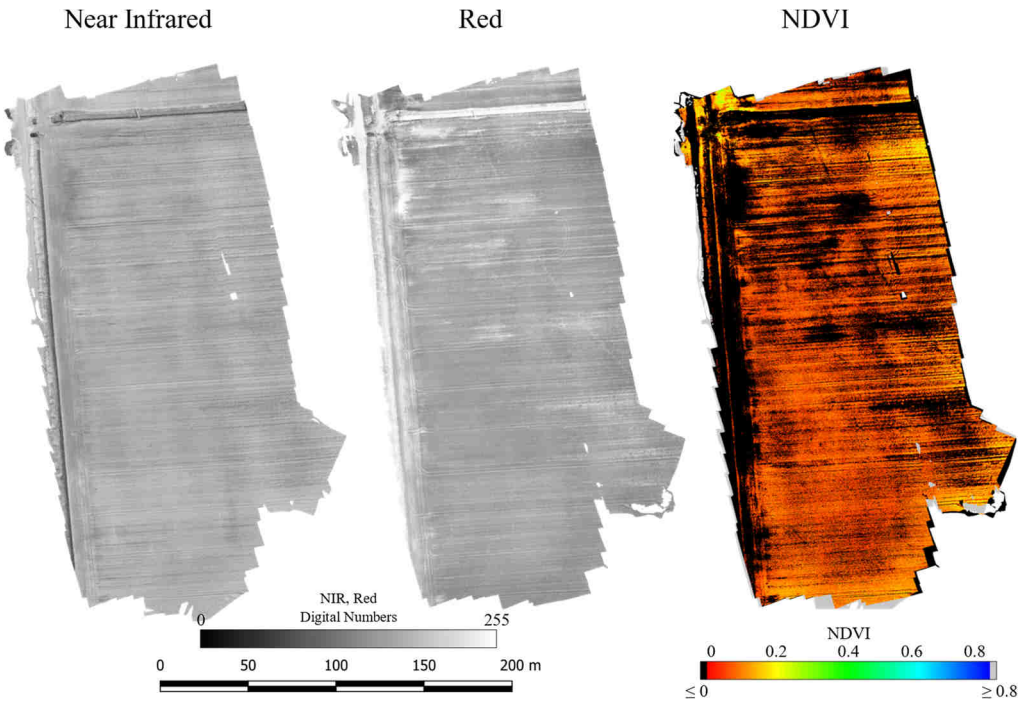

Figure 3.12 From the left to the right: near infrared orthomosaic, red orthomosaic, NDVI computation from raw digital numbers.

For an equal amount of incoming radiation at the camera's lens, the corresponding amount of radiation that is actually detected by the sensor in the different wavelengths results by computing the area under the curve that combines sensor's quantum efficiency and filter's transmittance. Considering that the area under the spectral transmittance of the red filter is approximately the double of the near infrared one and that the areas can be approximated by rectangles, due to the uncertainties in the assumptions made, these quantities are respectively:

- RED camera: $0.54 \cdot 0.925 \cdot 2 \approx 1$;
- NIR camera: $0.27 \cdot 0.84 \cdot 1 \approx 0.23$.

This computation shows that the raw digital numbers do not equally contribute in determining the final NDVI value. On the basis of the previous considerations, the following expression equalizes the raw digital numbers and provides the NDVI value:

$$NDVI = \frac{DN_{\mathrm{NIR}} - 0.23 \cdot DN_{\mathrm{red}}}{DN_{\mathrm{NIR}} + 0.23 \cdot DN_{\mathrm{red}}} \qquad \text{(Eq 2.6)}$$

Even though the index values appear to be more realistic for vegetation, the bare soil now exhibits a behaviour that is the opposite of the raw digital numbers

case: instead of be comprised in a range around $0.2 \div 0.3$, it is generally higher, with values from 0.4 up to $0.58 \div 0.60$.

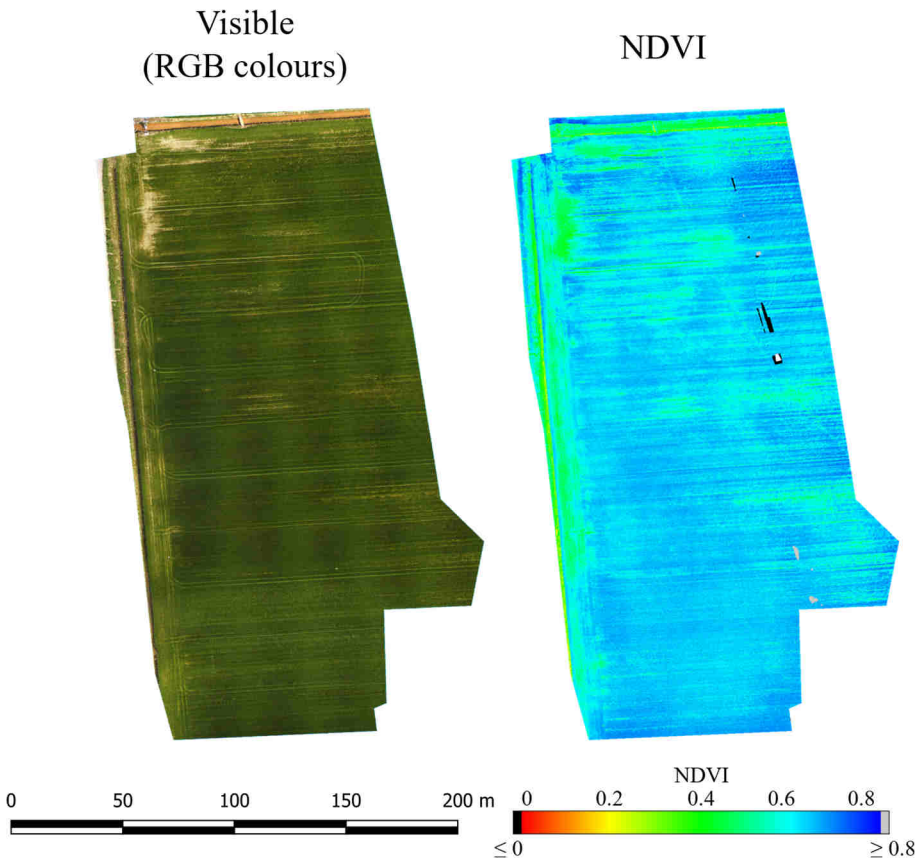

Figure 3.13 NDVI computation considering both the bandpass filters' properties and the quantum efficiency of the CMOS sensor in the red and near infrared wavelengths.

3.4.2 MAPIR NDVI (NIR+Blue) camera

The so-called MAPIR NDVI camera is equipped with a two-bandpass filter that enables both blue and near infrared wavelengths to reach the sensor array. Thanks to the possibility to install up to four different cameras on the 3DR Solo aircraft, this camera was set up whenever the MAPIR Red and MAPIR NIR cameras were used, in order to compare them.

Consequently, also the MAPIR NDVI camera was used for the first time on a wheat cultivated field in spring 2016. The main advantage of this camera is that the bands are already co-registered since they are channels of a same image. This fact enables both to compute an index based on blue and near infrared data on a single image or to build an orthomosaic that covers all the surveyed area. The

precise overlap is still guaranteed in the latter case, also in lack of ground control points. However, an accurate georeferencing is needed for monitoring over time.

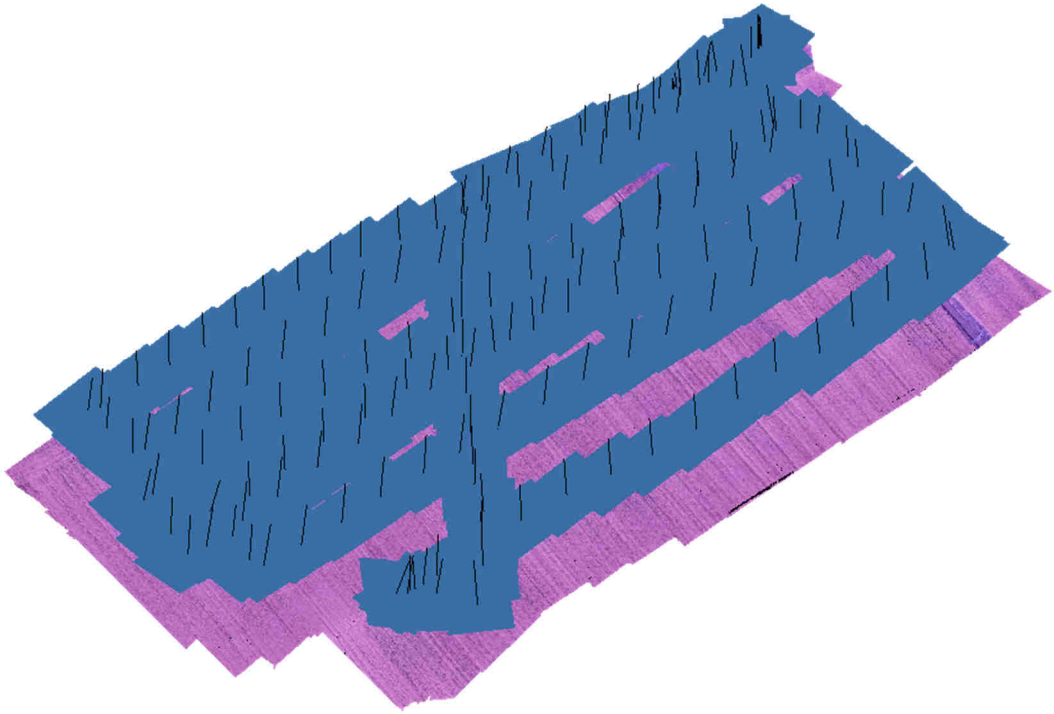

Figure 3.14 Flight plan for the MAPIR NDVI camera: since this camera was installed on the 3DR Solo aircraft together with the MAPIR NIR and Red camera, the same path was followed.

In spite of its name, the MAPIR NDVI camera does not actually allow to compute the NDVI index, since the red wavelengths are not detected. The alternative way for acquiring vegetation information that was proposed by the manufacturers of the MAPIR cameras is to calculate the simple ratio between near infrared and blue. Once again, the simplest approach is to use the raw digital numbers:

$$\frac{DN_{\mathrm{NIR}}}{DN_{\mathrm{blue}}} \qquad \text{(Eq 2.7)}$$

The resulting index values are shown in Figure 3.15. Since the quantum efficiency of the CMOS sensor and the transmittance of the filter in the blue and in the bear infrared wavelengths are different, an equalization approach similar to the one used for the MAPIR NIR and Red cameras was adopted. The same assumptions were made, thus the areas have been approximated by rectangles and the generic CMOS quantum efficiency in Figure 3.5 was used, as long as no specific sensor calibration was available. The resulting efficiencies for $450\ \mathrm{nm}$ and $800\ \mathrm{nm}$

wavelengths are respectively $QE_{\text{blue}} = 0.53$ and $QE_{\text{NIR}} = 0.25$. In addition, on the basis of Figure 3.2, the blue-wavelength area under the curve has been estimated as 0.8 times the near infrared-wavelength area. Finally, considering a 100% of incoming radiation that passes through the lens, the sensor detected fractions are:

- Blue band: $0.54 \cdot 0.91 \cdot 0.8 = 0.386 \approx 39\%$;
- NIR band: $0.25 \cdot 0.94 \cdot 1 = 0.235 \approx 24\%$.

Therefore, only the $\dfrac{0.235}{0.386} \approx 0.61$ of NIR is detected for a unitary blue amount of radiation. The ratio of the expression (Eq 2.7) can be adjusted for considering both quantum efficiency of the sensor and real transmittance of the filter by performing an equalization between blue and near infrared bands:

$$\frac{DN_{\text{NIR}}}{0.61 \cdot DN_{\text{blue}}} \qquad \text{(Eq 2.8)}$$

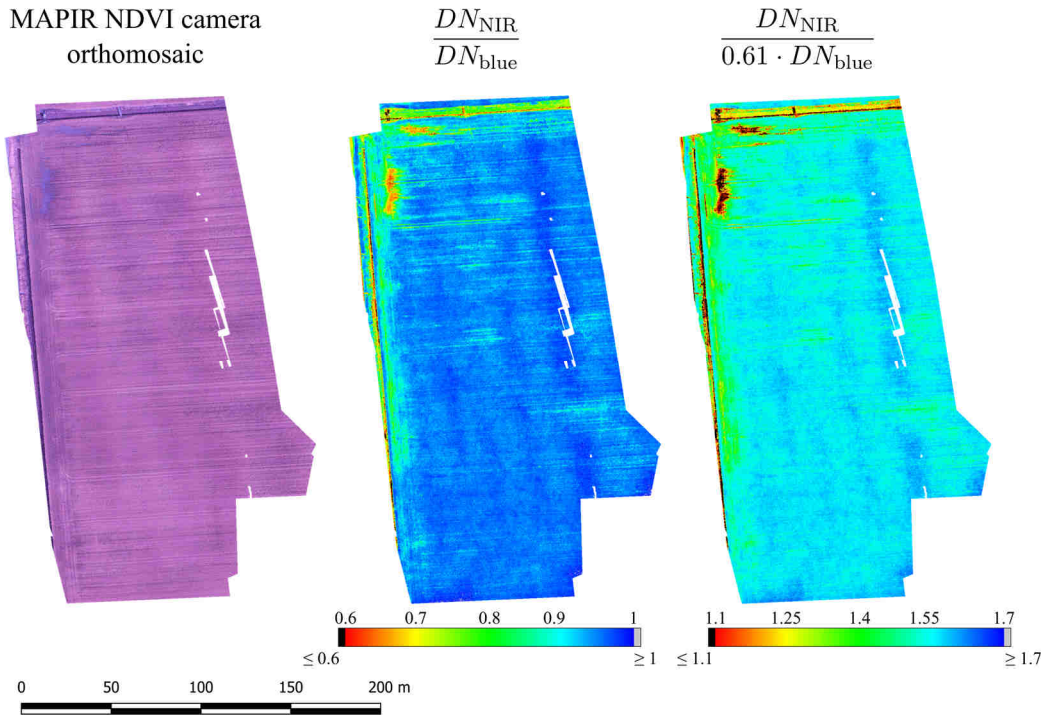

Figure 3.15 From the left to the right: the RGB visualization of the MAPIR NDVI camera orthomosaic (the colours are the result of having near infrared stored in red channel and green channel almost entirely black); the simple ratio between near infrared and blue digital numbers; the adjusted ratio that considers for both the quantum efficiency of the sensor and the filter's transmittance.

The resulting map with adjusted values is shown in Figure 3.15. The comparison between unadjusted and adjusted values shows that considering sensor's quantum efficiency and real filter transmittance the ratio increases for both bare soil and vegetation. However, in no case seams possible to accurately evaluate and assess the health status of the vegetation.

The MAPIR NDVI camera, able to detect blue and near infrared, can be certainly used for distinguish between vegetated and non-vegetated areas, but the evaluation and especially the monitoring over time of the status of a canopy appears to be unfeasible unless using methods to calibrate the reflectance, such as using calibrated reflectance panel to be photographed at the time of the flight. This implies to increase the cost of overall system.

3.4.3 Sentera Single

During the first test with the MAPIR cameras, the Sentera Single sensor was also used. Installed on a DJI Phantom 3 Professional aircraft, it is completely independent from the MAPIR cameras' system. This sensor is able to detect both the red and near infrared radiation, thus allowing to compute actual NDVI values. The main issue for accurately performing this computation, especially without using a calibrated panel, consists in transforming digital numbers into reflectances. In fact, the NDVI index requires the reflectance in red and near infrared as input and no information is available for performing the above task, with the only exception of considering the quantum efficiency of the Sentera single CMOS sensor. In this case, since there is a high-pass filter instead of a bandpass one, the red band is "contaminated" by near infrared. The process for modifying the expression (Eq 1.29) to calculate adjusted NDVI values has previously been explained in section 3.2.2.

Since every image contains green, red and near infrared data respectively in the green, red and blue channels, bands are already co-registered. However, the resolution of the Sentera Single is 1.2 megapixel that is much less than the 12 megapixel of the MAPIR cameras. This means that the ground sample distance, which is the pixel size on the ground, is much higher. In addition, the Bayer's filter is still present on the Sentera Single. Consequently, this resolution is not real, since

a photodiode is able to detect only those wavelengths that are transmitted by its overlying microfilter. The other components are computed by an interpolation.

A flight at a 40 m altitude was planned and performed, acquiring a total of 743 images. The longitudinal and transverse overlap were imposed respectively as 80% and 60%. The true colour (RGB) visualization of the Sentera Single sensor's images appears with a tinge of brown: this is because of the blue channel contains information about the near infrared radiation instead of the blue one. A false colour and equalized visualization, with RGB channels representing respectively the near infrared, red and green bands is more similar to the false colour satellite's images.

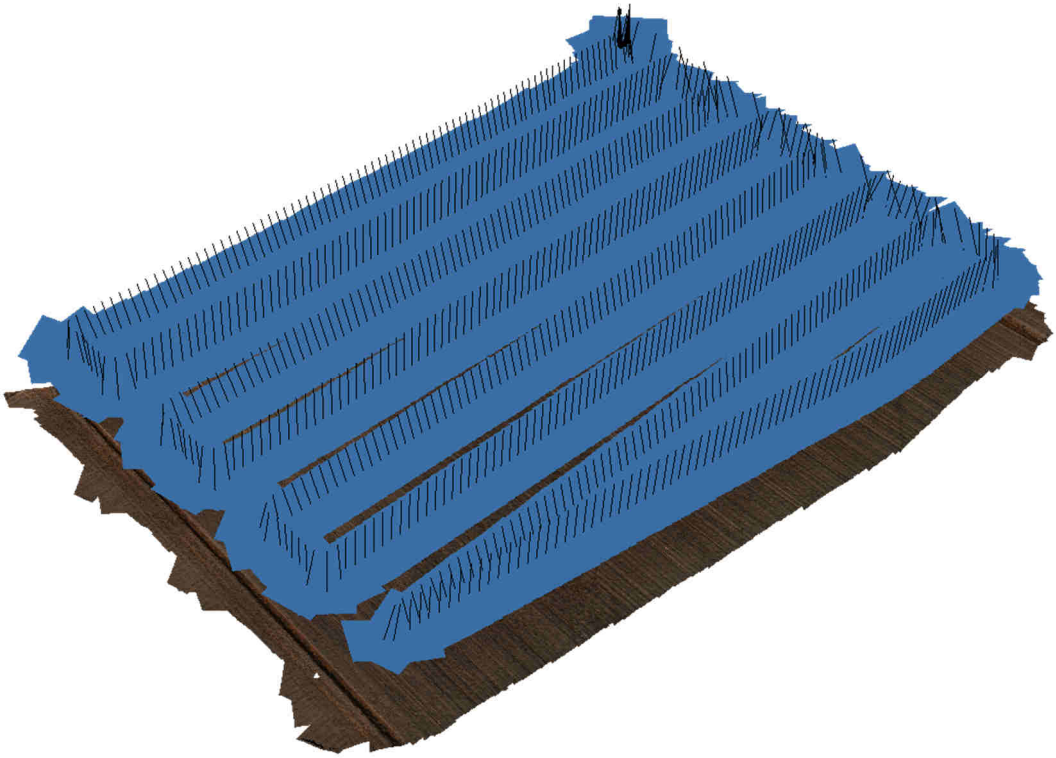

Figure 3.16 Flight plan of the survey performed with the Sentera Single on a wheat field in spring 2016. A total amount of 743 images were captured.

Once reconstructed the geometry, the orthomosaic of the whole surveyed area was thus generated and exported (Figure 3.18). Similarly, the RGB orthomosaic was generated with the DJI Phantom 3 Professional native camera's images for reference purpose in the visible region.

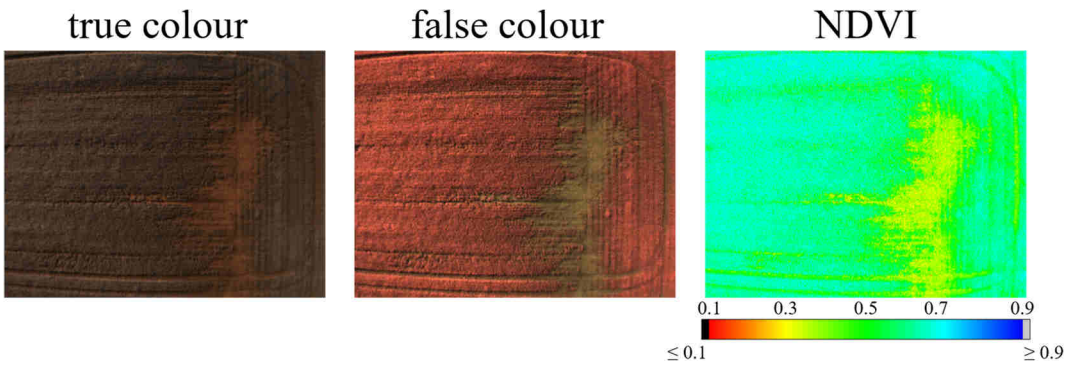

Figure 3.17 Sentera Single sensor's captured image. On the left: the true colour visualization, where the image appears with a tinge of brown due to the near infrared data stored in the blue channel. In the middle: the corresponding false colour visualization, in which near infrared has been magnified to equalize the actual quantum efficiency of the CMOS sensor. On the right: the NDVI computation on the single image.

It is worth noting that both the Sentera and the RGB orthomosaic are affected by strip effects. This phenomenon is due to a combination of the vignetting and the bidirectional reflectance of the canopy. By combining images that were acquired along strips during the flight, this implies that a difference in the digital numbers can be recognized. The centre of each strip appears darker, because in a nadiral captured image the centre of the image itself contains the soil shadow, while laterally this shadow is not present.

Actually, this effect was already recognizable with MAPIR cameras. For example, analysing the orthomosaic of the MAPIR NDVI camera in Figure 3.15, darker areas, coincident with centreline strips of the flight plan, can be detected. However, with the Sentera Single sensor it is possible to verify that this issue directly affects the NDVI computation. The analysis of the NDVI map in Figure 3.18 shows that most of the difference in the index values is related with this issue and not to the health status of the vegetation as it should be.

The use of the Sentera Single sensor enables the user to really collect spectral information in both the red and the near infrared wavelengths in order to compute the NDVI.

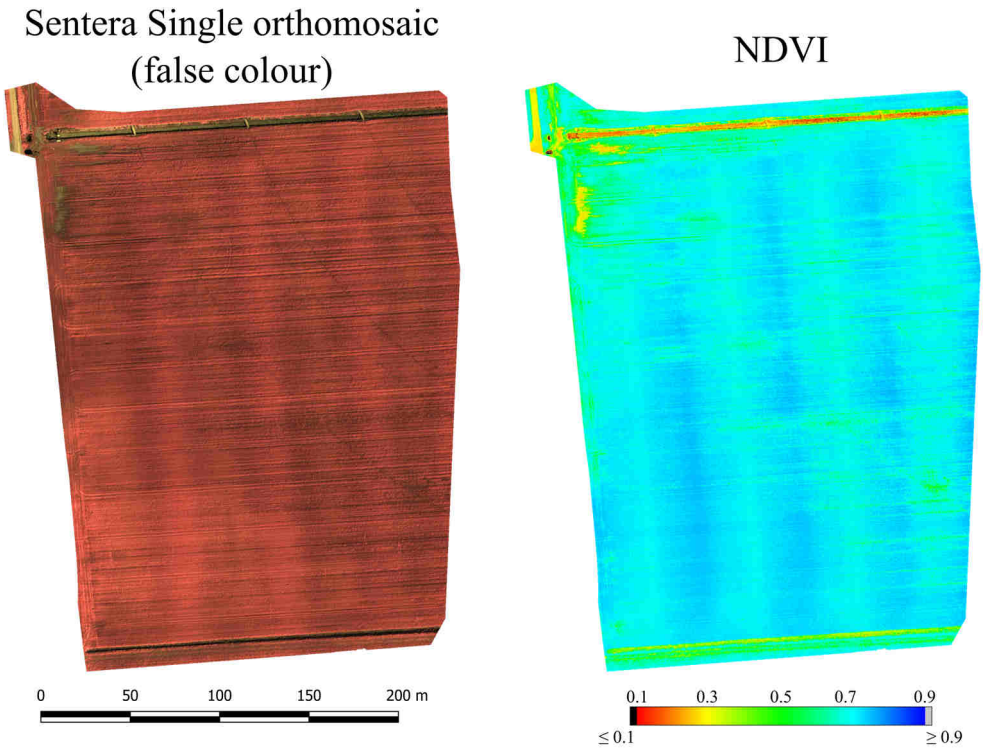

Figure 3.18 On the left: Sentera Single sensor's orthomosaic in false colour. On the right: NDVI computation.

3.4.4 A comparison between the MAPIR cameras and the Sentera Single sensor

Thanks to the availability of three indices computed with the low-cost MAPIR cameras and Sentera Single sensor, a wide overlapping area of the canopy has been defined to perform a simple correlation analysis between the information provided by the indices in relation to each other. Since the ground sample distance is not equal for all of the orthomosaic previously generated by the structure from motion processing, a resampling with the nearest neighbour technique was applied. This resampling approach preserves the raw data because no interpolation is performed. Each orthomosaic was therefore resampled at a 5 centimetres GSD ensuring the perfect overlap between pixels of the different orthomosaics in QGis software. The resulting images were merged into a single three-band image to further import and analyse them with MATLAB.

In particular, the analysis was focused on the correlation between the indices. Since the NDVI computed from the Sentera Single's data showed to be the most

reliable NDVI value among the computed indices, a linear regression between this latter index and the MAPIR cameras' indices was made.

For each pixel, three values are available, those representing the indices. The analysis considered respectively the following couples:

$$(NDVI_{\text{Sentera}},\ \frac{DN_{\text{NIR}}^{\text{MAPIR}} - 0.23 \cdot DN_{\text{red}}^{\text{MAPIR}}}{DN_{\text{NIR}}^{\text{MAPIR}} + 0.23 \cdot DN_{\text{red}}^{\text{MAPIR}}}) \qquad \text{(Eq 2.9)}$$

$$(NDVI_{\text{Sentera}},\ \frac{DN_{\text{NIR}}}{0.61 \cdot DN_{\text{blue}}}) \qquad \text{(Eq 2.10)}$$

As a remark, in the expression (Eq 2.9) the MAPIR NIR and red cameras were used, while in the expression (Eq 2.10) both the NIR and blue values are those detected by the MAPIR NDVI camera.

The linear regression, in the form of $y = a_0 + a_1 \cdot x$, was thus performed by estimating the coefficients $\widehat{a_0}$ and $\widehat{a_1}$ with a least squares method in MATLAB, that leads to the final relationship $y_{fit} = \widehat{a_0} + \widehat{a_1} \cdot x$. The correlation assessment can be done by computing the residuals $v = y - y_{fit}$ and then calculating the coefficient of determination $R^2 = 1 - \frac{\sum v^2}{(n-1) \cdot \sigma_y^2}$.

The results show that a linear correlation exists for both the MAPIR systems. However, the correlation is slightly stronger for the MAPIR NDVI camera: even though the computed index in this case is not a NDVI value, the ratio between the near infrared and the blue seems to be better correlated to the NDVI value obtained by the Sentera Single's data. The reason that could justify this behaviour, since no calibration were performed, is the perfect co-registration of the near infrared and blue images acquired by the MAPIR NDVI camera, because these bands are channels of the same captured image, thus a priori co-registered. In addition, this implies also that the ISO sensitivity and the exposure time are the same for the bands of a same image, even if they may vary during the flight.

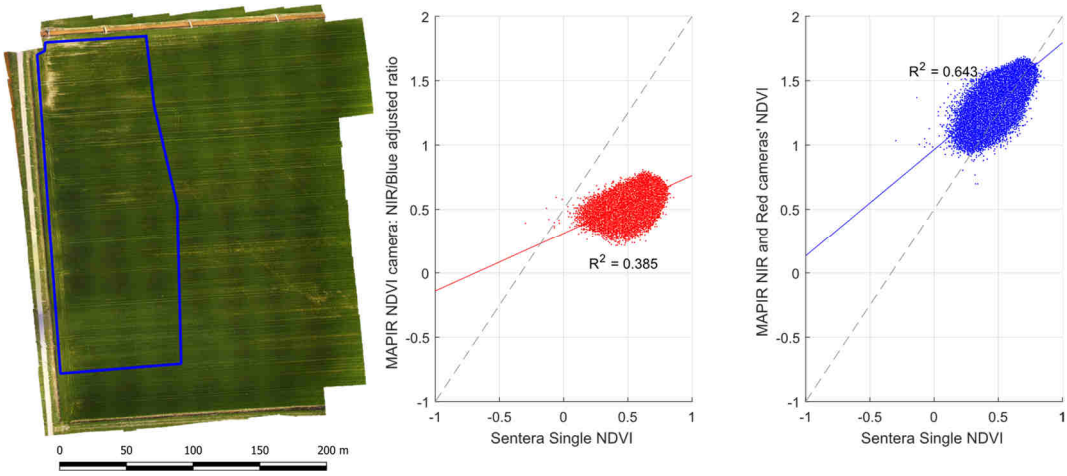

Figure 3.19 From the left to the right: area where the indices values obtained by the different sensors have been compared; scatterplot of the NDVI values obtained by the combination of MAPIR NIR and Red cameras (adjusted according to Eq.(Eq 2.6)) and the Sentera Single sensor; scatterplot of the NIR/Blue ratio (adjusted according to Eq.(Eq 2.8)) computed through the MAPIR NDVI camera data and the NDVI from the Sentera Single.

On the basis of the results obtained with the first test on a wheat field, further data acquisitions were performed with both the MAPIR cameras and the Sentera Single.

The repetition on the same field was executed two weeks after the first test, following a similar methodology. The flight was performed at a flying altitude of 100 meters, in order to attempt to minimize the previous detected effects. Both the MAPIR cameras and the Sentera Single sensor were used. The flight plans are shown in Figure 3.20. In addition, during the orthomosaic creation in Agisoft Photoscan Professional, the "enable colour correction" option was used to exploit the longitudinal and side overlaps in equalizing the different recorded digital numbers, thus the detected reflectance. This process, even though not rigorous, seems to be the most suitable for a low-cost system, since it is both simple to apply and does not imply additional costs.

The false colour orthomosaic of the Sentera Single appears now slightly less affected by the previous "strip effect". However, it is still present and still affects the NDVI, even if an improvement can be recognized. The complete elimination of this phenomenon is not possible using the low-cost sensor without performing any ground reflectance measurement for calibration and without having any information about the bidirectional reflectance distribution function of the canopy.

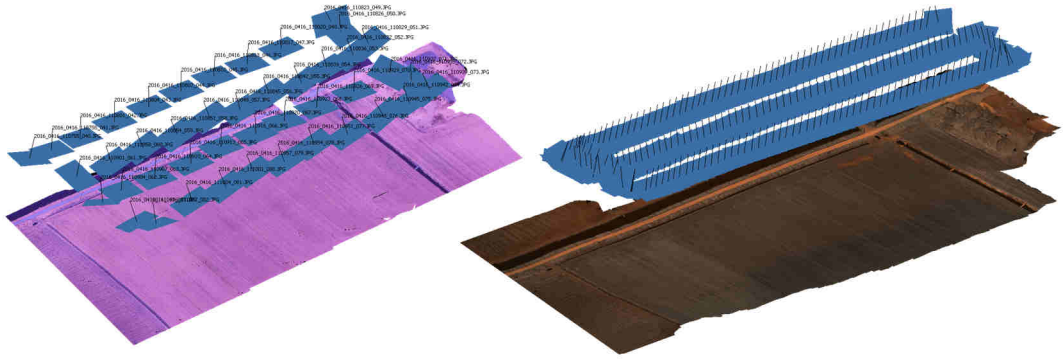

Figure 3.20 Flight plans at 100 meters altitude for the second survey on a wheat field with MAPIR cameras (left) and Sentera Single sensor (right).

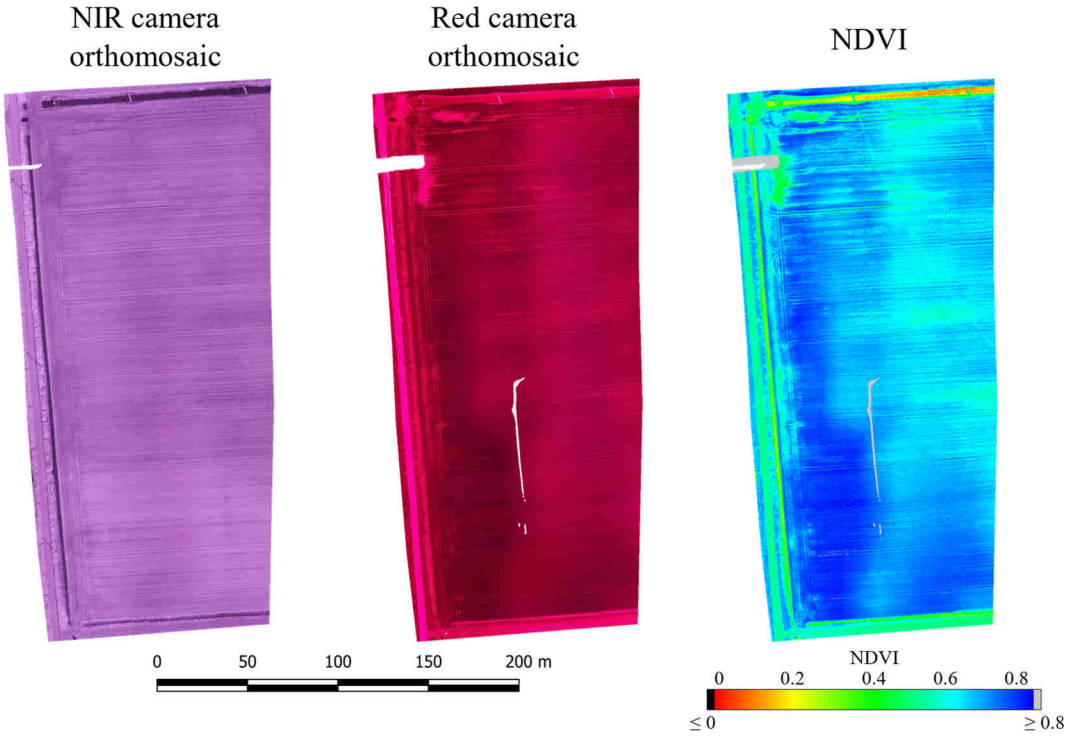

Figure 3.21 From the left to the right: orthomosaic generated through the MAPIR NIR camera image processing; orthomosaic generated through the MAPIR Red camera images; NDVI computed by the expression (Eq 2.6).

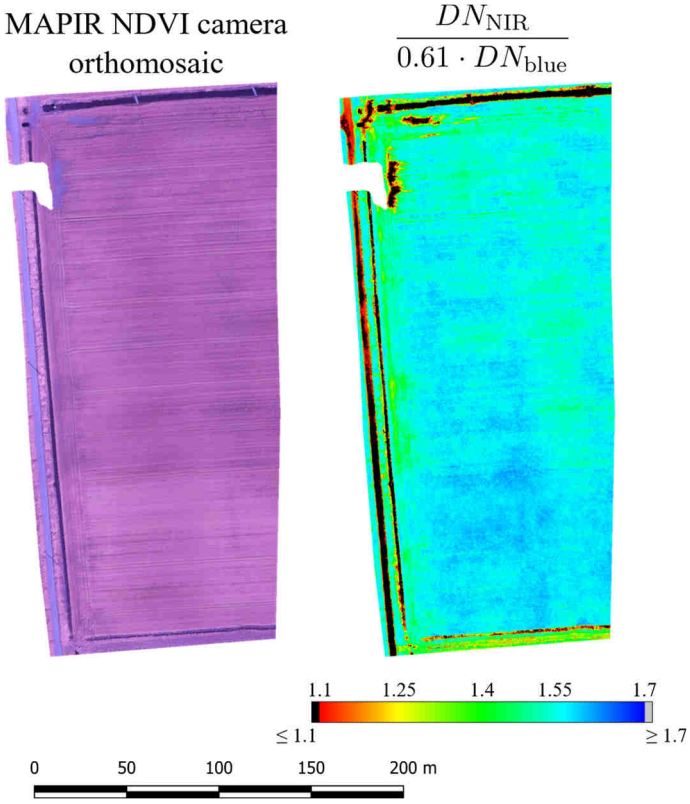

Figure 3.22 On the left: orthomosaic generated through the MAPIR NDVI (NIR+Blue) camera. On the right: the adjusted ratio of near infrared digital numbers over the corresponding blue ones, computed by the expression (Eq 2.8).

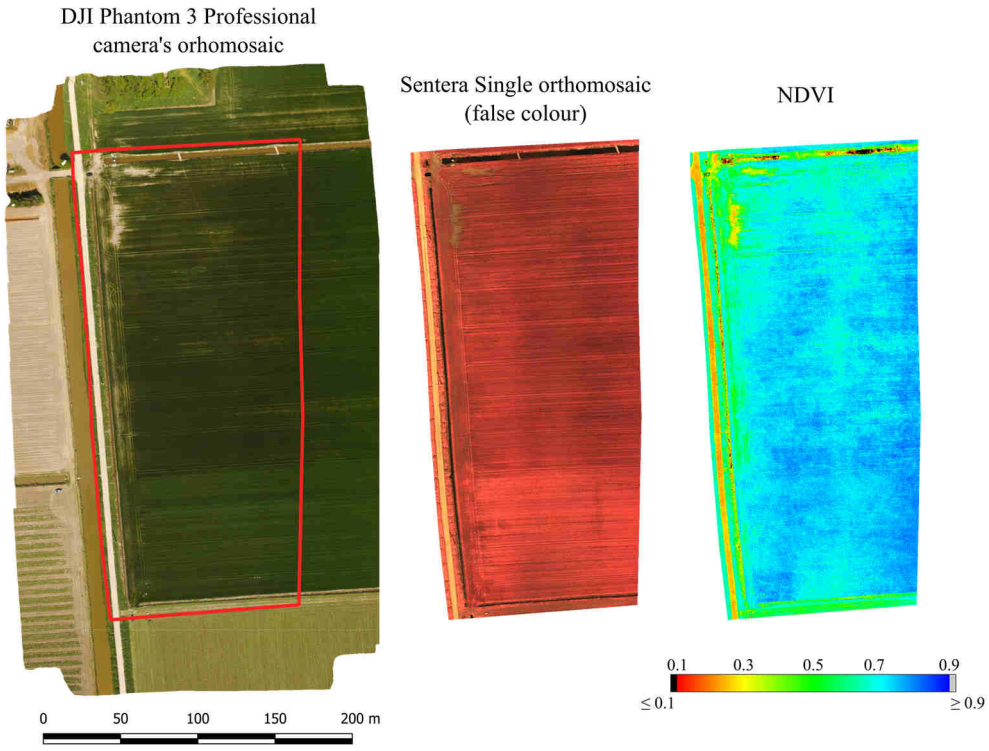

Figure 3.23 From the left to the right: RGB framework of the wheat field, where the multispectral surveyed area is highlighted with a red line; false colour visualization of the Sentera Single orthomosaic; NDVI computation from the Sentera Single sensor's data.

3.5 Viticulture: a further case study

The second experimentation for testing the potential in using low-cost sensors in the multispectral characterization of the canopy in a precision viticulture context involved the survey of a vineyard in the province of Piacenza.

Vineyards represent a crucial and strategic sector for the agriculture. The use of Unmanned Aerial Vehicles (UAVs) in this context has attracted increasing attention during the last years. In this further campaign, the attention was focussed on the use of the Sentera Single sensor. On the basis of the previous tests on a wheat field, this sensor proved to be the most suitable for conducting this further experimentation: the camera is very light-weight and is able to detect both near infrared and red spectral information. Furthermore, the bands are already co-registered since they are channels of a same image. These advantages lead to finally choose the Sentera Single as the sensor to be used for the proximal multispectral detection by UAV.

Since the landscape was characterized by the hills, the morphology of the vineyard was strongly three-dimensional. In such a context, the use of the Structure from Motion approach for the reconstruction of the actual geometry by detecting features on the images, matching them each other, computing a digital elevation model and finally building the final orthomosaic represents a real strength.

In this campaign, the main goal consisted in characterizing as well as possible the status of the vineyard in a specific epoch and thus no monitoring over time was considered in this case.

The survey was performed on July 26th, 2016 by using the DJI Phantom 3 Professional aircraft equipped with both its native RGB camera and the Sentera Single sensor mounted in a fixed nadiral arrangement. The vineyard extent was slightly more than one hectare.

The data acquisition consisted in planning a single flight at a 40 metres altitude in order to ensure a GSD of about 3 centimetres. Since the flight plan did not follow the changes in the ground elevation, the altitude previously mentioned above was actually set for the take-off point, that was established in the upper part of the vineyard. Consequently, in the lower part of it, the real altitude of the aircraft turned out to be up to 60 metres, with a GSD of about 3.5 centimetres. Therefore,

this latter value was assumed as the pixel size for generating the multispectral orthomosaic.

In order to georeference the survey and assessing the accuracy in the three-dimensional reconstruction of the geometry, twelve targets were deployed around the vineyard. Seven of them were used as ground control points, to frame the orthomosaics in the European Reference System ETRS9. Their coordinates were thus collected by a GNSS geodetic receiver in Network Real Time Kinematic (NRTK) mode. The datum, imposed from the network of permanent stations, was the ETRF2000(2008.0) that corresponds to the more recent realization of the ETRS89 in Italy at the time of the survey. Orthometric elevations were computed by applying the ITALGEO 2005 geoid model to the measured ellipsoidal heights. The remaining five targets were used as control points (also called check points) to evaluate the accuracy of the alignment.

A total of 224 multispectral images were collected through the Sentera Single camera during the flight. The overlap specified for the flight plan, that actually refers to the overlap in using the RGB native camera of the aircraft, was computed in order to ensure a longitudinal overlap of 80% and a side overlap of 60%. All of the acquired images succeeded in their alignment.

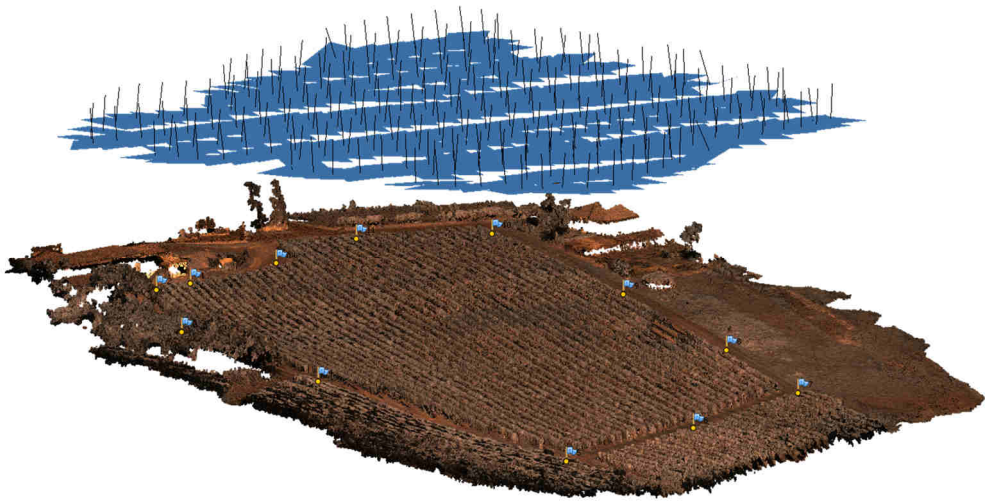

Figure 3.24 Position of the image captures, showing the flight plan. Due to the terrain slope, the real altitude above the ground was variable during the flight, from the planned 40 metres up to a maximum of 60 metres. The flags on the dense cloud represents both the Ground Control Points and the Control Points.

The root mean square error (RMSE) of the residuals computed for the control points as

$$\mathrm{RMSE} = \sqrt{\frac{\sum_{i}^{N} v_i^2}{N}} \qquad \text{(Eq 2.11)}$$

shows that the final accuracy (2 centimetres) is comparable with the Structure from Motion approach as well as with the NRTK technique. Table 3.5 provides a detailed report of the residuals for both the Ground Control Points and the Control Points used for the accuracy assessment.

Once that all the images were aligned, the dense cloud was then generated in Agisoft Photoscan Professional and is shown in Figure 3.24, where the brown shade is due to the replacement of the blue with the near infrared in the third channel of the images. This step allowed the creation of a further mesh representing a model of the surface on which it is possible to apply a texture and finally to reconstruct a multispectral orthomosaic of the vineyard. A false colour visualization (NIR-R-G) of it is presented in Figure 3.25.

Table 3.5 Residuals for both the Ground Control Points and the Control Points. The root mean square errors show that the accuracy of the survey was approximately 2 centimetres.

ID	Type	East [m]	North [m]	Elevation [m]	Residuals [m]			
					X	Y	Z	3D
0	GCP	528900.713	4981832.453	279.996	0.002	0.016	-0.004	0.017
2	GCP	528910.118	4981796.025	281.617	0	-0.005	-0.005	0.007
3	GCP	528930.252	4981788.185	276.922	-0.005	-0.006	0.008	0.011
5	GCP	529025.949	4981817.311	259.148	-0.001	-0.011	-0.002	0.011
7	GCP	529011.585	4981885.398	260.449	-0.002	0.01	0.018	0.021
8	GCP	528984.593	4981886.439	265.384	-0.002	-0.001	-0.023	0.023
10	GCP	528899.624	4981887.182	277.585	0	0.003	0.009	0.009
1	*CP*	*528908.096*	*4981805.893*	*281.041*	*0.014*	*-0.01*	*0.003*	*0.017*
4	*CP*	*528964.317*	*4981798.319*	*269.959*	*-0.011*	*-0.001*	*-0.019*	*0.021*
6	*CP*	*529018.72*	*4981854.127*	*259.18*	*-0.012*	*0.008*	*-0.009*	*0.018*
9	*CP*	*528948.23*	*4981886.173*	*271.881*	*-0.003*	*0.003*	*-0.025*	*0.026*
11	*CP*	*528890.891*	*4981859.295*	*279.722*	*0.007*	*-0.006*	*-0.012*	*0.015*
Ground Control Points RMSE [m]					0.002	0.009	0.012	0.015
Control Points RMSE [m]					*0.010*	*0.006*	*0.016*	*0.020*

On the basis of the multispectral orthomosaic channels, that represent the digital numbers in the red, green and near infrared wavelengths respectively, it was possible to compute the NDVI index.

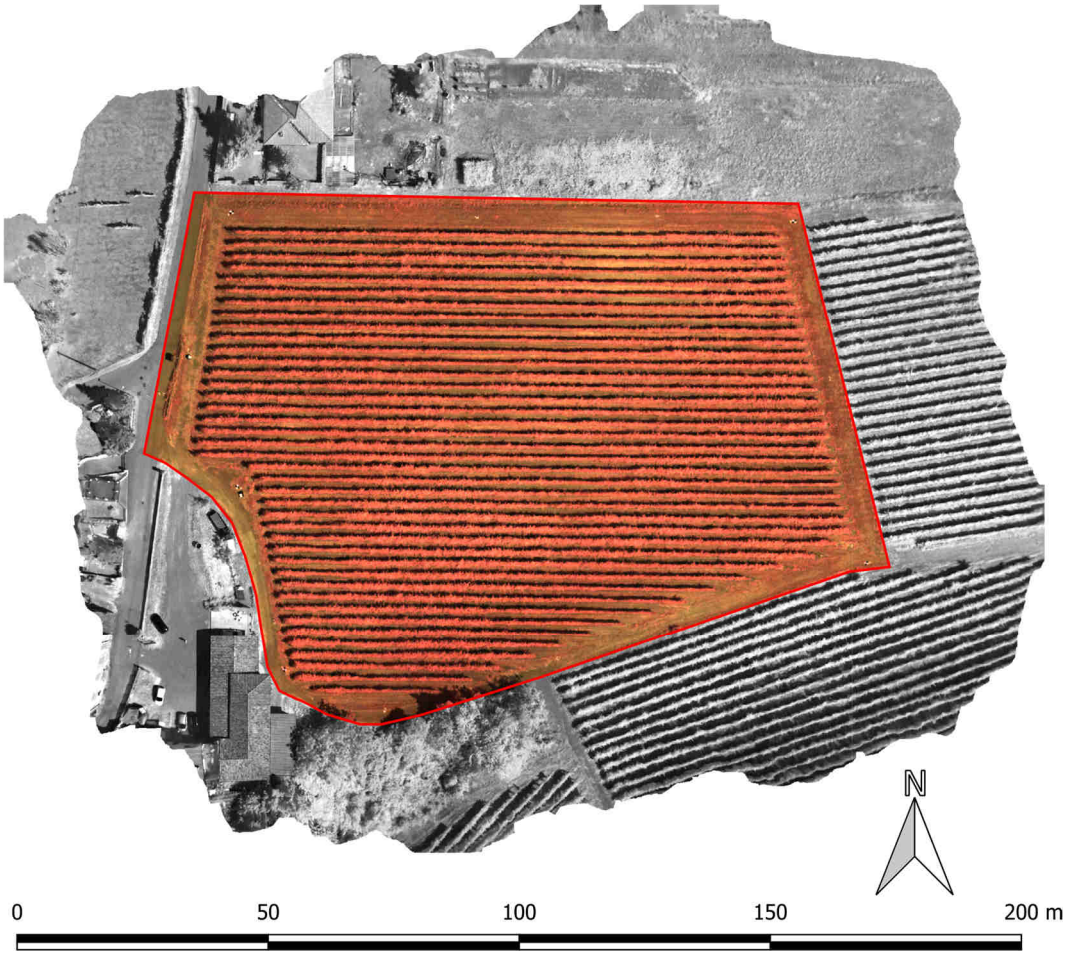

Figure 3.25 The multispectral orthomosaic of the vineyard generated through Agisoft Photoscan Professional. The visualization is in false colour, thus NIR-R-G.

The expression that was applied considers for the real quantum efficiency of the CMOS sensor. The overall analysis on the NDVI map revealed that only the values above 0.5 were significant for the characterization of the vineyard. Consequently, only these range of values were further considered in the subsequent analysis. However, the resulting map proved to be affected by an anomalous behaviour of the planting rows' shadows. In these regions, in fact, the NDVI value was abnormally high and thus definitely irrelevant for the assessment of the vineyard's health status. In order to solve this issue, the NDVI map was processed through a specially developed Matlab script. Essentially, it filtered out the shadow pixels by detecting them by a specified dark-value threshold for all of the orthomosaic's channels. The NDVI was thus computed only for the remaining

pixels. Figure 3.26 shows the issue represented by the shadows: the highlighted area, that has been also identified on the true colour orthomosaic obtained by processing the images capture through the native camera of DJI Phantom 3 Professional (on the left) for reference, contains abnormally high values mapped in grey on the raw NDVI (in the middle) that were finally filtered out using the threshold-based script (on the right).

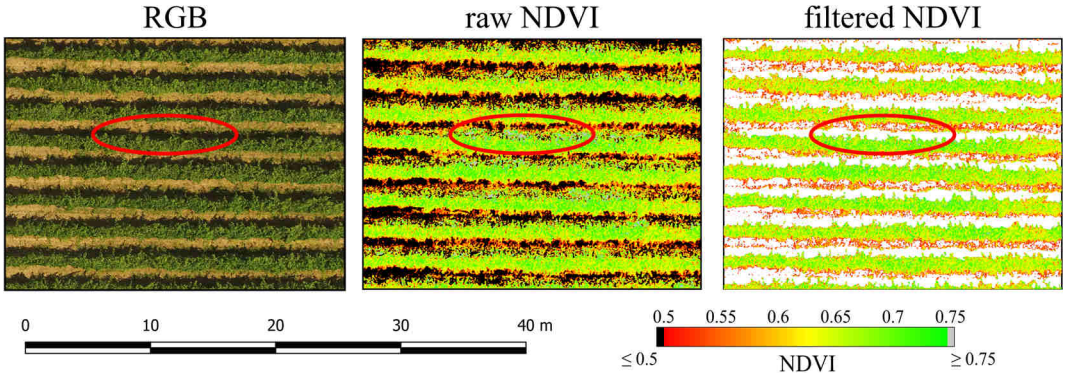

Figure 3.26 Abnormal high NDVI values in shadowed areas. The application of a filter solved this issue.

Once that the NDVI was filtered from both the bare soil, the grass (characterized by NDVI values less than 0.5) and the shadows, only the vineyard rows remained. The resulting NDVI map is shown in Figure 3.27. The analysis conducted on this map revealed that:

- high values can be generally detected in the regions where the rows are larger and a lush vegetation is present. However, sometimes the NDVI values were found to be lower: since no sensor related issue affected the survey, this might mean that in the area the health status of the vineyard could have been compromised, such as
- in the regions where the rows were narrower, the NDVI did not necessarily assume low values. If this happened, it was likely that the vineyard was found to be in a suffering status. If the index value was high, instead, probably the vineyard could be in a different phase of the growth. In both cases, the prompt intervention of an agronomist in the field is needed to better identify the reasons.

Two areas with an equal surface have been identified on the map, respectively rounded with a red polygon and a blue one. The first represents a region where the plants were founded to be lush and wider. The second one represents a region where

the rows were significantly narrower. The detail of the NDVI index within these regions is shown in Figure 3.28. The analysis conducted on these areas revealed that in very few pixels the NDVI exceeded the value of 0.8. However, this threshold was exceeded more times in the region with wider rows. Also, the estimated mean value was slightly higher, about 0.7, while in the region with narrower rows the mean value was around 0.65. Of course, this difference is affected by the presence of less pixels with higher NDVI values for the rows that have a narrower width. On the contrary, the edge between the grapevine and the soil is quite constant in its extent even for rows with different widths.

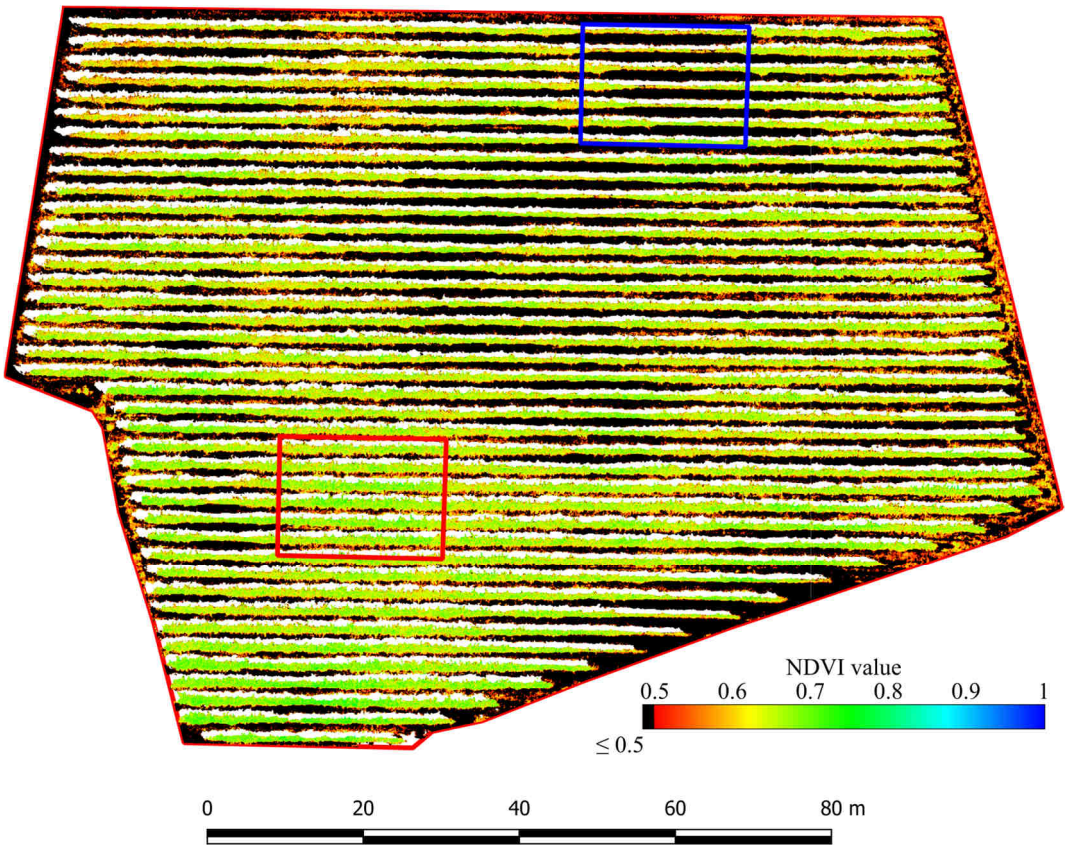

Figure 3.27 NDVI computation from the multispectral orthomosaic by considering the real quantum efficiency of the sensor and filtering the bare soil and the shadows.

Furthermore, the distribution of the NDVI index values was generally quite noisy. Adjacent pixels showed a variation between 0.05 and 0.1 in term of NDVI. However, the overall analysis of the index values in a full-width region along the row direction allowed to determine a reliable mean value. Therefore, the NDVI enables, in such a context, to assess the health status of the vineyard along the rows, even if the information at a single pixel level was not extremely accurate. This fact can be due to multiple factors:

- the spectral data acquired by the Sentera Single sensor is affected by the presence of the microfilters. This means that the data is not actually acquired for all of the bands in each pixel. On the contrary, the data is acquired according to the Bayer's filter scheme, thus an interpolation is performed to reconstruct the missing data. This can cause the NDVI to be spatially noisier.
- The actual orientation of the leaves constituting the canopy as well as the presence of grapes, affects the global spectral response for each pixel.

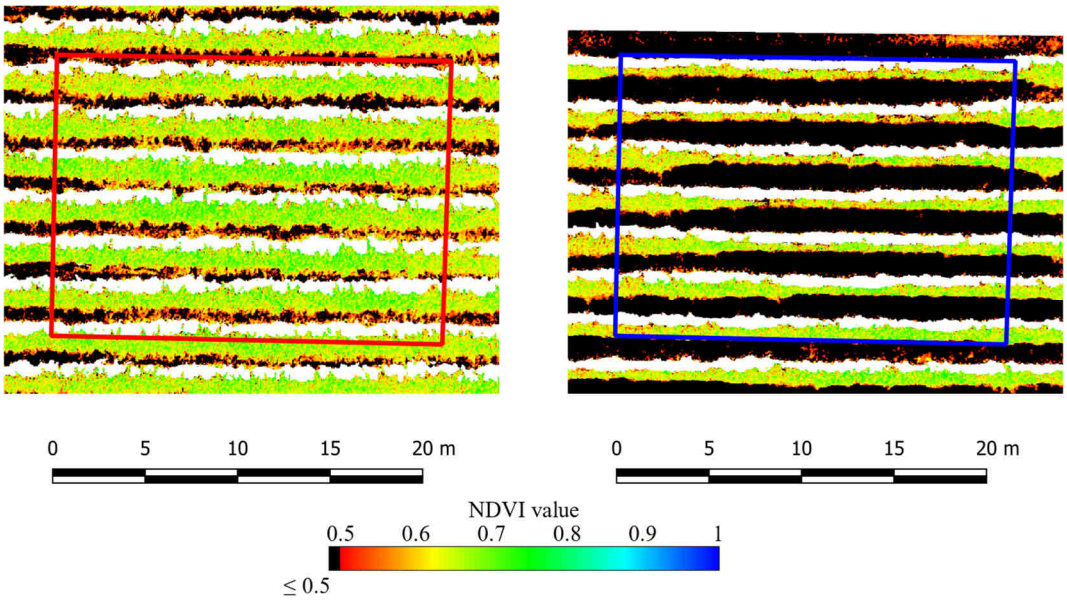

Figure 3.28 Detail of the NDVI on two regions characterized by different rows' width.

In any case, the considerations made above are very strongly related to the conditions at the time of the survey. Mean values that have been estimated are valid only within this survey. A comparison between regions that were surveyed during this flight is acceptable unless remarkable changes in light conditions happened. No further comparison is reliable for potential survey repetitions, since no reflectance values were ever computed.

In addition to the NDVI, other indices were also computed. The *ratio vegetation index* represents a basilar and very simple approach. Its expression, given in (Eq 1.28), actually requires reflectance values. Since no reflectance was computed from the data detected through the Sentera Single sensor because of the lack of a downwelling light sensor or a calibrated reflectance panel, the digital

numbers were used as input. Moreover, due to the spectral sensitivity of the sensor in its three channels, the red data is both contaminated by a small, but significant, response in the near infrared and the near infrared channel is much less efficient in converting NIR radiance to digital numbers. Therefore, the ratio vegetation index expression was modified as

$$RVI = \frac{\alpha \cdot \mathrm{B}_3}{\mathrm{B}_1 - \mathrm{B}_3} \qquad \text{(Eq 2.12)}$$

where the actual red is computed by subtracting the NIR stored in the third band from the recorded red in the first band. In addition, a coefficient is used to magnify the near infrared, according to real quantum efficiency of the sensor. The value of this parameter is derived from the proprietary information of Sentera.

The map of the RVI index computed through the modified expression in (Eq 2.12) is shown in Figure 3.29 and a detail on the same two regions previously shown is provided in Figure 3.30. Due to the fact that this index represents a ratio, a constant offset between the digital numbers in the red and near infrared translates differently on the basis on the near infrared response. In other words, this index is not normalized. Even if some outliers were present in both regions, the analysis of them highlighted that the RVI was generally slightly higher where the rows where wider.

As a remark, the spatial variation of the RVI index was still significant in this case. This implies that the signal-to-noise ratio was not extremely high. At a pixel level the information proved to be not very reliable. However, a mean value is already significant for a small group of pixels as it was for the NDVI.

A further index that was considered is the *soil adjusted vegetation index*. It is adjusted for considering the presence of the bare soil. Essentially, its expression is very similar to the NDVI and a parameter L ranging from 0 to 1 is introduced. Again, the expression given in (Eq 1.32) cannot be directly used in combination with the data from the Sentera Single sensor. First of all, digital numbers are available instead of the reflectances. In addition, the real quantum efficiency of the sensor has to be adequately considered. This leads to the following expression, where a coefficient is introduced for considering the real quantum efficiency on the basis of the spectral specifications provided by the manufacturer of the sensor:

$$SAVI = \frac{\left(1+\alpha\right)\cdot \mathrm{B}_3 - \alpha \cdot B_1}{\left(1-\alpha\right)\cdot \mathrm{B}_3 + \alpha \cdot B_1 + L} \cdot (1-L), \qquad L = 0.5 \qquad \text{(Eq 2.13)}$$

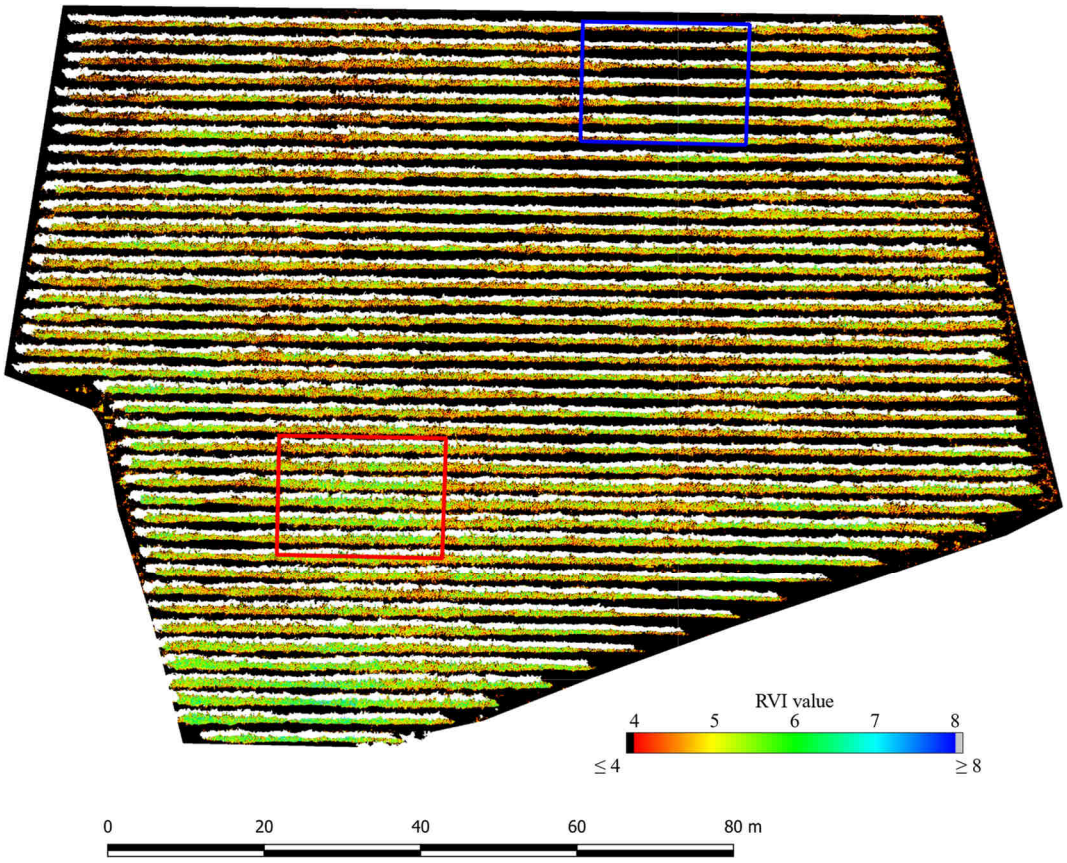

Figure 3.29 Ratio vegetation index (RVI) map of the vineyard.

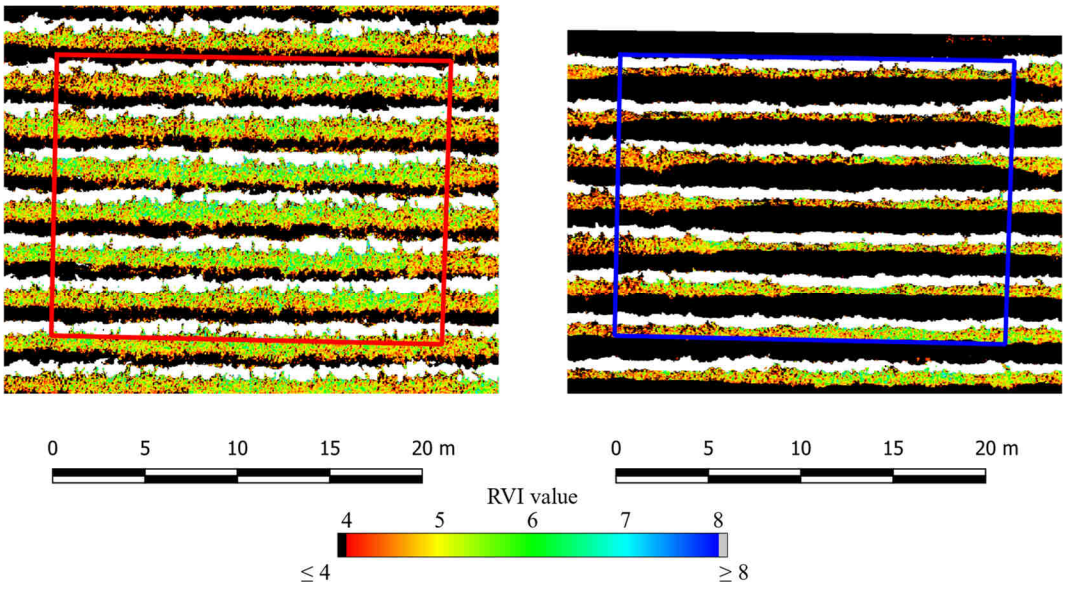

Figure 3.30 Detail of the RVI on two regions characterized by different rows' width.

The parameter *L* was assumed equal to 0.5, that represents the most used value in literature. In fact, the aim of this computation was to investigate the quality of

the index retrievable by the data sensed through a low-cost multispectral sensor and not to analyse the effect of varying the parameter.

The map of the SAVI index computed through the expression in (Eq 2.13) is shown in Figure 3.31 and a detail on two regions with a different width of the row in shown in Figure 3.32. Similarly to what was observed for the previous indices, the SAVI was found to be slightly higher in the region of the vineyard with wider rows. Furthermore, the spatial variation of the SAVI within the two regions was more similar to the NDVI one. The analysis of Figure 3.32 shows that the variation within the grapevine rows is more limited if compared to the variation of the RVI index.

Finally, since during the flight the vineyard was also surveyed by capturing images through the DJI Phantom 3 Professional native camera, able to acquire the red, green, and blue wavelength, this latter data was used to generate a further orthomosaic. To exploit this additional information a basic index was computed. The *Green Chromatic Coordinate* simply considers the fraction of green that contributes to the sum of all of the three RGB components. Digital numbers were the solely data available from the orthomosaic and no actual quantum efficiency of the RGB CMOS sensor was provided. Therefore, the expression for the *GCC* index was assumed as:

$$GCC = \frac{DN_{\text{green}}}{DN_{\text{red}} + DN_{\text{green}} + DN_{\text{blue}}} \qquad \text{(Eq 2.14)}$$

This index represents one of the simplest information that could be retrieved by a non-multispectral camera. The relationship between this greenness level estimation and the multispectral NIR-derived indices was further investigated.

The map of the *GCC* index is shown in Figure 3.33. Only the values within the range from 0.4 to 0.65 are displayed in colour. It is worth noting how this index allows to detect the rows as well as their width. In Figure 3.34 these two areas are shown with higher detail. With the only exception of the border between the edge of each row where a transition from the grapevine to the bare soil or the grass takes place, the GCC value does not differ in a significant way within the regions. No clear relationship between the response in the green wavelength, thus the GCC, the width of the rows and the health of the vineyard seemed to exist at the time of the

survey. The GCC information, however, could be helpful to estimate the width of the rows.

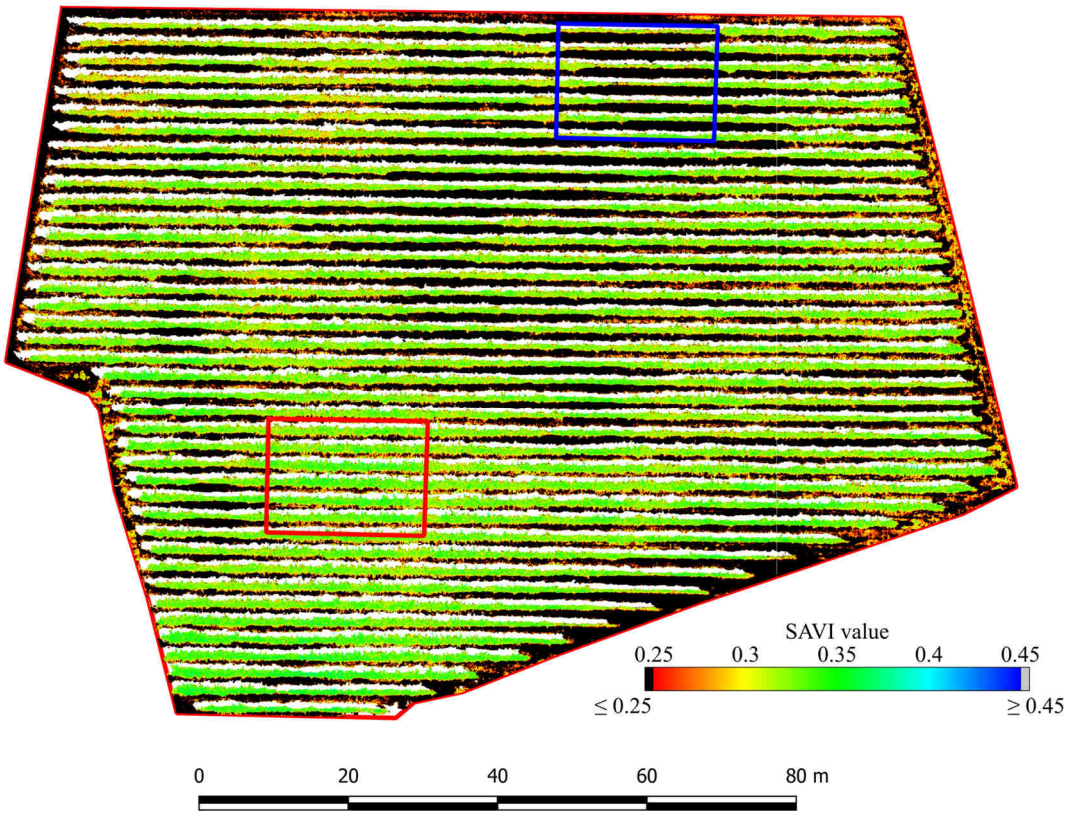

Figure 3.31 Soil adjusted vegetation index (SAVI) map of the vineyard.

In order to compare the data retrievable by the GCC, RVI, NDVI and SAVI indices, all the maps were resampled to the same pixel size. A MATLAB script was thus written for uploading all of the indices values. In particular, each pixel was characterized by a vector whose elements were the indices:

$$v = \left[GCC, RVI, NDVI, SAVI \right] \qquad \text{(Eq 2.15)}$$

The analysis was focused only on the pixels whose NDVI value was found to be within the range from 0.5 to 1, in order to consider only the grapevine pixels of the vineyard.

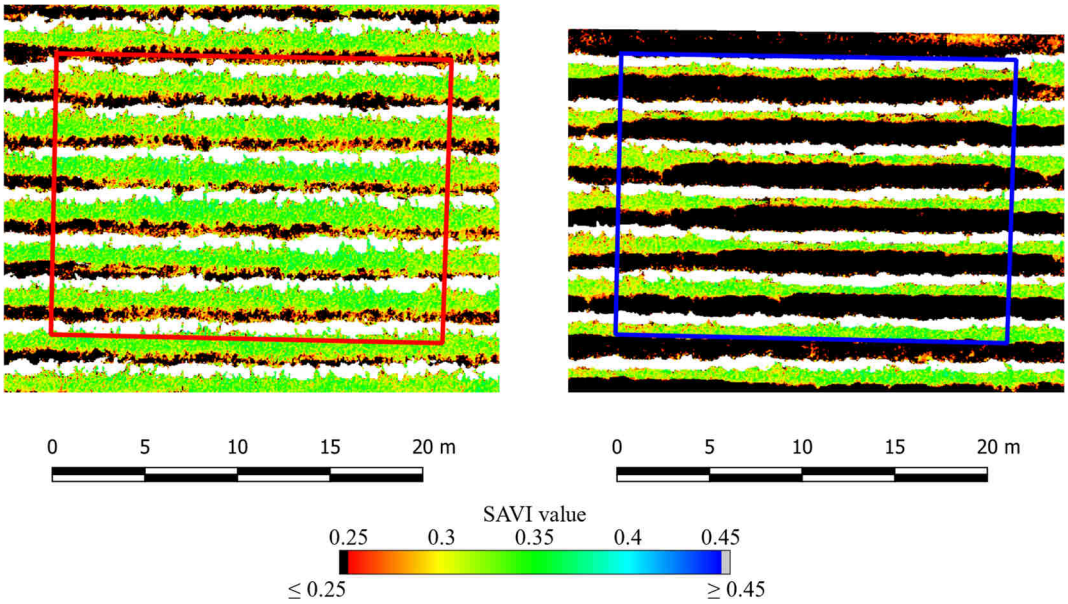

Figure 3.32 Detail of the SAVI on two regions characterized by different rows' width.

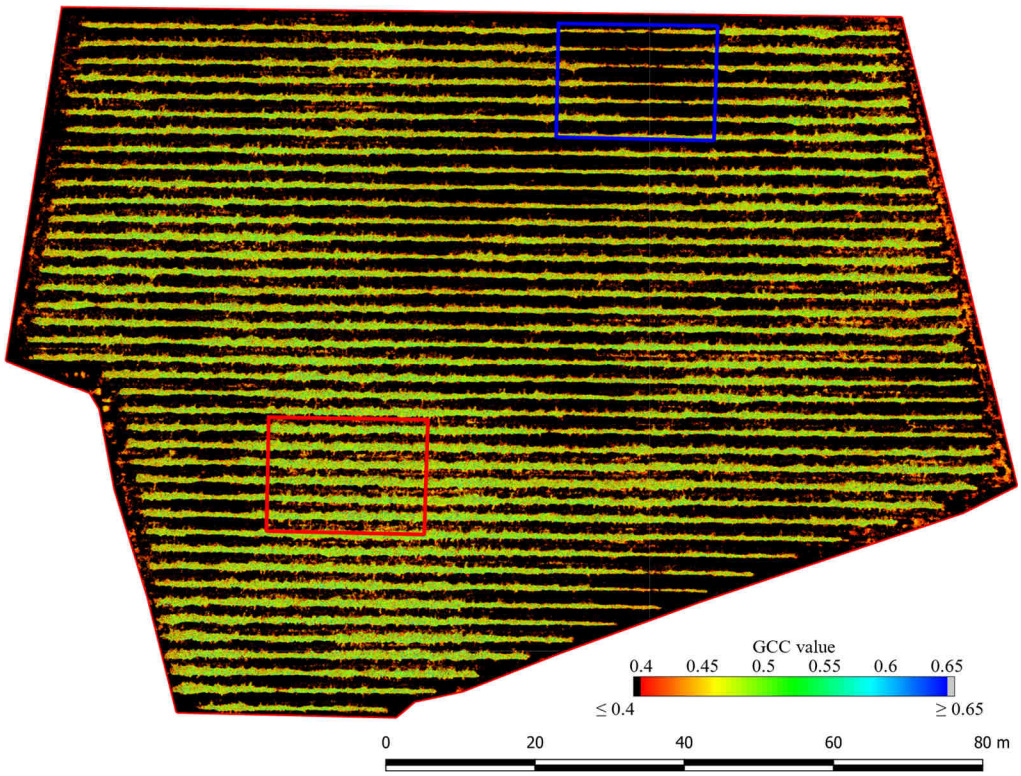

Figure 3.33 Green Chromatic Coordinate (GCC) map of the vineyard. The values are shown in colour within the range from 0.4 and 0.65. Rows are well identifiable through this index.

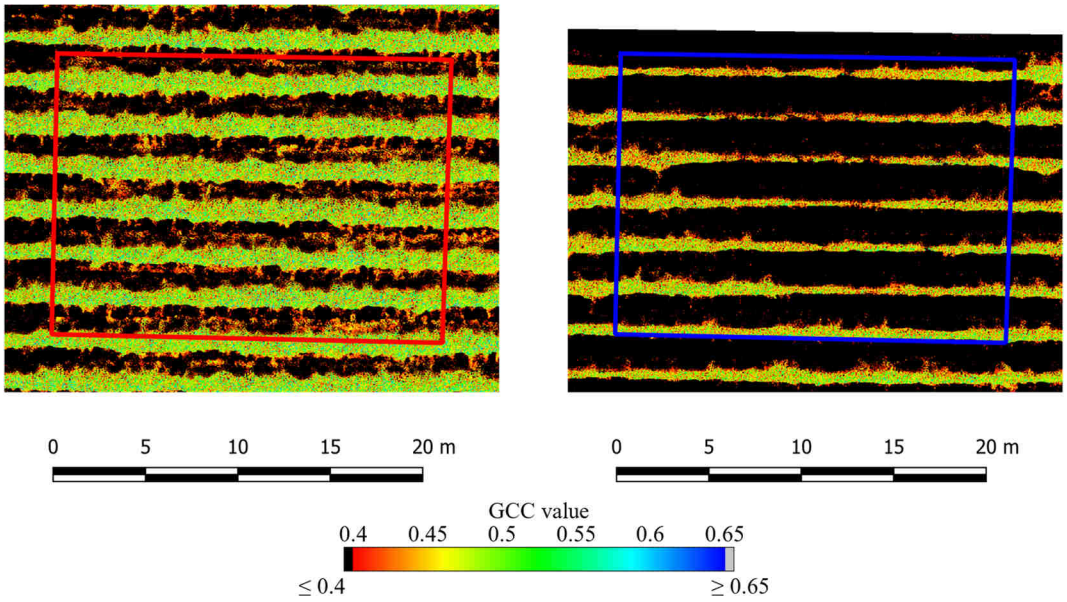

Figure 3.34 Detail of the GCC on two regions characterized by different rows' width.

The relationship between each couple of indices was finally investigated. First of all, the GCC index was compared to all of the other indices. The aim of such a comparison is to analyse if a clear relationship exists between a basic index computed from RGB images and the indices computed exploiting the multispectral detection. The results, in terms of graphs, are shown in Figure 3.35. No correlation exists between the GCC and the other indices, since the coefficient of determination r^2 assumes low values in each plot. In addition, the extent of the cloud points in the graphs visually confirms that there is no correlation between these couples of indices.

Similarly, the same analysis in term of distribution of the values in term of graphs were conducted comparing the different indices computed from the multispectral sensed data. The results are shown in Figure 3.36. Here the indices are strongly correlated each other, since they essentially derive from the same multispectral orthomosaic, whose pixel values were used to compute each index. The typology of relationship, form a mathematical point of view, depends on the expressions of the compared indices. Since NDVI and SAVI are very similar, the relationship was found to be almost perfectly linear. On the contrary, the RVI is characterized by an expression that differs significantly from the NDVI and the SAVI. In fact, no linear correlation was found for the RVI, even if it is still strongly correlated to both them for the reasons explained above. Using a fourth power

polynomial model, also for the RVI was finally found an almost perfect relationship between it and the NDVI and SAVI indices.

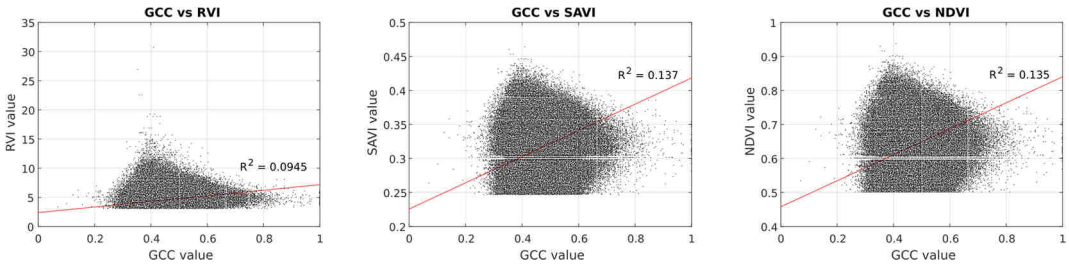

Figure 3.35 Scatterplots of the GCC index and all of the other multispectral derived indices.

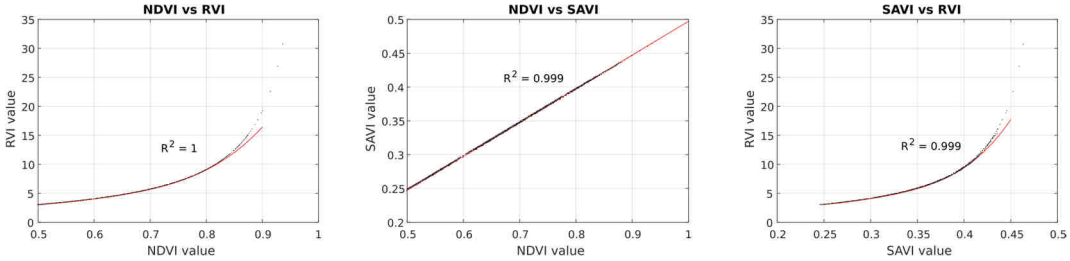

Figure 3.36 Scatterplots of all the combinations of multispectral derived indices for a comparison.

The results obtained in this experimentation shows that a multispectral low-cost camera is effectively able to provide additional information about the canopy.

The signal-to-noise ratio proved not to be extremely high, especially analysing the map in detail at a pixel level. Therefore, the information contained in a multispectral index computed using the data sensed through a low-cost sensor has to be considered carefully. An overall estimation considering groups of pixels is recommended. Despite these issues, the potential of the low-cost multispectral sensor, consisting in the ability to acquire information in the near infrared wavelengths, enables a computation of a variety of spectral indices. Their reliability is strongly affected by the unavailability of a downwelling light sensor for measuring the irradiance at the time of the survey, as well as the lack of a calibrated reflectance panel.

For a single survey with no monitoring over time purpose, the information retrievable by the low-cost multispectral sensor can be used for a standalone decision-making process with the aim to establish which areas are the most likely to be in a suffering status. In fact, the distribution of the NDVI values on the regions with a different width of the rows showed that higher index values occurred more

often where the rows were wider. Even though any further consideration should be made by specialised agronomists, the use of the low-cost multispectral sensor may speed up to detect which regions of the vineyard should be further investigated in detail.

On the contrary, the RGB data by itself could be useful to clearly identify the shape of the rows in the vineyard. In addition, it can be used to compute a basic index that considers for the green component and thus allowing to estimate a sort of greenness fraction. However, no information in the near infrared wavelengths is ever provided by a standard RGB camera.

3.6 A comparison between the Sentera Single and the Parrot Sequoia sensors

The limits highlighted by the experimentation on the vineyard in July, 2016 led to focus further analysis on the usage of a downwelling light sensor. In fact, this sensor is built with the same specifications of the main camera: it is made by the as many CMOS sensors as the ones of the main camera, each of those is equipped with a corresponding bandpass filters having the same spectral transmittance.

A new survey during the spring season in 2017 was therefore performed with the purpose of comparing the results that could be achieved using the Sentera Single sensor with the ones obtained by a more performant camera: the Parrot Sequoia.

As already depicted in section 0, the Parrot Sequoia is a five optics camera, where four of them are actual narrow-band detectors respectively in the green, red, red edge and near infrared wavelengths. In addition, the camera is equipped with a downwelling light sensor that continuously measures the solar irradiance and records this measurement in the metadata whenever an image is captured. Also in this comparison between sensors no calibrated reflectance panel was ever used.

Since the Sentera Single sensor was not able to detect the same spectral bands of the Parrot Sequoia and it did not have a comparable narrow detection in the near infrared wavelengths, the comparison between the performance of these sensors were made only in term of the NDVI. The reason why comparing this spectral index lies in the widespread use of the normalised vegetation difference index in the agricultural context for the detection of the vegetation status.

The survey was conducted on the same field used for the first comparison made between the MAPIR camera and the Sentera Single. Even though the cultivation was not the same, since the field was planted with chard for the production of the seed instead of the wheat of the previous year, this fact made no real difference in order to perform a comparison between the sensors.

A single flight was performed above the field on May 19th, 2017. Missions at the same altitude of 60 metres above the ground with an 80% of longitudinal overlap and a 60% of side overlap were planned. The cameras were set up on two different DJI Phantom 3 Professional aircrafts. The flights for the data acquisition were performed in a rapid succession in order to minimize any possible difference in the light conditions due to the lack of a DLS sensor on the Sentera Single (as previously mentioned).

A total amount of 1348 pictures were acquired by the Parrot Sequoia, 338 of them belonging to the same spectral band. In addition, RGB images were automatically acquired during the mission, even though they were not compared. The images were captured simultaneously by both the monochromatic and RGB sensors. The resulting camera location is shown in Figure 3.37.

Similarly, the Sentera Single sensor acquired 337 images and RGB pictures of the field were concurrently captured by the native camera of the DJI Phantom 3 Professional aircraft.

Three-dimensional models were therefore reconstructed through the structure from motion by finally generating dense point clouds.

Due to inability of the Agisoft PhotoScan software to apply radiometric corrections using the DLS data measurement of the Parrot Sequoia system, the Pix4D Mapper Pro was used for the processing of those images, while the Sentera Single's dataset was processed with the first software for simplicity. The corrections were directly computed by the software [42] by considering the vignetting, the actual ISO setting at the time of the capture, the exposure time and the irradiance value recorded by the DLS through the technique presented in the previous chapters.

In order to accurately georeference the models, a set of ground control points was deployed on the field by the means of target panels. Each GCP was surveyed

through a geodetic receiver in network real time kinematic (NRTK) mode and their coordinates were collected in the Italian reference system ETRS89-ETRF2000(2008.0). A smaller amount of targets was used to perform the accuracy assessment of the models, thus the coordinates of such check points were not used during the alignment process. Instead, they were subsequently compared with the corresponding targets' centres computed by the means of the model.

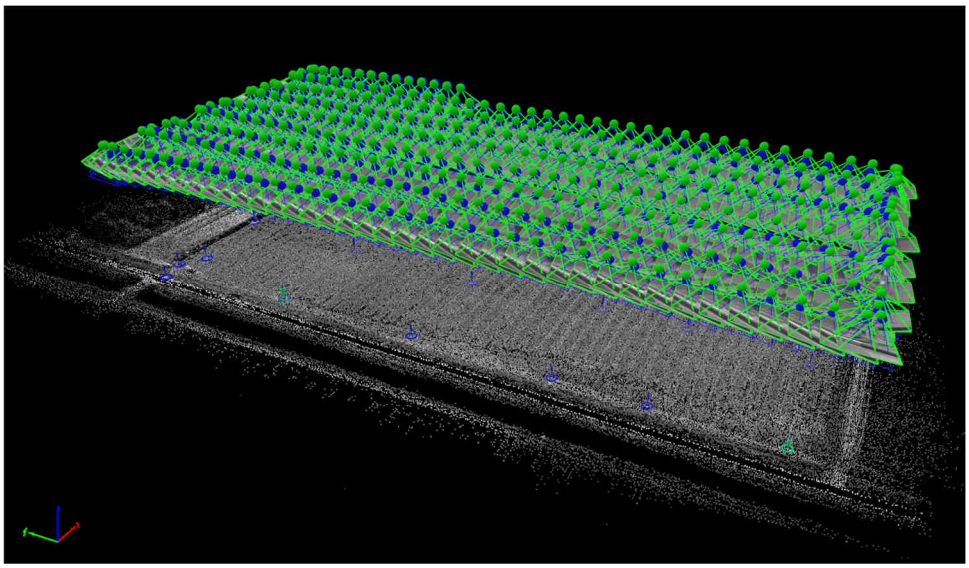

Figure 3.37 Camera and ground control points location for the Parrot Sequoia multispectral dataset with the dense point cloud reconstruction of the field's surface.

The residuals of both the ground control points and the check points are shown in Table 3.6 for the Sentera Single data processing through the Agisoft PhotoScan software. Similar values were obtained for the Parrot Sequoia imageries by the Pix4D Mapper Pro, thus no significant differences would had affected the comparison of the results obtained even though different software was used for the data processing.

Multi-band georeferenced orthomosaics were generated within the software by merging the orthorectified images. It is worth noting that the Pix4D Mapper Pro software is able to compute a real reflectance, while the Agisoft PhotoScan Professional limits the output to a digital number, thus an integer related to the resolution of the sensor. Furthermore, the sensors have a radiometric resolution respectively of 8bit for the Sentera Single and 10bit for the Parrot Sequoia. This implies that the second one is a better sampler and is able to distinguish among a higher number of different intensity levels in term of radiance.

Table 3.6 Residuals for both the ground control points used for the georeferencing of the model and the check points used to validate the accuracy level for the Sentera Single camera in Agisoft PhotoScan Professional. Similar values were obtained for the Parrot Sequoia through the Pix4D Mapper Pro software.

ID	Type	East [m]	North [m]	Elevation [m]	Residuals [m]			
					X	Y	Z	3D
102	GCP	268796.477	4964909.502	-3.958	0.006	0.001	0.004	0.008
104	GCP	268900.262	4964921.866	-3.909	-0.003	0.003	-0.004	0.006
106	GCP	268838.912	4964854.285	-3.919	0.006	-0.012	0.041	0.043
108	GCP	268905.339	4964792.627	-3.572	-0.005	0.010	-0.012	0.017
110	GCP	268851.078	4964728.520	-3.553	0.008	0.005	-0.006	0.011
112	GCP	268917.353	4964696.974	-3.519	0.001	0.018	-0.053	0.056
113	GCP	268919.501	4964649.912	-3.463	0.001	-0.004	0.003	0.005
114	GCP	268856.305	4964645.700	-3.470	-0.007	-0.007	0.024	0.025
115	GCP	268805.788	4964642.601	-3.554	-0.006	-0.000	-0.016	0.017
116	GCP	268802.265	4964689.550	-3.576	-0.010	0.000	-0.021	0.023
118	GCP	268794.013	4964786.189	-3.639	-0.008	-0.001	-0.055	0.055
103	*CP*	*268836.606*	*4964919.974*	*-3.868*	*-0.003*	*-0.005*	*0.027*	*0.028*
105	*CP*	*268902.528*	*4964857.194*	*-3.935*	*0.005*	*0.001*	*0.045*	*0.046*
107	*CP*	*268841.769*	*4964788.126*	*-3.584*	*0.003*	*-0.000*	*-0.020*	*0.020*
109	*CP*	*268906.408*	*4964732.126*	*-3.554*	*0.002*	*0.013*	*0.008*	*0.015*
111	*CP*	*268855.647*	*4964693.040*	*-3.545*	*-0.022*	*0.009*	*-0.003*	*0.024*
117	*CP*	*268798.960*	*4964725.556*	*-3.593*	*-0.017*	*-0.018*	*-0.045*	*0.052*
119	*CP*	*268788.480*	*4964850.827*	*-3.770*	*-0.010*	*-0.032*	*-0.048*	*0.058*
Ground Control Points RMSE [m]					0.006	0.008	0.029	0.030
Control Points RMSE [m]					*0.011*	*0.015*	*0.033*	*0.038*

The NDVI values were computed with the formula

$$NDVI = \frac{DN_{\mathrm{NIR}} - DN_{\mathrm{red}}}{DN_{\mathrm{NIR}} - DN_{\mathrm{red}}} \qquad \text{(Eq 2.16)}$$

for the data obtained in Agisoft PhotoScan Professional (Sentera Single) and the formula

$$NDVI = \frac{\rho_{\mathrm{NIR}} - \rho_{\mathrm{red}}}{\rho_{\mathrm{NIR}} - \rho_{\mathrm{red}}} \qquad \text{(Eq 2.17)}$$

for those generated by the Pix4D Mapper Pro software (Parrot Sequoia). Since the NDVI is a normalised index no remarkable difference affected the computations. The NDVI maps are shown in Figure 3.38. The first impression at a glance is that Parrot Sequoia derived values are higher on the vegetation. To

translate this into a more rigorous consideration, a frequency analysis was performed. The study focussed on the canopy values showing NDVI values higher than 0.5 and only within the cultivated field. In fact, the main aim was to assess the difference in the information retrievable by the compared sensors to evaluate the actual status of the crop. The analysis was performed by the means of frequency histograms. The width for each class was assumed equal to 0.005, thus the range between the adopted threshold of 0.5 and the maximum feasible value of the index (NDVI=1) was split into 100 classes.

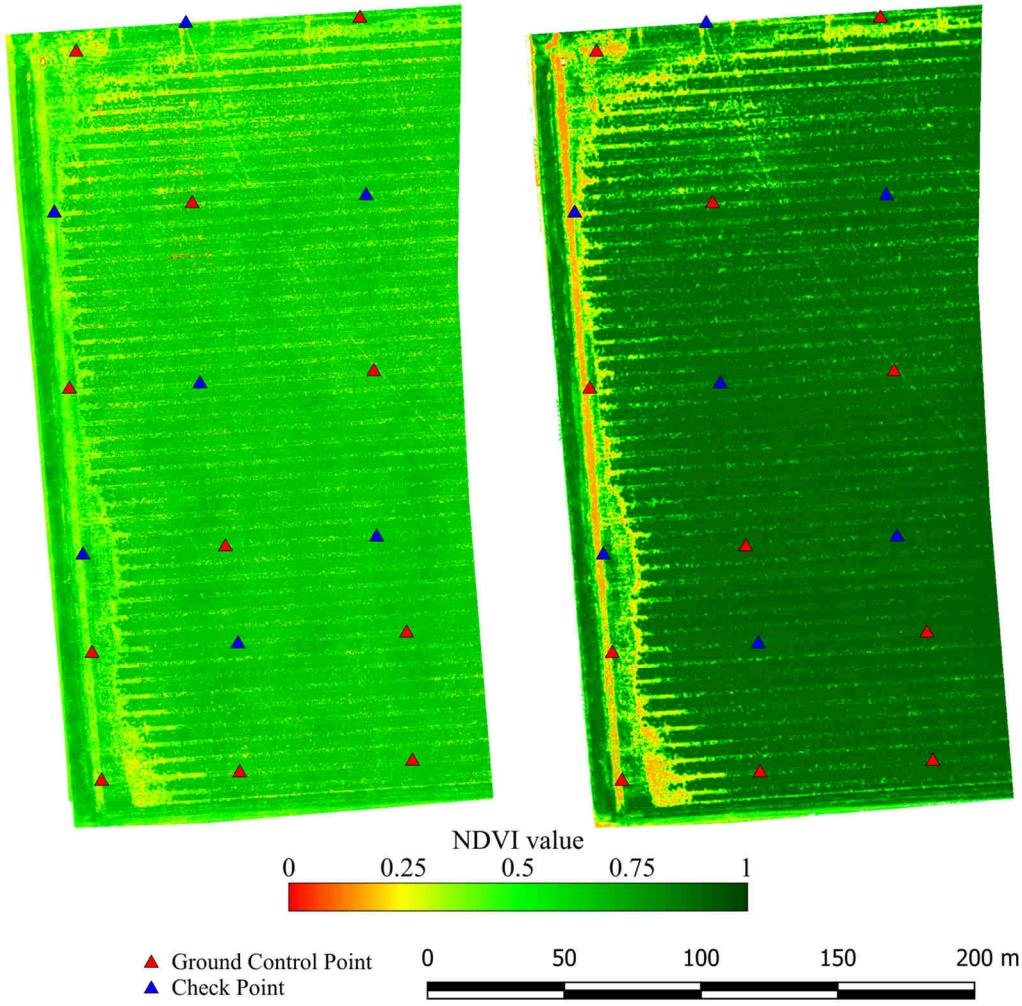

Figure 3.38 NDVI maps for the Sentera Single sensor (on the left) and the Parrot Sequoia (on the right). The second map exhibits higher values. Coloured triangles represent the position of ground control points and check points use to accurately georeference the index maps.

A MATLAB script, reported in Appendix A.1, was thus written for this task. First of all, the results were exported within a graph where each pixel was

represented by its pairs of value $\left(NDVI_{\text{Sentera Single}},\ NDVI_{\text{Parrot Sequoia}}\right)$ from the respective NDVI maps.

This scatterplot proved to be too much dense, due to the small pixel size of the orthomosaic and the corresponding huge number of pixels. In fact, the ground sample distance was 4 centimetres for both NDVI maps and the extent of the compared area was about 4.61 hectares. In order to better understand the real distribution of the values, a bidimensional grid with a step of 0.005 in terms of NDVI value was created. Therefore, the count of how many pairs belonged to each cell was computed and normalized dividing by the whole number of pairs. A threshold value of 0.1% was adopted to establish whether reporting the cell's counts on the graph or not. In addition, a colormap was used to highlight the actual density percentage for each cell. The resulting graph is shown in Figure 3.39.

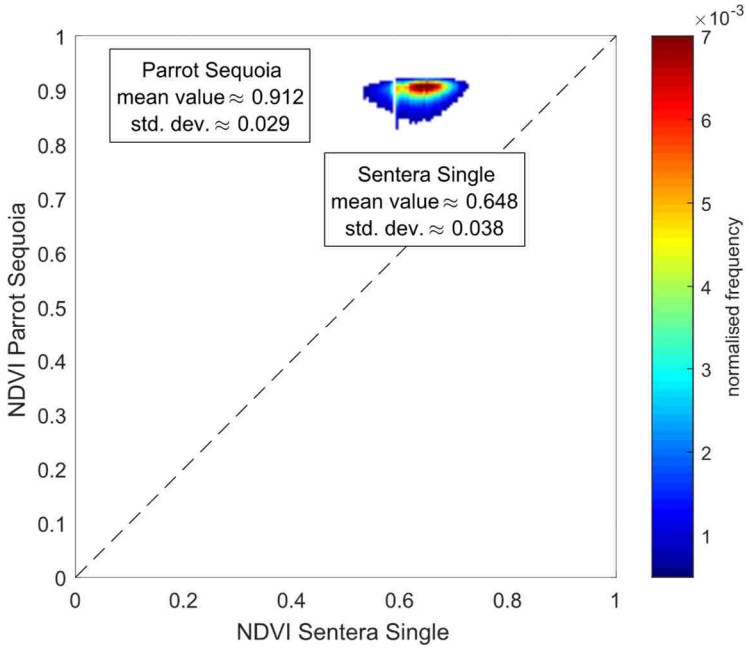

Figure 3.39 Graph of the pairs ($NDVI_{\text{Sentera Single}}$, $NDVI_{\text{Parrot Sequoia}}$) with a cell density normalised representation for counts exceeding the threshold value of 0.5%. The Sentera Single is the raw data sensed, while the Parrot Sequoia is the DLS radiometrically corrected data.

The distribution of more frequent values, hence those cells with a higher normalised frequency, shows that NDVI values are less dispersed and have a generally higher values when Parrot Sequoia was used. The computation of both the standard deviation and the mean value with regard of both the sensors proved that the mean rose from 0.648 to 0.912 and the standard deviation fell from 0.038

to 0.029 using the Parrot Sequoia. From the analysis of the graph in Figure 3.39, it is worth noting that at constant values of NDVI for the Parrot Sequoia sensor correspond a significative wide range of NDVI values compute on the raw data sensed by the Sentera Single sensor. This fact also implies that the Sentera Single NDVI values may be more dispersed and it is confirmed by a higher value of the standard deviation.

All of these considerations were also noticed by the graph of the frequency histograms of NDVI values computed respectively on the basis of the raw data sensed by the Sentera Single and by both the raw data and the DLS radiometrically calibrated data of the Parrot Sequoia (Figure 3.41).

In order to establish whether it was possible to correct the data acquired by the Sentera Single sensor an approach based on the formula used to compute the NDVI for this sensor was followed. In particular, the actual quantum efficiency of the CMOS sensor of the Sentera Single was varied. The response of the corresponding frequency histograms of the computed NDVI was assessed changing the factor α in the following expression:

$$NDVI = \frac{(1+\alpha)\cdot DN_{\mathrm{NIR}} - \alpha \cdot DN_{\mathrm{red}}}{(1-\alpha)\cdot DN_{\mathrm{NIR}} + \alpha \cdot DN_{\mathrm{red}}} \qquad \text{(Eq 2.18)}$$

This is close to the expression used for the formula applied by the Sentera for the computation of the NDVI, even if the actual expression is proprietary and thus it will not be reported here. It is important to highlight that this procedure for adjusting the computation of NDVI value by the raw data sensed through the Sentera Single was applied only to the raw NDVI values that were found to be not less than 0.5 using the Sentera provided formula to compute NDVI. In other words, the first computation of the NDVI makes possible to distinguish between vegetation and non-vegetation pixel (thus focussing the attention on the cultivated area of the field), while the second computation adjusted those values to make more reliable NDVI detections. The workflow of this approach is summarised in Figure 3.40.

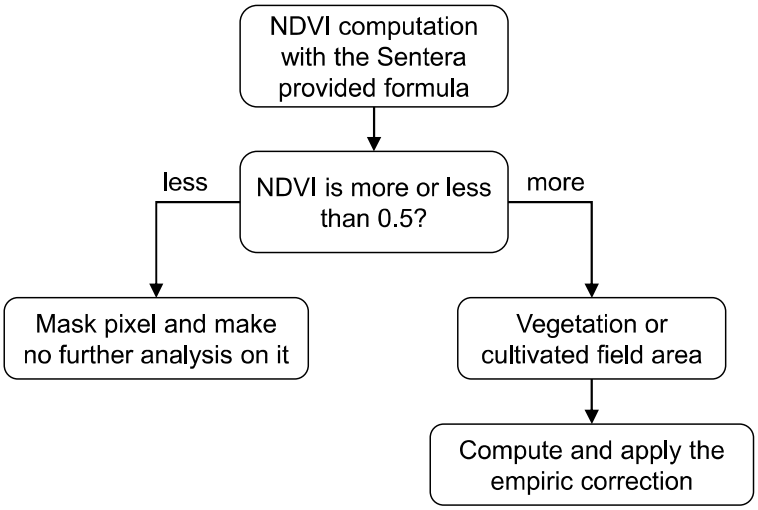

Figure 3.40 Workflow for the application of the empiric correction to the NDVI values computed from the Sentera Single sensor.

The most reliable fit for the empirically corrected NDVI was found for $\alpha = 0.065$. This value forces a magnification of the data recorded in the near infrared producing an increasing in the NDVI values. The most interesting fact lies in the modification of the shape of the frequency histogram. The new distribution of the values, reported in Figure 3.41 shows that the standard deviation decreases and the histogram fits with the one computed by the Parrot Sequoia detection with the radiometric calibration performed on the basis of the data recorded by the downwelling light sensor.

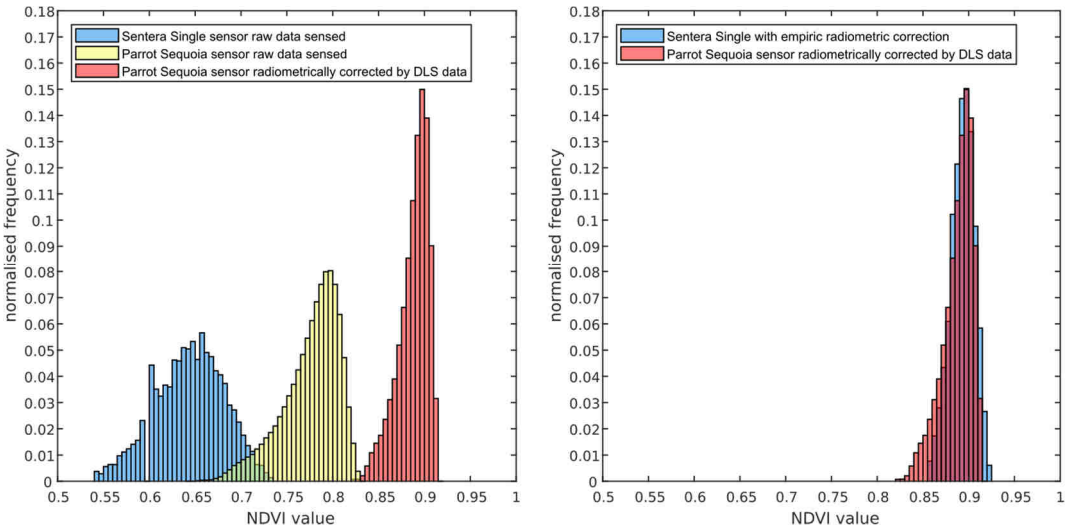

Figure 3.41 On the left: NDVI frequency histograms for the raw data acquired by the Sentera Single (blue) and both the raw data sensed by the Parrot Sequoia (yellow) and the corresponding radiometrically DLS-corrected data (red). On the right: the NDVI frequency histogram for the data sensed by the Sentera Single after the empiric radiometric correction (blue) fits with the DLS-calibrated Parrot Sequoia one (red).

The effectiveness of the fit can be also recognized on the graph showing the pairs of values $\left(NDVI_{\text{Sentera Single}}, NDVI_{\text{Parrot Sequoia}}\right)$ after the empiric correction of the NDVI Sentera Single's values (Figure 3.42). The region with the most frequent pairs, especially those exceeding the same threshold (0.5%) used for Figure 3.39, are now aligned on the bisector. This means that there is a correspondence between the results obtained through the use of data recorded by the DLS and the empiric corrections computed for the Sentera Single.

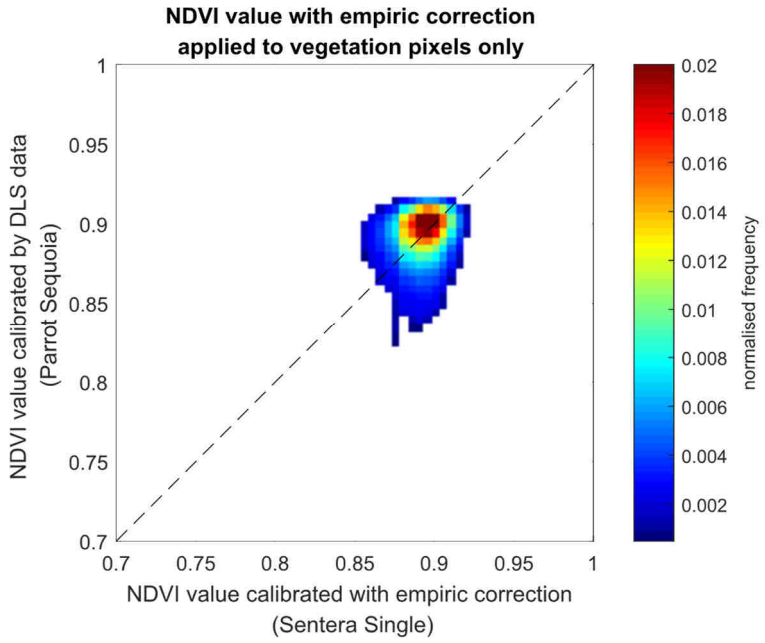

Figure 3.42 Graph of the pairs ($NDVI_{\text{Sentera Single}}$, $NDVI_{\text{Parrot Sequoia}}$) with a cell density normalised representation for counts exceeding the threshold value of 0.5% after the empiric calibration of the Sentera Single's NDVI values. The Parrot Sequoia data shown here it is still the DLS radiometrically corrected one.

Of course, the most limiting issue of this approach lies in which value it is the most suitable to be adopted for the α coefficient in order to correct the raw data. In addition, the presented correction approach works only in the case when no change in the light conditions happened during the image acquisition, thus within a flight. If some change occurs, the data may be equalized with a further empiric correction. This latter aspect was not covered by the study of the comparison between the sensors. However, the data collected by the means of the Sentera Single sensor, with a lower cost with respect to the Parrot Sequoia, proved to be consistent, since the effect of the empiric correction produced both an increase of the values and a decreasing of the standard deviation of them. Therefore, the study proved that an empiric procedure to correct the NDVI for a range of values that is typical used for

vegetation detection and precision agriculture with reliable results effectively exists.

Conversely, the Parrot Sequoia is able to measure the irradiance autonomously thanks to its downwelling light sensor and can compensate for any change in the environmental light conditions. This fact justifies the higher cost of the Sequoia multispectral camera, as well as the availability of narrow-band sensors.

CHAPTER 4

COASTAL DUNES MONITORING

At the same time of the precision agriculture experimentation with very low cost sensors, a coastal monitoring of a dune system in the northern Adriatic Sea, near the town of Rosolina Mare, started in the late 2015.

The same DJI Professional 3 aircraft with the Sentera Single sensor was used since the first survey repetition that took place in March, 2016.

This study was mainly focussed to the three-dimensional geometry of the monitored costal section, with special regard to the embryo dunes. The aim was therefore to assess the evolution of these small dunes over time, providing an innovative technique to detect their evolution.

Even though the multispectral detection in here did not constitute the main purpose, this study was still a sort of milestone in the overall experimental path and a prelude to the further coastal monitoring of the submerged seaweed in the lagoon of Goro that will be presented in Chapter 5. For these reasons the monitoring of embryo dunes [52] has been included and it is presented in this section.

4.1 Introduction

Beaches often have a vegetated dune system performing a multitude of functions valuable to the ecosystem. Protection against the ingression of the sea during storms, reserve deposits to mitigate the erosion of the shoreline, ecological niches for flora and fauna are some example of these crucial functions.

In a natural context of the system's evolution, the avandunes are preceded by embryo dunes which are characterized by high dynamics. The site chosen for the monitoring presents all the typical characteristics of the dune system mentioned above. It is located in the northern Adriatic Sea between the city of Venice and the Po River delta (Italy), more precisely in the southern part (3 km long) of Rosolina Mare, in the Porto Caleri area (Figure 4.1).

The beach is up to three hundred meters wide in the North-South direction and it is bounded to the land side by a complex strip of dunes consisting of stabilized fossil dunes, vegetated avandunes and embryo dunes, proceeding from the land to the sea. The back-dunes environment is characterized by the presence of infra-dune depressions where rainwater is collected, allowing the growth of a particular hygrophilous vegetation. Stabilized dunes are covered with a patch of bushy plants that spatially precedes arboreal formations, such as the forest of autochthonous holm oaks or pine forests of artificial origin. The inclusion of this coastal section in the *Coastal Botanical Gardens* of Porto Caleri (ca. 23 ha in extent) ensures the complete conservation and the natural evolution of this coastal environment, without any significant impact of human activities, hence the site is perfectly suitable for the study of the natural geomorphological evolution of dunes, from their creation to their stabilization.

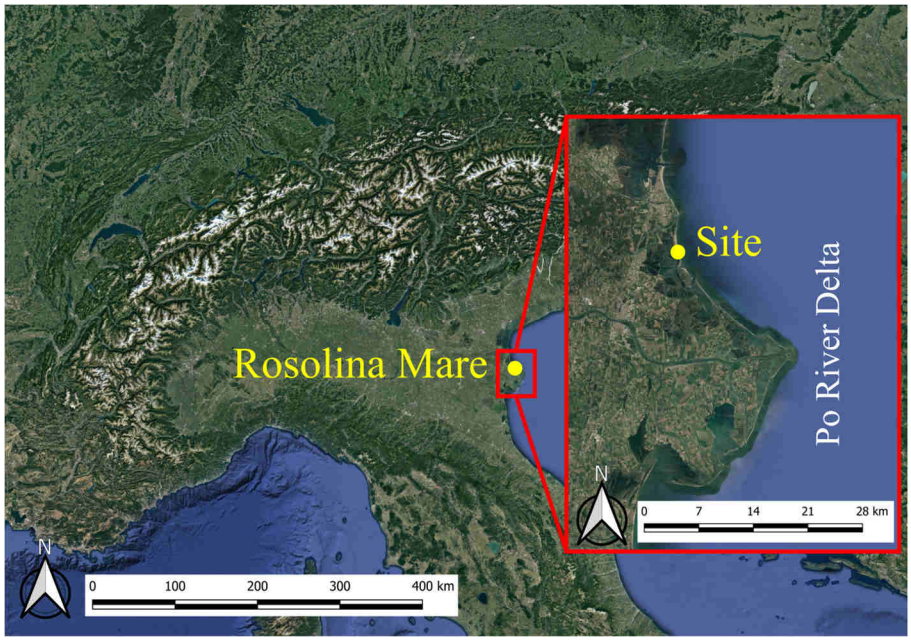

Figure 4.1 Location of the site, near the town of Rosolina Mare in the northern Adriatic Sea, Italy.

Over the past 50 years, the entire southern coast of Rosolina Mare has been characterized by a significant progradation of the shoreline (Figure 4.2), with a maximum magnitude up to 5 meters per year. Survey techniques based on remote sensing from satellites, often conducted with reference to the evolution of the shorelines, have been successfully used for this detection [53]. This progradation phenomenon is still active at the monitored site. From a geomorphological point of view, embryo dunes present the most interesting shapes because they are very

sensitive to even small changes of the coastal environment factors and they can quickly be destroyed as they are created. However, due to the progradation in this area, mainly caused by an aeolian transportation [54], the embryo dunes generally grow and join each other.

The reconstruction of Digital Elevation Models (DEMs) represents a fundamental tool to detect the morphology of complex systems, especially when the shapes change rapidly in both time and space.

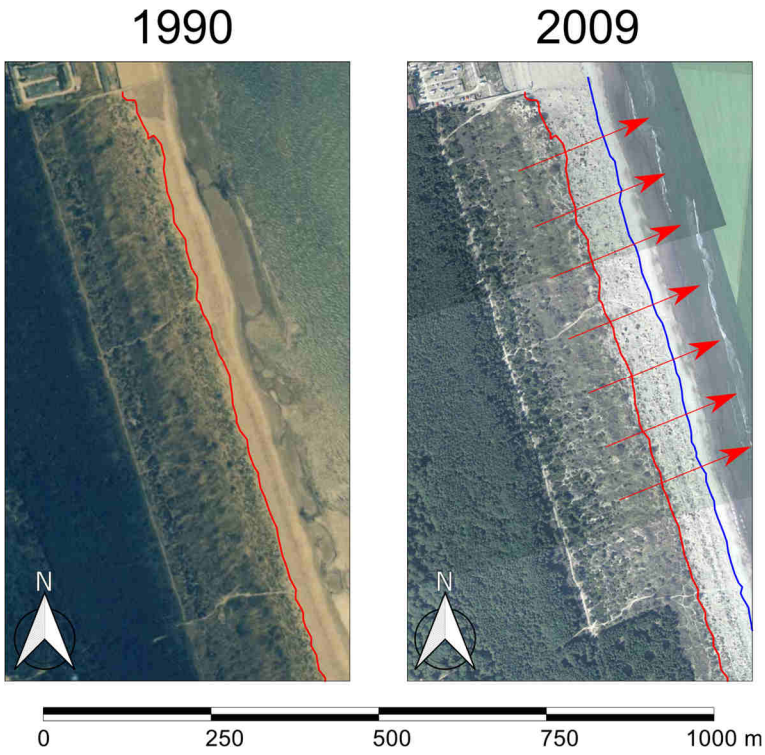

Figure 4.2 Progradation of the embryo dunes limit over 19 years in the site (about 50 metres).

By using a discrete approach, an even large number of points can be directly surveyed through GNSS geodetic receivers by means of a fast Network Real Time Kinematic (NRTK) technique, with the subsequent advantage to frame the survey in an official reference system. However, this method is very time consuming and cannot be applied to broad extensions. Other approaches, with a more dense (and practically continuous) data collection, such as Terrestrial Laser Scanners (TLS), airborne LiDAR (Light Detection And Ranging) and aerial photogrammetry by Unmanned Aerial Vehicles (UAVs), allow the mapping of wider areas with still good accuracies. In recent years, the LiDAR has been the most commonly employed technique with the aim to map long coastline stretches. Although the raw

data acquired by this technique have a high resolution, the raw data processing is generally set up to provide a resampled model to users, characterized by a Ground Sample Distance (GSD) of about 0.5÷1 metre. In addition, for the currently available LiDAR data in the area where the monitored site of this work is located, the characteristics of the instruments used to acquire the raw data are not well known actually, nor are the processing procedures (filtering and georeferencing techniques) applied to the raw data to obtain the final products (clouds, DEMs). However, the sandy coastal environment evolves rapidly and is easily affected by many natural and human factors. Hence for advanced studies in coastal geomorphology, a different method is needed, able to provide better spatial resolutions at a more reasonable cost and with a great flexibility.

A solution is therefore represented by the use of both small UAVs with a compact digital camera to acquire the imageries and the Structure from Motion (SfM) approach to reconstruct the three-dimensional geometry of the coastal section. This technique provides excellent results in terms of spatial resolution at a low cost [55].

The SfM approach allows 3D geometry reconstruction (the *structure*) from a set of 2D images of the scene (the *motion*). The detection of the key points and the tie points is the first step, performed with image-detection algorithms that look for features between multiple images and also able to recognize the same feature at different image scales (image-matching). No *a priori* assumption, such as the need of a set of Ground Control Points (GCPs), is binding to reconstruct the geometry, since classical collinearity equations can be solved in an arbitrary scale. In addition, SfM can estimate not only the camera extrinsics but also the intrinsics, by performing a self-calibration and thus allowing the use of even uncalibrated cameras. The lens distortion is also taken into account and modelled in terms of both symmetric and asymmetric radial distortion.

Once the 3D geometry is reconstructed, a more dense point cloud can be obtained with specialized algorithms able to reconstruct depths: the dense cloud, containing up to ca. 80 million points (on average) in the surveys of this study, represented the basis for any further data processing.

In order to accurately georeference the dense point cloud, a set of GCPs was therefore surveyed by GNSS geodetic receivers through NRTK: accuracies

achievable in this way are completely comparable with the SfM approach [56]. To frame the model in the same reference system of GCPs, a final bundle adjustment [57] procedure was adopted, performed within the same software used to reconstruct the 3D geometry (Agisoft PhotoScan Professional). The bundle adjustment can consider nonlinearities, providing better results than adopting a simpler similarity transformation.

The Structure from Motion by UAVs in the context of geomorphological coastal monitoring over time was hence adopted in this study for all the above reasons, especially its versatility, low cost, effectiveness [58] and significantly higher spatial resolution. There are increasingly reports in the literature of applications of UAV surveying for coastal monitoring [59]. The case study in [60] concerns a similar sandy coastal environment. The most recent application regarding the Adriatic littoral can be found in [61] for the neighbouring Emilia-Romagna region. Other authors tested the SfM approach with UAV [62] or investigated the accuracy of georeferenced point clouds produced via multi-view stereopsis from UAV imagery [63] in analogue operative conditions: all of these researches confirm the reliability of the SfM technique by UAVs.

An innovative aspect of the present study is the use of the SfM technique for the repetition of the survey with the purpose of monitoring the embryo dunes' morphological change over time. This will allow to analyse and explain the dynamics of such a morphological evolution of the beach and the complex dune system with higher detail by geologists and geomorphologists.

4.2 Data acquisition

Unmanned Aerial Vehicles were used to detect and reconstruct the morphology of the dune system [64], in particular with regards to the embryo dunes that are characterized by a small size.

This choice was dictated by the great potential of the SfM technique by UAVs, including relatively fast acquisition of individual images, the possibility to obtain very high resolution orthophotos [65] with a Ground Sample Distance of about 2 centimetres at a flight altitude of 40 meters, as well as the low cost.

Two different aircraft were used: a DJI Phantom 2 Vision and a DJI Phantom 3 Professional (Figure 4.3). They were equipped respectively with a Panasonic Lumix DMC-GM1 camera with a 16 megapixel RGB sensor and a DJI FC300X camera with a 12 megapixel RGB sensor. Specifications of aircrafts and camera are listed in Table 4.1. Actually, the DJI Phantom 2 was used for the first survey only (on November 2015), whereas the DJI Phantom 3 was used for all the subsequent survey repetitions.

Six survey repetitions were carried out respectively on November 2015, March 2016, June 2016, November 2016, May 2017 and December 2017 (Figure 4.4). For each flight, a specific programmed mission was set up. A number of flights between two and three (Figure 4.5) per repetition were necessary to map the full extension of the monitored area due to the limited autonomy of the UAV (related to battery capacity) as well as the need to maintain an altitude of about 40 meters to ensure the desired spatial resolution of 2 centimetres.

Table 4.1 Aircrafts and cameras specifications.

Aircrafts specifications			
		DJI Phantom 2 Vision	*DJI Phantom 3 Professional*
Take off weight		1160 g	1280 g
Max flight speed		15 m/s	16 m/s
Max flight time		16 min	18 min
Hovering accuracy	Horizontal	± 2.5 m	$\pm 0.3 \div 1.5$ m
	Vertical	± 0.8 m	$\pm 0.1 \div 0.5$ m
Cameras specifications			
		Panasonic Lumix DMC–GM1	*DJI FC300X*
Sensor format		17.3 mm×13.0 mm	6.5 mm×4.9 mm
Focal length		12 mm	3.6 mm
35 mm equiv. focal length		24 mm	20 mm
Image resolution		4592×3448	4000×3000
Field of View		72°	84°
Pixel size		3.8 μm	1.6 μm
GSD at 40 m altitude		1.3 cm	1.8 cm

In particular, the parameters were set as shown in Table 4.2 during the flight plans. The camera was in a nadiral arrangement. Some camera settings (e.g. exposure time) were varied according to the real brightness at the time of each flight.

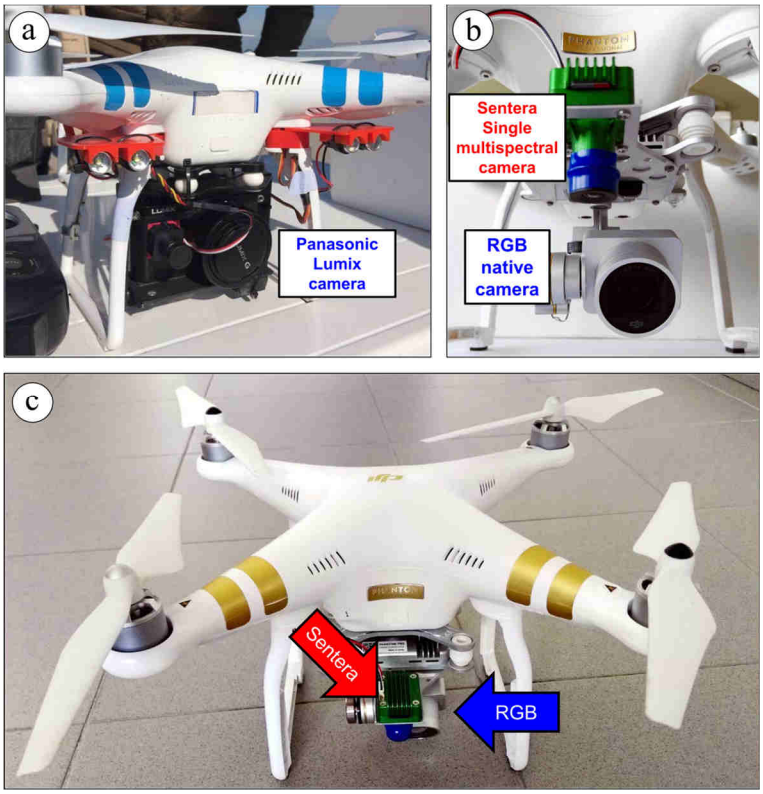

Figure 4.3 (a) The DJI Phantom 2 equipped with the Panasonic Lumix camera. (b) A detail on both the DJI Phantom 3 cameras, showing the nadiral fixed arrangement of the Sentera Single sensor. (c) The DJI Phantom 3 equipped with both the RGB native camera (highlighted in blue) and a Sentera Single multispectral sensor (highlighted in red).

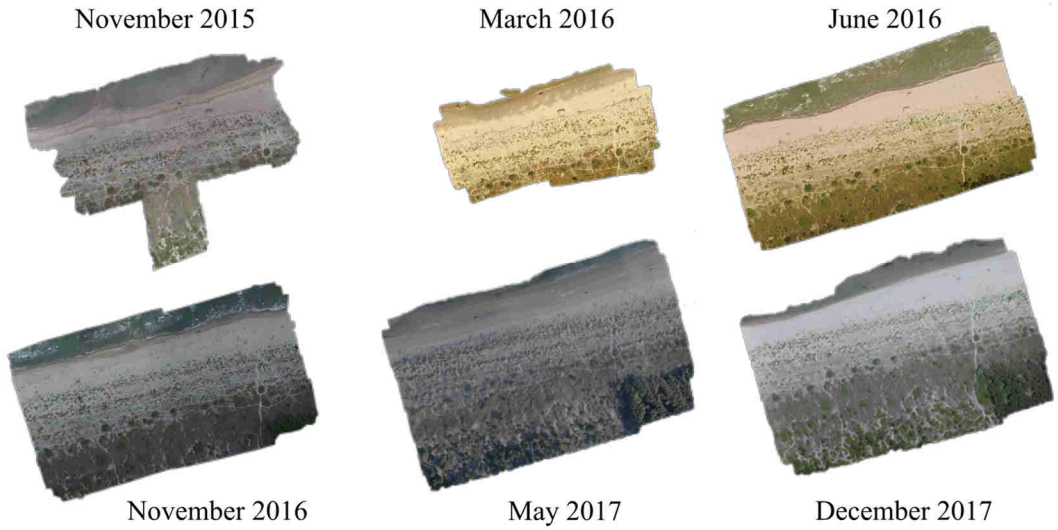

Figure 4.4 Orthophotos of the six different survey repetitions from November 2015 to December 2017 (sea on the top side).

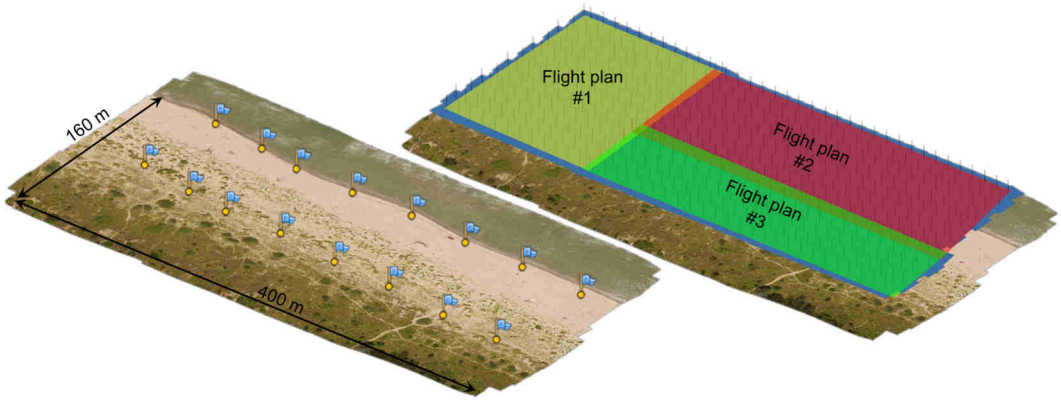

Figure 4.5 Ground Control Points location within the Agisoft PhotoScan Professional software (on the left) and the different flight plans' coverage with overlap for including all the study site (on the right).

Table 4.2 Flight plan specifications.

Flight plans specifications	
Altitude	40 m
Longitudinal overlapping	80%
Transverse overlapping	60%
Speed of aircraft	ca. 3 m/s
Exposure time	1/400 ÷ 1/1000 s
ISO sensitivity	100 ÷ 400

All the surveys were framed within the European Terrestrial Reference System (ETRS), in its ETRF2000(2008.0) realization. This reference system is materialized in Italy by the National Dynamic Network (RDN). Targets were distributed over the ground to almost completely enclose the surveyed area (Figure 4.5) and were thus used as Ground Control Points. Generally, an amount between 14 and 18 was deployed. The targets, well visible in aerial images and with a clear and unmistakable position of their centres, were surveyed with a GNSS geodetic receiver in Network Real Time Kinematic (NRTK) mode. The accuracy achievable with a kinematic “stop and go”' technique, with corrections transmitted in real time from a network of permanent stations (the ItalPoS service was used for this purpose), is sufficient and completely compatible with the precision of a 3D model generated by a Structure from Motion approach. In addition, the need for post-processing the GNSS collected data to calculate the coordinates of the targets is eliminated in this way. The ITALGEO05 geoidal separation model was finally used to convert ellipsoidal heights to orthometric elevations.

4.3 Data processing

In order to accurately reconstruct the three-dimensional geometry of the coastal section, all the imageries were aligned through the Agisoft PhotoScan Professional software and further processed.

The target recognition on each image was performed manually: this type of operation is not particularly complex because the software helps to locate a marker through a reprojection, once the marker itself has been placed on two aligned images at least. However, it is crucial to take into account that raw camera positions used for a first raw alignment are in the WGS84 geographical coordinate system (EPSG: 4326), while the GCPs coordinates, surveyed in the ETRF2000(2008.0), should be represented in a cartographic UTM projection (more precisely in zone 33) of the European Terrestrial Reference System (EPSG: 25833).

In a further alignment, in which the GCPs were taken into account, the camera positions were ignored due to their poor accuracy, and they were assigned with a very low weight or even directly deleted; a reprojection optimization was therefore performed after the final alignment in order to best fit the intrinsic parameters of the camera and to ensure the maximum reachable accuracy of the 3D model. A summary of the residuals for each survey repetition is shown in Table 4.3.

Table 4.3 Summary of the residuals for each survey repetition.

Residuals		**Survey Date**					
		Nov. 2015	Mar. 2016	Jun. 2016	Nov. 2016	May 2017	Dec. 2017
East	*RMSE* [m]	0.029	0.011	0.023	0.044	0.036	0.052
	Min [m]	-0.058	0.024	-0.096	-0.068	-0.102	-0.078
	Max [m]	0.050	0.020	0.043	0.050	0.054	0.107
North	*RMSE* [m]	0.018	0.016	0.026	0.02	0.037	0.032
	Min [m]	-0.037	-0.031	-0.102	-0.036	-0.069	-0.061
	Max [m]	0.03	0.027	0.034	0.045	0.090	0.057
Up	*RMSE* [m]	0.006	0.003	0.032	0.040	0.024	0.011
	Min [m]	-0.010	-0.006	-0.055	-0.041	-0.054	-0.027
	Max [m]	0.008	0.003	0.032	0.040	0.038	0.019
3D	*RMSE* [m]	0.035	0.019	0.036	0.053	0.057	0.062
	Min [m]	0.011	0.005	0.013	0.029	0.009	0.018
	Max [m]	0.063	0.032	0.142	0.073	0.104	0.121

The use of the robust algorithms of densification implemented in Agisoft PhotoScan allowed the creation of the dense cloud, once the geometry was successfully reconstructed. However, this dense cloud contains points belonging to the vegetation on the top of the dunes, that are not helpful to describe and analyse morphological changes of embryo dunes over time. To exclude these points in the

further data processing (including the creation of Digital Elevation Models) a filter essentially based on slope detection, already available within Agisoft PhotoScan, was applied. This filter [66] works through two steps: in the first one, the entire dense cloud is divided into several square cells of a specified size (5 metres × 5 metres is the value adopted in this study) and the detected lowest point of each cell is assumed to belong to the ground. A first raw model of the ground itself is thus created in this way. In the second step, all other points are classified by analysing both their distance and slope from the ground-classified points of step one. Threshold values for distances and slopes must be specified: in this work the adopted values were 0.15 meters and 15°. The final dense cloud of ground-classified points is shown in Figure 4.6, where all the points classified as effective ground are highlighted in yellow.

Since outliers were still present after the classification, a further statistical outliers filter was applied to the dense cloud (in the CloudCompare software) in order to remove residual points before proceeding with the creation of a Digital Elevation Model of the sandy terrain. Figure 4.7 shows the effect of this kind of filter: on the left (Figure 4.7a) a zoom on the raw dense cloud of ground-classified points, on the right (b) the same detail after the application of a statistical outliers filter (SOR), showing the effective outliers removal. The values for the parameters to be set in this filter were carefully assumed each time in order to maximize the filtering effect.

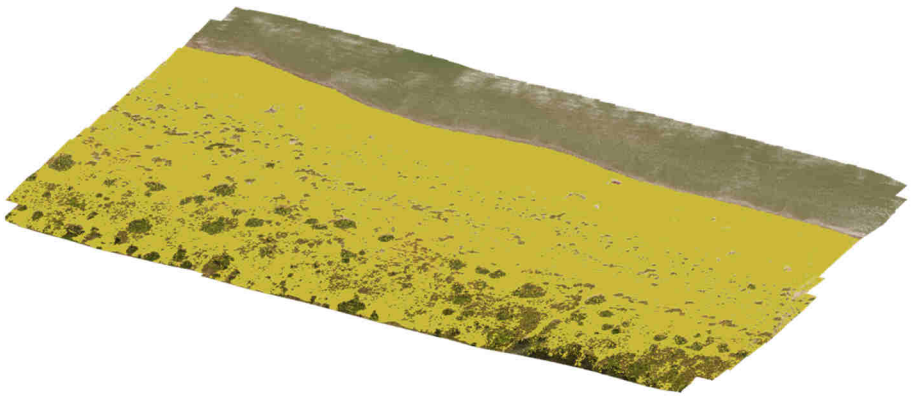

Figure 4.6 Dense point cloud (in yellow) after the detection of the ground points by the means of the slope-based classification algorithm in Agisoft Photoscan Professional.

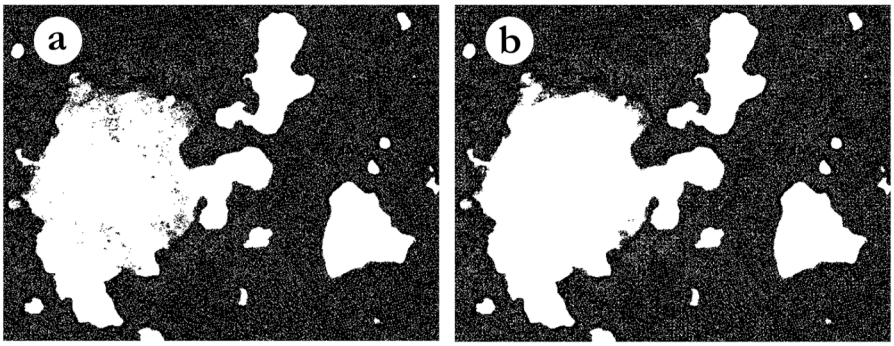

Figure 4.7 (a) Quality of the dense cloud after the detection of ground points on a detail. Some outliers are still present. (b) Quality of the dense cloud after the application of the statistical outliers filter (SOR) on the same detail. Outliers were removed.

Finally, a set of specially surveyed (by NRTK) points was added to the dense cloud to integrate zones where vegetation was removed. The entire process described above, with issues and adopted solutions, is summarized in Figure 4.8, which shows a raw dense cloud profile schematization (Figure 4.8a), the effect of the application of the slope detection algorithm for the ground points classification (Figure 4.8b) and the final integration with specially surveyed GNSS points to reconstruct a more faithful profile of the dense cloud itself (Figure 4.8c). Examples of botanical species found in the dune system and responsible for this issue were *Ammophila arenaria* (Figure 4.8d) and *Echinophora spinosa* (Figure 4.8e).

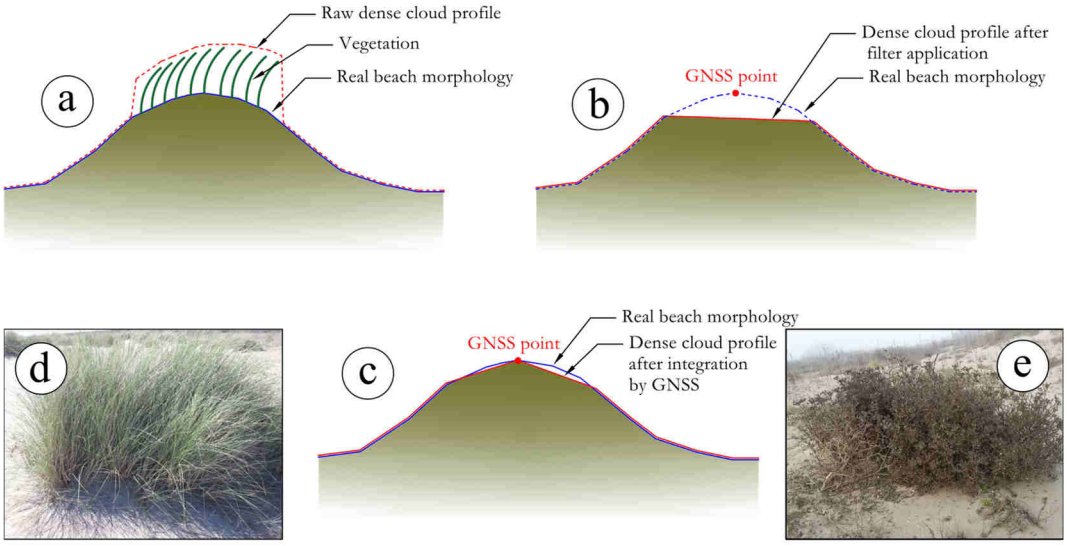

Figure 4.8 (a, b, c) Schematization of the GNSS integration process by filtering out the vegetation (a), the survey of a point by GNSS (b) and the subsequent reconstruction of a more faithful shape (c). (d, e) Botanical species of vegetation on the dunes that cause the issue.

Using the final integrated dense point cloud, the Digital Elevation Model (DEM) was created by a direct rasterization of it, since the density of points was high enough (up to 80 million points) to make it unnecessary the creation of a Triangulated Irregular Network (TIN) as intermediate step.

For each survey repetition, its own elevation model was preventively checked [67] by comparison with another set of points, completely independent of those points used for the integration process described above. In this way, the presence of systematic errors was accurately investigated and assessed. A particular care was adopted to survey directly on the sand, e.g. by using a plate in order to prevent the pole tip from sinking, which could have been an important source of errors. Furthermore, the check was used to validate the real accuracy of the elevation model with respect to the actual beach morphology. The results of the validation conducted for the DEM on November 2016, which represents the survey with the widest set of validation points collected along the beach, are shown in Figure 4.9. Both the mean and standard deviation values show the full compatibility with the NRTK method of surveying used to reference the model. Similar values, even if not explicitly reported, were obtained for the validation of the other DEMs.

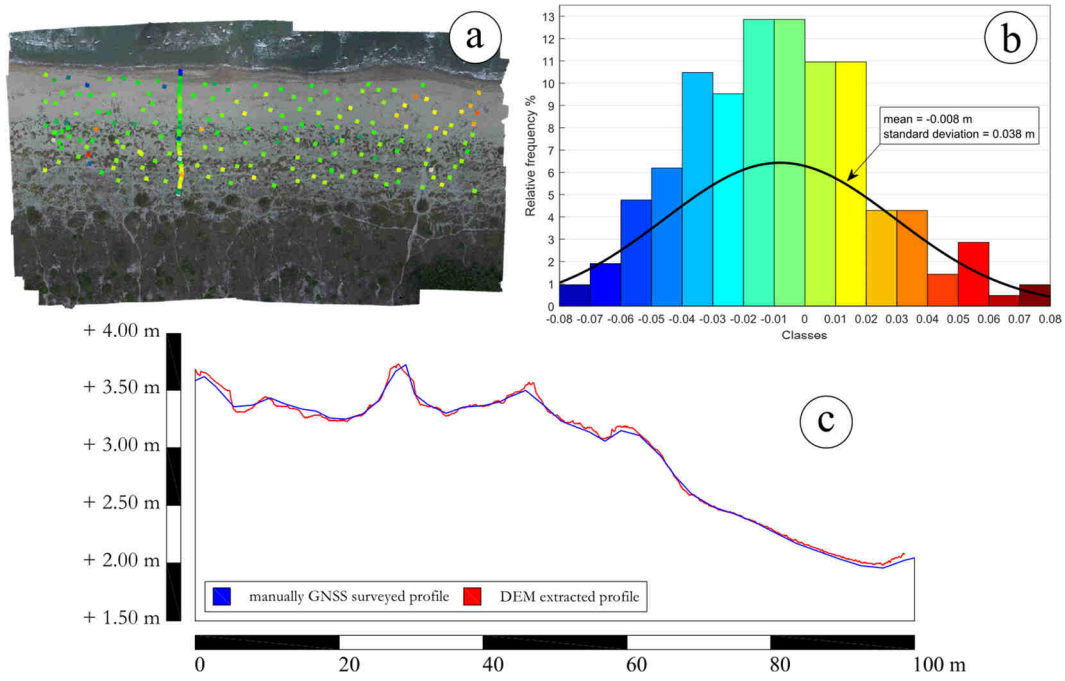

Figure 4.9 (a) Set of ground points used for the comparison between the DEM of November 2016 and the GNSS surveyed elevation. (b) Validation results by histograms: the standard deviation value is comparable with the assumed accuracies of the SfM approach. (c) Comparison between GNSS and DEM on a profile. Discrepancies are comparable with the SfM approach.

In addition, a cross section profile was reconstructed through GNSS NRTK during the survey on November 2016, in order to further validate the use of a plate under the pole as well as to assess the quality of profiles' reconstruction by DEM extraction. Figure 4.9c shows the results of such a comparison between this profile and its DEM derived one. Except for some outliers where the influence of vegetation was still present, the mean value of -1.2 centimetres for the difference between DEM (red line) and GNSS profiles (blue line) shows, once again, that the accuracy is comparable with the use of NRTK to provide the vertical datum.

4.4 Morphological detection of the embryo dunes evolution

After the validation of the Digital Elevation Models generated for each survey, with discrepancies values similar to those previously shown in Figure 4.9, a series of further information was thus extracted from them and then compared. The strength of aerial imagery by UAVs, with respect to traditional discrete and time-consuming methods of surveying based on the use of total stations or GNSS geodetic receivers in NRTK mode, is the possibility to make cross sections in any area of the model at any time, since the data is practically continuous.

In particular, in order to monitor the changes in the morphology of the beach, ten cross sections and three longitudinal sections (Figure 4.10a) were used to extract profiles. Figure 4.10b illustrates a profile analysis conducted on a cross section to evaluate the first winter season effects: five different steps in the evolution of embryo dunes can be recognized [68], numbered from 1 (very embryonic) to 5 (vegetation-stabilized embryo dunes). Some moderate change in the geomorphology is already detectable.

In addition, an elevation difference was computed for the whole extent of the overlapping between different surveys generating a DEM of Difference (DoD). In this way it was possible to compute a sediment budget through all the compared area extents, in a very simple manner. Figure 4.11c shows the elevation differences between the last and the first survey, respectively performed in December 2017 and November 2015. The expression is given by $H^{\text{ortho}}_{\text{Dec.2017}} - H^{\text{ortho}}_{\text{Nov.2015}}$, since the orthometric elevations were used.

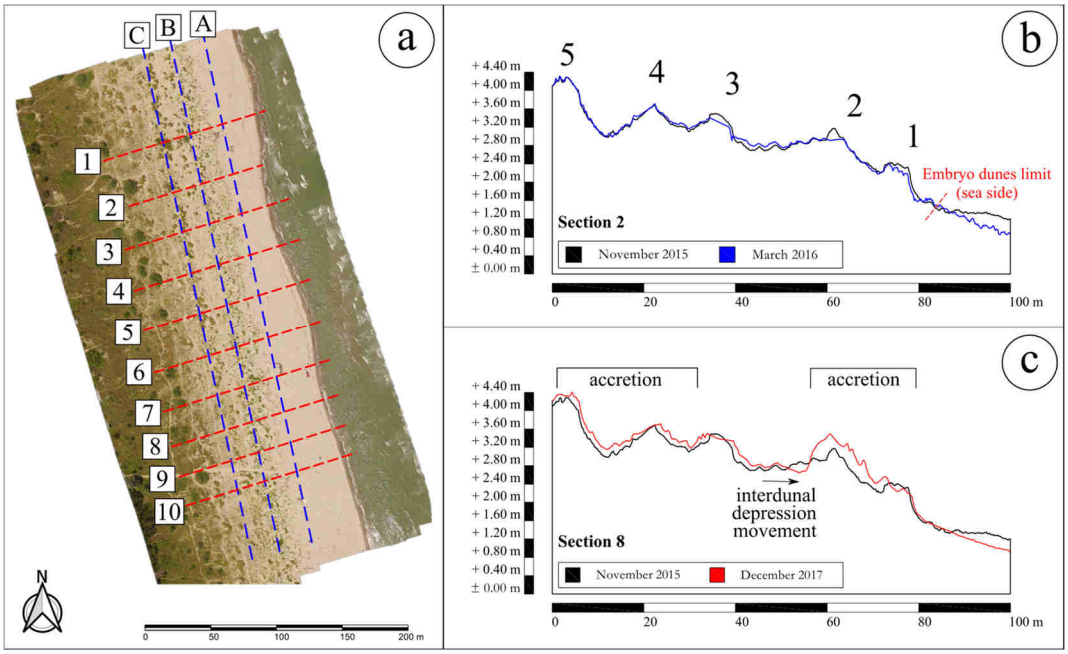

Figure 4.10 (a) Location of the cross and longitudinal sections. (b) Detection of the morphological evolution of dunes during first winter season by the comparison of the profiles of November 2015 (black) and March 2016 (blue) on cross section 2b. (c) Detection of the morphological evolution of dunes over two years by the comparison of the profiles of November 2015 (black) and December 2017 (red) on cross section 8.

Red zones represent accumulation (positive sediment budget), while blue zones represent erosion (negative budget). Differences between the last model and all the previous ones were computed each time in order to have a sort of chronology of geomorphological evolution of the whole dune system. The cross section (Figure 4.10c) helps to understand this progradation phenomenon.

The analysis of the DoD shows how the progradation phenomenon is detectable through two years of monitoring.

In particular, the back-zone (the nearest to land) is stable, with a very low rate of elevation increment. The zone labelled as *A* in Figure 4.11c represents the latest developed embryo dunes, while *B* and *C* highlight a change in the position of the interdunal depression. In fact, zone *B* is lower than two years before and this is probably due to the replacement of previous embryo dunes by the advancing interdunal depression. Similarly, zone *C* hence represents the area where the interdunal depression itself has been filled.

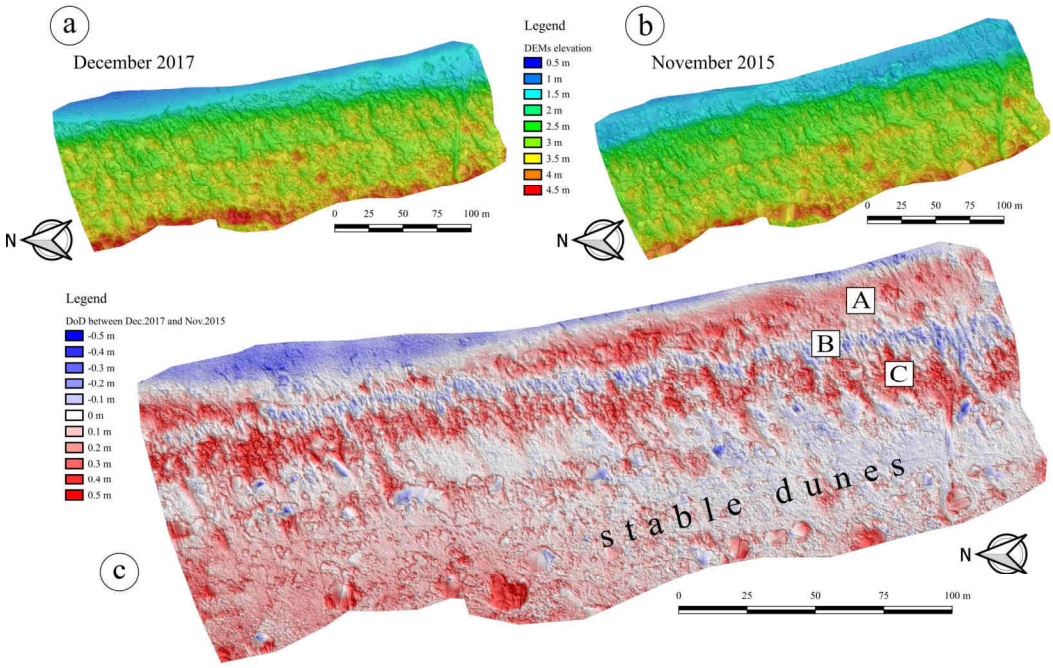

Figure 4.11 (a) DEM of the survey on December 2017. (b) DEM of the survey on November 2015. (c) DEM of Difference (DoD).

4.5 Multispectral imageries and vegetation on the beach

The availability of very high resolution orthomosaics for each survey repetition, with a ground sample distance of 2 centimetres, allowed also a precise mapping of the botanical species of the dune system [68].

With regard to Figure 4.10b, in the areas with the second of the five listed steps of the embryo dunes evolution the *Ammophila arenaria* was found. Furthermore, Figure 4.12 shows the mapping [68] of the vegetation for the survey performed in March, 2016. Using the multispectral imageries collected by the Sentera Single sensor with whom the DJI Professional 3 aircraft was stably equipped whenever it was flown, the corresponding NDVI map was generated.

The analysis of the map indicates a relationship between a change in the NDVI value from the shoreline to steps 1 and 2. In fact, higher NDVI values can be found where the first vegetation starts growing.

Even though the assessment of this NDVI separation should require the use of a more performant sensor in order to accurately compute the index, the spectral information suggested to further investigate the coastal monitoring by the use of

multispectral UAV-borne cameras with the aim to detect changes in the coastal environment through the computation of spectral indices or even performing an image classification. Therefore, this study constituted the prelude to the further algal monitoring by the means of the MicaSense RedEdge-M camera.

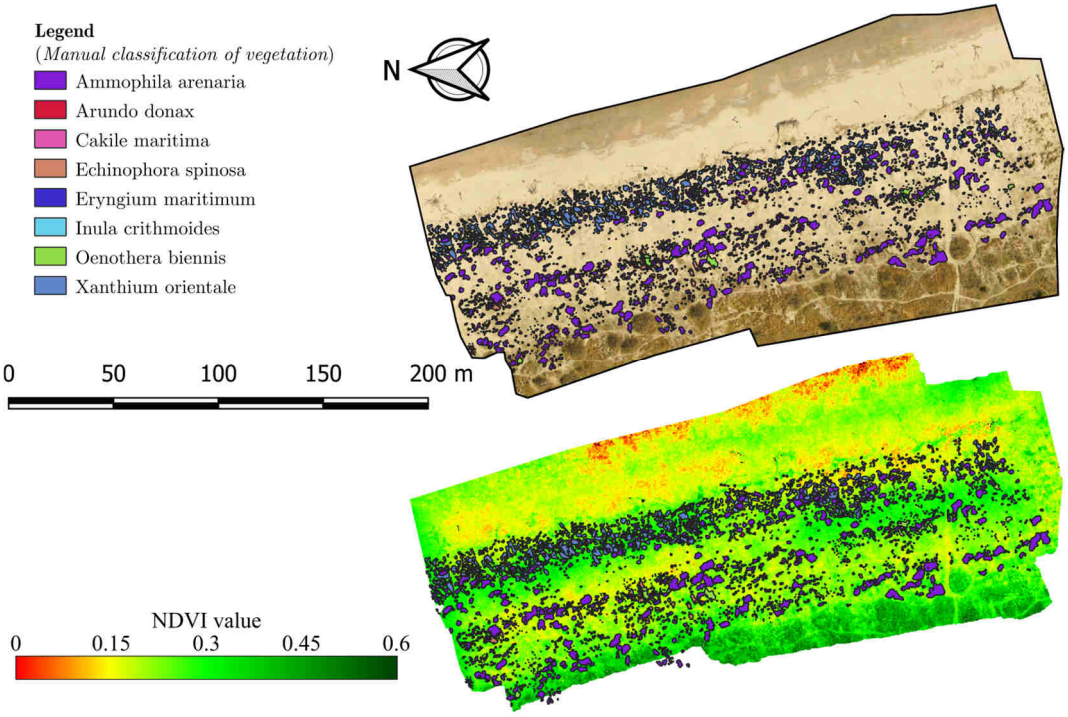

Figure 4.12 On the top: vegetation classification [68] conducted on the high resolution orthomosaic for the survey performed in March, 2016. On the bottom: NDVI map generated by the data acquired through the Sentera Single sensor with the overlap of the classification above. A change in the NDVI values is well recognizable in areas where the embryo dunes were not present along the shoreline.

CHAPTER 5

COASTAL SUBMERGED SEAWEED MONITORING

5.1 Introduction

The sudden algal bloom in shallow water is a serious phenomenon that quickly leads to anoxia conditions, threatening mollusc farming. Therefore, the accurate assessment of the algal bloom with high geometric and spectral resolution can really make the difference for the economy of fishing communities.

Recent studies conducted by the means of spectroradiometers, especially the Moderate Resolution Imaging Spectroradiometer (MODIS), in the southwestern Florida allowed to develop a prototype of a warning system forecasting the occurrence of particular conditions up to three days in advance [69]. The methodology proved to be reliable at a local scale and cost-effective.

Similarly, a high-spatial resolution monitoring was performed using airborne hyperspectral imagery in [70] in order to explore the relationship between the spatial distribution of phycocyanin, chlorophyll-a, total suspended solids and the algal distribution. The study area consisted in a reservoir that is part of the Geum River in South Korea. A hand held spectroradiometer was used to collect data on both radiance and irradiance with a 3 nanometres resolution.

Massive invasions of floating aquatic plants can be recognized also on satellite imageries having higher ground sample distances. A recent study on this phenomenon is reported in [71] and it shows how it is possible to use the multispectral information by the Sentinel-2/SMI (MultiSpectral Imager), the Landsat-8/OLI (Operational Land Imager) and the Aqua/MODIS for large extents. In particular, since the analysed plants were floating, their higher response in the near infrared wavelengths was exploited. The time series of these imageries were analysed in detail and it allowed to study the unusual floating macroalgae that occurred in the Rio de la Plata estuary in 2016.

Due to all of the above reasons and thanks to the support given by recent and almost contemporaneous similar studies previously mentioned, the use of

multispectral imageries collected by the means of an unmanned aerial vehicle [72] was studied in the site of the Lagoon of Goro [73]. The decision to choose this location lies in the fact that the Lagoon of Goro (in the northern Adriatic Sea, close to the Po River delta) represents a crucial environment for the clams' farming and its balance is also particularly delicate because of both the freshwater coming from the Po River and the saltwater ingression caused by tidal cycles of the Adriatic Sea. It combines both the need to develop a detecting system able to provide information on the possible occurrence of critical water conditions in advance as well as the prevention of an excessive formation of floating seaweed that generally leads to anoxia conditions.

Therefore, the MicaSense RedEdge M sensor was used in order to monitor the growth of the seaweed [74,75,76] in the lagoon of Goro. The study focussed on two different sites with a clear and shallow water, that were surveyed respectively on May 25th, 2018 and July 3rd, 2018 (Figure 5.1).

Figure 5.1 Location of the town of Goro, in the northern Adriatic Sea, Italy (on the left) and location of the surveyed sites (on the right) on a Worldview2 satellite imagery (courtesy of the ARPAE Emilia Romagna – Unità Acque Costiere – Ferrara).

Agisoft PhotoScan Professional and Pix4D Mapping Pro were used both to align the multispectral images and to perform a radiometric calibration.

In this experimentation different aspects were investigated:

- the effectiveness of using the downwelling light sensor;
- the effectiveness of using the calibrated reflectance panel;
- the improvement in using the combination of both the previous ones;

- the differences in processing the acquired datasets with two structure from motion commercial software able to manage multispectral data;
- the reliability of a supervised classification obtained with the MicaSense RedEdge M multispectral camera with and without the radiometric calibration;
- the overall potential in monitoring the algal growth in a shallow water coastal environment with multispectral UAV imageries.

5.2 Data acquisition

The data acquisition took place through two different campaigns. The first one, on May 25th, was performed at the initial growth phase of the seaweed. Most of the seaweed were therefore still completely submerged. The survey focussed on two different sites with similar characteristics both in term of geomorphology and previous history of algal presence. The species that generally can be found in the study area are *Ulva* and *Enteromorpha* and their presence were confirmed through a raking (Figure 5.2).

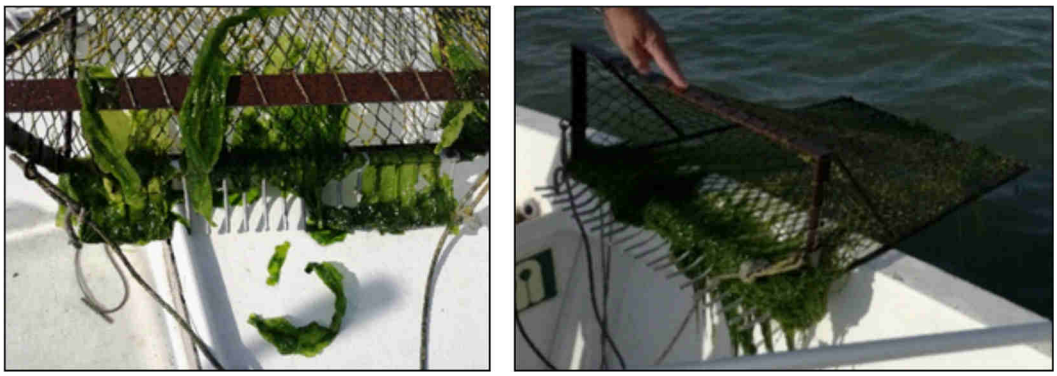

Figure 5.2 Typical seaweed species in the lagoon of Goro: *Ulva* (on the left) and *Enteromorpha* (on the right) found through a raking.

The flight altitude for each planned mission was 70 metres, with a resulting ground sample distance of about 5 centimetres. This size is smaller enough to allow a high-resolution mapping of the seaweed extent and it guarantees to cover a proper coastal area for the test, even with a single flight. The potential issues related to the autonomy of the battery represented an additional crucial aspect for this experimentation. Since the overall extension of the lagoon of Goro is about 30 square kilometres, the flight altitude adopted for the test should be higher than the

usual value used in a precision agriculture context, in order to assume that the approach may be further applied to wider extents.

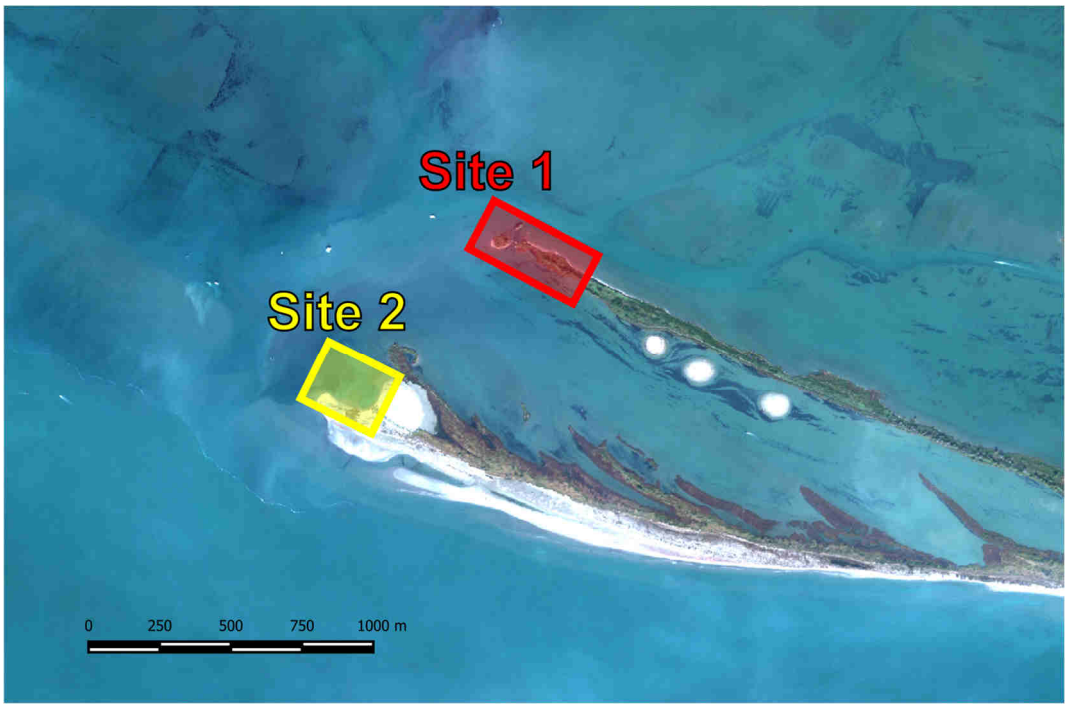

Figure 5.3 Approximate extent of the surveyed sites. The background image is a WorldView2 imagery acquired on November 20th, 2017 (courtesy of the ARPAE Emilia Romagna – Coastal Water Unit – Ferrara).

The MicaSense RedEdge M camera was thus set up for collecting data at a 70 metres flight altitude with a longitudinal overlap of 80%. A side overlap of 60% was imposed to the flight plan: even though this setting pertains to the strip offset computed on the basis of a native DJI Phantom 3 Professional aircraft's camera, the resulting side overlap for MicaSense RedEdge M camera was absolutely adequate for reconstructing a multispectral orthomosaic.

Immediately prior to flying the aircraft, as well as just after the completion of each flight, a picture of the calibrated reflectance panel was captured. By using the trigger button, the firmware of the camera applies a specific setting to ensure that there is no overexposed pixel in the captured image. Consequently, the relationship between the radiance detected by the camera on the panel region of the image and the actual reflectance of the panel is preserved.

All of the acquired images also contain metadata with the irradiance measured by the downwelling light sensor at the time of the capture. The imager settings like the ISO sensitivity and the exposure time, the radiometric calibration parameters

provided by the manufacturer as well as the coefficients for modelling the vignetting and row gradient effects are attached to the metadata as well.

For an accurate georeferencing of each dataset, a set of ground control points was deployed by the means of targets and consequently surveyed with a GNSS geodetic receiver in NRTK mode for both the site n°1 and the site n°2. The distribution of the GCPs in site n°1 was not optimal, since the target was placed around the most accessible. However, the results of the tests performed within a same software (Agisoft PhotoScan Professional and Pix4D Mapper Pro) were not affected by differences in the georeferencing of the orthomosaic since the alignment of the images was executed prior to apply the radiometric corrections and no significant differences were found on the reconstructed orthomosaics. Similarly, in order to conduct an analysis unaffected by any possible georeferencing issue, results obtained through different software were compared by assessing the differences in the distribution of the computed values for both NIR and red reflectances and NDVI over regions with a certain extent. In this way, a misalignment affected only the edge of each region and did not contribute to the estimation of the values distributions.

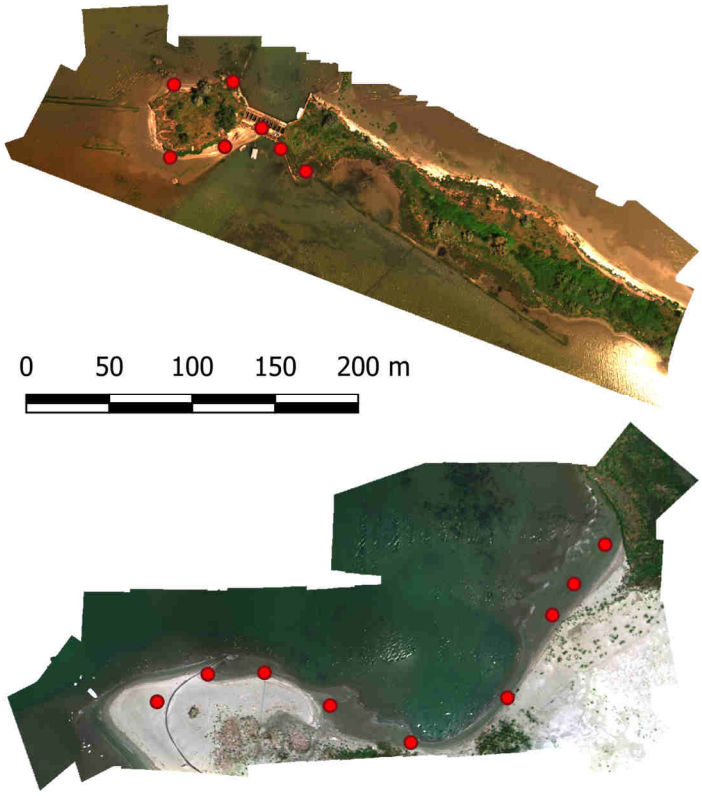

Figure 5.4 Distribution of the ground control points for the site n°1 (on the top) and the site n°2 (on the bottom).

5.3 Data processing

Each imagery dataset was processed through two of the most commonly used structure from motion commercial software: Agisoft Photoscan Professional and Pix4D Mapper Pro. The first one fully implemented the feature of handling DLS data and using images of panels to perform a radiometric calibration only in the early 2018.

Both the software can consider only the DLS measured irradiance (Figure 5.7 and Figure 5.8) to correct the raw digital numbers as well as only the acquired images of the calibrated reflectance panel (Figure 5.9). In this latter case, Agisoft Photoscan Professional is also able to take into account more than a single image of the panel, while Pix4D Mapper Pro can only handle one image of it for each band.

The first step was to load all the images into the software and then recognize the ground control points on the images themselves. As previously mentioned above, this process was made prior to apply any radiometric correction. In this way, no error due to a different target recognition on the images should affect the orthomosaic reconstruction, thus all the comparisons within the datasets processed through the same software were consistent. The residuals of the alignment for the data processing in both software for flights performed in May are reported in the tables from Table 5.1 to Table 5.4. Similar values were obtained for the flights later performed in July. The root mean square error (RMSE) was found to be less than the planned GSD size, thus the alignments were successfully executed in both Agisoft PhotoScan Professional and Pix4D Mapper Pro. The only exception was represented by the altitude component for the flight on the site n°2 processed through Pix4D Mapper Pro. However, the elevation was never considered for the multispectral detection of the seaweed, thus it did not affect any of the results.

Despite of the accuracy reached by the alignment process, some of the images were not aligned. Most of them did not capture any portion of land and the sea surface was slightly ruffled by the wind, hence the ripples blurred the image of the seabed causing difficulties in the detection of the features. In addition, the reflection of the sun on the sea surface was matched through the imageries and correctly filtered out as an outlier.

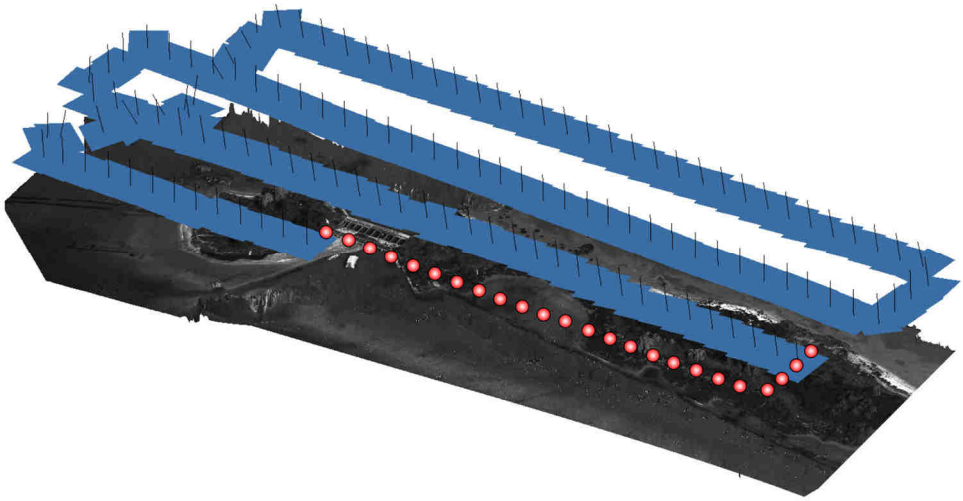

Figure 5.5 Aligned and unaligned images for the site n°1 (May).

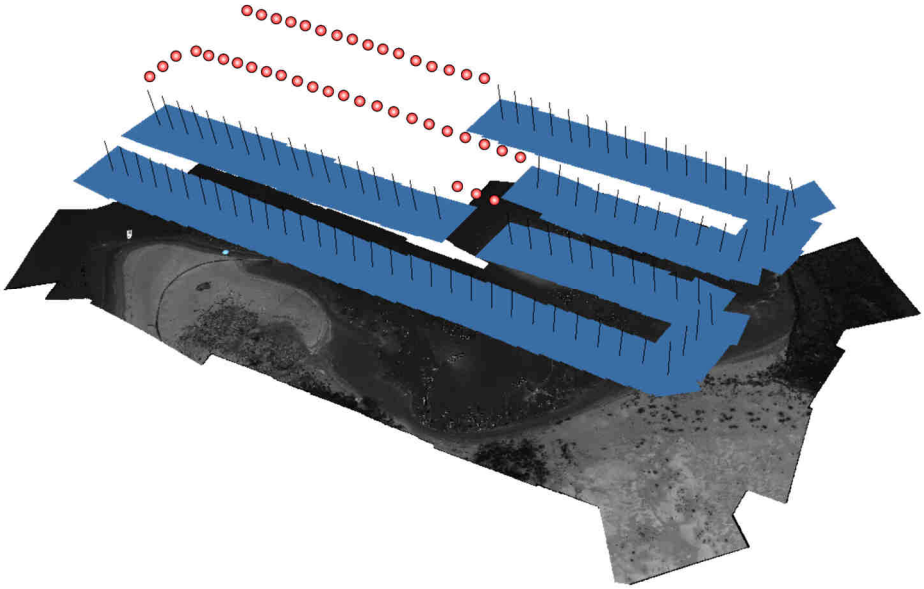

Figure 5.6 Aligned and unaligned images for the site n°2 (May).

Table 5.1 Residuals for the alignment of multispectral imageries of site n°1 acquired in May through the software Agisoft PhotoScan Professional.

ID	Type	East [m]	North [m]	Elevation [m]	Residuals [m]			
					X	Y	Z	3D
100	GCP	288559.155	4963779.749	0.281	0.008	-0.002	-0.024	0.026
101	GCP	288523.500	4963777.998	0.311	0.007	0.004	0.028	0.030
102	GCP	288603.013	4963725.839	0.408	0.003	-0.002	-0.011	0.012
104	GCP	288576.407	4963751.940	1.173	-0.016	0.007	-0.013	0.022
106	GCP	288521.259	4963734.272	0.350	-0.003	-0.011	-0.009	0.014
103	*CP*	*288587.866*	*4963739.405*	*0.754*	*-0.001*	*0.007*	*0.000*	*0.007*
105	*CP*	*288554.192*	*4963740.740*	*0.539*	*0.004*	*-0.001*	*0.023*	*0.023*
Ground Control Points RMSE [m]					0.009	0.006	0.019	0.022
Control Points RMSE [m]					*0.003*	*0.005*	*0.016*	*0.017*

Table 5.2 Residuals for the alignment of multispectral imageries of site n°2 acquired in May through the software Agisoft PhotoScan Professional.

ID	Type	East [m]	North [m]	Elevation [m]	Residuals [m]			
					X	Y	Z	3D
108	GCP	288170.270	4963304.354	0.263	0.000	-0.001	-0.031	0.031
110	GCP	288138.474	4963261.923	0.254	0.001	0.011	0.011	0.015
111	GCP	288111.369	4963212.164	0.341	-0.002	-0.006	-0.021	0.022
112	GCP	288053.239	4963185.298	0.296	0.012	0.013	0.036	0.040
114	GCP	287965.053	4963227.307	0.337	-0.027	-0.002	-0.010	0.029
116	GCP	287900.31	4963209.77	0.85	0.00	-0.01	-0.01	0.01
109	*CP*	*288151.504*	*4963280.626*	*0.248*	*0.002*	*-0.009*	*0.015*	*0.018*
113	*CP*	*288004.584*	*4963207.456*	*0.403*	*-0.003*	*-0.008*	*-0.025*	*0.027*
115	*CP*	*287930.91*	*4963226.40*	*0.52*	*0.01*	*0.01*	*0.01*	*0.02*
Ground Control Points RMSE [m]					0.012	0.008	0.022	0.027
Control Points RMSE [m]					*0.008*	*0.010*	*0.019*	*0.023*

Table 5.3 Residuals for the alignment of multispectral imageries of site n°1 acquired in May through the software Pix4D Mapper Pro.

ID	Type	East [m]	North [m]	Elevation [m]	Residuals [m]			
					X	Y	Z	3D
100	GCP	288559.155	4963779.749	0.281	-0.016	0.008	0.062	0.065
101	GCP	288523.500	4963777.998	0.311	0.025	-0.002	-0.082	0.086
102	GCP	288603.013	4963725.839	0.408	-0.028	0.003	0.019	0.034
104	GCP	288576.407	4963751.940	1.173	0.035	0.000	-0.007	0.036
106	GCP	288521.259	4963734.272	0.350	-0.039	-0.016	0.039	0.057
103	*CP*	*288587.866*	*4963739.405*	*0.754*	*0.023*	*0.002*	*-0.072*	*0.076*
105	*CP*	*288554.192*	*4963740.740*	*0.539*	*0.021*	*0.024*	*-0.053*	*0.062*
Ground Control Points RMSE [m]					0.030	0.008	0.050	0.059
Control Points RMSE [m]					*0.022*	*0.017*	*0.063*	*0.069*

Once that the alignment was successfully performed, the subsequent step was therefore to decide which kind of correction would be applied. Since every possibility was tested, including the no-correction option, different projects were saved for preserving the initial alignment and further processed. The images were merged to generate a comprehensive orthomosaic by densifying the dense cloud of tie points built by the software and reconstructing a texturized mesh beforehand.

Actually, a remark has to be done on this aspect. In fact, the final products of Agisoft Photoscan Professional always consisted in a real orthomosaic where each pixel contained a digital number. The maximum value depends on the radiometric

resolution. For the MicaSense RedEdge M camera, the "Bits per Sample" parameter equals to 16, thus the resulting maximum digital number is given by $2^{16} - 1 = 65535$.

Table 5.4 Residuals for the alignment of multispectral imageries of site n°2 acquired in May through the software Pix4D Mapper Pro

ID	Type	East [m]	North [m]	Elevation [m]	Residuals [m]			
					X	Y	Z	3D
108	GCP	288170.270	4963304.354	0.263	0.006	-0.014	-0.077	0.031
110	GCP	288138.474	4963261.923	0.254	-0.032	-0.046	0.003	0.015
111	GCP	288111.369	4963212.164	0.341	0.025	0.024	-0.057	0.022
112	GCP	288053.239	4963185.298	0.296	-0.048	0.017	0.063	0.040
114	GCP	287965.053	4963227.307	0.337	0.007	0.005	-0.007	0.029
116	GCP	287900.31	4963209.77	0.85	0.007	0.005	-0.007	0.012
109	*CP*	*288151.504*	*4963280.626*	*0.248*	*0.025*	*0.055*	*0.084*	*0.018*
113	*CP*	*288004.584*	*4963207.456*	*0.403*	*0.026*	*0.000*	*-0.012*	*0.027*
115	*CP*	*287930.91*	*4963226.40*	*0.52*	*-0.012*	*-0.026*	*0.002*	*0.024*
Ground Control Points RMSE [m]					0.026	0.023	0.047	0.027
Control Points RMSE [m]					*0.022*	*0.035*	*0.049*	*0.023*

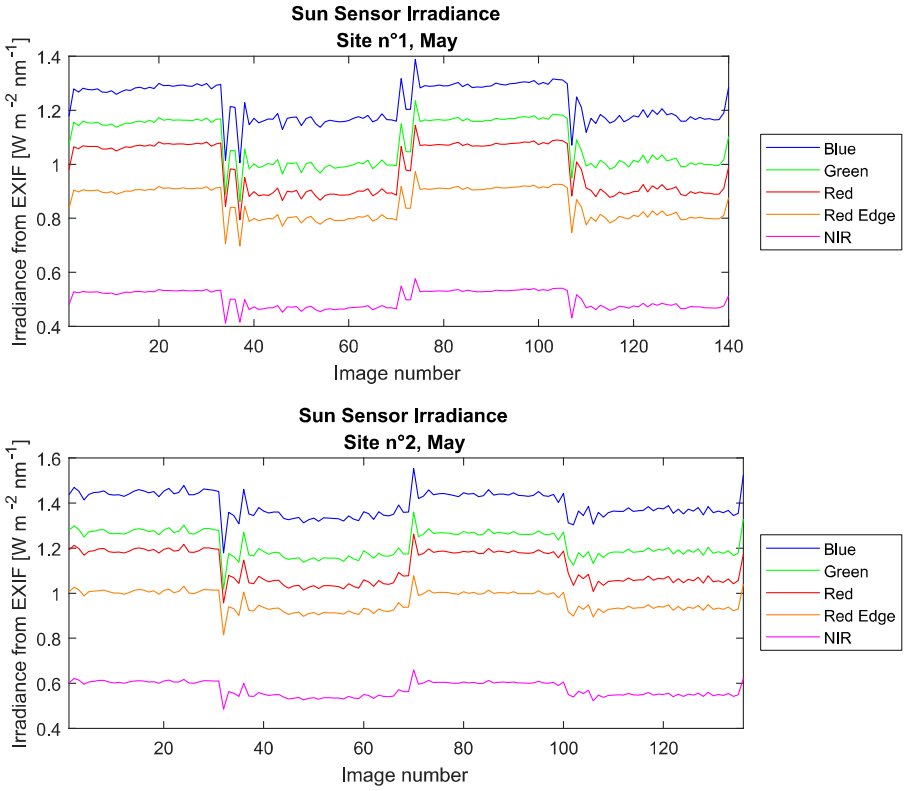

Figure 5.7 Spectral irradiance measured by the downwelling light sensor (DLS) of the MicaSense RedEdge-M camera during the flights in May. Notice how it is possible to detect the strips of the flight plans (the MATLAB script is reported in Appendix A.2).

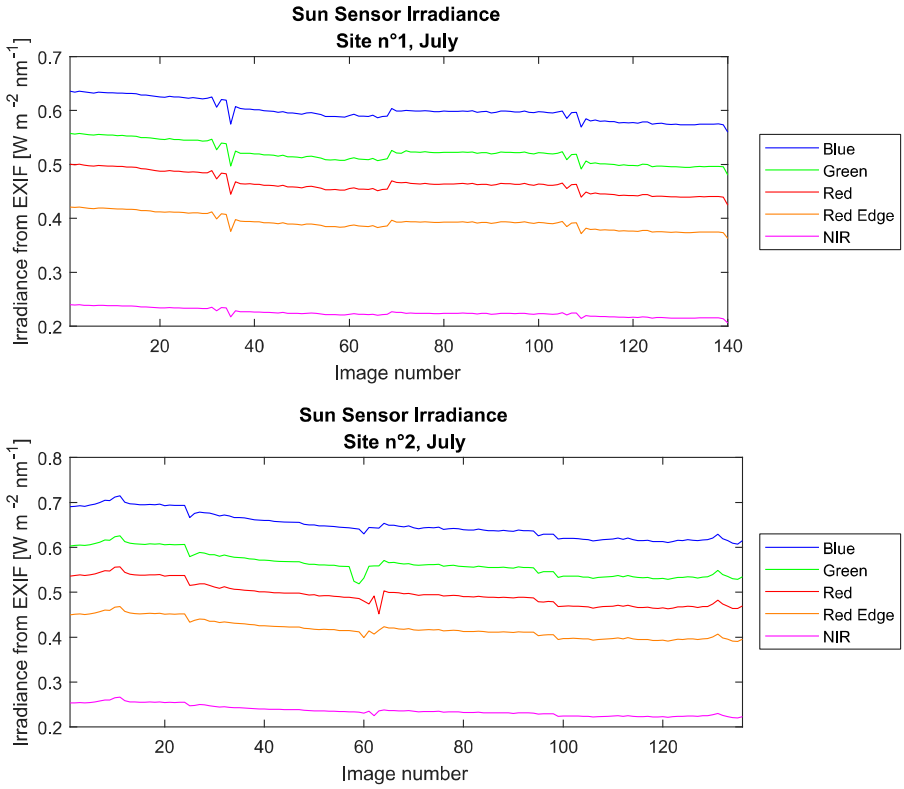

Figure 5.8 Spectral irradiance measured by the downwelling light sensor (DLS) of the MicaSense RedEdge-M camera during the flights in July.

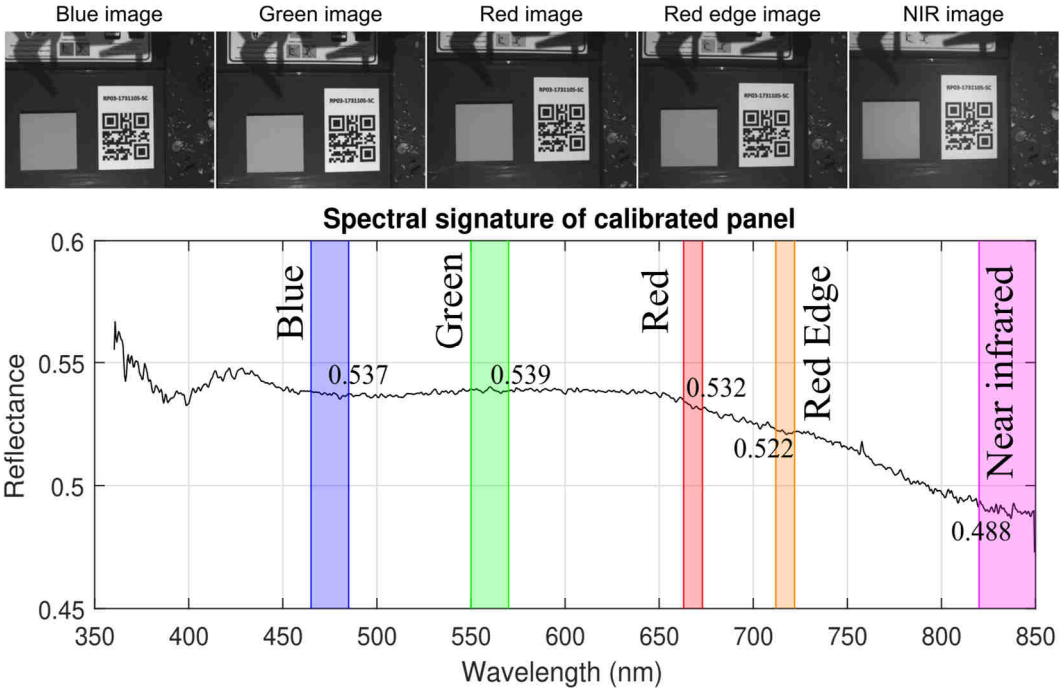

Figure 5.9 On the top: the images of the calibrated reflectance panel in the five spectral bands of the MicaSense RedEdge-M multispectral camera. On the bottom: the curve of the reflectance of the panel (computed from the data provided by MicaSense). The spectral bands detected by the camera have been overlapped to the curve. The numbers represent the mean reflectance value within those spectral bands.

On the contrary, Pix4D Mapper Pro provided the reflectance maps with values ranging from 0 to 1 in addition to the orthomosaics. The only exception was found when no correction was applied to the raw data: in this case the reflectance map looked like the orthomosaic with digital numbers within the range from 0 to 65535. Since the main difference between an orthomosaic and a reflectance map computed by this software is that no colour balancing is ever applied to a reflectance map in order to preserve the real reflectance of an object as it was recorded by the raw images [42], the products slightly differed in their pixel values. Only the best typology of final product retrievable by both the software was considered afterward.

Through the Agisoft Photoscan Professional software, a total of four orthomosaics per site and per survey execution were generated:

- the first without any kind of radiometric calibration;
- the second with a radiometric correction that the software self-computed by using the downwelling light sensor irradiance data;
- the third with a radiometric correction that the software self-computed by using the images of a calibrated reflectance panel taken just before and just after each flight;
- the last one by a combination of the data measured by the DLS and the information retrievable by the panel's images.

A similar workflow was followed in Pix4D Mapper Pro. In this case, the obtained products were respectively:

- an orthomosaic with no correction where pixel values consisted in digital numbers within the range from 0 to 65535;
- a radiance map that is computed by the software applying corrections for the vignetting effect, the ISO, the dark current and the exposure time (the so-called "camera only" option);
- a reflectance map computed by applying the "camera only" corrections and considering the DLS irradiance data in addition;
- a reflectance map computed by both applying the "camera only" corrections and considering the acquired image of the calibrated reflectance panel in order to compute reflectances;

- a reflectance map computed considering all of the available data, both those related to the vignetting effect, ISO and exposure time and those recorded by the DLS and retrievable by the panel image.

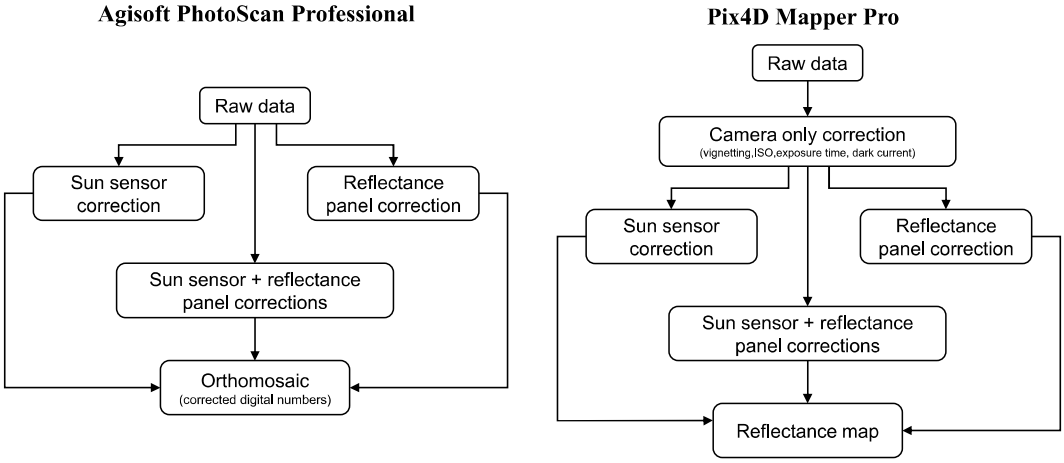

Figure 5.10 Radiometric calibration options in Agisoft Photoscan Professional (on the left) and Pix4D Mapper Pro (on the right) to correct the raw digital numbers sensed by the multispectral camera.

All of the products were also saved with their georeferencing information in order to make any further analysis on any portion of them later.

5.4 Data analysis

In order to evaluate the effectiveness in the distinction between the different categories of ground cover (including the seabed) varying the radiometric correction procedure, four regions were defined and analysed. Their delimiting polygons were created as shapefiles in QGis and further used as masks for extracting the data in those specific areas from the orthomosaics and the reflectance maps.

The following typology of homogeneous cover were specified for both the surveyed sites:

- *vegetation*, including the many different species that lie both on the front dunes (mainly filiform) and on the mid dunes (shrubs and even small trees);
- *sand*, that included an extent of the beach characterized by a uniform texture of a dry sand;

- *deep water*, with a depth of about 1÷1.5 metres that was much deeper than the shallow water around the shoreline;
- *submerged seaweed*, that represented a zone where the seaweeds were growing and were constantly beneath the water. This region included also pixels of shallow water.

Figure 5.11 and Figure 5.12 show the four regions on the orthomosaics generated by the processing of the images respectively acquired on the survey conducted on May 25th, 2018 and on July 3rd, 2018. The data extraction consisted in using each polygon as a mask for the orthomosaics generated with and without the application of the radiometric calibration procedures. A single multiband image was then assembled for each region.

The main difference was that Pix4D Mapper Pro extracted data had a fifth band, since this software has the "camera only" option in addition to the Agisoft PhotoScan Professional processing options. Consequently, for each multiband region extraction, the bands were as follows:

- Band 1: no correction applied to the raw data;
- Band 2:
  - Agisoft Photoscan Professional: calibration performed by using the data recorded by the downwelling light sensor;
  - Pix4D Mapper Pro: "camera only" correction, that considers for the vignetting effects, the ISO, the dark current and the exposure time;
- Band 3:
  - Agisoft Photoscan Professional: calibration performed by using the acquired images of the calibrated reflectance panel and introducing its calibration parameters;
  - Pix4D Mapper Pro: calibration performed by using the data recorded by the downwelling light sensor;

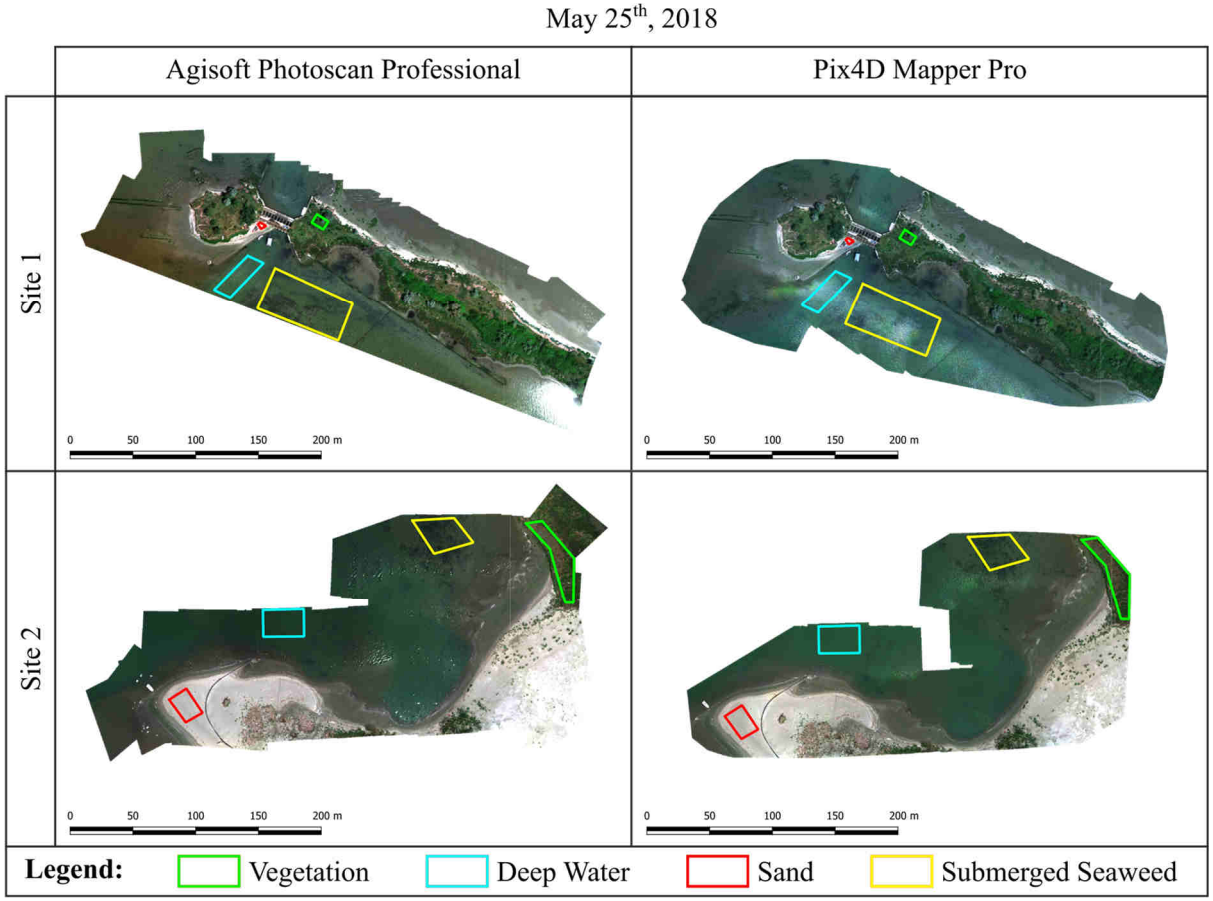

Figure 5.11 Orthomosaics for the surveys conducted on May 25th, 2018. The polygons identify the four areas analysed for the evaluation of the effectiveness of radiometric calibration procedures.

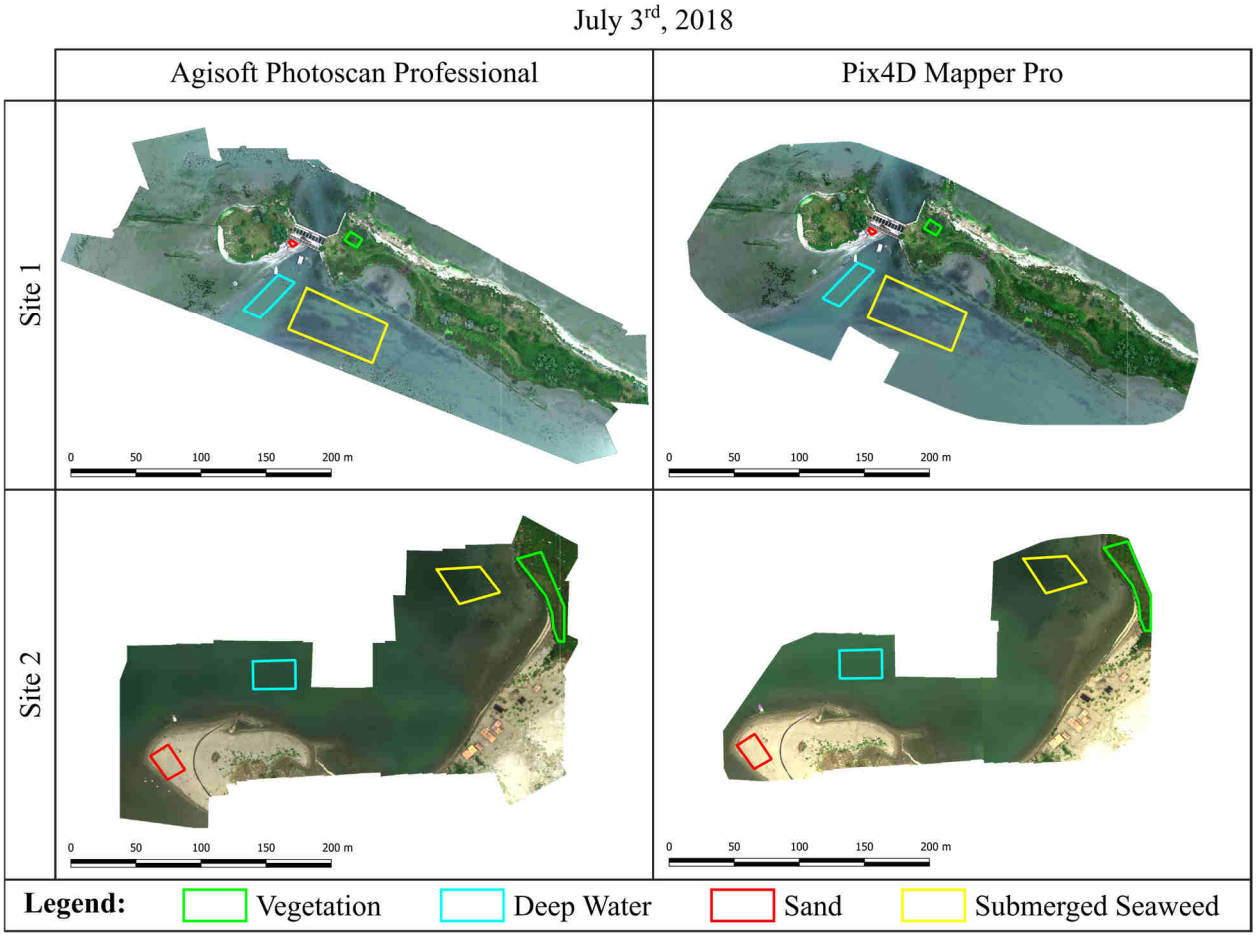

Figure 5.12 Orthomosaics for the surveys conducted on July 3rd, 2018. The polygons identify the four areas analysed for the evaluation of the effectiveness of radiometric calibration procedures.

- Band 4:
    - Agisoft Photoscan Professional: calibration performed by using both the DLS recorded data from the EXIF of each captured image and the acquired images of the calibrated reflectance panel introducing its calibration parameters;
    - Pix4D Mapper Pro: calibration performed by using the acquired images of the calibrated reflectance panel and introducing its calibration parameters;
- Band 5: calibration performed by using both the DLS recorded data from the EXIF of each captured image and the acquired images of the calibrated reflectance panel introducing its calibration parameters. This fifth band was present only for the Pix4D processed data.

The resulting multiband images, where the band was thus solely related to the kind of applied correction, were generated for both the Near Infrared (NIR) and the Red data of the MicaSense RedEdge M camera, as well as for the NDVI index computed starting from those bands.

A frequency analysis was performed in order to reconstruct the histograms of the distribution of the values of NIR, Red and NDVI varying the radiometric calibration approach that was adopted.

It is worth noting again that the pixel values for Agisoft Photoscan Professional processed data were within the range from 0 to 65535, since no real reflectance map was ever computed by this software. On the contrary, the Pix4D Mapper Pro was able to compute reflectance maps with values ranging from 0 to 1, in addition to the simple orthomosaics. However, when no calibration to the raw data was applied, the reflectance map actually contained digital numbers with a 16-bit resolution. In this latter case they were normalized in order to make a consistent comparison with the corresponding pixels of the other reflectance maps.

All the analysis were conducted assuming a class width of 256 for the Agisoft Photoscan Professional products and a class width of 0.005 for Pix4D Mapper Pro. The count of each class has been normalized dividing by the overall pixel count inside each polygon. Therefore, the values on the vertical axis represent the fraction

of pixel for each class. In this way it was possible to compare the distributions also when the count of the pixel in each region was fairly different.

Figures from Figure 5.14 to Figure 5.17 show the histograms for the survey conducted during the first survey on May 25th, 2018.

We can notice that:

- the raw data was always characterized by higher values with respect to the calibrated data. This is because at the time of the image capture the camera automatically applies the most suitable settings, such as the ISO sensitivity and the exposure time, in order to balance the brightness of the overall scene.
- whenever a calibration approach was adopted, each category of cover tended to be more compact and thus less dispersed in terms of digital numbers in the NIR and Red bands. The histograms appear much narrower, especially looking at the use of the reflectance panel in Agisoft Photoscan Professional (Figure 5.14).
- the use of the calibrated reflectance panel was the main responsible for the final reflectance values also in the case of its combined use with the DLS data. This fact confirms that the real (and more reliable) reflectance value is computed only if the images of a calibrated panel are considered. In this case, the DLS could help to assess for a change in the irradiance between the time of the panel's image acquisition and the time of the flight, thus operating in a differential way. Since any panel's image should be taken immediately prior to flight, this can be the case of transient clouds.
- The deep water and submerged seaweed regions generally presented a significant overlap in terms of histograms, also in the case when both DLS and reflectance panel corrections are applied. This could be explained considering that the seaweed region contains a significant amount of water pixels and thus a fraction of this region is substantially very close to the deep water one. However, the extent of the seaweed polygon should necessary include non-algal pixels,

especially if the same polygon had to be detected again by a survey repetition for a monitoring-over-time purpose.

Furthermore, analysing the NDVI histograms in Figure 5.14 (the MATLAB script is reported in A.3), the application of corrections to both the raw near infrared and raw red data allows to distinguish the sand from the deep water and the submerged seaweed. In fact, the NDVI histogram for the sand cover computed on the basis of the raw data overlaps to the histograms of the other two regions mentioned above. However, after the application of any calibration approach, the sand moves toward higher NDVI values and separates from those regions. Looking at the Figure 5.16, in which the analysis of the same imagery dataset just mentioned is presented and Pix4D Mapper Pro was used for the processing instead of Agisoft Photoscan Professional, the histogram separation already took place at the "camera only" level of data correction. This highlights the importance of considering the actual settings like the ISO and the exposure time when combining images, even the multispectral ones, or computing indices, especially whenever the spectral information is collected by sensors set up to create a single camera and they may work regardless each other.

Figures from Figure 5.18 to Figure 5.21 show the histograms for the survey conducted during the repetition on July 3rd, 2018. During the 39 days between the surveys, the seaweed grew up and began to pour along the shoreline (Figure 5.13). At the same time, the extent of the submerged seaweed increased significantly.

Figure 5.13 Seaweed along the shoreline on July.

The analysis of the distribution of the digital numbers and the reflectance values was thus performed on the orthomosaics and reflectance maps generated for this survey repetition as well.

All of the considerations made for the survey carried out in May were found to be still applicable to the one performed in July. The histograms confirm once again that the application of any kind of radiometric calibration, even the simple "camera only" option in Pix4D Mapper Pro, allows to distinguish the sand region from the submerged seaweed one. However, the "camera only" provides unreliable low values for the NDVI index, because no real reflectance is even computed using neither a DLS-based irradiance measurement nor the image of a known reflectance panel.

Conversely, the deep water and the submerged seaweed histograms of the NDVI index in Figure 5.18, that appeared well separated using the raw data, present a high overlap after the application of the DLS-based correction, the reflectance panel correction or even both them. Since a seawater absorption effect applies also to the submerged seaweed pixels as it happens for those belonging to the deep water region (due to the water column from the seabed to the tide level) and there were still water-only pixels inside the seaweed class, it is acceptable that these regions exhibit a similar distribution and their NDVI histograms partially overlap.

Comparing the distribution of the corresponding regions assuming the processing software as the unique variable, thus without changing neither the survey repetition date and the site nor the typology of applied radiometric correction, no significant differences were found. In fact, even though the shape of the distributions evaluated by the means of the histograms sometimes slightly differed, the range of values was substantially similar, especially for the computed NDVI and the differences in terms of bias between the distribution were negligible. For these reasons and to reduce the number of variables (i.e. the processing software) in the further seaweed extent detection, the orthomosaics generated by Agisoft PhotoScan Professional were used.

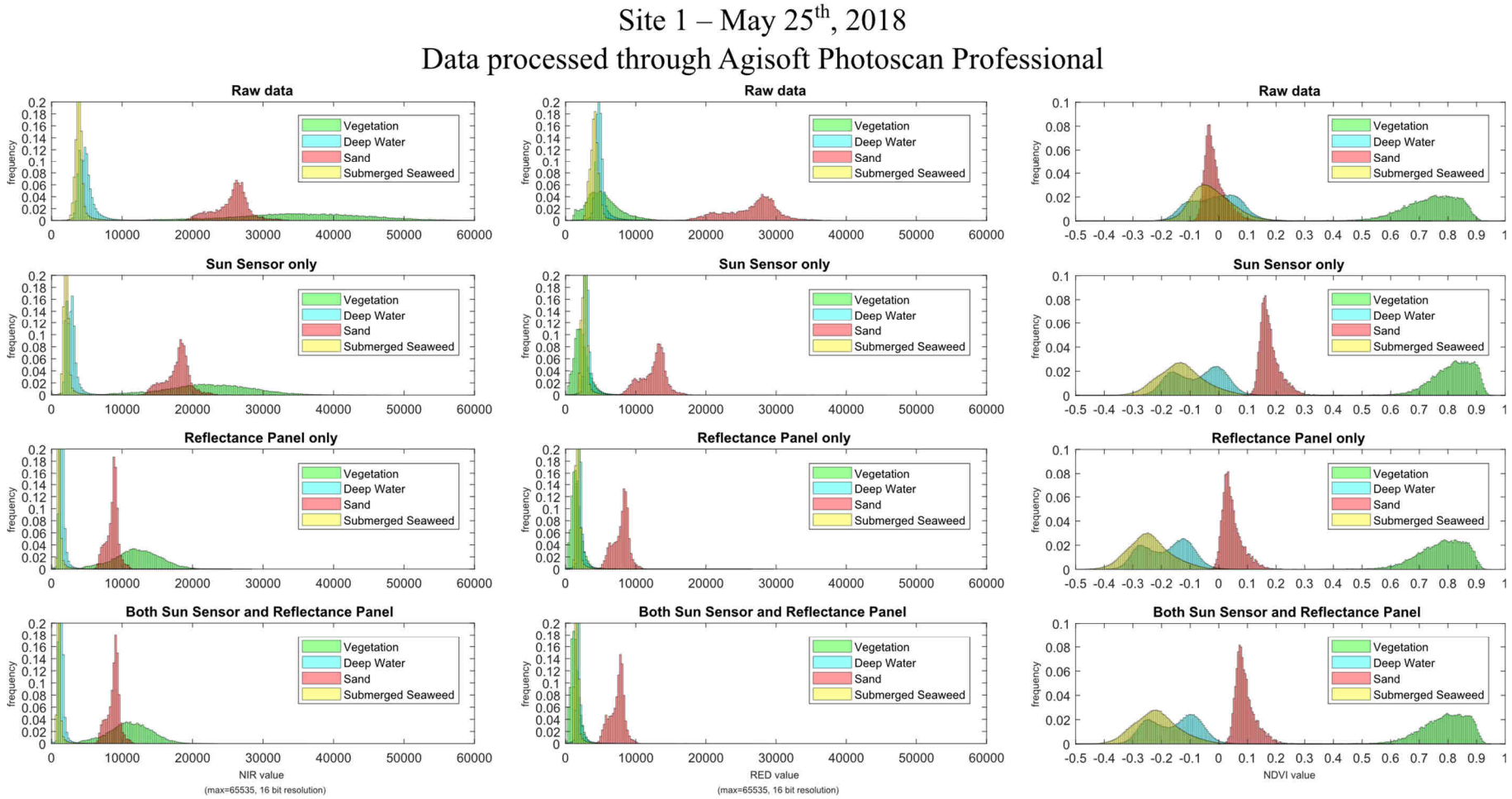

Figure 5.14 Histograms for the site n°1, survey performed on May 25th, 2018. Data were processed through Agisoft Photoscan Professional.

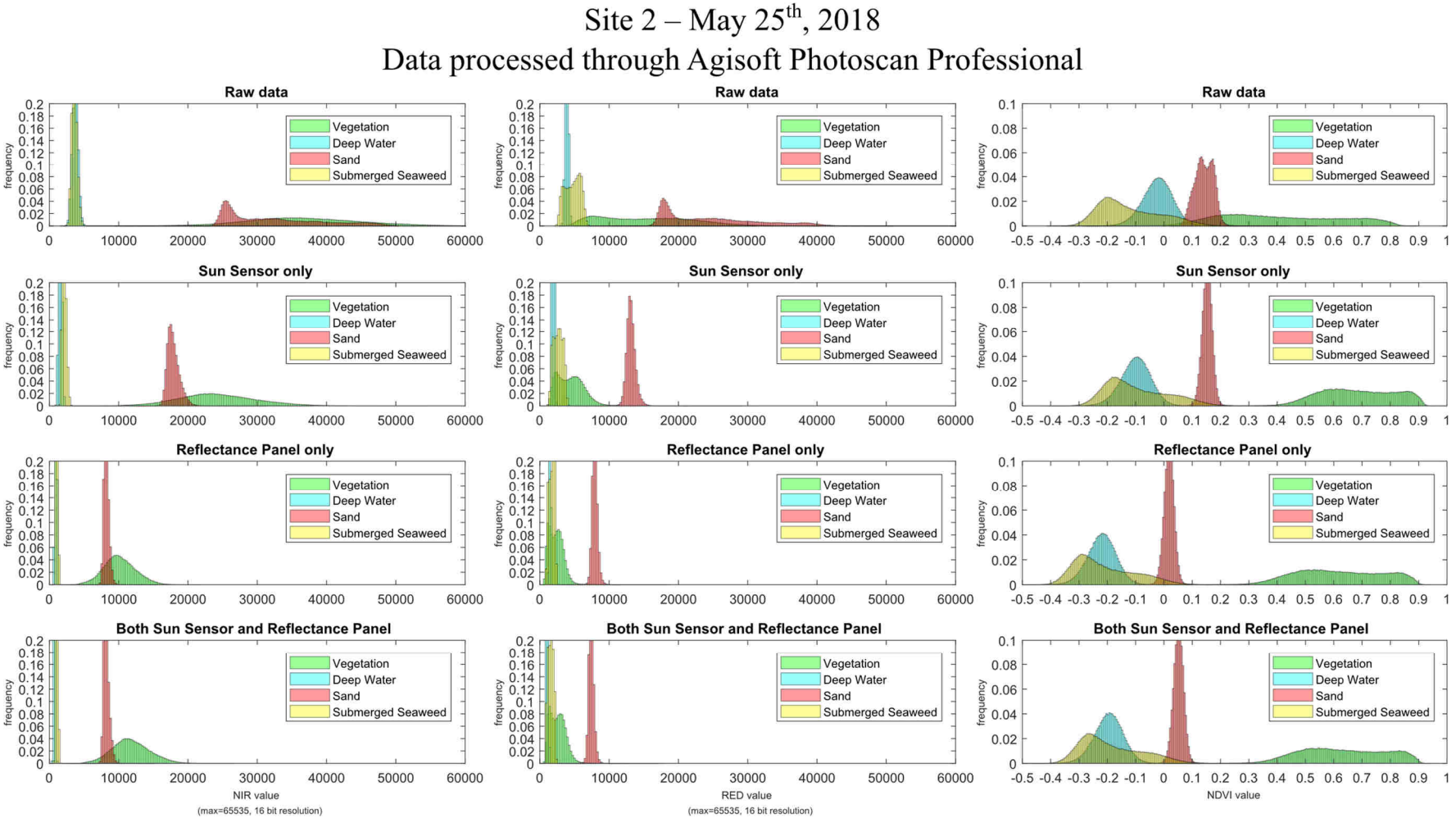

Figure 5.15 Histograms for the site n°2, survey performed on May 25th, 2018. Data were processed through Agisoft Photoscan Professional.

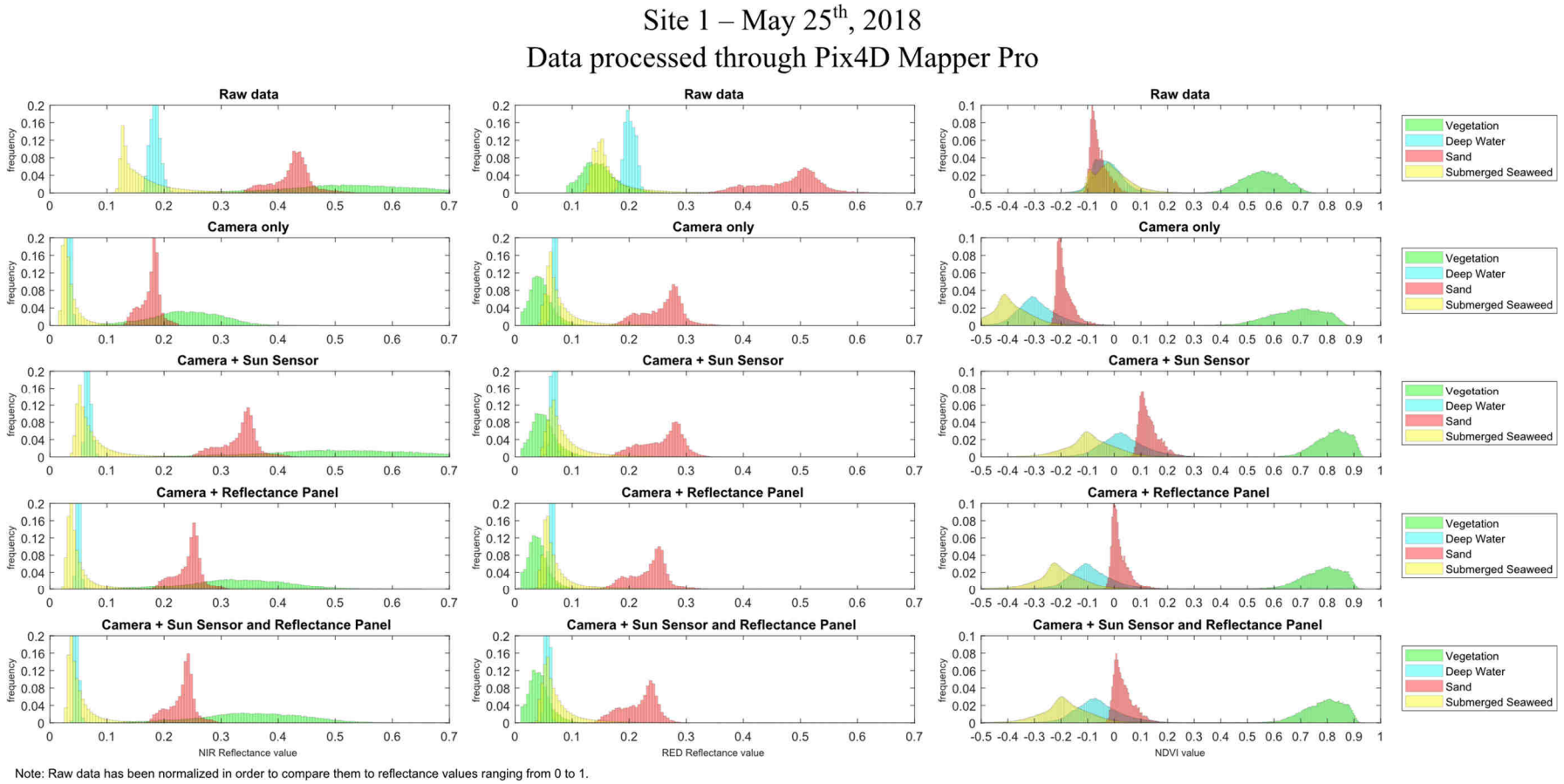

Figure 5.16 Histograms for the site n°1, survey performed on May 25th, 2018. Data were processed through Pix4D Mapper Pro.

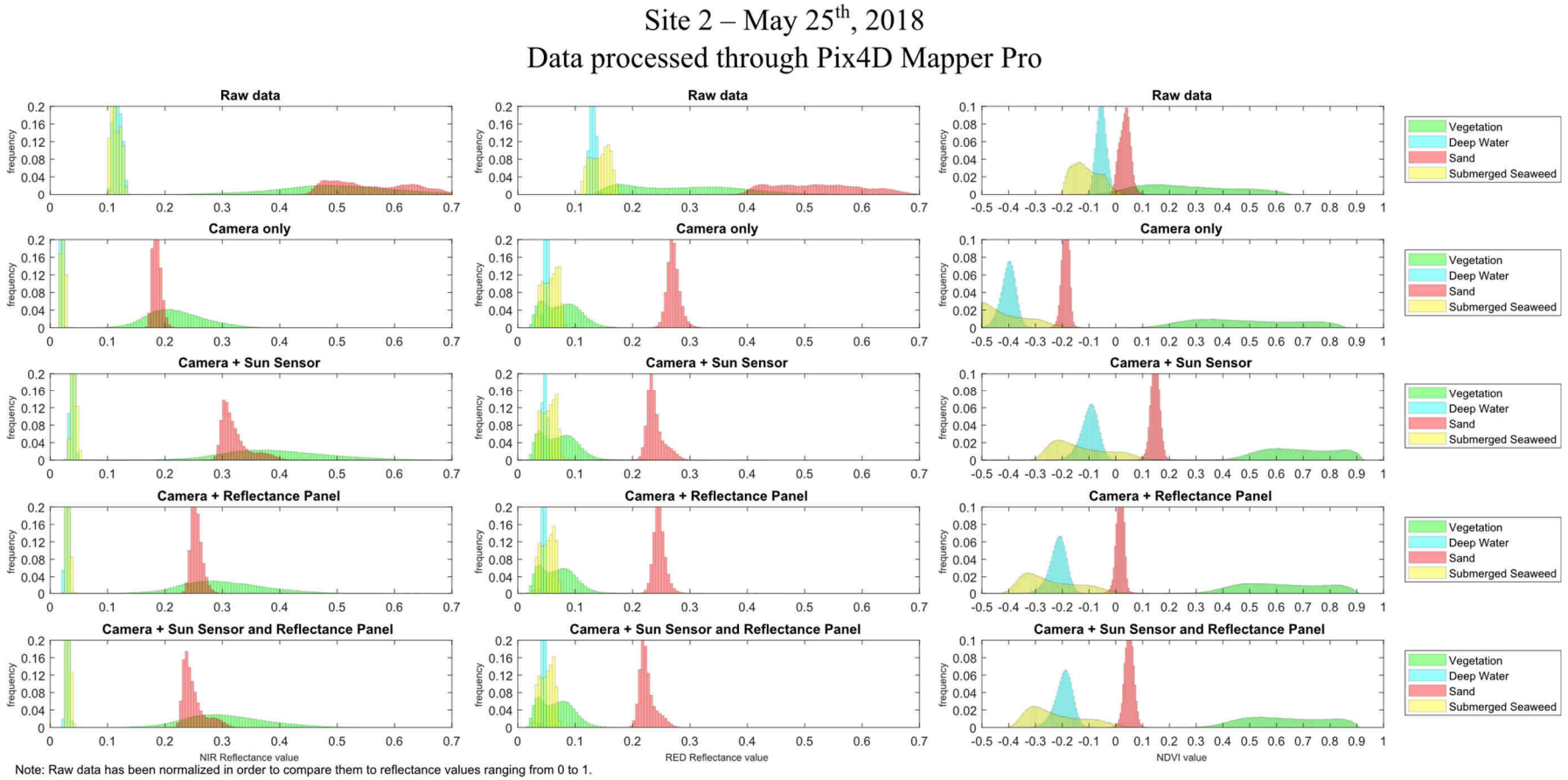

Figure 5.17 Histograms for the site n°2, survey performed on May 25th, 2018. Data were processed through Pix4D Mapper Pro.

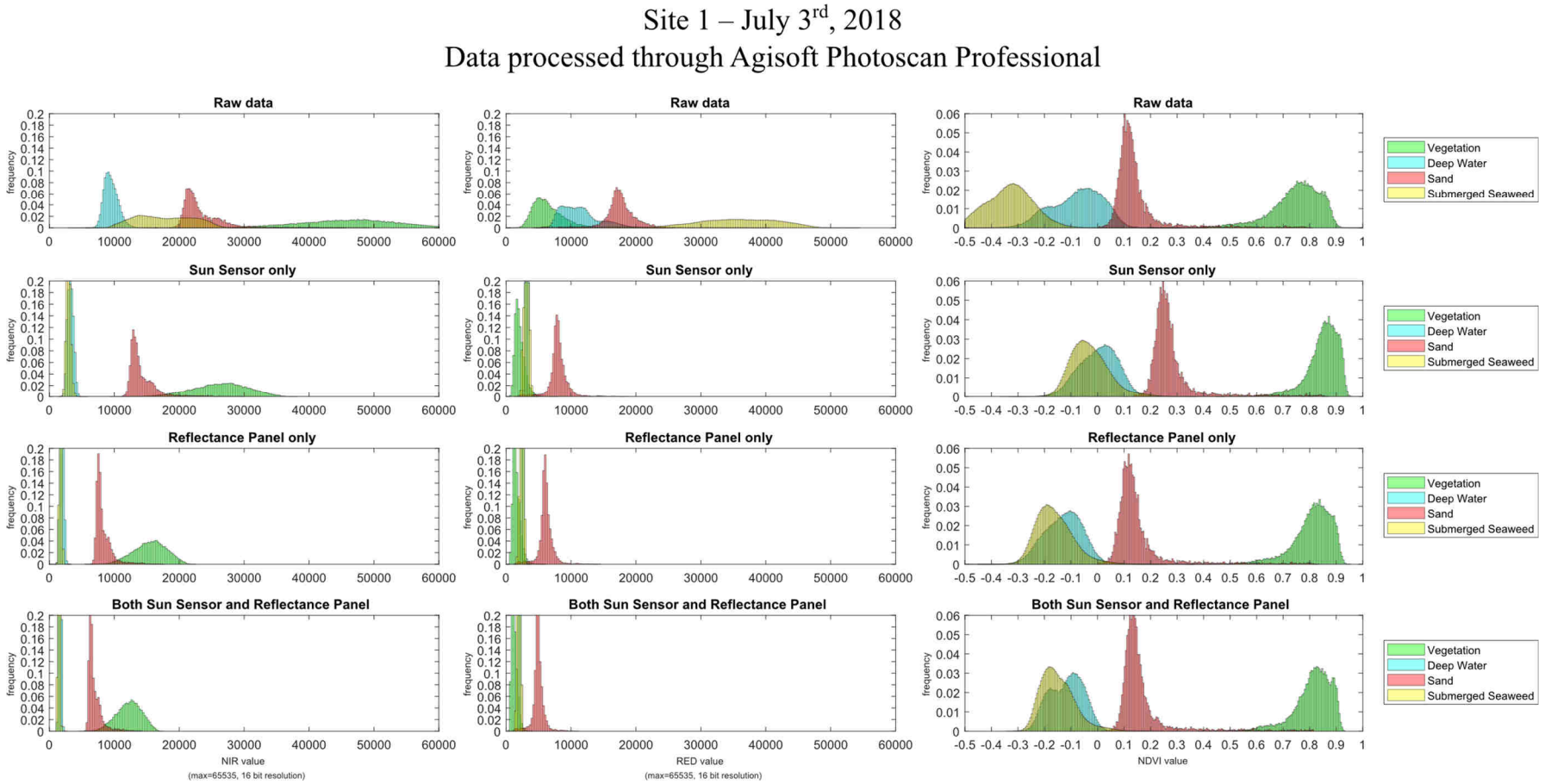

Figure 5.18 Histograms for the site n°1, survey performed on July 3rd, 2018. Data were processed through Agisoft Photoscan Professional.

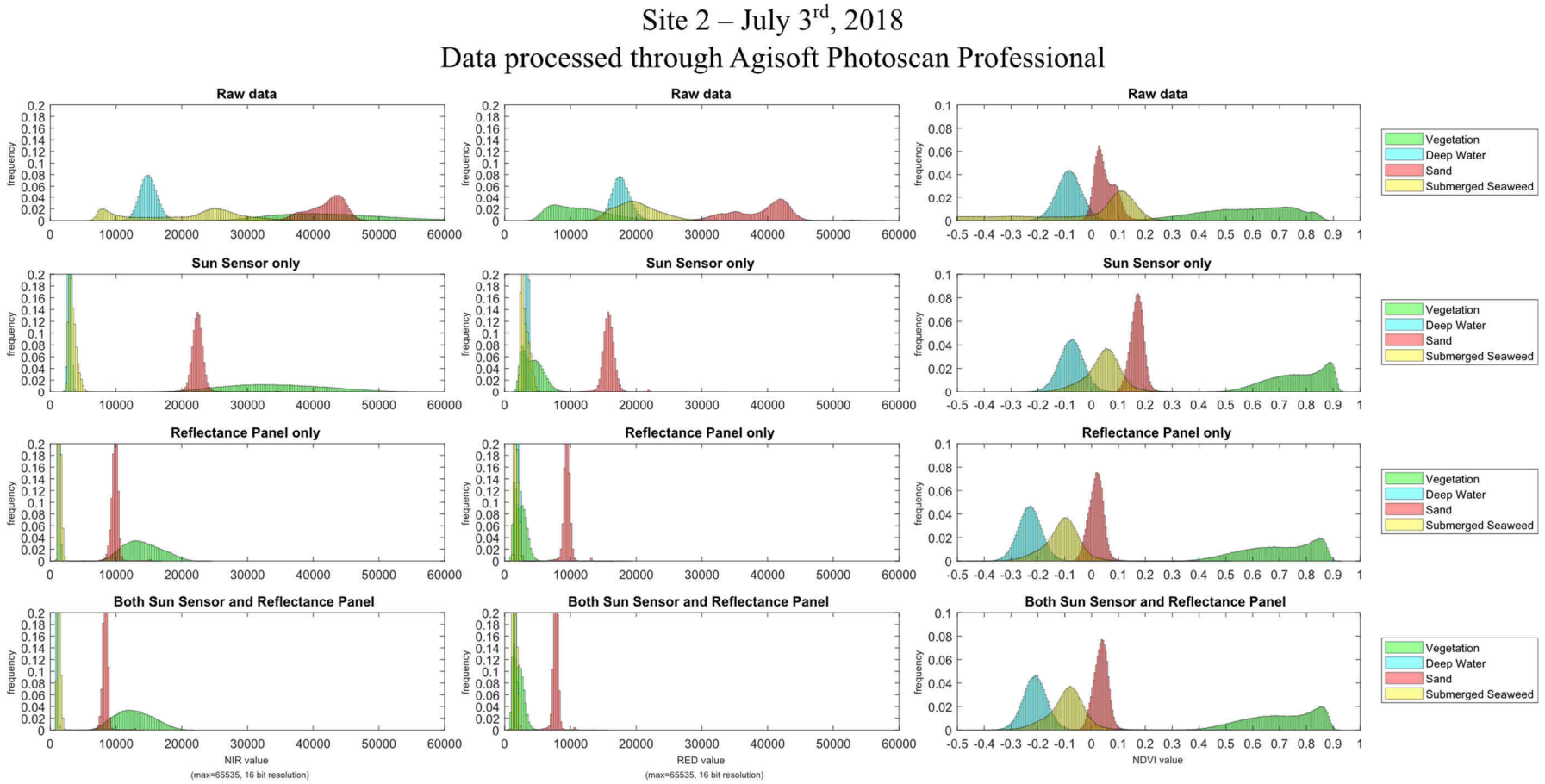

Figure 5.19 Histograms for the site n°2, survey performed on July 3rd, 2018. Data were processed through Agisoft Photoscan Professional.

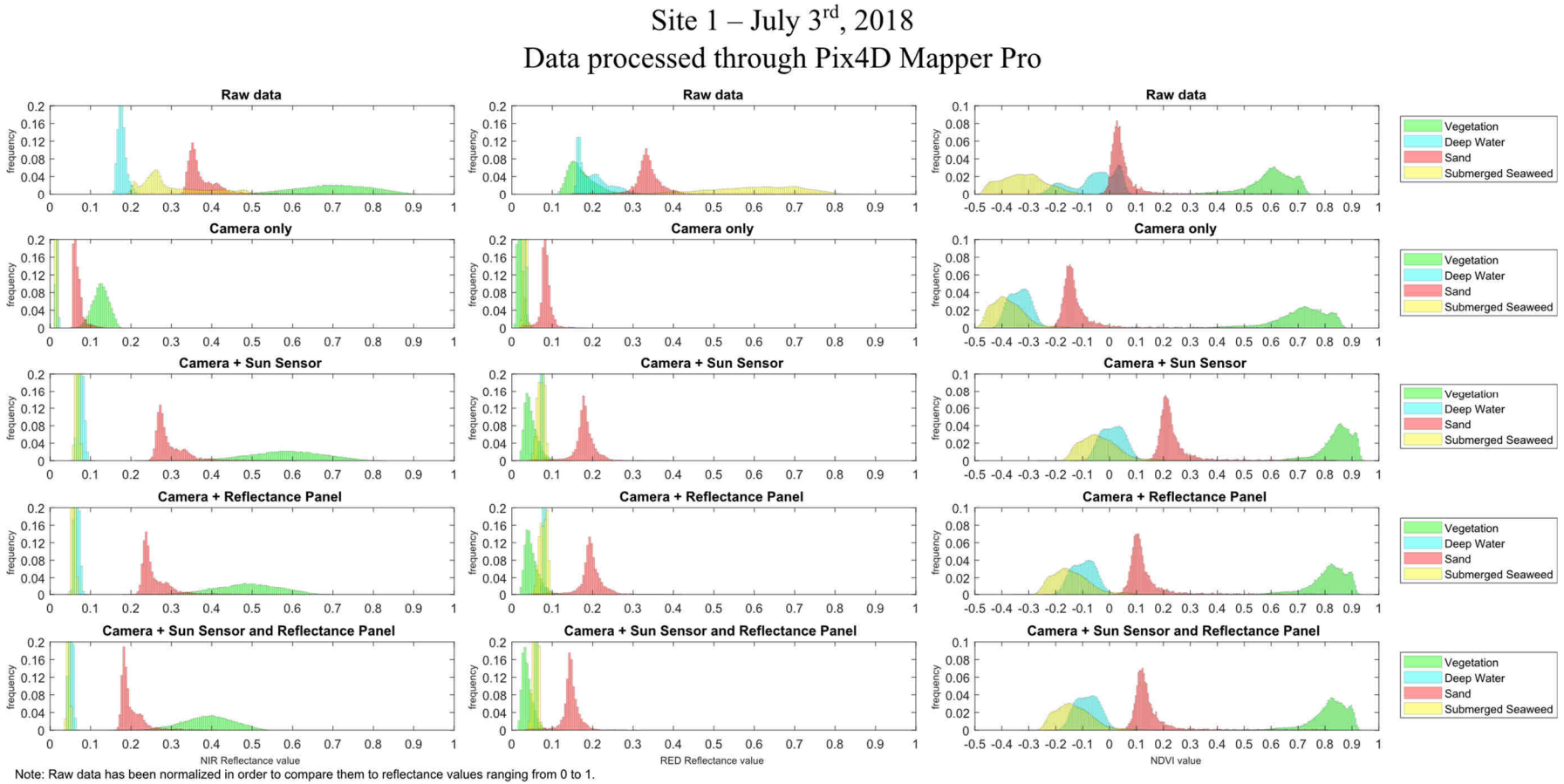

Figure 5.20 Histograms for the site n°1, survey performed on July 3rd, 2018. Data were processed through Pix4D Mapper Pro.

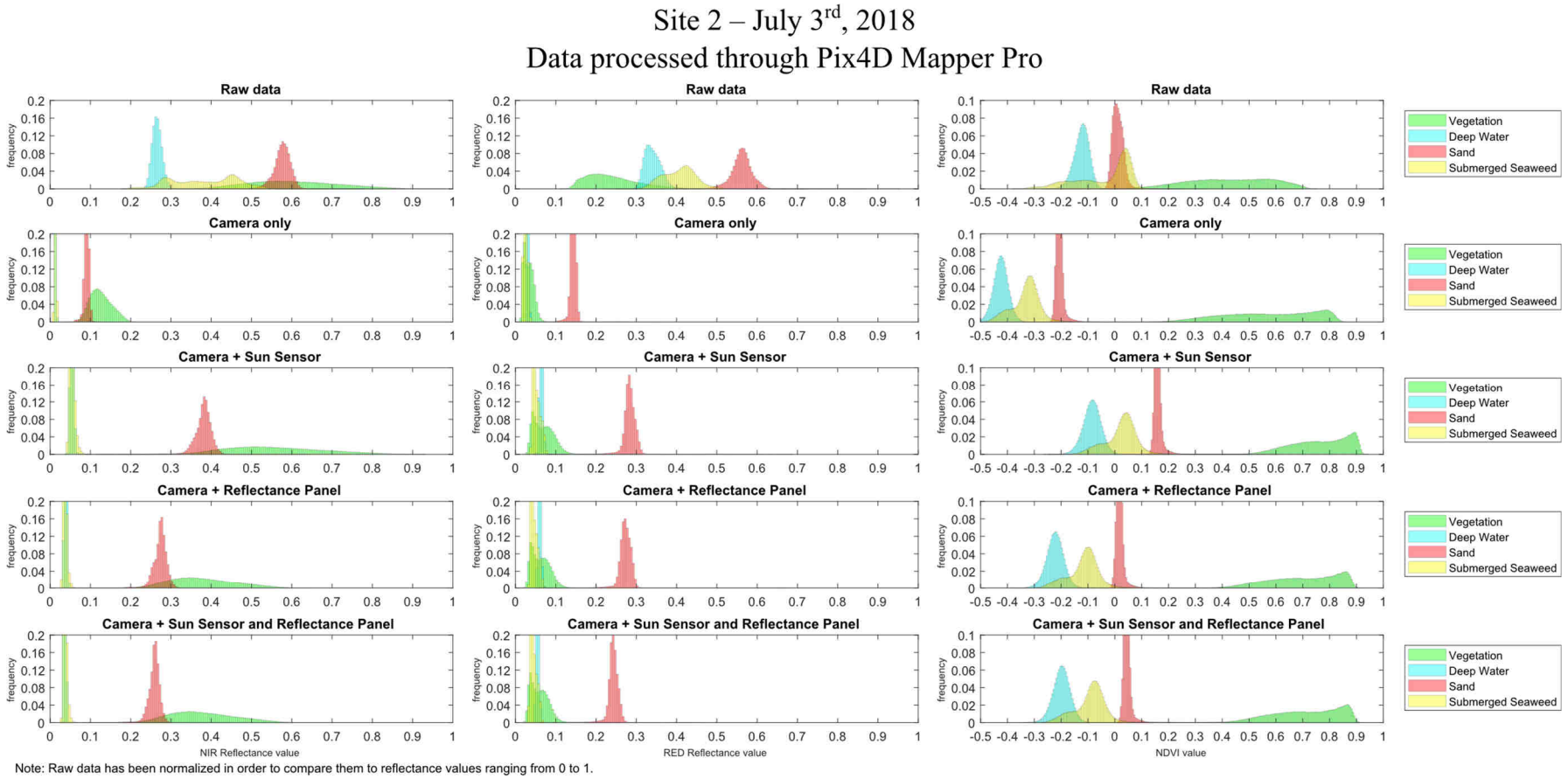

Figure 5.21 Histograms for the site n°2, survey performed on July 3rd, 2018. Data were processed through Pix4D Mapper Pro.

5.5 Seaweed expansion detection

One of the goals of this experimentation was to detect the algal status in the shallow water along the shoreline in order to monitor the seaweed growth and prevent the occurrence of harmful water conditions characterized by a very low oxygen content.

Once that the orthomosaics in Agisoft Photoscan Professional and the corresponding reflectance maps in Pix4D Mapper Pro were generated by considering both the DLS recorded data and the calibrated reflectance panel images, the orthomosaics of the first software were used to evaluate the growth of the submerged seaweed. As previously stated, this choice was made in order to reduce the number of the variable in the following comparisons and the most important factor lies in the fact that for both the software all the four options (no correction, only DLS, only panel, both the previous) were always considered to generate the final products.

Two different approach were therefore used for the purpose of quantifying the seaweed extent. The first one consisted in computing the NDVI index and then analysing the spatial distribution of its values inside the submerged seaweed region.

Even though this is one of the simplest approaches, the NDVI index represents itself a sort of classification that enables to distinguish between vegetated and non-vegetated areas, hence the analysis of its distribution and variation over time on a region characterized by the growth of submerged seaweed might theoretically lead to a reliable estimation.

This kind of quantification was conducted by comparing the flight performed in May and July on the site n°1 and it is shown in Figure 5.22. The figure reports also the distribution of both the near infrared and red values after the application of the radiometric correction accounting for both panel's and DLS data as well as the distribution of the NDVI. It is worth noting that both the mean values in the considered wavelengths increased within this region from May to July. This behaviour is due to a real change in the spectral response of the seabed, since the most performant radiometric calibration was applied to the raw digital numbers to obtain these final values and no significant issue of sunlight reflection by the sea

surface was recognized here. However, the near infrared increased its mean digital number value from 1069 in May to 1450 in July, with an absolute mean increase of 381 and a relative increase of about 36%, while the red rose from 1654 to 1965, with an absolute mean increase equal to 311 and a relative one of 19%. This implies that the NDVI index also increased from May to July. Its values remain generally negative inside the submerged seaweed region, due to the presence of a sea water absorptance that attenuates the response of the seaweed in the near infrared wavelengths.

The algal species within this region in site n°1 were *Ulva* and *Enteromorpha* and both are green seaweed. The mean NDVI in May was -0.21 and rose up to -0.15 in July. The map of the NDVI values on the submerged seaweed region (Figure 5.22, on the right) clearly shows that the higher NDVI values was detected in the seaweed pixels. The thermal-like colormap for the visualization in that figure serves to enhance the detection of the seaweed within this analysed region.

In terms of covered surface it is therefore possible to quantify the growth of the submerged seaweed by spatially monitoring the NDVI distribution. In order to this, a threshold value should be specified. This value has to be assumed as the most significant for the change detection in the algal coverage. However, no automatic procedure was used for this purpose and consequently the threshold was evaluated by changing the value and assessing the corresponding change in the detection of both surveys (May and July), also using the RGB visualization for reference. This represents an unavoidable element of subjectivity related to the adoption of one of the simplest approaches, as it was for the NDVI-based estimation. Finally, the threshold was set to -0.16: values greater than this latter were classified as submerged seaweed, while the others represented water pixels (Figure 5.23). The results of this NDVI-based classification are shown in Figure 5.24.

The area rose from $498.2\ m^2$ in May to $1179.6\ m^2$ in July, with an increase of about $681.4\ m^2$ in 39 days. In terms of percentage, the increase was $+137\%$ within this region, denotated as “submerged seaweed” in both Figure 5.11 and Figure 5.12. The validation of the classification was performed on the basis of what it was visible on the RGB orthomosaic (thanks to the shallow and fairly clear seawater) and proved to be both consistent and reliable within this region.

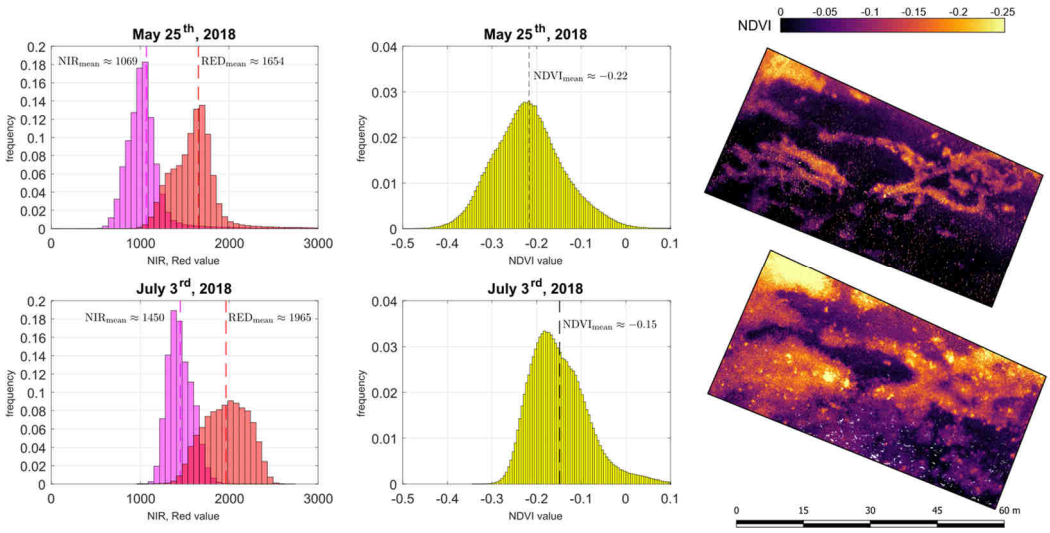

Figure 5.22 NDVI analysis on the submerged seaweed polygon (site n°1) for the surveys conducted in May (on the top) and July (on the bottom). The zoom on the histograms (respectively the same reported in Figure 5.14 and Figure 5.18) shows that the NDVI distribution within this region significantly increased. The thermal colormap for the NDVI visualization on the right serves to enhance the seaweed detection.

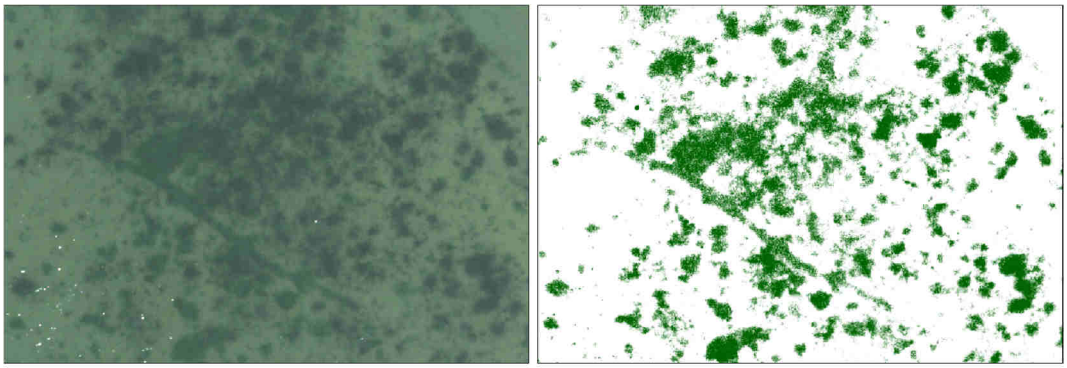

Figure 5.23 Detection of the seaweed in preliminary tests with an NDVI threshold of -0.16. On the left: RGB visualization. On the right: pixels exceeding the threshold highlighted in green.

Therefore, the NDVI can be successfully used to conduct a monitoring over time on a specific and spatially limited region, especially in a shallow water environment without significant water depth variations and with no turbidity issues. The application of the radiometric calibration based on both the DLS data and the calibrated reflectance panel images ensures to compute NDVI values from absolute near infrared and red data, allowing an actual comparison over time. In spite of this advantage, the assumption of the threshold value to be used for distinguish between

algal pixels and water pixels is still subjective and may potentially lead to a non-accurate estimation of the seaweed growth.

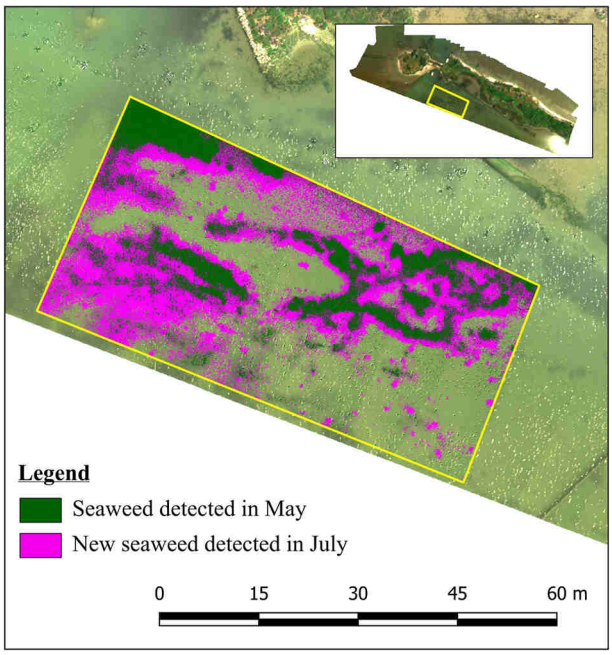

Figure 5.24 Quantification of the submerged seaweed extent through the NDVI, limited to the corresponding region selected in site n°1.

The second approach that was tested in order to quantify the seaweed extent consisted in performing a supervised classification in ENVI software. Since the NDVI proved to be effective in detecting the seaweed in the previous approach, a sixth band with the computed NDVI was considered in addition to the five spectral bands of the MicaSense RedEdge-M camera.

The most common supervised classification method that is used in the field of the remote sensing data analysis is represented by the *maximum likelihood classification*. Therefore, this method was used to perform the task.

Regions of interest (ROIs) have been created for each type of ground cover on the orthomosaics in order to use the maximum likelihood classifier. Different subsets of pixel at various location on the orthomosaic have been specified for a more homogeneous sampling of the training data. The number of these regions varied according to the effective covers that were found. In any case, it was always within the range from 8 to 13, including all the vegetation on the beach, the wet and dry sand and the emerged seaweed if present. The threshold was singularly evaluated for each class and varied from 0.3 to 0.7.

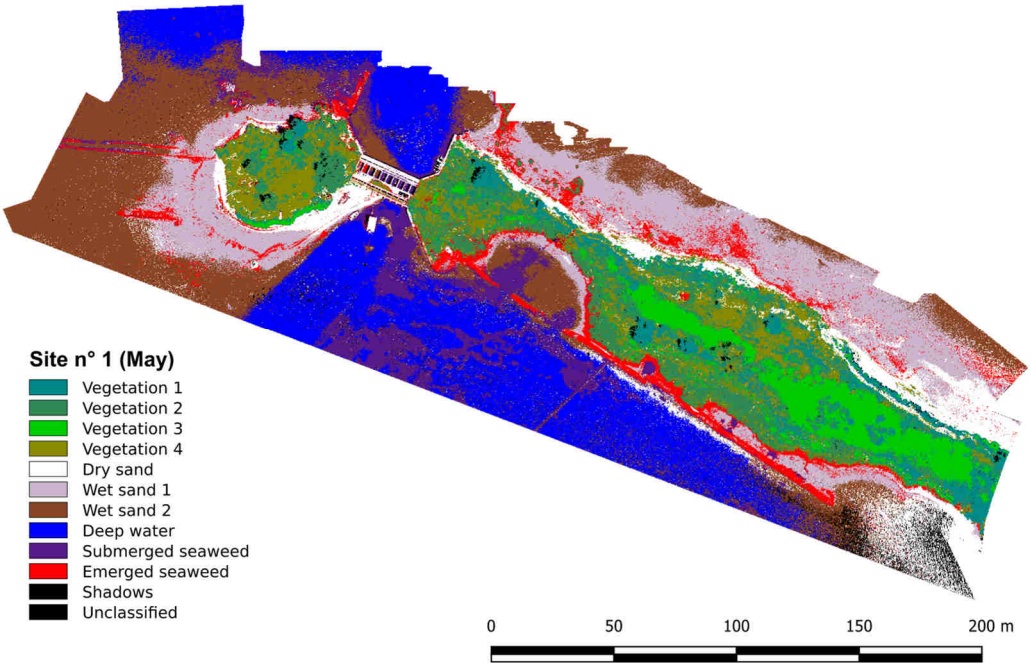

Figure 5.25 Supervised classification results with the maximum likelihood classifier using the orthomosaics with radiometrically corrected values and an additional sixth band consisting in the NDVI. The overall accuracy computed with ROIs truth was 97%.

Once that the supervised classification was performed, a first validation was conducted by specifying a further set of ROIs that were used for a check instead of a training, the so-called *ROI truth*. The computation of the overall accuracy (OA) in the form of

$$OA = \frac{\text{correctly classified pixels}}{\text{all the ROIs truth pixels}} \qquad \text{(Eq 4.1)}$$

where the pixels used for this computation belong to the ROIs truth, gives a parameter to assess the quality of the classification. The value tends to be one in the case of a "perfect" performance of the classifying algorithm. For the classification conducted on the radiometrically corrected orthomosaics the value of the overall accuracy was very close to 1 and always higher than 0.95.

The approach based on the supervised classification was thus tested using the same polygon delimiting the submerged seaweed region as a mask. Differently to what was made for the NDVI-based approach, no threshold has been specified since the maximum likelihood method already provided the seaweed classified pixels for both the survey repetition in May and July. The comparison of these amounts allows the detection of the occurred growth. In particular, the estimated submerged

seaweed extent was $809.2\ m^2$ in May and $1746.1\ m^2$ in July with a corresponding increase of $936.9\ m^2$. In terms of percentage, the seaweed rose in the measure of the $+116\%$.

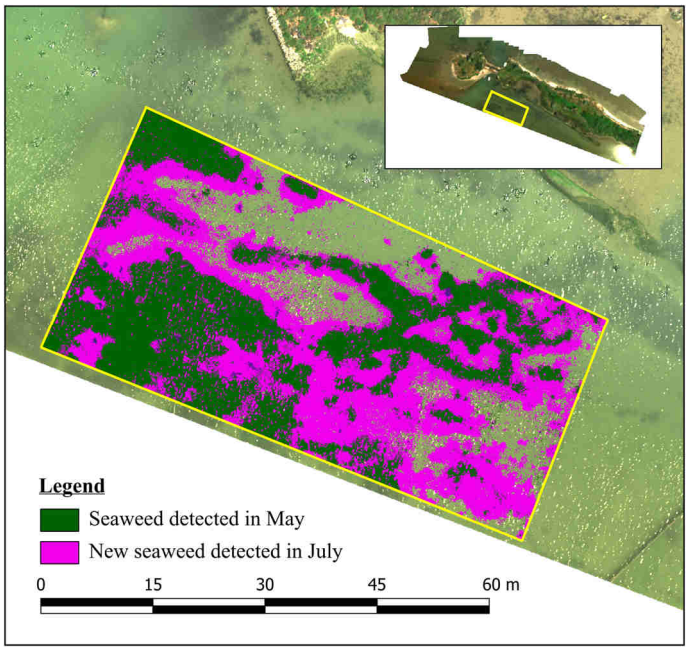

Figure 5.26 Quantification of the submerged seaweed extent through the maximum likelihood classifier, limited to the corresponding region selected in site n°1.

The increase evaluated in terms of percentage is quite similar for both the approaches tested (NDVI and supervised classification) and indicates that the submerged seaweed extent doubled in 39 days. However, the detection is significantly different in terms of seaweed surface estimation comparing the two methods. Considering that the background image in Figure 5.24 represents the survey in May, it seems that the NDVI-based approach might underestimate the actual amount. A possible solution might be to change the threshold value that was adopted, even if it was already adopted in order to make an estimation with a low noise. In any case, this confirms both the limits in using the NDVI for this type of estimation and the subjectivity due to the threshold value to be assumed.

After the study conducted within a limited region in site n°1 for estimating the submerged seaweed, both the methods were attempted to be used on wider zones, both in site né1 and in site n°2. The NDVI-based approach immediately showed its limits whenever the water depth varies. In fact, due to the different water absorption related to the seawater level, no threshold value was found to perform

an accurate detection of the seaweed. Therefore, only the supervised classification was further used to estimate the seaweed extent on the wider regions. Figure 5.27 shows the estimation for May and July carried out by using the results of the classification already obtained previously.

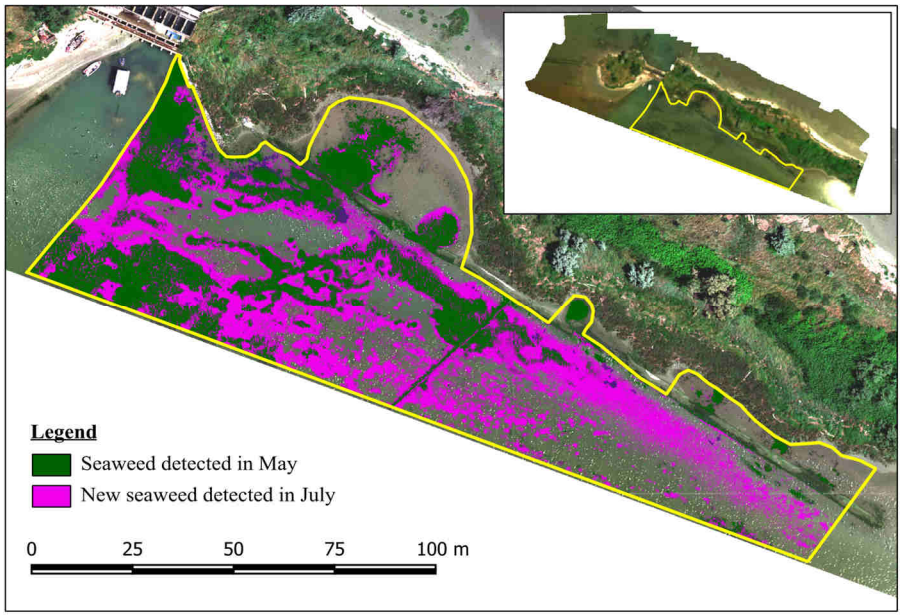

Figure 5.27 Submerged seaweed estimation on a wide region in site n°1 with the maximum likelihood method.

The amount of submerged seaweed pixels rose from $2323.0\ m^2$ to $4908.6\ m^2$, with an absolute detected increase of $2585.6\ m^2$ and a percentage of $+111\%$.

Similarly, in the site n°2 the submerged seaweed growth was detected through a supervised classification with the maximum likelihood method in the northern area. Also in this case the number of regions of interest was assumed as the most suitable to accurately describe the different ground cover types and the threshold values for the classifier were accordingly assumed, generally within the range from 0.3 and 0.7 as previously made for the site n°1.

The classification results were assessed by a validation conducted by both a high overall accuracy (over 95%) for the survey repetitions (in May and in July) on the ROIs truth and the comparison on the RGB orthomosaic. The estimation showed an increase of the submerged seaweed cover from $1049.7\ m^2$ to $3558.1\ m^2$, with

a difference of $2508.4\ m^2$. In terms of percentage the increase was therefore $+239\%$ in 39 days within the northern area in site n°2.

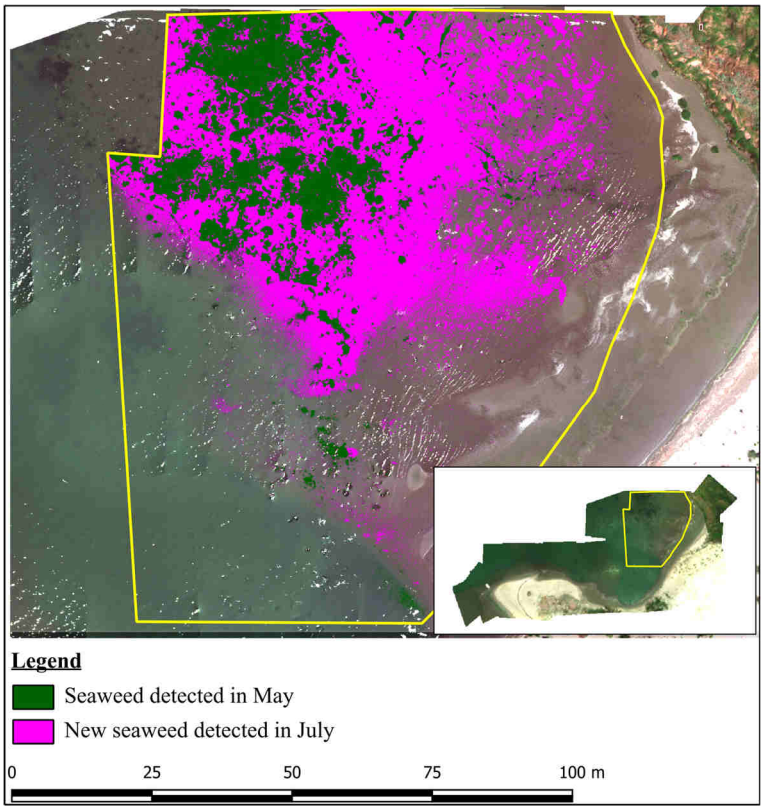

Figure 5.28 Submerged seaweed estimation on a wide region in site n°2 with the maximum likelihood method.

5.6 Supervised classification results with and without radiometric calibration

The estimation of the submerged seaweed expansion carried out in both the considered sites through a supervised classification with the maximum likelihood method led to further test whether the radiometric calibration of the raw data is necessary in order to quantify the various ground cover types and making a comparison over time.

For this purpose, the orthomosaic generated by applying no correction to the raw digital number sensed by the multispectral camera was therefore classified using the same regions of interest specified for the radiometrically calibrated one. The thresholds of the maximum likelihood classifier were maintained as well. In this way, both the training data used and the thresholds were eliminated among the variables in order to make a more consistent comparison.

Actually, the comparison was performed on the whole extent of the surveyed sites and was not limited to any submerged seaweed region. First of all, a lower overall accuracy was noticed whenever the orthomosaics without any radiometric correction were used. The values decreased as follows:

- from 97% to 74% for the survey carried out in May in the site n°1;
- from 99% to 82% for the survey carried out in May in the site n°2;
- from 98% to 71% for the survey carried out in July in the site n°1;
- from 95% to 54% for the survey carried out in July in the site n°2.

In addition, the amount of unclassified pixels increased:

- from 142,362 to 366,287 (+157%) for the survey carried out in May in the site n°1;
- from 423,513 to 1,291,431 (+205%) for the survey carried out in May in the site n°2;
- from 536,479 to 643,904 (+20%) for the survey carried out in July in the site n°1;
- from 399,138 to 751,184 (+88%) for the survey carried out in July in the site n°2.

This means that the performance of the classifier also decreased for all of the considered sites and survey repetitions that were compared. Table 5.5 shows the complete confusion matrix (in terms of percentage) of the comparison made for the orthomosaics with considering both the DLS and the known reflectance panel data and without the application of any radiometric correction to the raw data sensed for the flight performed in May for the site n°1. The MATLAB script file used to generate the data in Table 5.5 is reported in Appendix A.4.

The confusion matrix contains the number of pixels that were correctly classified within a ROI truth as well as the classification that was assigned if they were not correctly classified. Theoretically, the matrix should be diagonal. All the elements on the diagonal should have a value of 1 and all the others a value of 0 if the classification was “perfect”, thus meaning that all of the pixels within each ROI truth were correctly classified.

In order to assess the effect of the radiometric calibration of the raw data sensed by the multispectral camera on the results of the supervised classification, the assumption of using the overall classification previously made on the radiometrically corrected orthomosaic was made. This hypothesis represented the most feasible approach for the comparison, since the classification made on the basis of the calibrated imageries proved to be reliable and was successfully validated in a previous stage of the study.

The overall accuracy was thus computed using this assumption and it was found to be:

- 63% for the survey carried out in May in the site n°1;
- 72% for the survey carried out in May in the site n°2;
- 53% for the survey carried out in July in the site n°1;
- 60% for the survey carried out in July in the site n°2.

These values further confirm that the use of radiometrically uncalibrated imageries may lead to very different results in terms of class detection through a supervised classifier, even if the regions of interest are accurately specified.

Figure 5.29 shows the detail of the solely submerged seaweed class specified within the maximum likelihood classifier. It is worth noting that:

- a huge number of pixels was classified as submerged seaweed even though they were not;
- the main confusion in this sense was made between the submerged seaweed and the deep water classes. The evidence for this can be found in the confusion matrix in Table 5.5.
- an abnormal layout with a sort of lines on the sea surface can be found in the classification based on the raw data. These lines were found to be the border of the images that were merged to generate the orthomosaic.

Table 5.5 Comparison between the supervised classification performed on both the raw data sensed and radiometrically calibrated orthomosaics generated for site n°1 (May). The table reports a confusion matrix in percentage where the radiometrically calibrated classification was assumed as the truth.

		Radiometrically corrected orthomosaic classes											
		Unclassified	Vegetation 3	Vegetation 1	Vegetation 4	Vegetation 2	Dry sand	Wet sand 1	Deep water	Submerged seaweed	Emerged seaweed	Wet sand 2	Shadows
Radiometrically corrected orthomosaic classes	Unclassified	21.62	0.15	0.05	0.06	0.00	0.77	0.03	0.01	0.22	0.14	1.22	0.01
	Vegetation 3	2.70	96.53	8.98	0.18	20.23	1.12	2.59	1.56	0.47	0.77	2.21	14.78
	Vegetation 1	1.49	2.63	56.47	15.10	14.35	0.27	0.00	0.00	0.00	0.34	0.00	1.50
	Vegetation 4	0.93	0.00	3.54	66.17	1.33	3.20	0.31	0.00	0.00	10.52	0.00	0.00
	Vegetation 2	0.00	0.10	19.28	8.02	49.37	0.00	0.00	0.00	0.04	3.10	0.00	2.79
	Dry sand	35.00	0.00	0.08	2.78	0.00	60.20	13.28	0.04	1.42	3.85	3.05	0.00
	Wet sand 1	0.77	0.00	0.00	0.02	0.00	12.08	55.33	0.00	0.41	11.58	4.16	0.07
	Deep water	1.49	0.00	0.00	0.00	0.00	0.15	0.00	59.62	13.82	0.00	3.43	0.01
	Submerged seaweed	7.11	0.00	0.00	0.00	0.00	1.45	0.73	32.74	74.67	7.51	12.09	4.96
	Emerged seaweed	0.68	0.56	10.52	7.55	13.27	3.64	5.38	0.00	1.65	52.59	0.30	6.73
	Wet sand 2	28.19	0.00	0.00	0.05	0.00	17.12	22.35	6.03	6.99	9.05	73.55	0.21
	Shadows	0.02	0.03	1.07	0.06	1.44	0.01	0.00	0.00	0.31	0.56	0.01	68.94

Similarly, Table 5.6 reports the "true" classification of the submerged seaweed detected pixels, in terms of percentage. "True" classification pertains to the results obtained through the maximum likelihood classifier using the radiometrically calibrated imageries. As it was already evident by Figure 5.29 that shows the comparison for the only survey performed in May and in the site n°1, the pixels classified as submerged seaweed using the uncalibrated imageries were mainly confused with the deep water. The fraction of pixels that were correctly classified as submerged seaweed varied from 34% to 53%, hence the classification, even though it was performed through the same parameters of the classifier (ROIs, thresholds) proved to be both ineffective and unreliable.

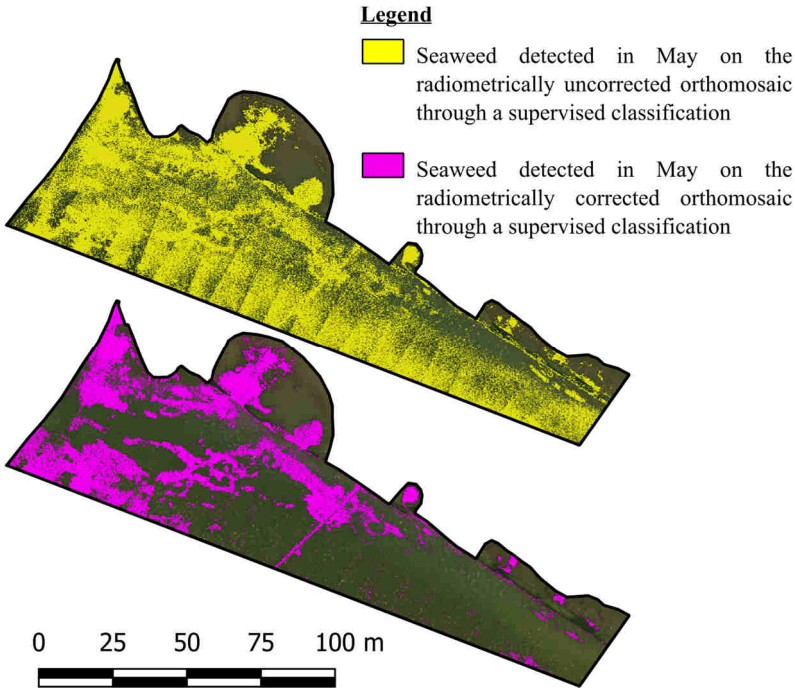

Figure 5.29 Differences in the detection of the submerged seaweed on the orthomosaics generated with and without a radiometric calibration for the site n°1 (May).

Table 5.6 Comparison between the seaweed detected on the uncalibrated orthomosaic and the corresponding classification obtained on the calibrated one. Most of the pixel were confused with deep water pixels. Seaweed detection proved to be unreliable.

	Site n°1, May	Site n°2, May	Site n°1, July	Site n°2, July
Submerged seaweed	38.7 %	42.6 %	55.3 %	34.0 %
Water	39.6 %	50.6 %	11.0 %	40.7 %
Other	21.7 %	6.8 %	33.7 %	25.3 %

This latter analysis conducted using the data of all the survey repetitions varying the variable consisting in applying or not applying a radiometric calibration to the raw data sensed by the MicaSense RedEdge-M multispectral camera highlights the importance to correct the acquired imageries. In term of a comparison among all the classes, the overall accuracy parameter enhances that significant differences and discrepancies were found. In addition, the focus on the submerged seaweed shows huge differences and a high level of confusion with the deep water class. Part of this issue is also due to a difference in the brightness of the single images to be merged. Consequently, the separation between the seaweed and the seawater become less evident and the border more labile. A high spatial sampling for the training dataset that forms the regions of interest cannot compensate the issue, since the classes become also more dispersed, having a higher standard deviation.

Conclusions

In this PhD dissertation, low-cost multispectral cameras have been tested and compared each other to assess their main differences and evaluating the performance of each system. In particular, the attention has been focussed on the *precision agriculture* and the *coastal monitoring* topics.

For the precision agriculture, the study analysed the use of simple modified cameras (MAPIR), consisting in traditional cameras with the further application of a filter and a specifically developed camera, the Sentera Single sensor, having a unique CMOS sensor able to detect red, green and near infrared in the channels of the image thanks to a high-pass filter.

The main limiting factor in using the MAPIR cameras proved to be the uncertainty in the knowledge of the sensor's characteristics. The quantum efficiency was not accurately known and the transmittance of the filters was provided in terms of graphs by the manufacturer. In addition, the overall system was made of up to four cameras concurrently mounted on an aircraft but not synchronised neither having actually all the same settings. Furthermore, the missing synchronization induced the creation of distinct orthomosaics of the surveyed areas that were overlapped each other thanks to their georeferencing by Ground Control Points (GCPs).

The empirical calibration performed on the basis of some typical CMOS sensor's properties led to more plausible NDVI values computed from the data recorder by the red and the near infrared MAPIR cameras, even though the lack of any spectral standard reference (like known reflectance panels) or Downwelling Light Sensors (DLSs) made practically impossible to normalise the image of any entire dataset. Similar results were obtained for the MAPIR camera commercialised as MAPIR NDVI, whose computed index was instead a near infrared over blue ratio, due to its inability to acquire red data.

On the other side, the Sentera Single sensor proved to provide better results, since the quantum efficiency was known by the manufacturer and each capture already contained the red, green and near infrared channels. However, also in this case the system performed no spectral calibration. Tests conducted on a wheat field

and on a vineyard highlighted that the Sentera Single seemed to provide more reliable NDVI values than the MAPIR cameras, but no comparison over time could be performed due to the lack of a strong calibration procedure.

The comparison between the Sentera Single sensor and the Parrot Sequoia, this latter interfaced with a DLS, confirmed the necessity of a calibration accounting for the actual irradiance at the time of each image exposure, with the double effect of computing accurate and reliable NDVI values and a higher spatial homogeneity. An empirical approach for a calibration of the Sentera Single was analysed, forcing the difference in the quantum efficiency of the sensor in red and near infrared spectral bands and only for particular NDVI predetermined values (over than 0.5). This method proved that the calibration, even with a simple approach, would effectively be possible, even the parameter to be used for the calibration should be evaluated case by case.

Conversely, the field of coastal monitoring regarded the use of the MicaSense RedEdge-M multispectral camera. After a brief study of the NDVI map within a context of embryo dunes monitoring over time, the seaweed detection and expansion assessment represented a further application of multispectral low-cost sensors. Thanks to its five spectral bands (blue, green, red, red edge and near infrared) and both a DLS and a known reflectance panel for the calibration of the imageries, the MicaSense RedEdge-M proved to be the most performant sensor, allowing a precise mapping with a supervised classification (maximum likelihood) procedure. The data processing was executed using two common commercial software able to handle this kind of multispectral images (Agisoft PhotoScan Professional and Pix4D Mapper Pro) and no significant differences were found between them.

The quantification of the seaweed was assessed by comparing the results through supervised classifications conducted on orthomosaics obtained by radiometrically calibrated images and by the raw images. The comparison highlighted that only with an accurate spectral calibration it is possible to detected the seaweed and distinguish it from the water.

The analysis of the distribution of near infrared, red and NDVI values conducted on four different ground cover types further confirmed how only the application of radiometric corrections allows to distinguish between the various

regions. This was clearly evident with the separation of frequency histograms. Furthermore, this kind of analysis showed that also the simple use of the DLS enables to effectively compute reliable reflectance values, even though it is only with a known reflectance panels that most accurate values can be computed.

It worth noting that nowadays also the MAPIR cameras (in their third version) and the new Sentera Single sensor are provided respectively with a known reflectance panel and a DLS, confirming the importance of the radiometric calibration.

The use of multispectral low-cost sensors makes therefore possible to extend the wide range of applications that satellite multispectral imageries have been in the past with a very high geometric resolution. Narrowband sensors allow to both calculating accurate and reliable spectral indices and to perform detailed classification of the ground covers. The limitation in the number of spectral bands that multispectral camera can acquire will be probably overcome in few years, thanks to the availability of lighter hyperspectral sensors at decreasing costs.

Even though probably hyperspectral sensors will provide a stronger instrument for the spectral characterization of ground covers by UAV in few years, at present multispectral imagers still represent one of the best compromise in terms of costs, overall system's weight, high geometric resolution (at a centimetre level) and detection of spectral information allowing the computation of the most used spectral indices.

References

[1] B.W. Levin, E.V. Sasorova, G.M. Steblov, A.V. Domanski, A.S. Prytkov, and E.N. Tsyba, **Variations of the Earth's rotation rate and cyclic processes in geodynamics**, *Geodesy and Geodynamics*, vol. 8, no. 3, pp. 206-212, 2017.

[2] U.S. Naval Observatory Astronomical Applications Department. Apsides and Seasons Calculator. [Online]. http://aa.usno.navy.mil/seasons?year=2018&tz=+0&dst=0

[3] Christian A. Gueymard, **A reevaluation of the solar constant based on a 42-year total solar irradiance time series and a reconciliation of spaceborne observations**, *Solar Energy*, vol. 168, pp. 2-9, 2018.

[4] ASTM, **Solar Constant and Zero Air Mass Solar Spectral Irradiance Tables**, ASTM International, Standard E490-00 2000.

[5] Christian A. Gueymard, **The sun's total and spectral irradiance for solar energy applications and solar radiation models**, *Solar Energy*, vol. 76, no. 4, pp. 426-453, 2004.

[6] Richard E. Bird and Carol Riordan, **Simple Solar Spectral Model for Direct and Diffuse Irradiance on Horizontal and Tilted Planes at the Earth's Surface for Cloudless Atmospheres**, *Journal of Climate and Applied Meteorology*, vol. 25, no. 1, pp. 87-97, 1986.

[7] Christian A. Gueymard, **Parameterized transmittance model for direct beam and circumsolar spectral irradiance**, *Solar Energy*, vol. 71, no. 5, pp. 325-346, 2001.

[8] Christian A. Gueymard, **SMARTS, A Simple Model of the Atmospheric Radiative Transfer of Sunshine: Algorithms and Performance Assessment**, Florida Solar Energy Center, 1679 Clearlake Rd., Cocoa, FL 32922, Professional Paper FSEC-PF-270-95 1995.

[9] F. E. Nicodemus, J. C. Richmond, J. J. Hsia, I. W. Ginsberg, and T. Limperis, **Geometrical Considerations and Nomenclature for Reflectance**. In *Radiometry*, USA: Jones and Bartlett Publishers, Inc., 1992, pp. 94-145.

[10] Hamlyn G. Jones and Robin A. Vaughan, *Remote sensing of vegetation: principles, techniques, and applications*. Oxford university press, 2010.

[11] G. Schaepman-Strub, M.E. Schaepman, T.H. Painter, S. Dangel, and J.V. Martonchik, **Reflectance quantities in optical remote sensing — definitions and case studies**, *Remote Sensing of Environment*, vol. 103, no. 1, pp. 27-42, 2006.

[12] Helge Aasen, Eija Honkavaara, Arko Lucieer, and Pablo J. Zarco-Tejada, **Quantitative Remote Sensing at Ultra-High Resolution with UAV Spectroscopy: A Review of Sensor Technology, Measurement Procedures, and Data Correction Workflows**, *Remote Sensing*, vol. 10, no. 7, 2018.

[13] Raymond F. Kokaly, Roger N. Clark, Gregg A. Swayze, K. Eric Livo, Todd M. Hoefen, Neil C. Pearson, Richard A. Wise, William M. Benzel, Heather A. Lowers, Rhonda L. Driscoll, and Anna J. Klein, **USGS Spectral Library Version 7**, U.S. Geological Survey, Report 2017.

[14] Miina Rautiainen, Petr Lukeš, Lucie Homolová, Aarne Hovi, Jan Pisek, and Matti Mõttus, **Spectral Properties of Coniferous Forests: A Review of In Situ and Laboratory Measurements**, *Remote Sensing*, vol. 10, no. 2, 2018.

[15] Jinru Xue and Baofeng Su, **Significant Remote Sensing Vegetation Indices: A Review of Developments and Applications,** *Journal of Sensors*, vol. 2017, 2017.

[16] A. Bannari, D. Morin, F. Bonn, and A. R. Huete, **A review of vegetation indices**, *Remote Sensing Reviews*, vol. 13, no. 1-2, pp. 95-120, 1995.

[17] A.R Huete, **A soil-adjusted vegetation index (SAVI)**, *Remote Sensing of Environment*, vol. 25, no. 3, pp. 295-309, 1988.

[18] Hongrui Ren, Guangsheng Zhou, and Feng Zhang, **Using negative soil adjustment factor in soil-adjusted vegetation index (SAVI) for aboveground living biomass estimation in arid grasslands**, *Remote Sensing of Environment*, vol. 209, pp. 439-445, 2018.

[19] E. Raymond Hunt, Paul C. Doraiswamy, James E. McMurtrey, Craig S.T. Daughtry, Eileen M. Perry, and Bakhyt Akhmedov, **A visible band index for remote sensing leaf chlorophyll content at the canopy scale**, *International Journal of Applied Earth Observation and Geoinformation*, vol. 21, pp. 103-112, 2013.

[20] Chang-Hua Ju, Yong-Chao Tian, Xia Yao, Wei-Xing Cao, Yan Zhu, and D. Hannaway, **Estimating Leaf Chlorophyll Content Using Red Edge Parameters**, *Pedosphere*, vol. 20, no. 5, pp. 633-644, 2010.

[21] I. Filella and J. Peñuelas, **The red edge position and shape as indicators of plant chlorophyll content, biomass and hydric status**, *International Journal of Remote Sensing*, vol. 15, no. 7, pp. 1459-1470, 1994.

[22] Michael T. Eismann, *Hyperspectral Remote Sensing*. Spie Press, 2012.

[23] John A. Richards and Xiuping Jia, *Remote Sensing Digital Image Analysis. An Introduction.* Springer, 2006.

[24] Jacob Cohen, **A Coefficient of Agreement for Nominal Scales**, *Educational and Psycholollgical Measurement*, vol. 20, no. 1, pp. 37-46, 1960.

[25] George H. Rosenfield and Katherine Fitzpatrick-Lins, **A Coefficient of Agreement as a Measure of Thematic Classification Accuracy**, *Photogrammetric Engineering and Remote Sensing*, vol. 52, no. 2, pp. 223-227, 1986.

[26] Ente Nazionale per l'Aviazione Civile, **Regolamento - Mezzi Aerei a Pilotaggio Remoto**, 2018. [Online]. https://www.enac.gov.it/sites/default/files/allegati/2018-Lug/Regolamento_APR_Ed2_Em4_180704.pdf

[27] European Aviation Safety Agency. https://www.easa.europa.eu/easa-and-you/civil-drones-rpas. [Online].

[28] Thomas Luhmann, Stuart Robson, Stephen Kyle, and Jan Boehm, *Close-Range Photogrammetry and 3D Imaging*. De Gruyter, 2013.

[29] Junichi Nakamura, *Image Sensor and Signal Processing for Digital Still Cameras.*, 2006.

[30] Joshua Kelcey and Arko Lucieer, **SENSOR CORRECTION AND RADIOMETRIC CALIBRATION OF A 6-BAND MULTISPECTRAL IMAGING SENSOR FOR UAV REMOTE SENSING**, *International Archives of the Photogrammetry, Remote Sensing and Spatial Information Sciences*, vol. XXXIX-B1, pp. 393-398, 2012.

[31] Pix4D. Camera radiometric correction specifications. [Online]. https://support.pix4d.com/hc/en-us/articles/115001846106-Camera-radiometric-correction-specifications

[32] MicaSense. MicaSense RedEdge image processing tutorials. [Online]. https://github.com/micasense/imageprocessing

[33] Parrot, **Application note: Pixel value to irradiance using the sensor calibration model**, SEQ-AN-01, 2017.

[34] Ronald E. Walker, *Marine Light Field Statistics*. Wiley, 1994.

[35] Yu-Hsuan Tu, Stuart Phinn, Kasper Johansen, and Andrew Robson, **Assessing Radiometric Correction Approaches for Multi-Spectral UAS Imagery for Horticultural Applications**, *Remote Sensing*, vol. 10, no. 11, 2018.

[36] Eija Honkavaara, Heikki Saari, Jere Kaivosoja, Ilkka Pölönen, Teemu Hakala, Paula Litkey, Jussi Mäkynen, and Liisa Pesonen, **Processing and Assessment of Spectrometric, Stereoscopic Imagery Collected Using a Lightweight UAV Spectral Camera for Precision Agriculture**, *Remote Sensing*, vol. 5, no. 10, pp. 5006-5039, 2013.

[37] T. Hakala, E. Honkavaara, H. Saari, J. Mäkynen, J. Kaivosoja, L. Pesonen, and I. Pölönen, **SPECTRAL IMAGING FROM UAVS UNDER VARYING ILLUMINATION CONDITIONS**, *ISPRS - International Archives of the Photogrammetry, Remote Sensing and Spatial Information Sciences*, vol. XL-1/W2, pp. 189-194, 2013.

[38] C. L. Walthall, J. M. Norman, J. M. Welles, G. Campbell, and B. L. Blad, **Simple equation to approximate the bidirectional reflectance from vegetative canopies and bare soil surfaces**, *Applied Optics*, vol. 24, no. 3, pp. 383-387, 1985.

[39] Eija Honkavaara and Ehsan Khoramshahi, **Radiometric Correction of Close-Range Spectral Image Blocks Captured Using an Unmanned Aerial Vehicle with a Radiometric Block Adjustment**, *Remote Sensing*, vol. 10, no. 2, 2018.

[40] David A. Forsyth and Jean Ponce, *Computer Vision A Modern Approach*. Pearson, 2012.

[41] Richard Szeliski, *Computer Vision: Algorithms and Applications*. Springer, 2011.

[42] Pix4D. Reflectance map vs orthomosaic. [Online]. https://support.pix4d.com/hc/en-us/articles/202739409

[43] A. Burkart, S. Cogliati, A. Schickling, and U. Rascher, **A Novel UAV-Based Ultra-Light Weight Spectrometer for Field Spectroscopy**, *IEEE Sensors Journal*, 2014.

[44] Sowmya Natesan, Costas Armenakis, Guy Benari, and Regina Lee, **Use of UAV-Borne Spectrometer for Land Cover Classification**, *Drones*, vol. 2, no. 2, 2018.

[45] (2018, November) MAIA WV Datasheet. [Online]. https://www.spectralcam.com

[46] Senop. Hyperspectral Camera Datasheet. [Online]. http://view.24mags.com/mera/datasheet-hyperspectral-camera

[47] S. Livens, K. Pauly, P. Baeck, J. Blommaert, D. Nuyts, J. Zender, and B. Delauré, **A SPATIO-SPECTRAL CAMERA FOR HIGH RESOLUTION HYPERSPECTRAL IMAGING**, *ISPRS - International Archives of the Photogrammetry, Remote Sensing and Spatial Information Sciences*, vol. XLII-2/W6, pp. 223-228, 2017.

[48] A. A. Sima, P. Baeck, D. Nuyts, S. Delalieux, S. Livens, J. Blommaert, B. Delaur\'e, and M. Boonen, **COMPACT HYPERSPECTRAL IMAGING SYSTEM (COSI) FOR SMALL REMOTELY PILOTED AIRCRAFT SYSTEMS (RPAS) – SYSTEM OVERVIEW AND FIRST PERFORMANCE EVALUATION RESULTS**, *ISPRS - International Archives of the Photogrammetry, Remote Sensing and Spatial Information Sciences*, vol. XLI-B1, pp. 1157-1164, 2016.

[49] Sebastian Candiago, Fabio Remondino, Michaela De Giglio, Marco Dubbini, and Mario Gattelli, **Evaluating Multispectral Images and Vegetation Indices for Precision Farming Aplplications from UAV Images**, *Remote Sensing*, vol. 7, pp. 4026-4047.

[50] Alessandro Matese, Piero Toscano, Salvatore Filippo Di Gennaro, Lorenzo Genesio, Francesco Primo Vaccari, Jacopo Primicerio, Claudio Belli, Alessandro Zaldei, Roberto Bianconi, and Beniamino Gioli, **Intercomparison of UAV, Aircraft and Satellite Remote Sensing Platforms for Precision Viticulture**, *Remote Sensing*, vol. 7, pp. 2971--2990, 2015.

[51] Alessandro Matese, Rita Baraldi, Andrea Berton, Carla Cesaraccio, Salvatore Filippo Di Gennaro, Pierpaolo Duce, Osvaldo Facini, Massimiliano Giuseppe Mameli, Alessandra Piga, and Alessandro Zaldei, **Estimation of Water Stress in Grapevines Using Proximal and Remote Sensing Methods**, *Remote Sensing*, vol. 10, no. 1, 2018.

[52] Y. Taddia, C. Corbau, E. Zambello, V. Russo, U. Simeoni, P. Russo, and A. Pellegrinelli, **UAVS TO ASSESS THE EVOLUTION OF EMBRYO DUNES**, *ISPRS - International Archives of the Photogrammetry, Remote Sensing and Spatial Information Sciences*, vol. XLII-2/W6, pp. 363--369, 2017.

[53] A. A. Alesheikh, A. Ghorbanali, and N. Nouri, **Coastline change detection using remote sensing**, *International Journal of Environmental Science & Technology*, vol. 4, no. 1, pp. 61-66, 2007.

[54] Kevin Lynch, Derek W.T. Jackson, and J. Andrew G. Cooper, **Foredune accretion under offshore winds**, *Geomorphology*, vol. 105, no. 1-2, pp. 139-146, 2009.

[55] M.J. Westoby, J. Brasington, N.F. Glasser, M.J. Hambrey, and J.M. Reynolds, **'Structure-from-Motion' photogrammetry: A low-cost,effective tool for geoscience applications**, *Geomorphology*, vol. 179, pp. 300-314, 2012.

[56] Francois Clapuyt, Veerle Vanacker, and Kristof Van Oost, **Reproducibility of UAV-based earth topography reconstructions based on Structure-from-Motion algorithms**, *Geomorphology*, vol. 260, pp. 4-15, 2016.

[57] M.R. James, S. Robson, S. d'Oleire-Oltmanns, and U. Niethammer, **Optimising UAV topographic surveys processed with structure-from-motion: Ground control quality, quantity and bundle adjustment**, *Geomorphology*, vol. 280, pp. 51-66, 2017.

[58] Kristen L. Cook, **An evaluation of the effectiveness of low-cost UAVs and structure from motion for geomorphic change detection**, *Geomorphology*, vol. 278, pp. 195-208, 2017.

[59] Christopher D Drummond, Mitchell D Harley, Ian L Turner, A Nashwan A Matheen, William C Glamore, and other, **UAV applications to coastal engineering**, in *Australasian Coasts & Ports Conference 2015: 22nd Australasian Coastal and Ocean Engineering Conference and the 15th Australasian Port and Harbour Conference*, 2015, p. 267.

[60] J.A. Goncalves and R. Henriques, **UAV photogrammetry for topographic monitoring of coastal areas**, *ISPRS Journal of Photogrammetry and Remote Sensing*, vol. 104, pp. 101-111, 2015.

[61] Frederico M. Scarelli, Flavia Sistilli, Stefano Fabbri, Luigi Cantelli, Eduardo G. Barboza, and Giovanni Gabbianelli, **Seasonal dune and beach monitoring using photogrammetry from UAV surveys to apply in the ICZM on the Ravenna coast (Emilia-Romagna, Italy)**, *Remote Sensing Applications: Society and Environment*, vol. 7, pp. 27-39, 2017.

[62] Francesco Mancini, Marco Dubbini, Mario Gattelli, Francesco Stecchi, Stefano Fabbri, and Giovanni Gabbianelli, **Using Unmanned Aerial Vehicles (UAV) for High-Resolution Reconstruction of Topography: The Structure from Motion Approach on Coastal Environments**, *Remote Sensing*, vol. 5, no. 12, pp. 6880-6898, 2013.

[63] Steve Harwin and Arko Lucieer, **Assessing the Accuracy of Georeferenced Point Clouds Produced via Multi-View Stereopsis from Unmanned Aerial Vehicle (UAV) Imagery**, *Remote Sensing*, vol. 4, no. 6, pp. 1573-1599, 2012.

[64] Ian L. Turner, Mitchell D. Harley, and Christopher D. Drummond, **UAVs for coastal surveying**, *Coastal Engineering*, vol. 114, pp. 19-24, 2016.

[65] Michael A. Wulder, Ronald J. Hall, Nicholas C. Coops, and Steven E. Franklin, **High Spatial Resolution Remotely Sensed Data for Ecosystem Characterization**, *BioScience*, vol. 54, no. 6, p. 511, 2004.

[66] Agisoft, **Agisoft Photoscan User Manual, Professional Edition, Version 1.4**, 2018.

[67] Chris H. Hugenholtz, Ken Whitehead, Owen W. Brown, Thomas E. Barchyn, Brian J. Moorman, Adam LeClair, Kevin Riddell, and Tayler Hamilton, **Geomorphological mapping with a small unmanned aircraft system (sUAS): Feature detection and accuracy assessment of a photogrammetrically-derived digital terrain model**, *Geomorphology*, vol. 194, pp. 16-24, 2013.

[68] Yuri Taddia, Corinne Corbau, Elena Zambello, Valentina Russo, Alberto Pellegrinelli, Paolo Russo, and Umberto Simeoni, **Monitoraggio RPAS delle dune embrionali di Rosolina Mare (Alto Adriatico)**, *Studi Costieri*, vol. 26, pp. 83-94, 2017.

[69] Sita Karki, Mohamed Sultan, Racha Elkadiri, and Tamer Elbayoumi, **Mapping and Forecasting Onsets of Harmful Algal Blooms Using MODIS Data over Coastal Waters Surrounding Charlotte County, Florida**, *Remote Sensing*, 2018.

[70] Jong Cheol Pyo, Mayzonee Ligaray, Yong Sung Kwon, Myoung-Hwan Ahn, Kyunghyun Kim, Hyuk Lee, Taegu Kang, Seong Been Cho, Yongeun Park, and Kyung Hwa Cho, **High-Spatial Resolution Monitoring of Phycocyanin and Chlorophyll-a Using Airborne Hyperspectral Imagery**, *Remote Sensing*, 2018.

[71] Ana I. Dogliotti, Juan I. Gossn, Quinten Vanhellemont, and Kevin G. Ruddick, **Detecting and Quantifying a Massive Invasion of Floating Aquatic Plants in the Río de la Plata Turbid Waters Using High Spatial Resolution Ocean Color Imagery**, *Remote Sensing*, 2018.

[72] James P. Duffy, Laura Pratt, Karen Anderson, Peter E. Land, and Jamie D. Shutler, **Spatial assessment of intertidal seagrass meadows using optical imaging systems and a lightweight drone**, *Estuarine, Coastal and Shelf Science*, vol. 200, pp. 169-180, 2018.

[73] Yuri Taddia, Paolo Russo, Stefano Lovo, and Alberto Pellegrinelli, **Multispectral UAV Monitoring of Submerged Seaweed in Shallow Water**, *Applied Geomatics*, (Submitted on November, 2018).

[74] M.S. Hossain, J.S. Bujang, M.H. Zakaria, and M. Hashim, **The application of remote sensing to seagrass ecosystems: an overview and future research prospects**, *International Journal of Remote Sensing*, vol. 36, no. 1, pp. 61-114, 2015.

[75] Pramaditya Wicaksono, Ignatius Salivian Wisnu Kumara, Muhammad Kamal, Muhammad Afif Fauzan, Zhafirah Zhafarina, Dwi Agus Nurswantoro, and Rifka Noviaris Yogyantoro, **Multispectral Resampling of Seagrass Species Spectra: WorldView-2, Quickbird, Sentinel-2A, ASTER VNIR, and Landsat 8 OLI**, *IOP Conference Series: Earth and Environmental Science*, vol. 98, no. 1, 2017.

[76] Chippie Kislik, Iryna Dronova, and Maggi Kelly, **UAVs in Support of Algal Bloom Research: A Review of Current Applications and Future Opportunities**, *Drones*, vol. 2, no. 4, 2018.

ADDITIONAL RESOURCES CONSULTED BUT NOT CITED IN THE TEXT

[77] Nkeiruka Nneti Onyia, Heiko Balzter, and Juan-Carlos Berrio, **Normalized Difference Vegetation Vigour Index: A New Remote Sensing Approach to Biodiversity Monitoring in Oil Polluted Regions**, *Remote Sensing*, vol. 10, no. 6, 2018.

[78] Hankui K. Zhang, David P. Roy, Lin Yan, Zhongbin Li, Haiyan Huang, Eric Vermote, Sergii Skakun, and Jean-Claude Roger, **Characterization of Sentinel-2A and Landsat-8 top of atmosphere, surface, and nadir BRDF adjusted reflectance and NDVI differences**, *Remote Sensing of Environment*, vol. 215, pp. 482-494, 2018.

[79] Xiaochi Zhou, Marco Marani, John D. Albertson, and Sonia Silvestri, **Hyperspectral and Multispectral Retrieval of Suspended Sediment in Shallow Coastal Waters Using Semi-Analytical and Empirical Methods**, *Remote Sensing*, vol. 9, no. 4, 2017.

[80] Fubiao Feng, Wei Li, Qian Du, and Bing Zhang, **Dimensionality Reduction of Hyperspectral Image with Graph-Based Discriminant Analysis Considering Spectral Similarity**, *Remote Sensing*, vol. 9, no. 4, 2017.

[81] Emanuele Mandanici and Gabriele Bitelli, **Preliminary Comparison of Sentinel-2 and Landsat 8 Imagery for a Combined Use**, *Remote Sensing*, vol. 8, no. 12, 2016.

[82] Javier Marcello, Francisco Eugenio, Ulises Perdomo, and Anabella Medina, **Assessment of Atmospheric Algorithms to Retrieve Vegetation in Natural Protected Areas Using Multispectral High Resolution Imagery**, *Sensors*, vol. 16, no. 10, 2016.

[83] D.P. Roy, H.K. Zhang, J. Ju, J.L. Gomez-Dans, P.E. Lewis, C.B. Schaaf, Q. Sun, J. Li, H. Huang, and V. Kovalskyy, **A general method to normalize Landsat reflectance data to nadir BRDF adjusted reflectance**, *Remote Sensing of Environment*, vol. 176, pp. 255-271, 2016.

[84] S. Wang and C. Wang, **Research on dimension reduction method for hyperspectral remote sensing image based on global mixture coordination factor analysis**, *ISPRS - International Archives of the Photogrammetry, Remote Sensing and Spatial Information Sciences*, vol. XL-7/W4, pp. 159-167, 2015.

[85] G. Meera Gandhi, S. Parthiban, Nagaraj Thummalu, and A. Christy, **Ndvi: Vegetation Change Detection Using Remote Sensing and Gis – A Case Study of Vellore District**, *Procedia Computer Science*, vol. 57, pp. 1199-1210, 2015.

[86] Genesis T. Yengoh, David Dent, Lennart Olsson, Anna E. Tengberg, and Compton J. Tucker, **The use of the Normalized Difference Vegetation Index (NDVI) to assess land degradation at multiple scales: a review of the current status, future trends, and practical considerations**, Lund University Center for Sustainability Studies (LUCSUS) and The Scientific and Technical Advisory Panel of the Global Facility (STAP/GEF), 2014.

[87] Mervin St. Luce, Noura Ziadi, Bernie J. Zebarth, Cynthia A. Grant, Gaëtan F. Tremblay, and Edward G. Gregorich, **Rapid determination of soil organic matter quality indicators using visible near infrared reflectance spectroscopy**, *Geoderma*, vol. 232-234, pp. 449-458, 2014.

[88] Xia Cui, Cerian Gibbes, Jane Southworth, and Peter Waylen, **Using Remote Sensing to Quantify Vegetation Change and Ecological Resilience in a Semi-Arid System**, *Land*, vol. 2, no. 2, pp. 108-130, 2013.

[89] D. Summers, M. Lewis, B. Ostendorf, and D. Chittleborough, **Visible near-infrared reflectance spectroscopy as a predictive indicator of soil properties**, *Ecological Indicators*, vol. 11, no. 1, pp. 123-131, 2011.

[90] P.J. Verkerk, M. Lindner, G. Zanchi, and S. Zudin, **Assessing impacts of intensified biomass removal on deadwood in European forests**, *Ecological Indicators*, vol. 11, no. 1, pp. 27-35, 2011.

[91] A. Volkan Bilgili, H.M. van Es, F. Akbas, A. Durak, and W.D. Hively, **Visible-near infrared reflectance spectroscopy for assessment of soil properties in a semi-arid area of Turkey**, *Journal of Arid Environments*, vol. 74, no. 2, pp. 229-238, 2010.

[92] Yichun Xie, Zongyao Sha, and Mei Yu, **Remote sensing imagery in vegetation mapping: a review**, *Journal of Plant Ecology*, vol. 1, no. 1, pp. 9-23, 2008.

[93] M.T.Y. Tadros, M. El-Metwally, and A.B. Hamed, **A comparative study on SPCTRAL2, SPCTR-1881 and SMARTS2 models using direct normal solar irradiance in different bands for Cairo and Aswan, Egypt**, *Journal of Atmospheric and Solar-Terrestrial Physics*, vol. 67, pp. 1343-1356, 2005.

[94] Dimitris Manolakis, David Marden, and Gary A. Shaw, **Hyperspectral Image Processing for Automatic Target Detection Applications**, *Lincoln Laboratory Journal*, vol. 14, no. 1, pp. 79-116, 2003.

[95] J. Peñuelas, J. Pinol, R. Ogaya, and I. Filella, **Estimation of plant water concentration by the reflectance Water Index WI (R900/R970)**, *International Journal of Remote Sensing*, vol. 18, no. 13, pp. 2869-2875, 1997.

[96] J. Peñuelas, I. Filella, C. Biel, L. Serrano, and R. Savé, **The reflectance at the 950–970 nm region as an indicator of plant water status**, *International Journal of Remote Sensing*, vol. 14, no. 10, pp. 1887-1905, 1993.

[97] Charles K. Gatebe and Michael D. King, **Airborne spectral BRDF of various surface types (ocean, vegetation, snow, desert, wetlands, cloud decks, smoke layers) for remote sensing applications**, *Remote Sensing of Environment*, vol. 179, pp. 131-148, 2016.

[98] Ziti Jiao, Crystal B. Schaaf, Yadong Dong, Miguel Román, Michael J. Hill, Jing M. Chen, Zhuosen Wang, Hu Zhang, Edward Saenz, Rajesh Poudyal, Charles Gatebe, Francois-Marie Bréon, Xiaowen Li, and Alan Strahler, **A method for improving hotspot directional signatures in BRDF models used for MODIS**, *Remote Sensing of Environment*, vol. 186, pp. 135-151, 2016.

[99] Shree K. Nayar, Katsushi Ikeuchi, and Takeo Kanade, **Surface Reflection: Physical and Geometrical Perspectives**. In *Radiometry*, USA: Jones and Bartlett Publishers, Inc., 1992, pp. 60-83.

[100] K. E. Torrance and E. M. Sparrow, **Theory for Off-specular Reflection from Roughened Surfaces**. In *Radiometry*, USA: Jones and Bartlett Publishers, Inc., 1992, pp. 32-41.

[101] Berthold K. P. Horn and Robert W. Sjoberg, **Calculating the Reflectance Map**. In *Radiometry*, USA: Jones and Bartlett Publishers, Inc., 1992, pp. 84-93.

[102] Jinru Xue and Baofeng Su, **Significant Remote Sensing Vegetation Indices: A Review of Developments and Applications**, *Journal of Sensors*, vol. 2017, 2017.

[103] A. A. Gitelson and M. N. Merzlyak, **Remote estimation of chlorophyll content in higher plant leaves**, *International Journal of Remote Sensing*, vol. 18, no. 12, pp. 2691-2697, 1997.

[104] Yan-Lin and Wang, R.-C and Huang, Jing-feng Tang, **Relations between red edge characteristics and agronomic parameters of crops**, *Pedosphere*, vol. 14, pp. 467-474, 2004.

APPENDIX A

MATLAB SCRIPT FILES

This appendix includes the main script files used to perform the analysis and generating some of the figures.

A.1 Script for the Sentera Single – Parrot Sequoia comparison (Section 3.6)

```
clc;
clear variables;
close all;
cd ..

D=imread('differenze.tif');
SEQUOIA=imread('poligono_sequoia.tif');
SEQUOIA_no_corr=imread('poligono_sequoia_no_corr.tif');
RGNIR=imread('poligono_RGNIR_no_ombre.tif');
NDVIsen=imread('poligono_NDVIsen.tif');
cd results

RGNIR=double(RGNIR);
soglia_NDVI=0.5
NDVIsen=NDVIsen.*(NDVIsen(:,:)>soglia_NDVI).*(SEQUOIA(:,:)>soglia_NDVI);
b=0.065
NDVIsen_corr=((1+b).*RGNIR(:,:,3)-b.*RGNIR(:,:,1))./((1-
b).*RGNIR(:,:,3)+b.*RGNIR(:,:,1)+eps);
NDVIsen_corr=NDVIsen_corr.*(NDVIsen(:,:)>soglia_NDVI).*(SEQUOIA(:,:)>soglia_NDVI);

SEQUOIA=SEQUOIA.*(NDVIsen(:,:)>soglia_NDVI).*(SEQUOIA(:,:)>soglia_NDVI);
SEQUOIA_no_corr=SEQUOIA_no_corr.*(NDVIsen(:,:)>soglia_NDVI).*(SEQUOIA(:,:)>soglia_
NDVI).*(SEQUOIA_no_corr(:,:)>soglia_NDVI);
diff=SEQUOIA-NDVIsen;
NDVIsen=reshape(NDVIsen,numel(NDVIsen),1);
SEQUOIA=reshape(SEQUOIA,numel(NDVIsen),1);
SEQUOIA_no_corr=reshape(SEQUOIA_no_corr,numel(SEQUOIA_no_corr),1);
NDVIsen_corr=reshape(NDVIsen_corr,numel(NDVIsen_corr),1);

NDVIboth=[NDVIsen SEQUOIA ones(size(SEQUOIA)) SEQUOIA_no_corr NDVIsen_corr];
NDVIboth(any(NDVIboth==0,2),:)=[];

NDVIsen=NDVIboth(:,1);
```

```
SEQUOIA=NDVIboth(:,2);
soglia_densita=max(size(NDVIboth))*0.0005
n=hist3([SEQUOIA,NDVIsen],{0.0025:0.005:0.9975 0.0025:0.005:0.9975});
tic
for k=1:numel(NDVIboth(:,1))
       NDVIboth(k,3)=n(ceil(SEQUOIA(k).*200),ceil(NDVIsen(k).*200));
end
toc
NDVIboth=NDVIboth.*(NDVIboth(:,3)>soglia_densita);
NDVIboth(any(NDVIboth==0,2),:)=[];
NDVIsen=NDVIboth(:,1);
SEQUOIA=NDVIboth(:,2);
SEQUOIA_no_corr=NDVIboth(:,4);
NDVIsen_corr=NDVIboth(:,5);
n=n.*(n>soglia_densita);
n=n./max(size(NDVIboth));
%%
figure(1)
clf
axis([0 1 0 1])
coeff=polyfit(NDVIsen,SEQUOIA,1)
hold on
x=linspace(0,1); y=zeros(size(x));
for k=0:length(coeff)-1
    y=y+coeff(length(coeff)-k).*x.^(k);
end
hold on
imagesc([0.0025 0.9975],[0.0025 0.9975],n,'CDataMapping','scaled',...
    'AlphaData',1,'alphadata',n>0.0005);
set(gca,'YDir','normal')
load map
colormap(map)
caxis([0.0005 0.007])
hh=colorbar;
ylabel(hh,'normalised frequency')
plot([0 1],[0 1],'--k')
axis([0 1 0 1])
axis square
box on
xlabel('NDVI Sentera Single')
ylabel('NDVI Parrot Sequoia')
text(double(mean(NDVIsen)),0.7,...
    {'Sentera Single',['mean value \approx ' num2str(mean(NDVIsen),3)],['std. dev.
\approx                                                                    '
num2str(std(NDVIsen),2)]},'verticalalignment','middle','horizontalalignment','cent
er',...
        'backgroundcolor',[1 1 1],'edgecolor',[0 0 0])
text(0.25,double(mean(SEQUOIA))-0.02,{'Parrot  Sequoia',['mean  value  \approx  '
num2str(mean(SEQUOIA),3)],['std.            dev.            \approx            '
num2str(std(SEQUOIA),2)]},'verticalalignment','middle','horizontalalignment','cent
er',...
```

```
    'edgecolor',[0 0 0])
print('-dpng','-r300','A')
set(gcf,'renderer','painters')
print('-depsc','A')

%%
figure(2)
set(gcf,'units','normalized','position',[0.1 0.2 0.8 0.6])
subplot(1,2,1)
h1=histogram(NDVIsen,'facecolor',[5 131 240]./255,'facealpha',0.5);
h1.BinWidth = 0.005;
h1.Normalization='probability';
hold on
h2=histogram(SEQUOIA,'facecolor',[255 0 0]./255,'facealpha',0.5);
h2.BinWidth = 0.005;
h2.Normalization='probability';
h3=histogram(SEQUOIA_no_corr,'facecolor',[244 255 91]./255,'facealpha',0.5);
h3.BinWidth = 0.005;
h3.Normalization='probability';
xlabel('NDVI value'), ylabel('normalised frequency')
plots=get(gca,'children');
legend(plots([3,1,2]),{'Sentera Single sensor raw data sensed',...
    'Parrot Sequoia sensor raw data sensed',...
    'Parrot Sequoia sensor radiometrically corrected by DLS data'},...
    'location', 'northwest')
xlim([0.5,1])
ylim([0 0.18]), yticks(0:0.01:0.18)
% print('-dpng','-r300','B')
% set(gcf,'renderer','painters')
% print('-depsc','B')


subplot(1,2,2)
h1=histogram(NDVIsen_corr,'facecolor',[5 131 240]./255,'facealpha',0.5);
h1.BinWidth = 0.005;
h1.Normalization='probability';
hold on
h2=histogram(SEQUOIA,'facecolor',[255 0 0]./255,'facealpha',0.5);
h2.BinWidth = 0.005;
h2.Normalization='probability';
legend('Sentera Single with empiric radiometric correction',...
    'Parrot Sequoia sensor radiometrically corrected by DLS data',...
    'location', 'northwest')
xlim([0.5 1])
ylim([0 0.18]), yticks(0:0.01:0.18)
xlabel('NDVI value'), ylabel('normalised frequency')
print('-dpng','-r300','C')
set(gcf,'renderer','painters')
print('-depsc','C')

%%
```

```
figure(4)
clf
axis([0 1 0 1])
hold on
ncorr=hist3([SEQUOIA,NDVIsen_corr],{0.0025:0.005:0.9975
0.0025:0.005:0.9975})./max(size(NDVIboth));
imagesc([0.0025 0.9975],[0.0025 0.9975],ncorr,'CDataMapping','scaled',...
    'AlphaData',1,'alphadata',ncorr>0.0005);
set(gca,'YDir','normal')
load map
colormap(map)
caxis([0.0005 0.02])
hhh=colorbar;
ylabel(hhh,'normalised frequency')
plot([0 1],[0 1],'--k')
axis square
axis([0.7 1 0.7 1])
box on
xlabel({'NDVI value calibrated with empiric correction','(Sentera Single)'})
ylabel({'NDVI value calibrated by DLS data','(Parrot Sequoia)'})
title({'NDVI value with empiric correction','applied to vegetation pixels only'})
print('-dpng','-r300','D')
set(gcf,'renderer','painters')
print('-depsc','D')
```

A.2 Script for the extraction of EXIF irradiance values recorded by the DLS using *exiftool*

The extraction have been performed using both the ExifTool by Phil Harvey (https://www.sno.phy.queensu.ca/~phil/exiftool/) and the functions by Petern Burn available at https://www.mathworks.com/matlabcentral/fileexchange/42000-run_exiftool.

A.2.1 Extraction from the image dataset

```
clc,clear,close all

firstimage=0
lastimage=162
imagesnumber=lastimage-firstimage+1;
ground_base_ellipsoidal_altitude=0;
datum='wgs84';
warning('off')

cd ../../../..
cd foto_RedEdge/0001SET/000
p=[pwd '\'];
```

```
cd ../../..
cd elaborazioni\RedEdge\MATLAB_script\EXIF

for band=1:5
    for i=1:imagesnumber
        if i+firstimage-1<10
            f=['IMG_000' num2str(i+firstimage-1) '_' num2str(band) '.tif'];
        elseif i+firstimage-1<100
            f=['IMG_00' num2str(i+firstimage-1) '_' num2str(band) '.tif'];
        elseif i+firstimage-1<1000
            f=['IMG_0' num2str(i+firstimage-1) '_' num2str(band) '.tif'];
        else
            f=['IMG_' num2str(i+firstimage-1) '_' num2str(band) '.tif'];
        end

        % Read Exif data

        [exifdata,nf] = getexif([p,f]);

        ListCell=num2cell(exifdata);
        tf=(find(exifdata==char(10)));
        for j=1:length(tf)
            if j==1
                currentdata=num2str(cell2mat(ListCell(1:tf(j))));
                dp=min(find(exifdata==':'));
                sp1=min(find(exifdata(1:dp-1)==' '));
                field=num2str(cell2mat(ListCell(1:sp1-1)));
                sp2=(exifdata(dp+1:tf(j))==' ');
                sp2min=min(find(sp2==0));
                sp2max=max(find(sp2==0));
                value=cell2mat(ListCell(dp+sp2min:dp+sp2max-1));
                data=struct(field,value);
            else
                currentdata=num2str(cell2mat(ListCell(tf(j-1):tf(j))));
                dp=min(find(exifdata==':'));
                sp1=min(find(exifdata(tf(j-1)+1:tf(j-1)+dp-1)==' '));
                if isempty(sp1)
                    sp1=0;
                end
                field=num2str(cell2mat(ListCell(tf(j-1)+1:tf(j-1)+sp1-1)));
                sp2=(exifdata(tf(j-1)+dp+1:tf(j))==' ');
                sp2min=min(find(sp2==0));
                sp2max=max(find(sp2==0));
                value=cell2mat(ListCell(tf(j-1)+dp+sp2min:tf(j-1)+dp+sp2max-1));
                data.(field)=value;
            end
        end

        if band==1
            Label(i,:)=f;
        end
```

```
        Irradiance(i,band)=str2num(data.Irradiance);

        switch band
            case 1
                if i==1
                    wb=waitbar(i/imagesnumber,sprintf('%0.1f%%
Completed',i/imagesnumber*100),...
                        'Name','Processing BLUE images (step 1/5)',...
                        'CreateCancelBtn','setappdata(gcbf,''canceling'',1)');
                    setappdata(wb,'canceling',0);
                end
                waitbar(i/imagesnumber,wb,sprintf('%0.1f%%
Completed',i/imagesnumber*100))
                % Check for clicked Cancel button
                if getappdata(wb,'canceling')
                    delete(wb)
                    return
                end
            case 1
                if i==1
                    wb=waitbar(i/imagesnumber,sprintf('%0.1f%%
Completed',i/imagesnumber*100),...
                        'Name','Processing BLUE images (step 1/5)',...
                        'CreateCancelBtn','setappdata(gcbf,''canceling'',1)');
                    setappdata(wb,'canceling',0);
                end
                waitbar(i/imagesnumber,wb,sprintf('%0.1f%%
Completed',i/imagesnumber*100))
                % Check for clicked Cancel button
                if getappdata(wb,'canceling')
                    delete(wb)
                    return
                end
            case 2
                if i==1
                    wb=waitbar(i/imagesnumber,sprintf('%0.1f%%
Completed',i/imagesnumber*100),...
                        'Name','Processing GREEN images (step 2/5)',...
                        'CreateCancelBtn','setappdata(gcbf,''canceling'',1)');
                    setappdata(wb,'canceling',0);
                end
                waitbar(i/imagesnumber,wb,sprintf('%0.1f%%
Completed',i/imagesnumber*100))
                % Check for clicked Cancel button
                if getappdata(wb,'canceling')
                    delete(wb)
                    return
                end
            case 3
                if i==1
```

```
                    wb=waitbar(i/imagesnumber,sprintf('%0.1f%%
Completed',i/imagesnumber*100),...
                        'Name','Processing RED images (step 3/5)',...
                        'CreateCancelBtn','setappdata(gcbf,''canceling'',1)');
                    setappdata(wb,'canceling',0);
                end
                waitbar(i/imagesnumber,wb,sprintf('%0.1f%%
Completed',i/imagesnumber*100))
                % Check for clicked Cancel button
                if getappdata(wb,'canceling')
                    delete(wb)
                    return
                end
            case 4
                if i==1
                    wb=waitbar(i/imagesnumber,sprintf('%0.1f%%
Completed',i/imagesnumber*100),...
                        'Name','Processing NIR images (step 4/5)',...
                        'CreateCancelBtn','setappdata(gcbf,''canceling'',1)');
                    setappdata(wb,'canceling',0);
                end
                waitbar(i/imagesnumber,wb,sprintf('%0.1f%%
Completed',i/imagesnumber*100))
                % Check for clicked Cancel button
                if getappdata(wb,'canceling')
                    delete(wb)
                    return
                end
            case 5
                if i==1
                    wb=waitbar(i/imagesnumber,sprintf('%0.1f%%
Completed',i/imagesnumber*100),...
                        'Name','Processing RED EDGE images (step 5/5)',...
                        'CreateCancelBtn','setappdata(gcbf,''canceling'',1)');
                    setappdata(wb,'canceling',0);
                end
                waitbar(i/imagesnumber,wb,sprintf('%0.1f%%
Completed',i/imagesnumber*100))
                % Check for clicked Cancel button
                if getappdata(wb,'canceling')
                    delete(wb)
                    return
                end
        end
    end
    delete(wb)
end

format short

fid=fopen('irradiance_report_VOLO1.txt','wt+');
```

```
fprintf(fid,'Label\t    BLUE_Irradiance\t    GREEN_Irradiance\t    RED_Irradiance\t
NIR_Irradiance\t RED_EDGE_Irradiance \n');
for i=1:imagesnumber
    fprintf(fid,'%s\t',Label(i,:));
    fprintf(fid,'%6.15f\t%6.15f\t%6.15f\t%6.15f\t%6.15f\n',Irradiance(i,:)');
end
fclose(fid);

fid=fopen('irradiance_values_VOLO1.txt','wt+');
for i=1:imagesnumber
    fprintf(fid,'%6.15f\t%6.15f\t%6.15f\t%6.15f\t%6.15f\n',Irradiance(i,:)');
end
fclose(fid);
```

A.2.2 Generation of the graph in Figure 5.7

```
clc, clear, close all

% FLIGHT 1
load irradiance_values_VOLO1.txt
Irradiance1=irradiance_values_VOLO1;
clear irradiance values_VOLO1
sz1=size(Irradiance1);
n1=11:150; % only aerial captured photos

% FLIGHT 2
load irradiance_values_VOLO2.txt
Irradiance2=irradiance_values_VOLO2;
clear irradiance values_VOLO2
sz2=size(Irradiance2);
n2=11:146; % only aerial captured photos

figure

subplot(2,1,1)
plot(n1-n1(1)+1,Irradiance1(n1+1,1),'color','b','displayname','Blue')
hold on
plot(n1-n1(1)+1,Irradiance1(n1+1,2),'color','g','displayname','Green')
plot(n1-n1(1)+1,Irradiance1(n1+1,3),'color','r','displayname','Red')
plot(n1-n1(1)+1,Irradiance1(n1+1,5),'color',[1 0.5 0],'displayname','Red Edge')
plot(n1-n1(1)+1,Irradiance1(n1+1,4),'color','m','displayname','NIR')
legend('show','location','eastoutside')
title({'Sun Sensor Irradiance', 'Site n°1, May'})
xlim([1 length(n1)])
xlabel('Image number')
ylabel('Irradiance from EXIF [W m^{-2} nm^{-1}]')

subplot(2,1,2)
plot(n2-n2(1)+1,Irradiance2(n2+1,1),'color','b','displayname','Blue')
hold on
plot(n2-n2(1)+1,Irradiance2(n2+1,2),'color','g','displayname','Green')
```

```
plot(n2-n2(1)+1,Irradiance2(n2+1,3),'color','r','displayname','Red')
plot(n2-n2(1)+1,Irradiance2(n2+1,5),'color',[1 0.5 0],'displayname','Red Edge')
plot(n2-n2(1)+1,Irradiance2(n2+1,4),'color','m','displayname','NIR')
legend('show','location','eastoutside')
title({'Sun Sensor Irradiance', 'Site n°2, May'})
xlim([1 length(n2)])
xlabel('Image number')
ylabel('Irradiance from EXIF [W m^{-2} nm^{-1}]')
h=gcf;
set(h,'units','normalized','position',[0.25 0.2 0.5 0.7])

cd ../..
set(gcf,'renderer','painters')
print('-depsc','figure\Irradiance')
cd MATLAB_script/EXIF
```

A.3 Script for the generation of Figure 5.14

Similar scripts were used for the generation of figures from Figure 5.15 to Figure 5.21.

```
%% Importing data
clc;
clear variables;
close all;

if exist('DATA/PHOTOSCAN/Volo_1/NDVI_data')==9
    cd DATA/PHOTOSCAN/Volo_1/NDVI_data
    load('NDVI_data.mat')
    cd ../../../../..
else
    mkdir DATA/PHOTOSCAN/Volo_1/NDVI_data
cd ..

V=imread('POLIGONI\PHOTOSCAN\VOLO_1\NDVI\VEGETATION\VEGETAZIONE_VOLO1.tif');
V=double(V);
V1=reshape(V(:,:,1),numel(V(:,:,1)),1);
V2=reshape(V(:,:,2),numel(V(:,:,2)),1);
V3=reshape(V(:,:,3),numel(V(:,:,3)),1);
V4=reshape(V(:,:,4),numel(V(:,:,4)),1);
V=[V1 V2 V3 V4];

M=imread('POLIGONI\PHOTOSCAN\VOLO_1\NDVI\DEEP_WATER\VOLO_1_DEEP_WATER_NDVI.tif');
M=double(M);
M1=reshape(M(:,:,1),numel(M(:,:,1)),1);
M2=reshape(M(:,:,2),numel(M(:,:,2)),1);
M3=reshape(M(:,:,3),numel(M(:,:,3)),1);
M4=reshape(M(:,:,4),numel(M(:,:,4)),1);
M=[M1 M2 M3 M4];
```

```
S=imread('POLIGONI\PHOTOSCAN\VOLO_1\NDVI\SAND\SAND_VOLO1.tif');
S=double(S);
S1=reshape(S(:,:,1),numel(S(:,:,1)),1);
S2=reshape(S(:,:,2),numel(S(:,:,2)),1);
S3=reshape(S(:,:,3),numel(S(:,:,3)),1);
S4=reshape(S(:,:,4),numel(S(:,:,4)),1);
S=[S1 S2 S3 S4];

A=imread('POLIGONI\PHOTOSCAN\VOLO_1\NDVI\SEA_AND_SEAWEED\SEA_AND_SEAWEED_VOLO_1_ND
VI.tif');
A=double(A);
A1=reshape(A(:,:,1),numel(A(:,:,1)),1);
A2=reshape(A(:,:,2),numel(A(:,:,2)),1);
A3=reshape(A(:,:,3),numel(A(:,:,3)),1);
A4=reshape(A(:,:,4),numel(A(:,:,4)),1);
A=[A1 A2 A3 A4];

D1=[V1;M1;S1;A1];
D2=[V2;M2;S2;A2];
D3=[V3;M3;S3;A3];
D4=[V4;M4;S4;A4];

clear V1 V2 V3 V4
clear M1 M2 M3 M4
clear S1 S2 S3 S4
clear A1 A2 A3 A4

V(any(V>1,2),:)=[]; V(any(V<-1,2),:)=[];
V1=V(:,1); V2=V(:,2); V3=V(:,3); V4=V(:,4); clear V
M(any(M>1,2),:)=[]; M(any(M<-1,2),:)=[]; M(any(M==0,2),:)=[];
M1=M(:,1); M2=M(:,2); M3=M(:,3); M4=M(:,4); clear M
S(any(S>1,2),:)=[]; S(any(S<-1,2),:)=[];
S1=S(:,1); S2=S(:,2); S3=S(:,3); S4=S(:,4); clear S
A(any(A>1,2),:)=[]; A(any(A<-1,2),:)=[];
A1=A(:,1); A2=A(:,2); A3=A(:,3); A4=A(:,4); clear A

cd MATLAB_script/DATA/PHOTOSCAN/Volo_1/NDVI_data
save('NDVI_data.mat','V1','V2','V3','V4','M1','M2','M3','M4','S1','S2','S3',...
    'S4','A1','A2','A3','A4')
cd ../../../../..

end

%% Regions Scatterplot
close
figure('name','Regions Scatterplot')
subplot(1,4,1)
    scatter(V1,V2,1,'r','filled'),axis square, hold on,
    scatter(V1,V3,1,'b','filled'),axis square, hold on,
    scatter(V1,V4,1,'k','filled'),axis square, hold on,
    plot([-1 1],[-1 1],'linestyle','--','color',[0.5 0.5 0.5]), grid on
```

```
    xlabel('Raw NDVI'), ylabel('Corrected NDVI'), title('Vegetation')
    legend('Sun Sensor only', 'Reflectance Panel only',...
        'Both Sun Sensor and Reflectance Panel',...
        'location', 'southoutside')
subplot(1,4,2)
    scatter(M1,M2,1,'r','filled'),axis square, hold on,
    scatter(M1,M3,1,'b','filled'),axis square, hold on,
    scatter(M1,M4,1,'k','filled'),axis square, hold on,
    plot([-1 1],[-1 1],'linestyle','--','color',[0.5 0.5 0.5]), grid on
    xlabel('Raw NDVI'), ylabel('Corrected NDVI'), title('Deep Water')
    legend('Sun Sensor only', 'Reflectance Panel only',...
        'Both Sun Sensor and Reflectance Panel',...
        'location', 'southoutside')
subplot(1,4,3)
    scatter(S1,S2,1,'r','filled'),axis square, hold on,
    scatter(S1,S3,1,'b','filled'),axis square, hold on,
    scatter(S1,S4,1,'k','filled'),axis square, hold on,
    plot([-1 1],[-1 1],'linestyle','--','color',[0.5 0.5 0.5]), grid on
    xlabel('Raw NDVI'), ylabel('Corrected NDVI'), title('Sand')
    legend('Sun Sensor only', 'Reflectance Panel only',...
        'Both Sun Sensor and Reflectance Panel',...
        'location', 'southoutside')
subplot(1,4,4)
    scatter(A1,A2,1,'r','filled'),axis square, hold on,
    scatter(A1,A3,1,'b','filled'),axis square, hold on,
    scatter(A1,A4,1,'k','filled'),axis square, hold on,
    plot([-1 1],[-1 1],'linestyle','--','color',[0.5 0.5 0.5]), grid on
    xlabel('Raw NDVI'), ylabel('Corrected NDVI'), title('Submerged Seaweed')
    legend('Sun Sensor only', 'Reflectance Panel only',...
        'Both Sun Sensor and Reflectance Panel',...
        'location', 'southoutside')
h=gcf;
set(h,'units','normalized','position',[0 0.5 1 0.5])
set(h,'renderer','painters')
print('-
depsc','figure\PHOTOSCAN\VOLO_1\NDVI\Scatterplot_Regions_NDVI_comparison_VOLO1')

%% Vegetation histograms
ea=0.2;
close
limiti_assi=[-0.5 1 0];
figure('Name','Vegetation histograms')
subplot(4,1,1)
hV1=histogram(V1,'facecolor',[5 131 240]./255,'facealpha',0.4,'edgealpha',ea);
hV1.BinWidth = 0.005;
% xlabel('NDVI value','fontsize',8),
ylabel('frequency','fontsize',8)
title('Raw data')
axis([limiti_assi 1000]), ax=gca; ax.XAxis.Exponent=0; ax.YAxis.Exponent=0;
text((limiti_assi(1)+limiti_assi(2))/2,1000*1.35,'Vegetation',...
    'horizontalalignment','center','fontsize',14,'fontangle','italic')
```

```
subplot(4,1,2)
hV2=histogram(V2,'facecolor',[255 0 0]./255,'facealpha',0.4,'edgealpha',ea);
hV2.BinWidth = 0.005;
% xlabel('NDVI value','fontsize',8),
ylabel('frequency','fontsize',8)
title('Sun Sensor only')
axis([limiti_assi 1000]), ax=gca; ax.XAxis.Exponent=0; ax.YAxis.Exponent=0;
subplot(4,1,3)
hV3=histogram(V3,'facecolor',[244 255 91]./255,'facealpha',0.4,'edgealpha',ea);
hV3.BinWidth = 0.005;
% xlabel('NDVI value','fontsize',8),
ylabel('frequency','fontsize',8)
title('Reflectance Panel only')
axis([limiti_assi 1000]), ax=gca; ax.XAxis.Exponent=0; ax.YAxis.Exponent=0;
subplot(4,1,4)
hV4=histogram(V4,'facecolor',[90 255 90]./255,'facealpha',0.4,'edgealpha',ea);
hV4.BinWidth = 0.005;
title('Both Sun Sensor and Reflectance Panel')
axis([limiti_assi 1000]), ax=gca; ax.XAxis.Exponent=0; ax.YAxis.Exponent=0;
xlabel('NDVI value','fontsize',8), ylabel('frequency','fontsize',8)

hV=gcf;
set(hV,'units','normalized','position',[0 0 0.4 1])

%% Shallow Water histograms
ea=0.2;
close
figure('Name','Shallow Water histograms')
subplot(4,1,1)
hM1=histogram(M1,'facecolor',[5 131 240]./255,'facealpha',0.4,'edgealpha',ea);
hM1.BinWidth = 0.005;
% xlabel('NDVI value','fontsize',8),
ylabel('frequency','fontsize',8)
title('Raw data')
axis([limiti_assi 3500]), ax=gca; ax.XAxis.Exponent=0; ax.YAxis.Exponent=0;
text((limiti_assi(1)+limiti_assi(2))/2,3500*1.35,'Shallow Water',...
    'horizontalalignment','center','fontsize',14,'fontangle','italic')
subplot(4,1,2)
hM2=histogram(M2,'facecolor',[255 0 0]./255,'facealpha',0.4,'edgealpha',ea);
hM2.BinWidth = 0.005;
% xlabel('NDVI value','fontsize',8),
ylabel('frequency','fontsize',8)
title('Sun Sensor only')
axis([limiti_assi 3500]), ax=gca; ax.XAxis.Exponent=0; ax.YAxis.Exponent=0;
subplot(4,1,3)
hM3=histogram(M3,'facecolor',[244 255 91]./255,'facealpha',0.4,'edgealpha',ea);
hM3.BinWidth = 0.005;
% xlabel('NDVI value','fontsize',8),
ylabel('frequency','fontsize',8)
title('Reflectance Panel only')
axis([limiti_assi 3500]), ax=gca; ax.XAxis.Exponent=0; ax.YAxis.Exponent=0;
```

```
subplot(4,1,4)
hM4=histogram(M4,'facecolor',[90 255 90]./255,'facealpha',0.4,'edgealpha',ea);
hM4.BinWidth = 0.005;
title('Both Sun Sensor and Reflectance Panel')
axis([limiti_assi 3500]), ax=gca; ax.XAxis.Exponent=0; ax.YAxis.Exponent=0;
xlabel('NDVI value','fontsize',8), ylabel('frequency','fontsize',8)

hM=gcf;
set(hM,'units','normalized','position',[0 0 0.4 1])

%% Wet Sand histograms
ea=0.2;
close
figure('Name','Wet Sand histograms')
subplot(4,1,1)
hS1=histogram(S1,'facecolor',[5 131 240]./255,'facealpha',0.4,'edgealpha',ea);
hS1.BinWidth = 0.005;
% xlabel('NDVI value','fontsize',8),
ylabel('frequency','fontsize',8)
title('Raw data')
axis([limiti_assi 600]), ax=gca; ax.XAxis.Exponent=0; ax.YAxis.Exponent=0;
text((limiti_assi(1)+limiti_assi(2))/2,600*1.35,'Wet Sand',...
    'horizontalalignment','center','fontsize',14,'fontangle','italic')
subplot(4,1,2)
hS2=histogram(S2,'facecolor',[255 0 0]./255,'facealpha',0.4,'edgealpha',ea);
hS2.BinWidth = 0.005;
% xlabel('NDVI value','fontsize',8),
ylabel('frequency','fontsize',8)
title('Sun Sensor only')
axis([limiti_assi 600]), ax=gca; ax.XAxis.Exponent=0; ax.YAxis.Exponent=0;
subplot(4,1,3)
hS3=histogram(S3,'facecolor',[244 255 91]./255,'facealpha',0.4,'edgealpha',ea);
hS3.BinWidth = 0.005;
% xlabel('NDVI value','fontsize',8),
ylabel('frequency','fontsize',8)
title('Reflectance Panel only')
axis([limiti_assi 600]), ax=gca; ax.XAxis.Exponent=0; ax.YAxis.Exponent=0;
subplot(4,1,4)
hS4=histogram(S4,'facecolor',[90 255 90]./255,'facealpha',0.4,'edgealpha',ea);
hS4.BinWidth = 0.005;
title('Both Sun Sensor and Reflectance Panel')
axis([limiti_assi 600]), ax=gca; ax.XAxis.Exponent=0; ax.YAxis.Exponent=0;
xlabel('NDVI value','fontsize',8), ylabel('frequency','fontsize',8)

hS=gcf;
set(hS,'units','normalized','position',[0 0 0.4 1])

%% Sea and Seaweed histograms
ea=0.2;
close
figure('Name','Sea and Seaweed histograms')
```

```
subplot(4,1,1)
hA1=histogram(A1,'facecolor',[5 131 240]./255,'facealpha',0.4,'edgealpha',ea);
hA1.BinWidth = 0.005;
% xlabel('NDVI value','fontsize',8),
ylabel('frequency','fontsize',8)
title('Raw data')
axis([limiti_assi 30000]), ax=gca; ax.XAxis.Exponent=0; ax.YAxis.Exponent=0;
text((limiti_assi(1)+limiti_assi(2))/2,30000*1.35,'Sea and Seaweed',...
    'horizontalalignment','center','fontsize',14,'fontangle','italic')
subplot(4,1,2)
hA2=histogram(A2,'facecolor',[255 0 0]./255,'facealpha',0.4,'edgealpha',ea);
hA2.BinWidth = 0.005;
% xlabel('NDVI value','fontsize',8),
ylabel('frequency','fontsize',8)
title('Sun Sensor only')
axis([limiti_assi 30000]), ax=gca; ax.XAxis.Exponent=0; ax.YAxis.Exponent=0;
subplot(4,1,3)
hA3=histogram(A3,'facecolor',[244 255 91]./255,'facealpha',0.4,'edgealpha',ea);
hA3.BinWidth = 0.005;
% xlabel('NDVI value','fontsize',8),
ylabel('frequency','fontsize',8)
title('Reflectance Panel only')
axis([limiti_assi 30000]), ax=gca; ax.XAxis.Exponent=0; ax.YAxis.Exponent=0;
subplot(4,1,4)
hA4=histogram(A4,'facecolor',[90 255 90]./255,'facealpha',0.4,'edgealpha',ea);
hA4.BinWidth = 0.005;
title('Both Sun Sensor and Reflectance Panel')
axis([limiti_assi 30000]), ax=gca; ax.XAxis.Exponent=0; ax.YAxis.Exponent=0;
xlabel('NDVI value','fontsize',8), ylabel('frequency','fontsize',8)

hA=gcf;
set(hA,'units','normalized','position',[0 0 0.4 1])

%% All Regions histograms
limiti_assi=[-0.5 1 0]; ea=0.5; yml=0.1;
close
figure('Name','All Regions histograms')
subplot(4,1,1)
hV1=histogram(V1,'facecolor',[0 1 0],'facealpha',0.4,'edgealpha',ea);
hV1.BinWidth = 0.005; hold on
hM1=histogram(M1,'facecolor',[0 1 1],'facealpha',0.4,'edgealpha',ea);
hM1.BinWidth = 0.005;
hS1=histogram(S1,'facecolor',[1 0 0],'facealpha',0.4,'edgealpha',ea);
hS1.BinWidth = 0.005;
hA1=histogram(A1,'facecolor',[1 1 0],'facealpha',0.4,'edgealpha',ea);
hA1.BinWidth = 0.005;
% xlabel('NDVI value','fontsize',8),
ylabel('frequency','fontsize',8)
title('Raw data')
hV1.Normalization = 'probability';
hM1.Normalization = 'probability';
```

```
hS1.Normalization = 'probability';
hA1.Normalization = 'probability';
axis([limiti_assi yml]), ax=gca; ax.XAxis.Exponent=0; ax.YAxis.Exponent=0;
ax.XTick = limiti_assi(1):0.1:limiti_assi(2);
ax.YTick = 0:0.02:yml;
legend('Vegetation','Deep Water','Sand','Submerged Seaweed',...
    'location','eastoutside')

subplot(4,1,2)
hV2=histogram(V2,'facecolor',[0 1 0],'facealpha',0.4,'edgealpha',ea);
hV2.BinWidth = 0.005; hold on
hM2=histogram(M2,'facecolor',[0 1 1],'facealpha',0.4,'edgealpha',ea);
hM2.BinWidth = 0.005;
hS2=histogram(S2,'facecolor',[1 0 0],'facealpha',0.4,'edgealpha',ea);
hS2.BinWidth = 0.005;
hA2=histogram(A2,'facecolor',[1 1 0],'facealpha',0.4,'edgealpha',ea);
hA2.BinWidth = 0.005;
% xlabel('NDVI value','fontsize',8),
ylabel('frequency','fontsize',8)
title('Sun Sensor only')
hV2.Normalization = 'probability';
hM2.Normalization = 'probability';
hS2.Normalization = 'probability';
hA2.Normalization = 'probability';
axis([limiti_assi yml]), ax=gca; ax.XAxis.Exponent=0; ax.YAxis.Exponent=0;
ax.XTick = limiti_assi(1):0.1:limiti_assi(2);
ax.YTick = 0:0.02:yml;
legend('Vegetation','Deep Water','Sand','Submerged Seaweed',...
    'location','eastoutside')

subplot(4,1,3)
hV3=histogram(V3,'facecolor',[0 1 0],'facealpha',0.4,'edgealpha',ea);
hV3.BinWidth = 0.005; hold on
hM3=histogram(M3,'facecolor',[0 1 1],'facealpha',0.4,'edgealpha',ea);
hM3.BinWidth = 0.005;
hS3=histogram(S3,'facecolor',[1 0 0],'facealpha',0.4,'edgealpha',ea);
hS3.BinWidth = 0.005;
hA3=histogram(A3,'facecolor',[1 1 0],'facealpha',0.4,'edgealpha',ea);
hA3.BinWidth = 0.005;
% xlabel('NDVI value','fontsize',8),
ylabel('frequency','fontsize',8)
title('Reflectance Panel only')
hV3.Normalization = 'probability';
hM3.Normalization = 'probability';
hS3.Normalization = 'probability';
hA3.Normalization = 'probability';
axis([limiti_assi yml]), ax=gca; ax.XAxis.Exponent=0; ax.YAxis.Exponent=0;
ax.XTick = limiti_assi(1):0.1:limiti_assi(2);
ax.YTick = 0:0.02:yml;
legend('Vegetation','Deep Water','Sand','Submerged Seaweed',...
    'location','eastoutside')
```

```
subplot(4,1,4)
hV4=histogram(V4,'facecolor',[0 1 0],'facealpha',0.4,'edgealpha',ea);
hV4.BinWidth = 0.005; hold on
hM4=histogram(M4,'facecolor',[0 1 1],'facealpha',0.4,'edgealpha',ea);
hM4.BinWidth = 0.005;
hS4=histogram(S4,'facecolor',[1 0 0],'facealpha',0.4,'edgealpha',ea);
hS4.BinWidth = 0.005;
hA4=histogram(A4,'facecolor',[1 1 0],'facealpha',0.4,'edgealpha',ea);
hA4.BinWidth = 0.005;
xlabel('NDVI value','fontsize',8), ylabel('frequency','fontsize',8)
title('Both Sun Sensor and Reflectance Panel')
hV4.Normalization = 'probability';
hM4.Normalization = 'probability';
hS4.Normalization = 'probability';
hA4.Normalization = 'probability';
axis([limiti_assi yml]), ax=gca; ax.XAxis.Exponent=0; ax.YAxis.Exponent=0;
ax.XTick = limiti_assi(1):0.1:limiti_assi(2);
ax.YTick = 0:0.02:yml;
legend('Vegetation','Deep Water','Sand','Submerged Seaweed',...
    'location','eastoutside')

h=gcf;
set(h,'units','normalized','position',[0 0 0.5 1])
set(h,'renderer','painters')
print('-
dpdf','figure\PHOTOSCAN\VOLO_1\NDVI\Istogrammi_All_Regions_NDVI_comparison_VOLO1')

%% End of Script
cd MATLAB_script
close
return
```

A.4 Script to compute data for Table 5.5

```
clc, clear, close all

classi=12;   % numero delle classi (ROI)

if exist('DATA/25maggio/Sito_1')==7
    cd DATA/25maggio/Sito_1
    load('pixel_classificati.mat')
    cd ../../..
else
    mkdir DATA/25maggio/Sito_1

    nC=imread('F:\Sacca_di_Goro\25mag2018\elaborazioni\RedEdge\ENVI\Volo          1
nuovo\Corretto\Volo_1_6_bande_11_roi.tif');
    % nC=[0 2 1;2 1 0;2 3 3]; %test
    nC=double(nC);
    nC=reshape(nC(:,:,1),numel(nC(:,:,1)),1);
```

```
    C=imread('F:\Sacca_di_Goro\25mag2018\elaborazioni\RedEdge\ENVI\Volo 1 nuovo\Non
corretto\Volo_1_non_corretto_6_bande_11_roi.tif');
    % C=[2 1 1;2 1 1;2 2 3]; %test
    C=double(C);
    C=reshape(C(:,:,1),numel(C(:,:,1)),1);

    cd DATA/25maggio/Sito_1
    save('pixel_classificati.mat','C','nC')
    cd ../../..

end

G=[nC C]+1; % perché le classi in ENVI partono da zero

%%%%%%%%%%%%%%%%%%%%%%%
% per filtrare i dati in ingresso:
G(any(G>classi,2),:)=[]; G(any(G<1,2),:)=[];
%%%%%%%%%%%%%%%%%%%%%%%

M=zeros(classi,classi);
for i=1:classi
    for j=1:classi
       M(j,i)=length(G)-sum(any(G-[i j],2));
    end
end, r=0;

% così com'è adesso si legge in questo modo:
%            C
%      [... ... ...]
%   nC [...  M  ...]
%      [... ... ...]

%%%%%%%%%%%%%%%%%%%%%%%%%%%%%%%%%%%%
% per invertire righe e colonne in caso di necessità...
% M=M'; r=1; % (decommentare nel caso...)
% e diventa:
%            nC
%      [... ... ...]
%    C [...  M  ...]
%      [... ... ...]
%%%%%%%%%%%%%%%%%%%%%%%%%%%%%%%%%%%%


% Matrice di confusione in pixel:
disp('Matrice di confusione in pixel:'), disp(' ')
disp(M), disp(' ')
disp('Totale delle singole colonne:'), disp(' ')
disp(sum(M))

% Matrice di confusione in percentuale:
```

```
Mp=M*100./sum(M);
Mp(isnan(Mp))=0; % Sostituisco i NaN con 0
disp('Matrice di confusione in percentuale:')
disp('(La somma delle colonne è pari a 100)'), disp(' ')
disp(Mp)

% Calcolo la overall accuracy:
ov_acc=sum(diag(M))/sum(sum(M))*100;
disp(['The overall accuracy is: <<< ' num2str(ov_acc,4) ' % >>>'])

%%%%%%%%%%%%%%%%%%%%%%%%%%%%%%%%%%%%%%%%%%%%%%%%%%%%%%%%%%%%%%%%%%%%%%%%%%%%%%%
% Scrivo i risultati in un file di testo:
cd DATA/25maggio/Sito_1
    fid=fopen('report.txt','wt+');

    fprintf(fid,'Sito1 25maggio2018\n');
    fprintf(fid,'Matrice_di_confusione_in_pixel:\n');
    fprintf(fid,'\n');
    if r~=1
        fprintf(fid,'<<<-----_Corrected_orthomosaic_classes----->>>\n');
    else
        fprintf(fid,'<<<-----_Uncorrected_orthomosaic_classes_----->>>\n');
    end
    fprintf(fid,'Unclassified\t');
    fprintf(fid,'Vegetation_3\t');
    fprintf(fid,'Vegetation_1\t');
    fprintf(fid,'Vegetation_4\t');
    fprintf(fid,'Vegetation_2\t');
    fprintf(fid,'Dry_sand\t');
    fprintf(fid,'Wet_sand_1\t');
    fprintf(fid,'Deep_water\t');
    fprintf(fid,'Submerged_seaweed\t');
    fprintf(fid,'Emerged_seaweed\t');
    fprintf(fid,'Wet_sand_2\t');
    fprintf(fid,'Shadows\t');
    fprintf(fid,'Total\n');

    str=''; i=1;
    while i<=classi+1
        if i<=classi
            str=horzcat(str,['%0.0f\t']);
        else
            str=horzcat(str,['%0.0f\n']);
        end
        i=i+1;
    end
    M=[M sum(M')']
    fprintf(fid,str,M'); fprintf(fid,'\n');
    fprintf(fid,'Totale_delle_singole_colonne:\n');
    fprintf(fid,str,sum(M)');
    fprintf(fid,'\n'); fprintf(fid,'\n');
```

```
    fprintf(fid,'Matrice_di_confusione_in_percentuale:\n');
    fprintf(fid,'\n');
    if r~=1
        fprintf(fid,'<<<-----_Corrected_orthomosaic_classes_----->>>\n');
    else
        fprintf(fid,'<<<-----_Uncorrected_orthomosaic_classes_----->>>\n');
    end
    fprintf(fid,'Unclassified\t');
    fprintf(fid,'Vegetation_3\t');
    fprintf(fid,'Vegetation_1\t');
    fprintf(fid,'Vegetation_4\t');
    fprintf(fid,'Vegetation_2\t');
    fprintf(fid,'Dry_sand\t');
    fprintf(fid,'Wet_sand_1\t');
    fprintf(fid,'Deep_water\t');
    fprintf(fid,'Submerged_seaweed\t');
    fprintf(fid,'Emerged_seaweed\t');
    fprintf(fid,'Wet_sand_2\t');
    fprintf(fid,'Shadows\t');
    fprintf(fid,'Total\n');

    str=''; i=1;
    while i<=classi+1
        if i<=classi
            str=horzcat(str,['%3.2f\t']);
        else
            str=horzcat(str,['%3.2f\n']);
        end
        i=i+1;
    end
    Mp=[Mp [sum(M')*100./sum(sum(M))]']
    fprintf(fid,str,Mp'); fprintf(fid,'\n');
    fprintf(fid,'Totale_delle_singole_colonne:\n');
    fprintf(fid,str,sum(Mp)');
    fprintf(fid,'\n'); fprintf(fid,'\n');

    fprintf(fid,'The_overall_accuracy_is:_<<<_');
    fprintf(fid,'%3.2f',ov_acc);
    fprintf(fid,'%%_>>>');

    fclose(fid);
    clear str
cd ../../..
%%%%%%%%%%%%%%%%%%%%%%%%%%%%%%%%%%%%%%%%%%%%%%%%%%%%%%%%%%%%%%%%%%%%%%%%%%%%%%%%
```